Ion Beam Effects in GaAs-AlGaAs Materials and Devices

Hark Hoe Tan

A thesis submitted for the degree of

Doctor of Philosophy

of the

Australian National University

November 1996

This thesis does not incorporate any material previously submitted for a degree or diploma at any university and to the best of my knowledge and belief, does not contain any material previously published or written by another person except where due reference is made in the text.

H.H. Tan

November 1996

To my parents and my wife.

Acknowledgments

I would like to extend my sincere thanks to my supervisors, Prof. Jim Williams and Dr. Chennupati Jagadish for their invaluable guidance and continual support. They have been a constant source of inspiration. Their patience and encouragement are also greatly appreciated throughout the ups and downs of my PhD work. Thanks are also due to my co-adviser, Prof. Greg Clark, for his support.

I would also like to thank the following staff and fellow students at the department for providing a conducive working atmosphere and the many enjoyable discussions and conversations, in both science and otherwise :
Drs. Rob Elliman and Mark Ridgway (ion beam area),
Mr. Andrew Clark and Dr. Gang Li (aspects of epitaxial growth),
Drs. Tim Thompson, Nick Hauser, Mladen Petravic (various technical aspects)
Dr. Nick Welham (for proof reading my thesis)
Mr. Michael Aggett, Mr. Tony Watt, Mr. Alan Hayes, Mr. Bernie King and Mr. Tom Halstead (technical support),
Mr. John Glasko, Mr. Kidane Belay, Ms. Jennifer Wong-Leung and Mr. W.C. Wong (for being great fellow students to work with) and
Ms. Toni Purdy, Mrs. Annemarie Boyan and Mrs. Julia Peric (administrative support).

The Electron Microscope Unit at the University of Sydney is gratefully acknowledged for the transmission electron microscopy analyses, in particular Dr. Zou Jin for working on countless number of my samples and Prof. David Cockayne for stimulating discussions.

My appreciation is also extended to Assoc. Prof. Mike Gal for granting me access to his laboratory at The University of New South Wales for low temperature photoluminescence measurements. His support and encouragement have always been welcoming. The assistance of Mr. Patrick Burke in bringing me up to speed in the photoluminescence setup is greatly appreciated.

Special thanks are due to Dr. Fouad Karouta from the Eindhoven University of Technology for introducing me to the world of device processing. Without his guidance and patience there would not be a chapter 7 in the thesis.

It has also been a great pleasure working with Dr. Yong Kim from the Korean Institute of Science and Technology, who has passed on his invaluable experience in the growth of low dimensional structures on non-planar substrates.

The staff at the Department of Engineering at the Faculties are acknowledged for providing access to the cleanroom for photolithography work.

Both the financial assistance provided by AusAid (John Crawford Scholarship) and The Australian National University (PhD scholarship) are acknowledged.

I am indebted to my uncle and his wife in Melbourne for their undiminished support throughout my student years in Australia.

This thesis is dedicated to my parents, for without their understanding, encouragement and patience, this thesis would not be possible.

Finally, I thank my wife for her unconditional support, encouragement and belief in what I do.

Abstract

The objective of this thesis was to investigate and understand ion beam damage processes in GaAs-AlGaAs multilayers and apply this knowledge to specific optoelectronic devices. This ambitious project has not only covered many areas in the field of semiconductors, such as epitaxial growth, ion beam processing, material characterisation and device fabrication, but has also addressed the critical issues that often exist when these areas are collectively brought together during the fabrication of new generation optoelectronic devices. This work has bridged the gap that often exists between material science and device technology in the sense that it has brought together a variety of techniques of the two disciplines under a single theme.

The first part of this work has focussed on the systematic study of ion beam-induced defect formation, damage buildup and amorphisation processes in AlGaAs of various Al compositions. It was found that with increasing Al content, damage became more difficult to accumulate in AlGaAs due to strong dynamic annealing, even at liquid nitrogen temperatures. A difference in the amorphisation threshold dose of more than two orders of magnitude was observed between GaAs and AlAs with two different amorphisation processes observed depending on the Al content. This study was then extended to GaAs-AlGaAs multilayers under a range of implant conditions. The disordering processes were extremely complex in the multilayer system due to dynamic annealing, defect migration, trapping, annihilation across the interfaces and multilayer intermixing. Damage (amorphisation) built up preferentially in the GaAs layer. However, narrow regions in the GaAs layers near the interfaces could either delay amorphisation or induce amorphous phase formation in adjacent AlGaAs layers depending upon the implantation conditions.

In a parallel study, controlled amount of damage was introduced at very low doses ($\leq 10^{10}$ ions.cm^{-2}) into GaAs for comparison to the behaviour studied above at higher doses (10^{12}-10^{16} ions.cm^{-2}). In this dose regime, where the generation of simple discrete defects dominates, a comparative study of the defect behaviour for proton, oxygen and silicon implantation was investigated to indicate the nature of stable defects and the evolution of more complex clusters. Proton irradiation resulted in the creation of several discrete electron traps together with a broad U-band which was associated with the interaction between the discrete traps; whereas the results with the heavier ions (O and Si) were dominated by the broad U-band. Full recovery of the electrical properties was attained at 600 °C for samples implanted with protons but much higher temperatures ($\geq$ 800 °C) were required for oxygen and silicon implanted samples.

The second part of this work involved ion beam processing of quantum well structures for post-growth modification of the band structures. This section drew heavily on the knowledge and understanding of defect generation and interaction from the studies in the two dose regimes. Proton irradiation was found to controllably alter the emission wavelengths of the quantum wells after moderate annealing conditions with minimal loss of intensities. The wavelength shifts obtained were the largest achieved (> 200 meV) for wavelength tuning of GaAs-AlGaAs quantum wells and are most encouraging for optoelectronic device applications. The effects of heavy (arsenic) and chemically active ions (oxygen) were also compared to those of protons to form a correlation between disordering and intermixing processes. Protons were found to be more efficient in creating intermixing than the heavier arsenic ions, whereas oxygen retarded intermixing through the formation of oxygen-related complexes, which were thermally more stable during annealing.

Finally, two specific devices were fabricated to exploit the above technological advances. Ion implantation was used to modify the emission wavelengths of broad area GaAs-AlGaAs graded-index separate-confinement heterostructure (GRINSCH) quantum well lasers. Significant blue shift was observed with almost no degradation in the current threshold characteristics. This is the first time ion implantation was used to shift the emission wavelengths of GaAs-based quantum well lasers. A simple self-aligned dual-implantation technique was proposed and used to define current confinement region in quantum wire laser arrays grown on patterned V-groove substrates. This method could also be extended to create intermixing/disordering of the side walls enhancing the lateral energy confinement of the quantum wire regions.

In short, the main advances in GaAs-based technology resulting from this work are :

(i) a fundamental understanding of ion beam-induced damage/amorphisation processes and discrete defects and their evolution during annealing

(ii) development of wavelength shifting in quantum well structures by an optimised implantation and annealing scheme

(iii) use of ion implantation in the fabrication of novel optoelectronic devices

TABLE OF CONTENTS

Acknowledgments iv

Abstract vi

Chapter 1 Introduction 1

Chapter 2 Experimental Techniques 5

2.1 Introduction 5

2.2 Epitaxial growth 5

2.2.1 Growth rate 7

2.2.2 Al composition 8

2.2.3 Double-crystal X-ray diffraction (DCXRD) 10

2.2.4 *n*- and *p*-type doping 12

2.3 Ion implantation (ion irradiation) 13

2.4 Material characterisation 15

2.4.1 Rutherford backscattering spectrometry - ion channeling 15

2.4.2 Transmission electron microscopy 20

2.4.3 Capacitance-voltage (C-V) profiling and deep level transient spectroscopy (DLTS) 21

2.4.4 Photoluminescence (PL) 25

2.5 Device processing and testing 26

References 29

Chapter 3 Ion damage buildup in $Al_xGa_{1-x}As$ 31

3.1 Introduction 31

3.2 Experimental 32

3.3 Results 32

3.3.1 Damage buildup as a function of Al composition 32

3.3.2 Damage profiles in AlGaAs 42

3.3.3 Dose rate effects in AlGaAs 43

3.3.4 Recrystallisation effects in AlGaAs 46

3.4 Discussion 49

3.5 Conclusions 55

References 56

Chapter 4 Ion damage buildup in GaAs-$Al_xGa_{1-x}As$ multilayers 59
4.1 Introduction 59
4.2 Experimental 60
4.3 Results 61
4.3.1 AlGaAs layer between two GaAs layers (keV beams) 61
4.3.2 GaAs layer between two AlGaAs layer (keV beams) 68
4.3.3 MeV beams 74
4.4 Discussion 82
4.4.1 Damage buildup and dynamic annealing at heterointerfaces 83
4.4.2 Model to explain observations 84
4.4.3 Variation of damage with nuclear energy deposition 85
4.4.4 Stability of (liquid nitrogen temperature) implantation damage 86
4.5 Conclusions 89
References 90

Chapter 5 Deep levels in ion implanted GaAs at low doses 93
5.1 Introduction 93
5.2 Experimental 94
5.3 Effects of proton irradiation and annealing in undoped (intrinsic) GaAs 94
5.3.1 DLTS observations 94
5.5.2 Carrier compensation 102
5.3.3 Discussion 108
5.4 Deep levels created by oxygen and silicon in n-type GaAs 111
5.4.1 Results 111
5.4.2 Discussion 115
5.5 Conclusions 117
References 118

Chapter 6 Ion beam-induced intermixing in quantum wells 122
6.1 Introduction 122
6.2 Experimental 124
6.3 Proton irradiation 125
6.3.1 GaAs quantum wells with $Al_{0.54}Ga_{0.46}As$ barriers 125
6.3.2 GaAs quantum wells with $Al_{0.75}Ga_{0.25}As$ and $Al_{0.3}Ga_{0.7}As$ barriers 135
6.4 Arsenic and oxygen irradiation 138
6.4.1 Arsenic irradiation of GaAs quantum wells with $Al_{0.54}Ga_{0.46}As$ barriers 138
6.4.2 Oxygen irradiation of GaAs quantum wells with $Al_{0.54}Ga_{0.46}As$ barriers 141

6.5 Discussion 145
6.5.1 Al-Ga interdiffusion coefficient 145
6.5.2 Roles of defects 147
6.5.3 Proton irradiation 148
6.5.4 Comparison with arsenic and oxygen irradiations 151
6.6 Conclusions 153
References 154

Chapter 7 Optoelectronic device applications of ion beams 160
7.1 Introduction 160
7.2 Experimental 161
7.2.1 Wavelength shifting in ion implanted GaAs lasers 161
7.2.2 Quantum wire laser arrays 163
7.3 Results and discussion 166
7.3.1 Wavelength shifting in ion implanted GaAs lasers 166
7.3.2 Quantum wire laser arrays 169
7.4 Conclusions 171
References 172

Chapter 8 Summary 174

Appendix A Processing schedules 178
Appendix B Publication list 182

Chapter 1

Introduction

Ion implantation has been used to dope silicon for the past twenty years or so. During this time there has been much development of this technique due to its many desirable properties. Not surprisingly, the ion implantation technique has now reached maturity and forms an integral part of integrated-circuit fabrication. The advantages of ion implantation include, (i) precise and uniform incorporation of dopants (impurities), (ii) reproducibility and (iii) the incorporation of ions in certain localised regions (planar technology). However, there is a lag in development of this technology to GaAs-based devices, primarily due to the instability of GaAs during thermal annealing (in comparison to Si) to remove defects caused by ion implantation. Nevertheless, several significant advances have been made in the use of ion implantation doping in GaAs and more recently in heterojunction-based devices. Although defects induced by ion implantation are generally required to be annealed out for the dopant activation and to minimise device degradation, they have been intentionally used to selectively modify or fine tune a number of electrical and/or optical properties of semiconductors. For example, ion implantation is routinely used to create electrical isolation in III-V materials and devices. However, these defects must be introduced in a controlled manner or otherwise the material or device properties may be degraded. Thus, in order to optimise these processes, the need to study and understand irradiation-induced defects and their interactions in the material become crucial. Although a wealth of information has been gathered on damage formation and defect interaction in 'bulk' semiconductors such as Si, Ge, GaAs and InP in the past few decades, it is impossible to generalise across the range of semiconductors. This is particularly true for heterostructures with multilayers of differing materials and compositions due to the lack of detailed knowledge. Thus, these processes in heterostructures remain poorly understood. This issue needs to be addressed critically if ion beam techniques are to be developed and accepted for fabricating and processing multilayer heterojunction devices. Furthermore, as the device

dimensions become smaller, the effect of heterointerfaces on defect interactions and trapping becomes important.

The major aim of this thesis is to address the key issues associated with ion beam processing and to study the disordering and annealing processes in GaAs-AlGaAs materials. The results and understanding from these processes can then be applied to modify the properties of quantum well structures. Finally, this knowledge is combined in the fabrication of novel optoelectronic devices using ion beam techniques. No previous study has attempted such a comprehensive investigation such as this. In this sense, this study is useful in that covers the full spectrum from growth to devices in terms of the understanding of defects and their applications. The work reported in this thesis involves epitaxial growth, ion beam processing, characterisation of macroscopic and discrete defects, the application of controllable amount of defects to modify the properties of optoelectronic structures and the fabrication of novel optoelectronic devices using ion beams. Due to the vast spectrum of this work, many experimental techniques for characterisation, analysis, device fabrication and testing have been used.

The various experimental techniques and equipment used in this work are summarised in Chapter 2. Specifically engineered multilayer structures are grown by the Metal-Organic-Chemical-Vapour-Deposition (MOCVD) technique. Prior to being able to grow materials precisely and controllably, a great amount of work has been put into the calibration of the MOCVD reactor. The precise structures grown are to suit subsequent processing, device applications or analysis and characterisation techniques. Ion implantation is then carried out on these structures with a range of implantation parameters such as ion dose, energy, dose rate and implant temperature. A variety of techniques are used to analyse/characterise as-grown structures and to probe the effect of ion beams. These techniques include Rutherford backscattering spectrometry - ion channeling (RBS-C), cross-sectional transmission electron microscopy (XTEM), capacitance-voltage (C-V) profiling, deep level transient spectroscopy (DLTS) and photoluminescence (PL) spectroscopy. Device processing and testing are also briefly described in this chapter although the details of the processing steps are found in Appendix A.

In Chapter 3, the ion beam-induced damage accumulation and amorphisation processes are systematically investigated in 'bulk' $Al_xGa_{1-x}As$ of seven different Al compositions under Si bombardment. AlGaAs with high Al content is extremely difficult to amorphise and consequently, only implantation at liquid nitrogen temperature is investigated in detail. Analyses of the ion implanted materials are carried out *ex-situ* mainly by RBS-C

but selected samples are studied with XTEM to examine the microstructure. Since the samples have to be warmed up to room temperature for analysis, some recrystallisation may occur during the warming up process. Thus, selected samples are monitored *in situ* by an optical (time-resolved reflectivity) technique during implantation and following subsequent warming up. The experimental results are correlated with Monte-Carlo simulations of the damage profiles caused by the incoming ions. Results show that damage production dominates in GaAs but substantial dynamic annealing occurs in high Al content AlGaAs. This latter effect result in damage profiles which are significantly different from those expected from Monte Carlo calculations.

The ion implantation study is extended in Chapter 4 to GaAs-$Al_xGa_{1-x}As$ multilayers of two different Al compositions (x = 0.5 and 0.9). In this case, both keV and MeV energies are used. The low energy is used to study the effect near the surface where the energy deposition density of the ions varies sharply across the heterointerfaces. For MeV beams, the effects occurring at the heterointerfaces are investigated for a slowly varying deposition energy density of the ions. Both RBS-C and XTEM techniques are employed to characterise the disorder. Substantial effects at the interfaces on damage buildup and dynamic annealing are observed and the results of Chapter 3 are used to assist in explaining the observed behaviour.

In a parallel study, the characterisation of discrete deep level defects created by very low ion doses ($\leq 10^{10}$ cm^{-2}) in *n*-type GaAs has been undertaken with the results presented and discussed in Chapter 5. In this dose regime, simple discrete defects dominate, their thermal stability and effect on electronic properties are examined. DLTS and C-V profiling techniques are used to characterise the behaviour of such discrete defects. A comparative study of the nature of defects created by proton, oxygen and silicon ions and their annealing behaviour is also carried out. The results are discussed in terms of prior literature. This study formed a useful platform for the applications of ion beams discussed in Chapters 6 and 7.

In Chapter 6, ion implantation is used to induce intermixing in GaAs quantum wells to controllably modify their band structures. The resulting excitonic energies of the wells, as monitored by low temperature (12 K) photoluminescence (PL) spectroscopy technique, are shifted to higher energies. The effect of light ions (H) is compared with that of heavier ions, such as arsenic, and also chemically active impurities, such as oxygen. Various processing parameters such as implantation dose and temperature and annealing temperature and time are also investigated. The influence of Al content in the AlGaAs barriers on intermixing is also examined.

The results and understanding from all chapters are combined and applied to device processing in Chapter 7. In this chapter, two specific examples of the use of ion beams in the fabrication of devices are illustrated. First, proton irradiation is used to modify the band structure, and hence the emission wavelengths, of GRaded-INdex Separate-Confinement Heterostructure (GRINSCH) GaAs quantum well lasers. The effects of ion beam and annealing parameters on the current-threshold characteristics are investigated. This technique is very promising in integrating multiple lasers of different wavelengths onto a single chip for wavelength-division-multiplexing applications and can also be extended for the fabrication of other photonic integrated circuits. In another example, a *self-aligned dual-implantation* technique is proposed and used to provide current confinement in quantum wire laser arrays grown on V-groove patterned substrates. Although ion beam-induced electrical isolation is not specifically studied as part of this thesis, it has been a well-established technique to selectively define current confinement regions in III-V semiconductors. This self-aligned technique thus provides a very simple method of defining contact regions in quantum wire laser arrays without the need for further photolithography steps. This method could also be extended to create intermixing/disordering of the side walls of these V-grooves structures such that the lateral energy confinement of the quantum wire regions may be enhanced. Devices with excellent characteristics have been fabricated using such methods.

Finally, a summary and conclusions of this work are presented in Chapter 8.

Chapter 2

Experimental Techniques

2.1 Introduction

The main aim of this chapter is to outline the various experimental techniques used in this thesis such that any reader who is not familiar with any of these techniques can gain a general understanding of the technique. Since detailed explanation is way beyond the scope of this chapter, only the major principles and issues involved will be mentioned. Appropriate references will be given if further information about a specific technique is required. The experimental techniques employed here can essentially be separated into the four categories below :

- epitaxial growth,
- ion implantation (ion irradiation),
- material characterisation (ion beam analysis, electron microscopy, electrical and optical techniques) and
- device processing and testing.

2.2 Epitaxial growth

All the samples used in this work were grown at the Australian National University by Metal-Organic-Chemical-Vapour-Deposition (MOCVD), also commonly known as Metal-Organic-Vapour-Phase-Epitaxy (MOVPE). MOCVD is a cold wall thin film deposition process capable of depositing thin layers with atomically abrupt interfaces. The fundamental principle of this deposition process involves the vapour phase reactions between metal alkyls, such as trimethylgallium (TMG) and/or trimethylaluminium

(TMA) with hydrides such as arsine (AsH_3) or more recently, non-metallic alkyls, such as tertiarybutylarsine (TBA).

A typical reaction for the growth of GaAs is as follows :

$$Ga(CH_3)_3 + AsH_3 \rightarrow GaAs + 3CH_4 \quad (1)$$

or for $Al_xGa_{1-x}As$:

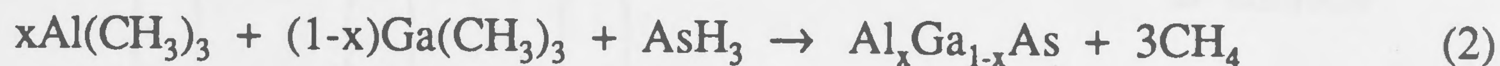

$$xAl(CH_3)_3 + (1-x)Ga(CH_3)_3 + AsH_3 \rightarrow Al_xGa_{1-x}As + 3CH_4 \quad (2)$$

The metal-organic precursors are normally volatile liquids at or near room temperature and are immersed in temperature controlled baths. The hydrides are highly toxic gases. The transport of the group III sources is done by flowing a carrier gas, normally ultrapure H_2 or N_2, through the metal-organic compounds *via* bubblers. A carefully control flow mixture of the metal-organic precursors and the hydride gases is then introduced into the growth chamber by means of electronic mass flow controllers. Growth takes place on the substrate which sits on a heated graphite or SiC coated graphite susceptor. Intentional doping may be achieved by introducing the appropriate dopant sources, such as dimethyl-zinc (*p*-type) or silane (*n*-type). The unreacted gas mixture which may still contain the toxic gases is then passed through a system to remove these gases before being released to the atmosphere. The system is normally an activated charcoal scrubber or a pyrolysis furnace. Further details of the MOCVD growth techniques can be found in various good textbooks and reviews.[1-3]

The MOCVD reactor used in this work was a modified MR Semicon reactor with a Thomas Swan cell. Fig. 2-1 shows the schematic of the MOCVD reactor. Two bubblers each of TMG and TMA were used to enable uninterrupted growth of GaAs-AlGaAs multilayers. AsH_3 was used as the group V source which was fed into two separately controlled lines to improve the controllability of the gas flow. Dimethyl-zinc (DMZ) of 5000 ppm dilution and silane (SiH_4) of 500 ppm dilution in ultra-high-purity H_2 were used as the *p*- and *n*-type dopants, respectively. SiC-coated graphite was used as the susceptor while heating was done via a three-zone infra-red lamp. All growths had been carried out at low pressure (76 Torr).

In order to achieve precise control of the growth of multilayer and quantum well structures, the reactor had been carefully calibrated in terms of growth rate, Al composition in AlGaAs, unintentional and intentional doping concentration and

uniformity. A variety of critical parameters were investigated such as carrier flow, growth pressure and temperature, metal-organic, hydride and dopant flow rates to optimise the growth conditions and establish a set of conditions relating the growth parameters to the desired epilayers. A detail discussion of the calibration procedures is beyond the scope of this thesis but several key results will be presented below.

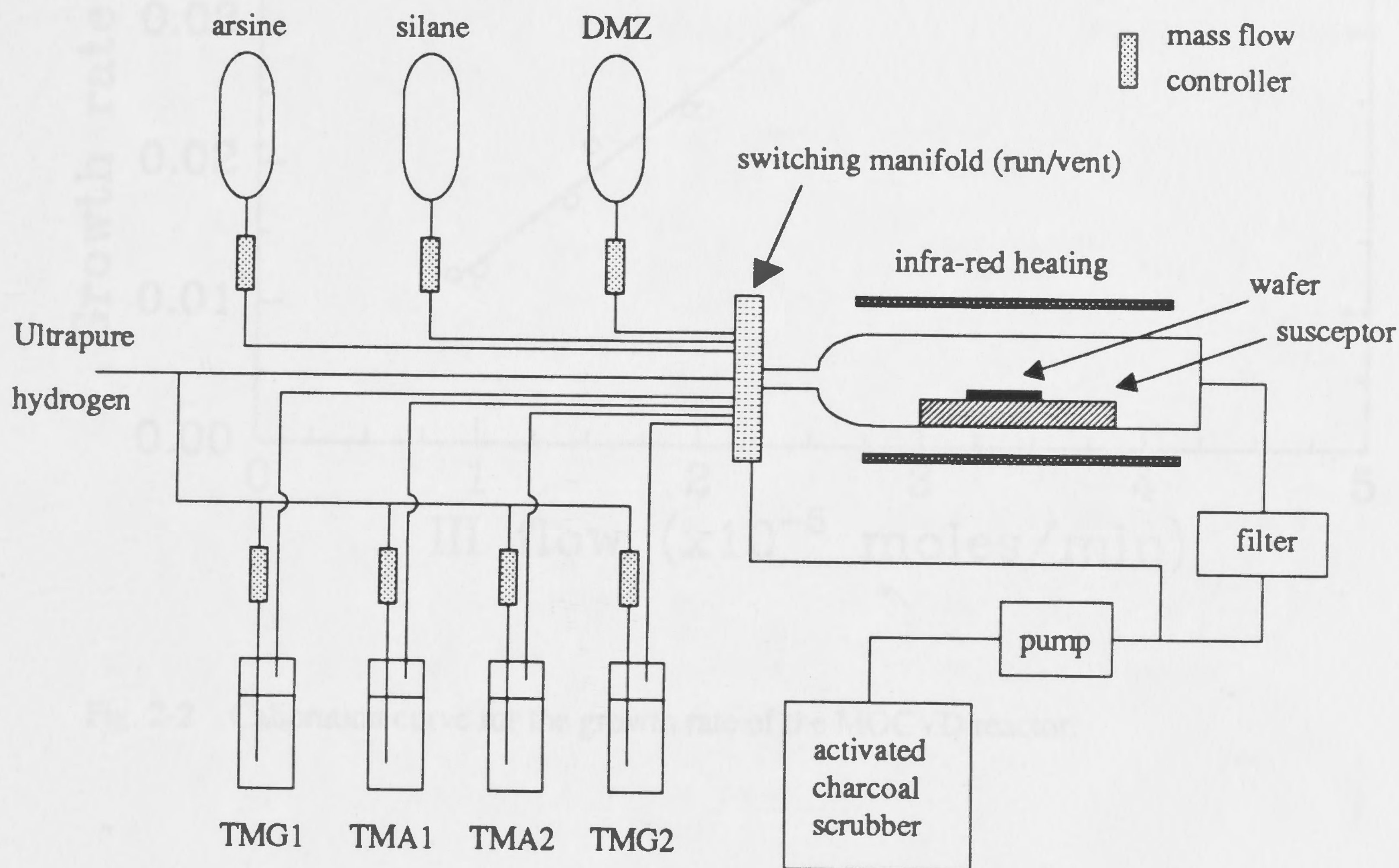

Fig. 2-1 Schematic of the MOCVD reactor used in this work.

2.2.1 *Growth rate*

The growth ambient generally has a large excess of the group V constituent over the metal alkyl. Thus, the growth rate is limited by the mass transport of the group III reactants to the growth surface. Fig. 2-2 shows a plot of the growth rate versus the flow of group III sources for this reactor. A linear relationship was found as

$$g = 1263.82 f_{III} + 4.497 \times 10^{-4} \tag{2.1}$$

where g is the growth rate in µm/min and f_{III} is the flow rate of group III reactants in moles/min.

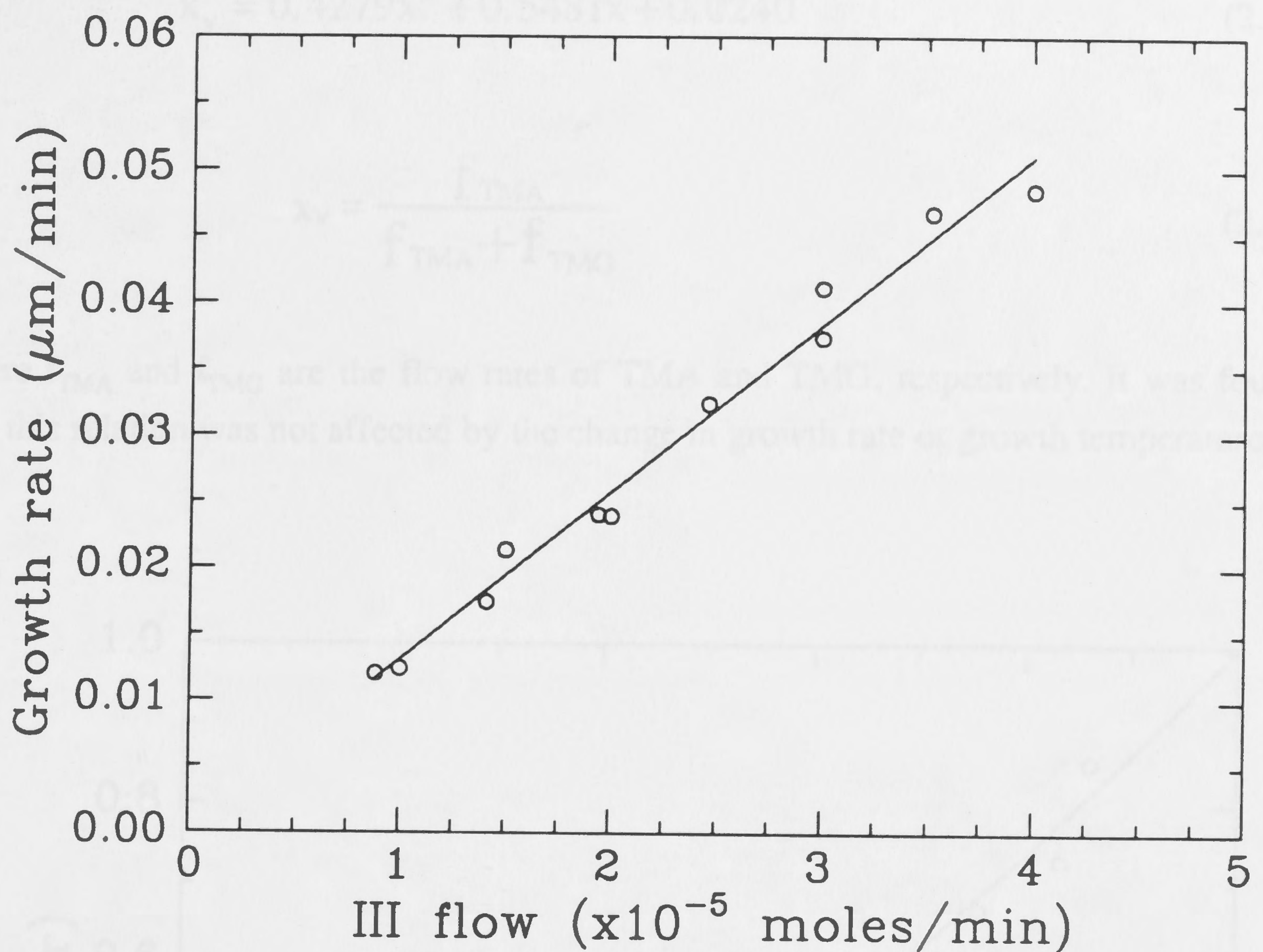

Fig. 2-2 Calibration curve for the growth rate of the MOCVD reactor.

Typical flow rates used were in the range of 8×10^{-6} to 4×10^{-5} moles/min which corresponds to the growth rate range of about 0.6 to 3 μm/hr. This range was sufficient to cover the growth of very thin quantum wells up to bulk layers (≥ 1 μm). It was found that the growth rate was almost independent of typical growth temperatures in the range of 600-750 °C. The carrier flow rate was also optimised to 17.5 standard litres/min to achieve a thickness uniformity of better than 2% over a 50 mm wafer.

2.2.2 Al composition

The Al mole fraction, x, in solid $Al_xGa_{1-x}As$ is related to the vapour phase ratio, x_v, of $Al(CH_3)_3/Ga(CH_3)_3$. This relationship was determined to follow a quadratic expression, as shown in Fig. 2-3. Thus, the Al content in $Al_xGa_{1-x}As$ as a function of TMG and TMA flow rates can be expressed as :

$$x_v = 0.4279x^2 + 0.5481x + 0.0240 \tag{2.2}$$

$$x_v = \frac{f_{TMA}}{f_{TMA} + f_{TMG}} \tag{2.3}$$

where f_{TMA} and f_{TMG} are the flow rates of TMA and TMG, respectively. It was found that this relation was not affected by the change in growth rate or growth temperature.

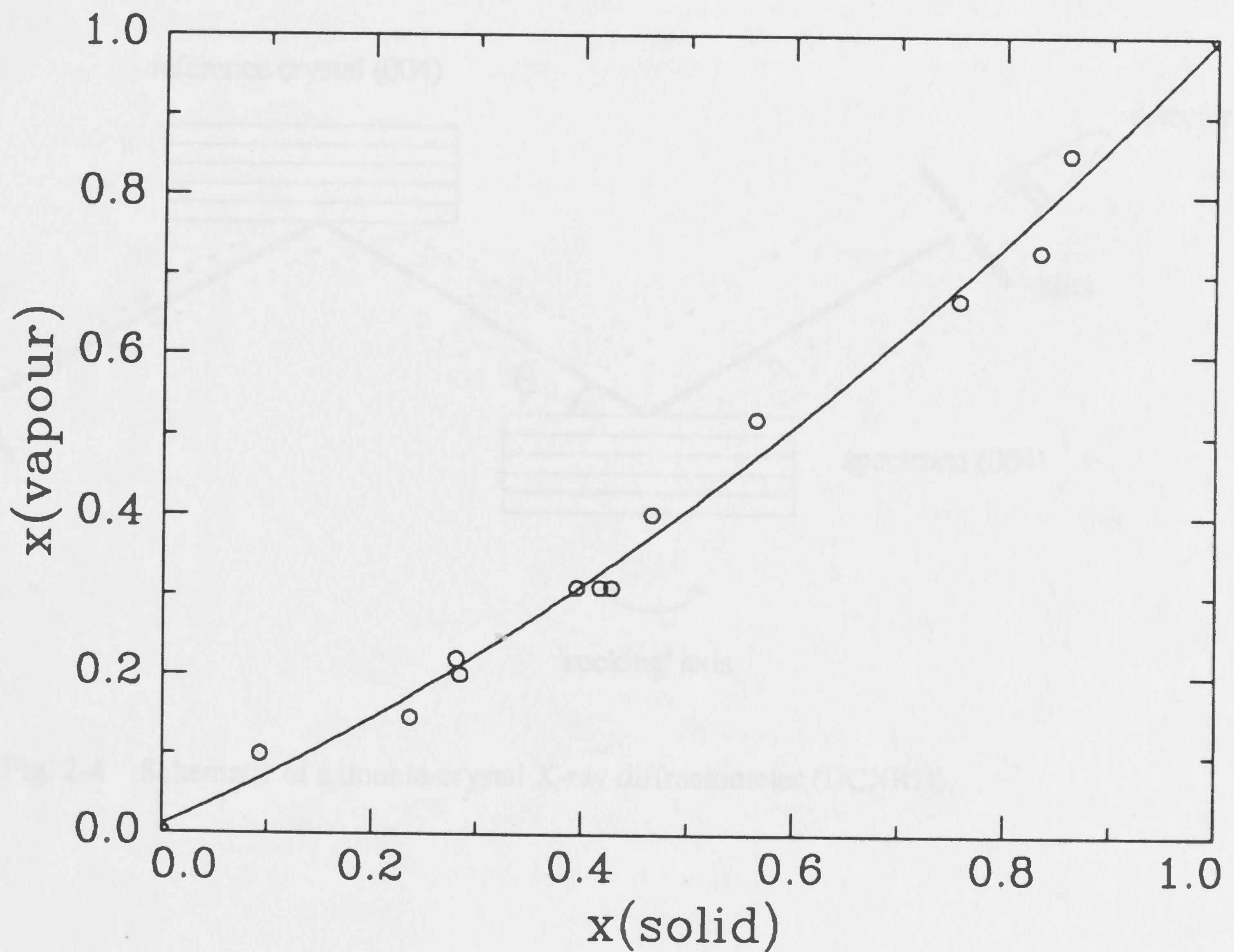

Fig. 2-3 $Al_xGa_{1-x}As$ calibration curve showing the relation between the Al mole fractions in the vapour and the solid phases.

2.2.3 *Double crystal X-ray diffraction (DCXRD)*

The determination of the Al mole fraction in AlGaAs was done using a double-crystal X-ray diffractometer (DCXRD) due to the small difference in the lattice parameters between GaAs and AlGaAs (or AlAs), which makes the separation of the epilayer and substrate Bragg peaks impossible in a single axis diffractometer. DCXRD is a non-destructive technique widely used for measurements of compositions, layer thickness and strain in epitaxial structures.[4,5] A Bede QC2a diffractometer was used in this work. The schematic of this system is shown in Fig. 2-4.

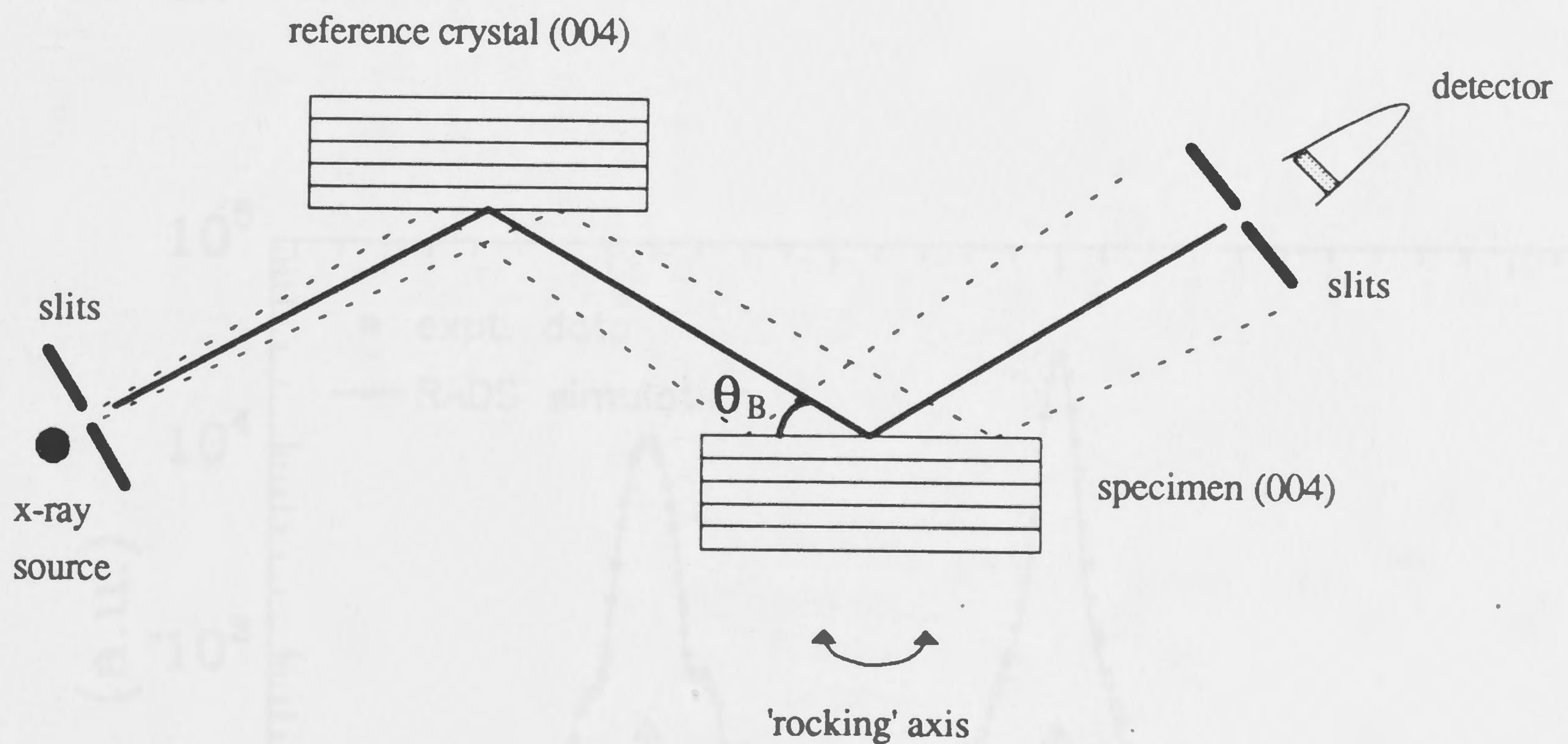

Fig. 2-4 Schematic of a double-crystal X-ray diffractometer (DCXRD).

A beam of Cu Kα X-rays is collimated to a reference crystal of the same material and orientation as the specimen which also acts as a monochromator. Bragg conditions are satisfied when the planes of the specimens are parallel to those of the reference crystal, i.e.

$$n\lambda = 2d\sin\theta_B \tag{2.4}$$

where d is the spacing of the Bragg planes, λ is the X-ray wavelength, θ_B is the Bragg angle [33.026° for (004) GaAs] and n is the order of diffraction (n=1,2,....). A slit is positioned in front of the detector to limit the angular divergence and hence improved resolution. A small rotation of the specimen with respect to the reference crystal will

result in the loss of intensity from the substrate. However, when the conditions of diffraction are satisfied for the Bragg spacing of the AlGaAs epilayer, a secondary peak is observed. The Al mole fraction in the AlGaAs layer can then be obtained from the 'rocking curve' by measuring the peak splitting and calculating the mismatch, assuming that the lattice constant of AlGaAs varies according to Vegard's law. However, if the layer is thin (< 0.5 μm), layer peak broadening and shifting of the AlGaAs peak may occur, making accurate determination of the Al composition impossible.[4] This problem can be overcome by simulating the rocking curves using a commercial software package, RADS.[6] This package is based on the generalised theory of diffraction developed by Takagi[7,8] and Taupin.[9] From the input variables of this simulation the Al content can be determined as illustrated in Fig. 2-5 for a rocking curve of an $Al_{0.46}Ga_{0.54}As$ layer.

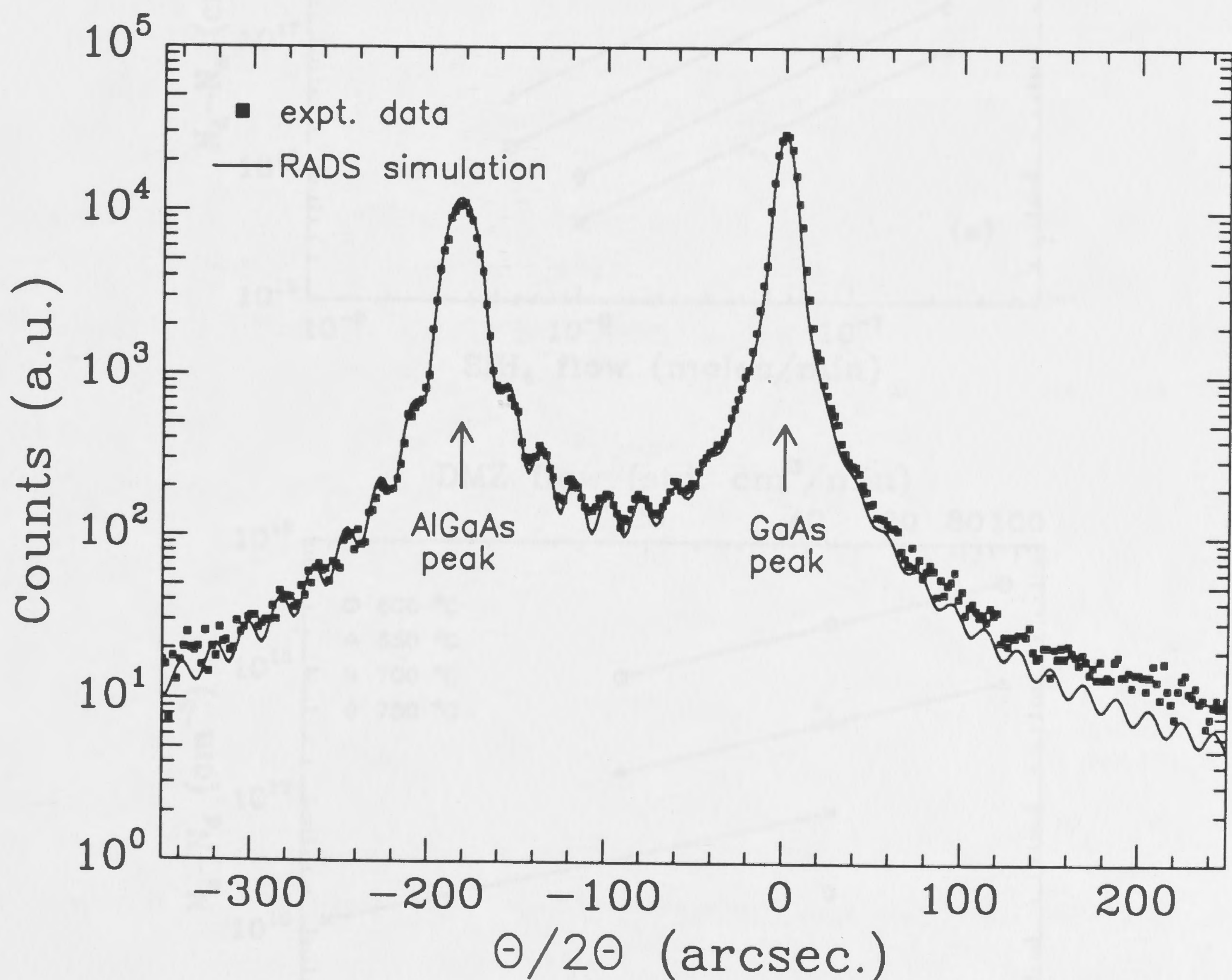

Fig. 2-5 DCXRD spectrum of an $Al_{0.46}Ga_{0.54}As$ layer grown on GaAs and the simulation curve obtained by RADS.[6]

2.2.4 *n- and p-type doping*

Doping of (Al)GaAs can be achieved by introducing either SiH_4 (*n*-type) or DMZ (*p*-type) into the gas phase along with group III and V precursors. The Si doping concentration was found to increase with the SiH_4 flow (partial pressure) or growth temperature while the Zn doping level increased with increasing DMZ flow (partial pressure) and decreasing temperature. These results are illustrated in Fig. 2-6.

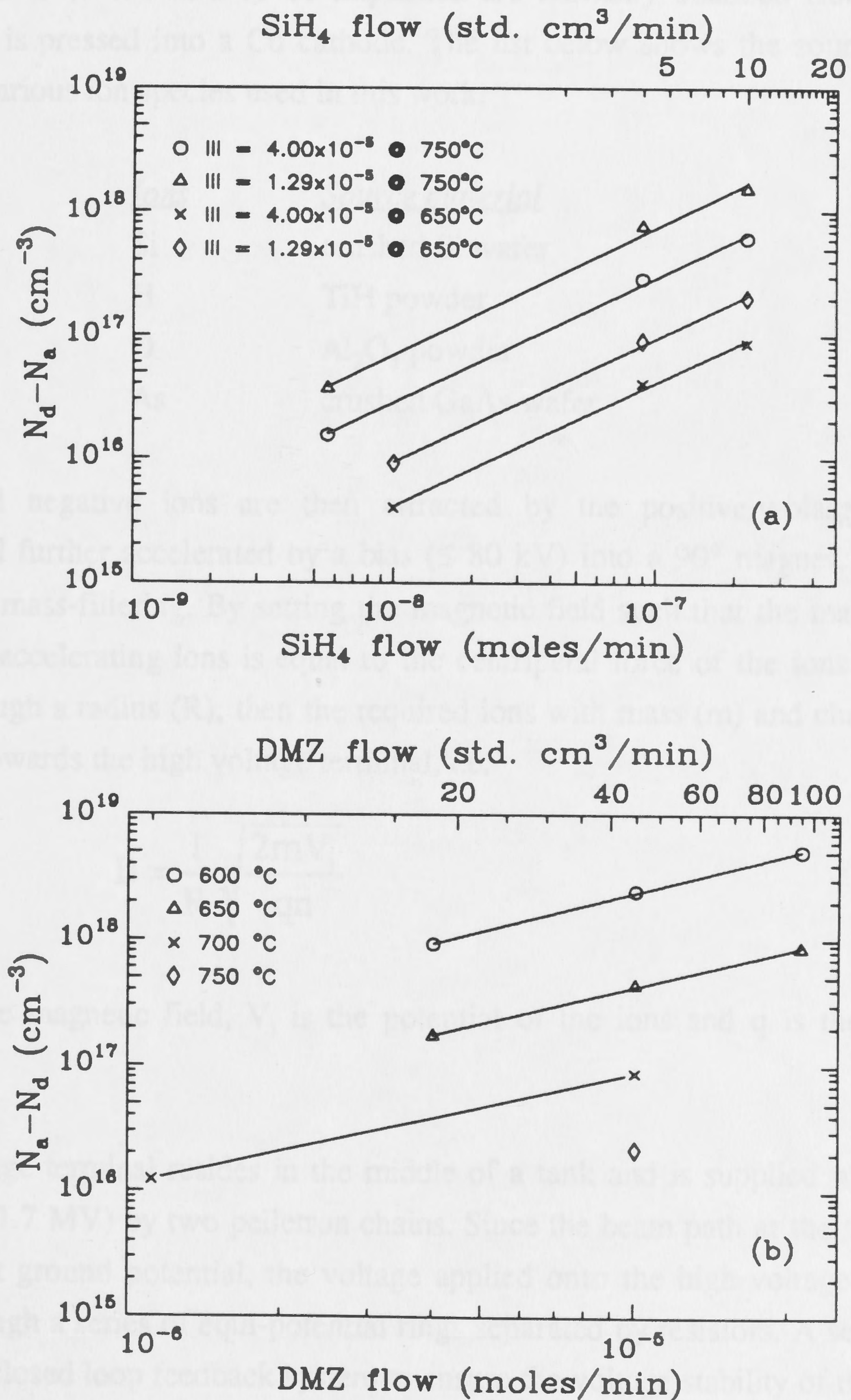

Fig. 2-6 Calibration curves for (a) *n*-type and (b) *p*-type doping of GaAs.

2.3 Ion implantation (ion irradiation)

The concept of ion implantation may be found in several good textbooks.[10-12] All ion implantation used in this work was performed on the National Electrostatics Corporation 5SDH-4 ion implanter. The accelerator is a tandem machine with a rating of 1.7 MV on the terminal. Fig. 2-7 shows the schematic of the ion implanter. The ion source is a SNICS-type[13,14] (Source of Negative Ions by Cesium Sputtering) where a stream of Cs vapour is ionised into Cs^+ which are then attracted to a negatively biased cathode ($\leq$ 10 kV). The ions to be implanted are normally obtained from a powder source which is pressed into a Cu cathode. The list below shows the source materials used for the various ion species used in this work.

Ions	*Source material*
Si	crushed Si wafer
H	TiH powder
O	Al_2O_3 powder
As	crushed GaAs wafer

The sputtered negative ions are then attracted by the positively-biased extractor ($\leq$ 15 kV) and further accelerated by a bias ($\leq$ 80 kV) into a 90° magnet, with a path radius, R, for mass-filtering. By setting the magnetic field such that the magnetic force acting on the accelerating ions is equal to the centripetal force of the ions as they are deflected through a radius (R), then the required ions with mass (m) and charge (n) will be deflected towards the high voltage terminal, i.e.

$$B = \frac{1}{R}\sqrt{\frac{2mV_i}{qn}} \tag{2.5}$$

where B is the magnetic field, V_i is the potential of the ions and q is the electronic charge.

The high voltage terminal resides in the middle of a tank and is supplied with positive charge (up to 1.7 MV) by two pelletron chains. Since the beam path at the two ends of the tank are at ground potential, the voltage applied onto the high voltage terminal is sustained through a series of equi-potential rings separated by resistors. A set of corona points form a closed loop feedback system to ensure the voltage stability of the terminal. Due to the high voltages in the tank, pressurised SF_6 gas is used in the tank for insulation purposes. The mass-filtered negative ions are then electrostatically steered

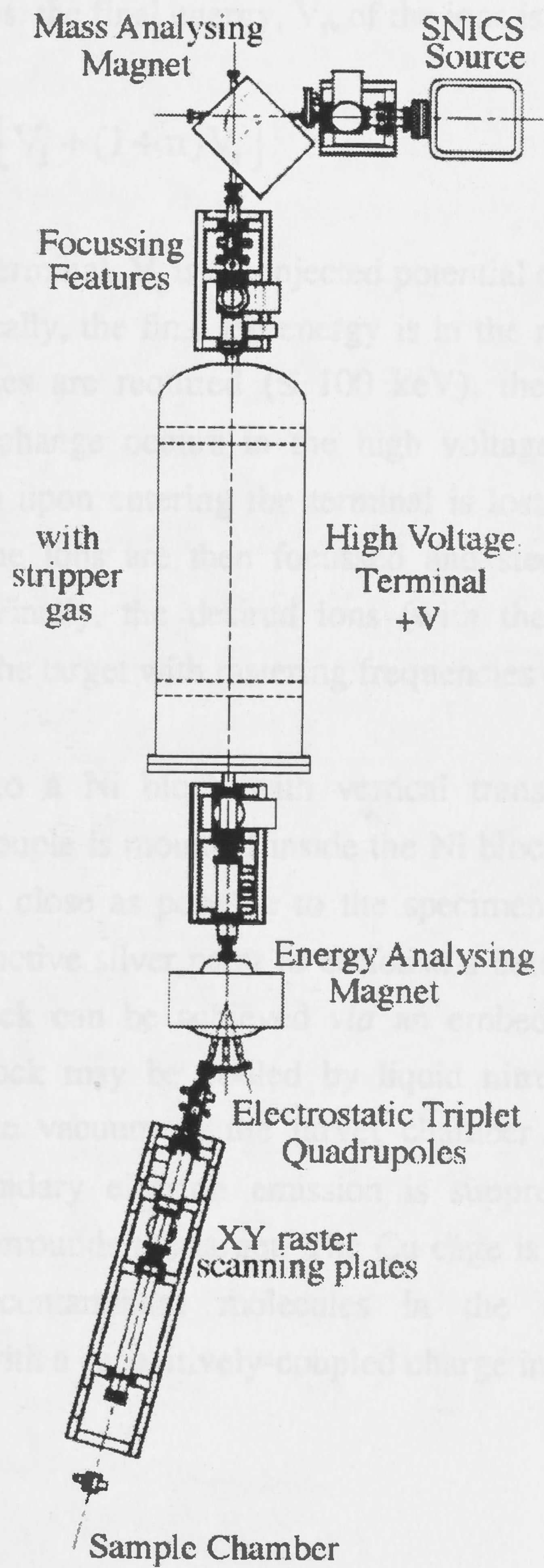

Fig. 2-7 Schematic of the 1.7 MV tandem ion accelerator used for ion implantation.

into the tank and accelerated towards the positive high voltage terminal. At this terminal, they are partially stripped of electrons in a nitrogen charge-exchange cell to become positive ions and as a result are further accelerated towards the other end of the tank (at ground potential). Thus, the final energy, V_f, of the ions is

$$V_f = q\left[V_i + (1+n)V_t\right] \tag{2.6}$$

where V_t is the voltage at the terminal, V_i is the injected potential of the ions and n is the charge state of the ions. Typically, the final ion energy is in the range of 0.2-10 MeV. However, if lower ion energies are required (≤ 100 keV), the stripping gas is not introduced and no charge exchange occurs in the high voltage terminal. Thus, the potential that the ions pick up upon entering the terminal is lost through deceleration upon leaving the terminal. The ions are then focussed and steered through another magnet for energy filtering. Finally, the desired ions (with the desired energy) are electrostatically scanned onto the target with rastering frequencies of 517 Hz by 64 Hz.

The targets are mounted onto a Ni block with vertical translation and rotational movements. A k-type thermocouple is mounted inside the Ni block close to the surface to measure the temperature as close as possible to the specimens. The specimens are held onto the block with conductive silver paint to establish a better thermal contact to the block. Heating of the block can be achieved *via* an embedded resistive heating element. Alternatively, the block may be cooled by liquid nitrogen. Implantation is normally carried out when the vacuum in the target chamber is ≤ 1×10^{-6} Torr to minimise contamination. Secondary electron emission is suppressed by a Cu cage maintained at -300 V that surrounds the target. The Cu cage is also cooled by liquid nitrogen to condense any contaminant molecules in the chamber. Dosimetry measurements are carried out with a capacitively-coupled charge integrator.

2.4 Material characterisation

2.4.1 Rutherford backscattering spectrometry - ion channeling

Rutherford backscattering spectrometry (RBS) is a well-established quantitative ion beam analysis technique. With this technique, a beam of mono-energetic light ions (such as H or He) is bombarded onto the specimen to be analysed. The backscattered ions are then collected and analysed for their energy distribution which will yield information

about the atomic constituents and also a depth profile of the target. If the incident ions are aligned along a low index crystallographic direction of a crystalline target (axial channeling), then most of the ions are steered into the 'channels' of the crystal, resulting in a much reduced backscattered ion yield. On the other hand, if the target is randomly oriented with respect to the incident ions, then less ions may be channeled along the crystallographic axes and more direct scattering will occur. This aligned technique is commonly referred to as ion channeling or RBS-channeling (RBS-C). Thus, if defects are present in the specimen, such as displaced atoms in the channeling paths, then the yield of the backscattered ions will increase. Hence, channeling spectrum may give a depth profile and the type of defects present in the material. Therefore, this technique is suitable in analysing ion beam-induced defects.

The geometry of the RBS detection system is important in the quantitative analysis of the results, such as, the depth profile. The energy loss of an incident ion with energy E_o in traversing a distance x, from the surface and backscattered by an As atom is related to the following expression,[15] as illustrated in Fig. 2-8 :

$$\Delta E_{As} = K_{As}E_o - E_{1,As} = [S]_{As}\, x \tag{2.7}$$

$$[S]_{As} = \frac{K_{As}}{\cos\theta_1}\frac{dE}{dx}\Big|_{in} + \frac{1}{\cos\theta_2}\frac{dE}{dx}\Big|_{out} \tag{2.8}$$

where K_{As} is the kinematic factor of As, $E_{1,As}$ is the energy of the ion backscattered off an As atom at x, $[S]_{As}$ is the energy loss factor of As and $dE/dx\,|_{in}$ and $dE/dx\,|_{out}$ are the rate of energy loss evaluated at the inward and outward paths, respectively. For regions near the surface, the depth, x, is small and hence, the relative change of the ion energy along an incident path is also small. Thus, it is sufficient to use a surface energy approximation which reduces the latter expression to

$$[S]_{As} = \frac{K_{As}}{\cos\theta_1}\frac{dE}{dx}\Big|_{E_o} + \frac{1}{\cos\theta_2}\frac{dE}{dx}\Big|_{K_{As}E_o} \tag{2.9}$$

Similar expressions are true for an ion scattering off a Ga atom. Further treatment of RBS and ion channeling may be found in references [15] and [16].

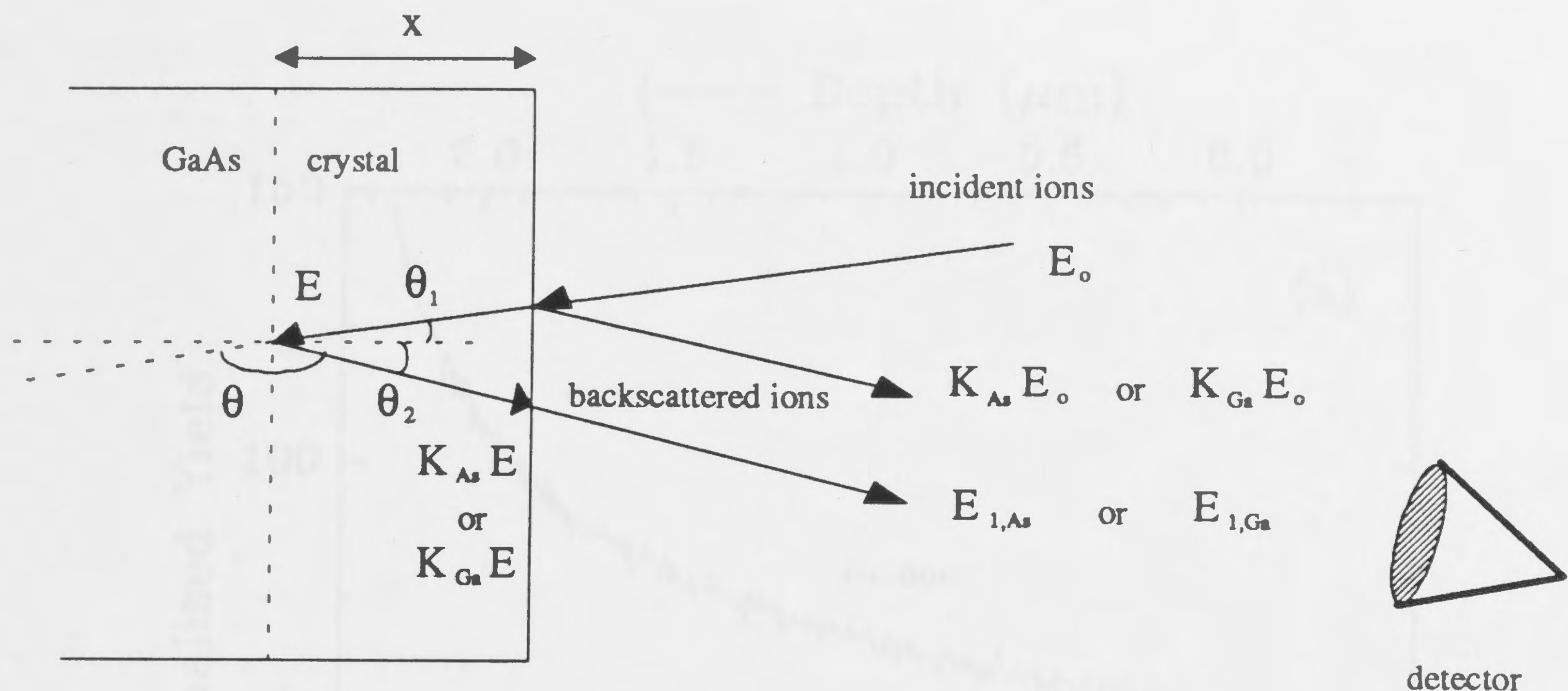

Fig. 2-8 Schematic representation of the backscattering process for a specific geometry.

Figs. 2-9(a) and (b) show the random and the aligned (channeled) spectra of a GaAs sample for a scattering angle, θ, of 168° and 100°, respectively. The corresponding depth scales as determined by equations (2.7) - (2.9) are also shown on the top axes. It can be seen from these figures that the depth resolution may be improved with a glancing angle (θ=100°) geometry.

Fig. 2-10 shows a schematic of a single-ended van de Graaff accelerator used for RBS-C analyses. Helium ions are generated by means of RF discharge of the He gas plasma which are then accelerated to the high voltage terminal which is maintained at 2 MeV. The positive charge on the terminal is supplied by charge transfer from the ground by means of an insulated belt. Similar to the ion implanter, a series of equi-potential rings are spaced along the ion source to the terminal to sustain the potential difference. A set of corona points are also in place to maintain and stabilise the terminal at the desired potential. The ions are then mass/energy-filtered for 2 MeV He^+ through a magnet before being steered onto the target. A collimator box is set along the path of the ions to define a well-collimated beam of particles. The target to be analysed is mounted onto a 4-axis goniometer for channeling measurements. Backscattered ions are collected by two Si Au-surface barrier detectors. One of the detectors is fixed at a scattering angle of 168° (backward detector) while the other is movable in the scattering angle range of 90-120° (glancing-angle detector). When a backscattered ion impinges on the detector, electron-hole pairs are generated which are then swept by an applied electric field. The resulting current pulse is proportional to the energy of the backscattered ions and is electronically amplified and recorded onto a multi-channel analyser.

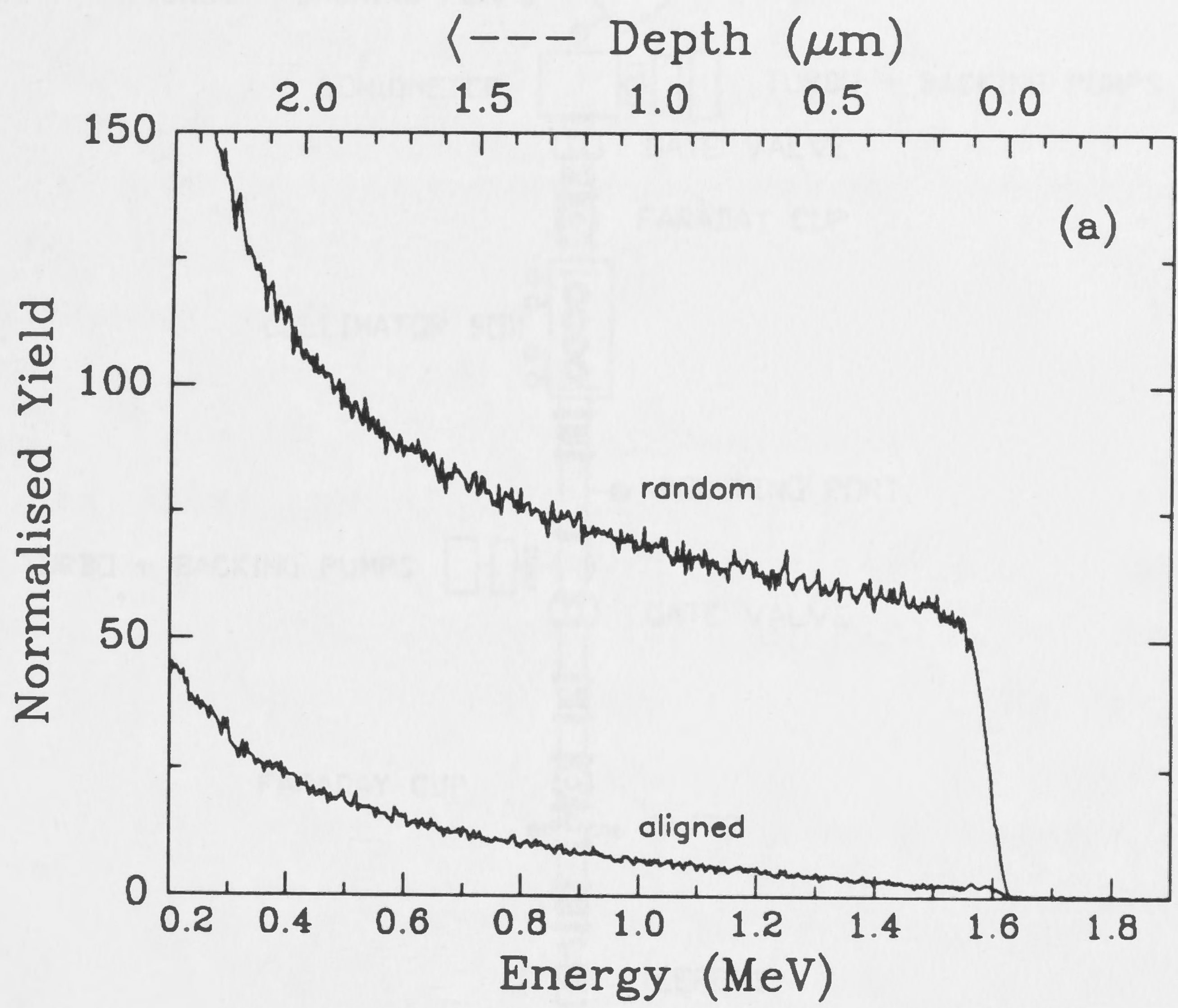

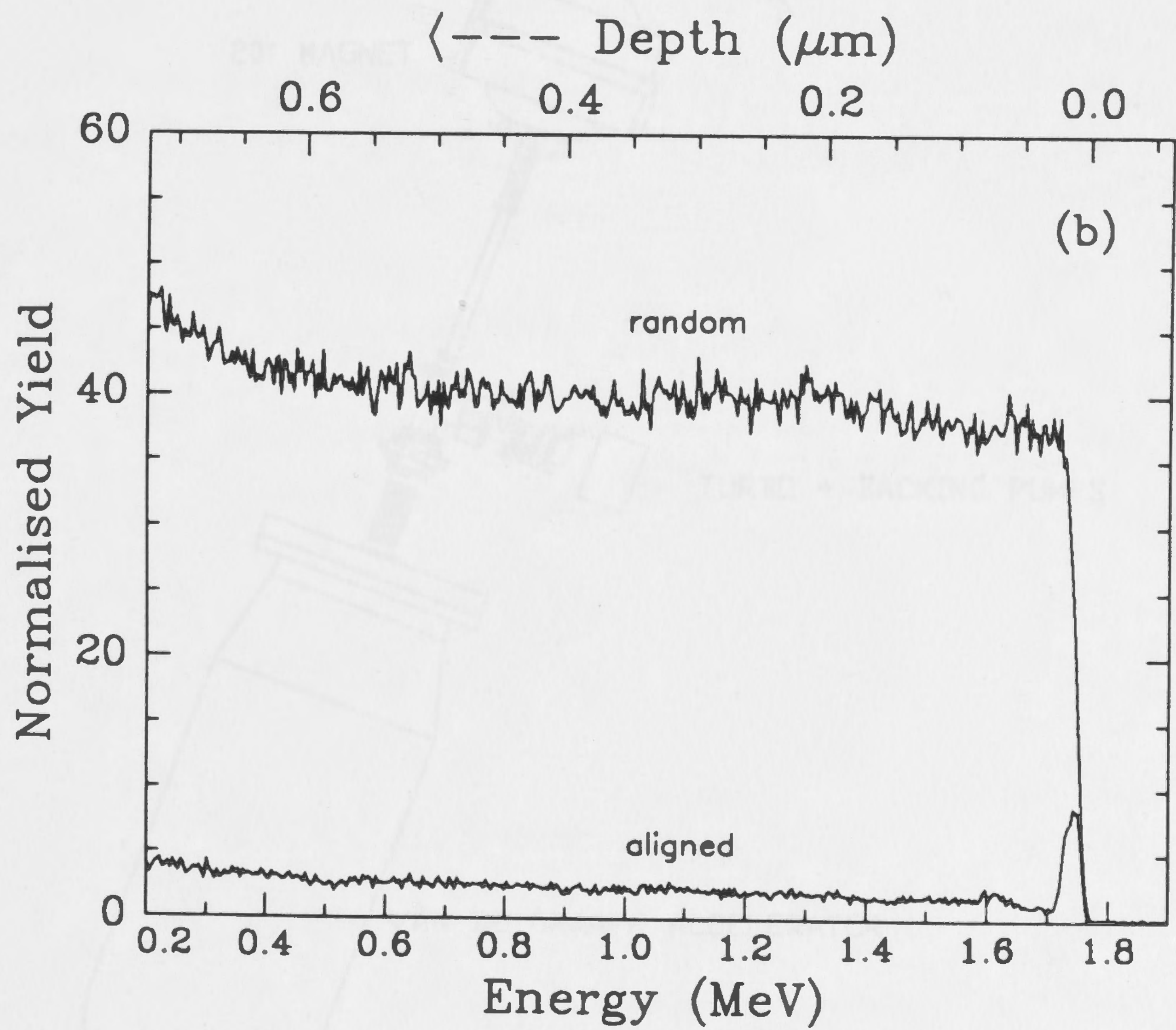

Fig. 2-9 Random and aligned (channeled) RBS spectra of GaAs at a scattering angle, θ of (a) 168° and (b) 100°.

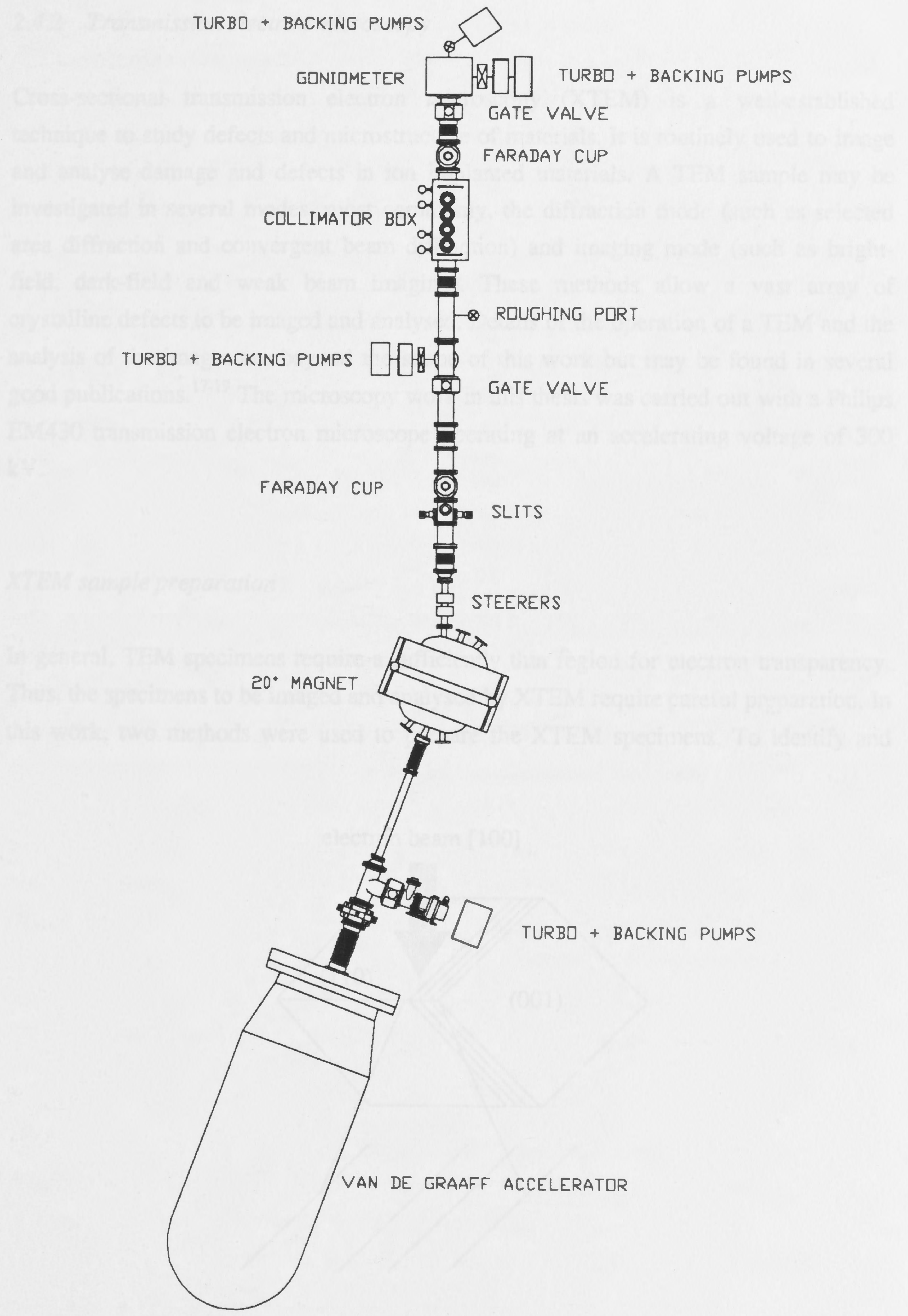

Fig. 2-10 Schematic of the single-ended van de Graaff accelerator used for RBS-C analysis.

2.4.2 Transmission electron microscopy

Cross-sectional transmission electron microscopy (XTEM) is a well-established technique to study defects and microstructure of materials. It is routinely used to image and analyse damage and defects in ion implanted materials. A TEM sample may be investigated in several modes, most commonly, the diffraction mode (such as selected area diffraction and convergent beam diffraction) and imaging mode (such as bright-field, dark-field and weak beam imaging). These methods allow a vast array of crystalline defects to be imaged and analysed. Details of the operation of a TEM and the analysis of the images are beyond the scope of this work but may be found in several good publications.[17-19] The microscopy work in this thesis was carried out with a Philips EM430 transmission electron microscope operating at an accelerating voltage of 300 kV.

XTEM sample preparation

In general, TEM specimens require a sufficiently thin region for electron transparency. Thus, the specimens to be imaged and analysed by XTEM require careful preparation. In this work, two methods were used to prepare the XTEM specimens. To identify and

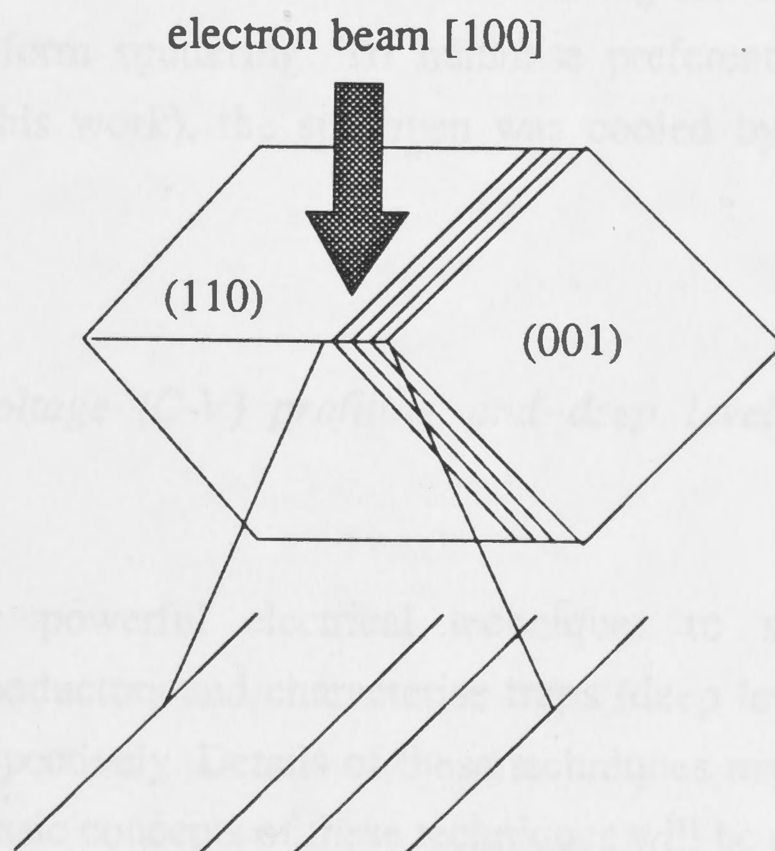

Fig. 2-11 A schematic illustrating the concept of imaging a 90° cleavage specimen by transmission electron microscopy. The electron beam is oriented parallel to the [100] axis.

image the basic structure of multilayers, a cleavage technique[20] was employed in which the sample was cleaved along two orthogonal {100} planes from a (100) top surface. The specimen was then mounted on a home-made Cu grid using silver paint. When the specimen was inserted in the transmission electron microscope, the [100] zone axis was oriented with the 90° wedge along the electron path as shown in Fig. 2-11. This technique provides a simple way for identifying the GaAs-AlGaAs multilayer structures.

For the study and analysis of defects in ion implanted materials, the conventional method of 'ion beam thinning' was employed. In this method, a piece of (ion implanted) sample was cleaved along {110} planes into a few thin slices, measuring about 3x1 mm^2. Two slices were then glued with the implanted sides face-to-face with each other using M-Bond 610 glue. The glue could be cured by either baking the sample in an oven at 130 ° C for 2 hours for maximum strength or leaving it in air for 24 hours (if the sample should not be subjected to heat treatment). The sample was then mechanically polished to achieve reasonably smooth surfaces on both sides of the sample, perpendicular to the glue seam by successively using finer grades of SiC paper until about 100 μm of material was left. Then one side of sample was polished with 0.05 μm Al polishing suspension to achieve a very smooth finish. The other side was mechanically dimpled at the centre of sample until about 10 μm of material was left and finally polished to achieve a very smooth finish using a Gatan 655 Dimple Grinder. The sample was then mounted on a Cu slot grid with silver paint. Final thinning to electron transparency was carried out by a 3 keV beam of Ar ions in a Gatan 600 Ion Mill. During ion milling the specimen was rotated to ensure uniform sputtering. To minimise preferential sputtering of certain elements (arsenic in this work), the specimen was cooled by a liquid nitrogen stage during ion milling.

2.4.3 Capacitance-voltage (C-V) profiling and deep level transient spectroscopy (DLTS)

C-V and DLTS are powerful electrical techniques to spatially resolve carrier distributions in semiconductors and characterise traps (deep levels) within the bandgap of semiconductors, respectively. Details of these techniques may be found in references [21] and [22] but the basic concepts of these techniques will be outlined below.

For a metal-semiconductor (or abrupt p-n) junction, the effect of band bending results in a region with depleted carriers (depletion region). By measuring the depletion capacitance in this region as a function of applied bias, spatial information about the

ionised impurities in this region may be obtained, which can ultimately be related to the carrier distribution according to the following equations[21] :

$$C = A\left(\frac{\varepsilon N}{2}\right)^{\frac{1}{2}}\left\{V - \frac{kT}{e}\left[1 - \exp\left(\frac{-eV}{kT}\right)\right]\right\}^{-\frac{1}{2}} \cdot \left\{1 - \exp\left(\frac{-eV}{kT}\right)\right\} \quad (2.10)$$

$$x_d = \frac{\varepsilon A}{C} \quad (2.11)$$

with the following meaning for the symbols :

C	depletion capacitance (F)	T	temperature (K)
ε	dielectric constant (Fm^{-1})	e	electronic charge (C)
N	donor or acceptor density (m^{-3})	x_d	depletion width or depth (m)
V	applied voltage (V)	A	area of contact (m^2)
k	Boltzmann's constant (JK^{-1})		

Fig. 2-12 illustrates the concept behind the DLTS technique.[23] This technique is related to the observation of transient emission from a majority trap following a pulse excitation of the deep levels. In this work, the capacitance transient is being observed. The diode (sample) under test is held under a reverse bias, $-V_r$, and then pulsed (V_p) at a rate of t_m to near zero bias to fill the traps with majority carriers. The pulse is held for a fixed time, t_p, (10 ms in this work) and then removed. Immediately after the pulse is removed, the reverse bias causes the trapped carriers to be emitted at a particular rate which can then be monitored by measuring the capacitance transient. The key feature behind DLTS is to relate this transient to a 'rate window' which provides maximum output when the time constant of a particular trap is equal to the time constant of the rate window. Thus, by measuring the capacitance transient as a function of temperature, traps with different emission rates (time constants) will coincide with the time constant of the rate window at different temperatures, resulting in peaks in the DLTS spectrum corresponding to the different traps. The are several methods of implementing the rate window and in this work a lock-in type method with a square wave weighting function was used.

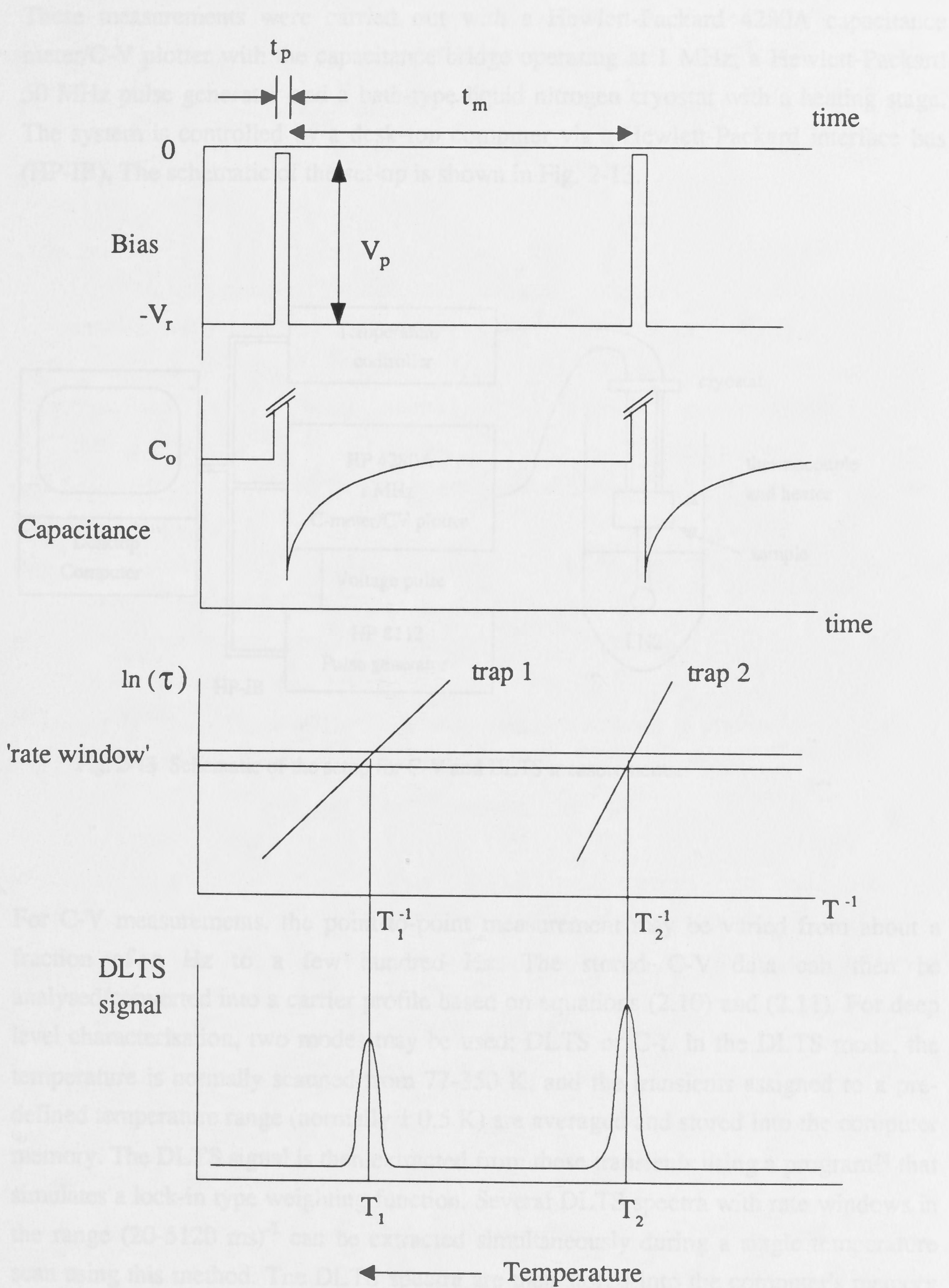

Fig. 2-12 Diagram illustrating the concept of DLTS (from reference [21]).

These measurements were carried out with a Hewlett-Packard 4280A capacitance meter/C-V plotter with the capacitance bridge operating at 1 MHz, a Hewlett-Packard 50 MHz pulse generator and a bath-type liquid nitrogen cryostat with a heating stage. The system is controlled by a desk-top computer via a Hewlett-Packard interface bus (HP-IB). The schematic of the set-up is shown in Fig. 2-13.

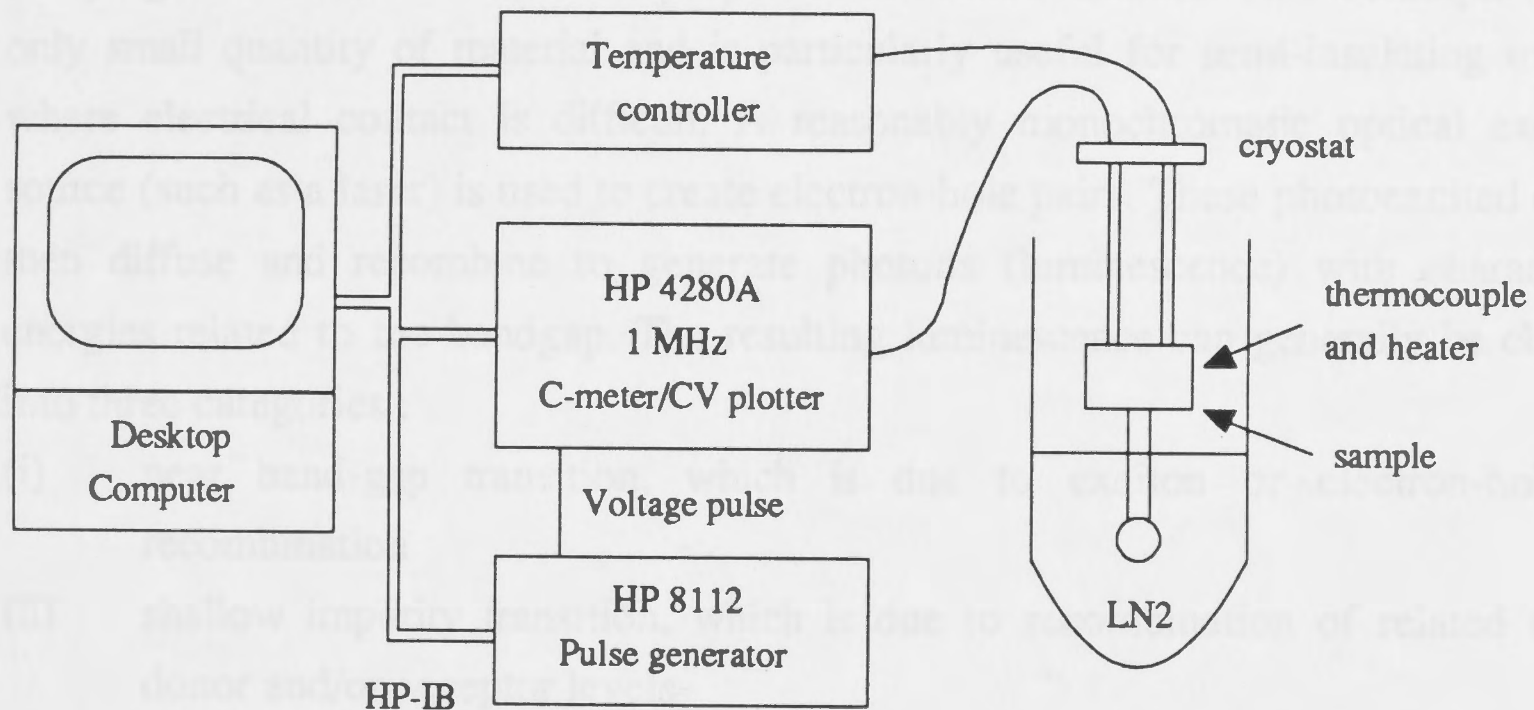

Fig. 2-13 Schematic of the setup for C-V and DLTS measurements.

For C-V measurements, the point-to-point measurement may be varied from about a fraction of a Hz to a few hundred Hz. The stored C-V data can then be analysed/converted into a carrier profile based on equations (2.10) and (2.11). For deep level characterisation, two modes may be used; DLTS or C-t. In the DLTS mode, the temperature is normally scanned from 77-350 K, and the transients assigned to a pre-defined temperature range (normally ± 0.5 K) are averaged and stored into the computer memory. The DLTS signal is then extracted from these transients using a program[24] that simulates a lock-in type weighting function. Several DLTS spectra with rate windows in the range $(20\text{-}5120\ \text{ms})^{-1}$ can be extracted simultaneously during a single temperature scan using this method. The DLTS spectra are then stored into the computer's memory or on a diskette for later analysis or simulation for determining the energy levels and capture cross sections of the traps. For C-t measurements, the temperature is kept fixed to within a pre-defined range (normally ±0.5 K) as the transients are repetitively measured and averaged in the computer's memory. This procedure may be repeated at

other temperatures of interest. The energy levels and capture cross sections of the traps can then be extracted by fitting the averaged transients with exponentials.

2.4.4 Photoluminescence (PL)

Photoluminescence is a very powerful and non-destructive spectroscopic technique for studying the intrinsic and extrinsic properties of semiconductors. This technique requires only small quantity of material and is particularly useful for semi-insulating materials where electrical contact is difficult. A reasonably monochromatic optical excitation source (such as a laser) is used to create electron-hole pairs. These photoexcited carriers then diffuse and recombine to generate photons (luminescence) with characteristic energies related to the bandgap. The resulting luminescence can generally be classified into three categories :

(i) near band-gap transition, which is due to exciton or electron-hole pair recombination

(ii) shallow impurity transition, which is due to recombination of related shallow donor and/or acceptor levels

(iii) deep level transition, in which recombination at deep impurities/defects occurs (typically > 100 meV from the bottom of the conduction band)

By using light of different energies (above or below the band gap), different energy levels may be probed. Typically, in standard PL measurements, light with an energy higher than the band gap is used and in good quality materials, transition (i) dominates. The photoexcited carriers then diffuse and recombine to emit photons. Due to the lower energy states in quantum wells, the diffusing photoexcited carriers are preferentially trapped in the wells and the recombination of the electron-hole pairs generates photons with energies characteristic of the quantised energy levels of the wells which can then be collected and analysed. Detailed theory and experimental aspects of PL and optical processes in semiconductors may be found in references [25] and [26].

The PL setup used in this work is schematically shown in Fig. 2-14. A 4 W Coherent Innova 70 Ionpure water-cooled Ar ion laser is used as the excitation source. The laser has several lines but in this work an excitation wavelength of 514.5 nm is used. The specimens for PL measurements are mounted with vacuum grease on a closed-cycle liquid He cryostat. The laser beam is directed onto the sample through a chopper operating at a few hundred Hz. The resulting luminescence is then collected by a Si photodiode with a built-in pre-amplifier *via* a set of lenses and a 0.75 m SPEX 1702/04

spectrometer. The signal from the photodetector is analysed by a lock-in amplifier, which is tuned to the frequency of the chopper. A desktop computer is then used to control the spectrometer for a wavelength scan and also records the PL signal.

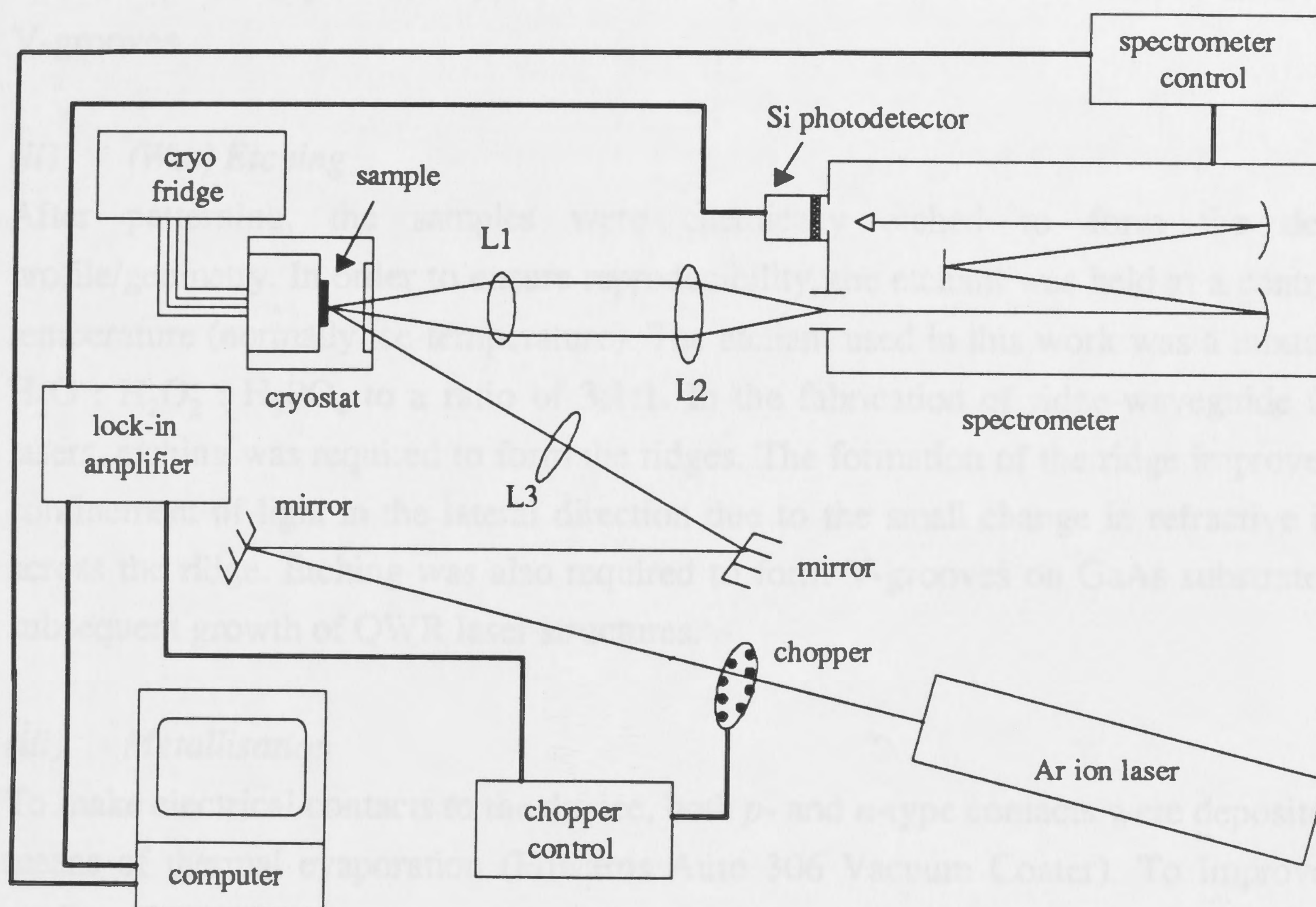

Fig. 2-14 Schematic of the setup for photoluminescence experiments.

2.5 Device processing and testing

A series of processing sequences is required to fabricate the multilayered materials into devices. This series normally involves photolithography, etching and metallisation. In this work, two classes of (optoelectronic) devices are fabricated; (i) quantum well (QWL) lasers and (ii) quantum wire (QWR) lasers. Details of the processing steps may be found in Appendix A but three basic steps used in this work will be briefly discussed below.

(i) Photolithography

In this process, a layer of photoresist (AZ5214-E) was spun on the sample. The desired device was then patterned by exposing the photoresist with ultra-violet light through a mask using a mask aligner (Quintel Q-2001CT). After exposure, the photoresist was

developed by means of a developing solution (AZ312). The AZ5214-E photoresist allowed both standard and image-reversal work, which could be accomplished by selecting the right exposure and photoresist baking conditions. In the case of QWL lasers, stripes of various widths (1-50 μm) were patterned on the wafer. For QWR lasers, a set of stripes (50x2 μm width) was patterned for the formation of an array of V-grooves.

(ii) (Wet) Etching

After patterning, the samples were chemically etched to form the desired profile/geometry. In order to ensure reproducibility, the etchant was held at a controlled temperature (normally ice-temperature). The etchant used in this work was a mixture of H_2O : H_2O_2 : H_3PO_4 to a ratio of 3:1:1. In the fabrication of ridge-waveguide QWL lasers, etching was required to form the ridges. The formation of the ridge improves the confinement of light in the lateral direction due to the small change in refractive index across the ridge. Etching was also required to form V-grooves on GaAs substrates for subsequent growth of QWR laser structures.

(iii) Metallisation

To make electrical contacts to the device, both *p*- and *n*-type contacts were deposited by means of thermal evaporation (Edwards Auto 306 Vacuum Coater). To improve the quality of the contacts, evaporation was normally carried out at pressures $< 8\times10^{-6}$ Torr. Au-Zn-Au or Al were used for making ohmic contact to *p*-type materials while Au-Ge was used for ohmic contact to *n*-type materials. After evaporation, an alloying step was required to ensure good ohmic contact formation. The alloying step involved rapid-thermal-annealing of the device at around 400 °C for ~1 min. Since the alloying temperature of *p*-type contacts was higher than *n*-type contacts, metallisation was first carried out on the *p*-type material.

Fig. 2-16 illustrates the concept behind the three main steps in device processing. It should, however, be noted that many more processing steps were required both between and after these steps. A complete schedule of the processing steps is tabulated in Appendix A. After fabrication, the lasers were cleaved along the [100] directions to form the cavity mirrors and then tested for both their electrical and optical characteristics.

In this work, only the current-threshold (light-intensity vs. current, L-I) characteristics and the lasing spectra were measured. L-I measurements were carried out both in CW and pulsed modes. The lasing spectra were collected by coupling the light output into a

Digiköm 480 monochromator through some lenses. A Si photodiode was used as the detector.

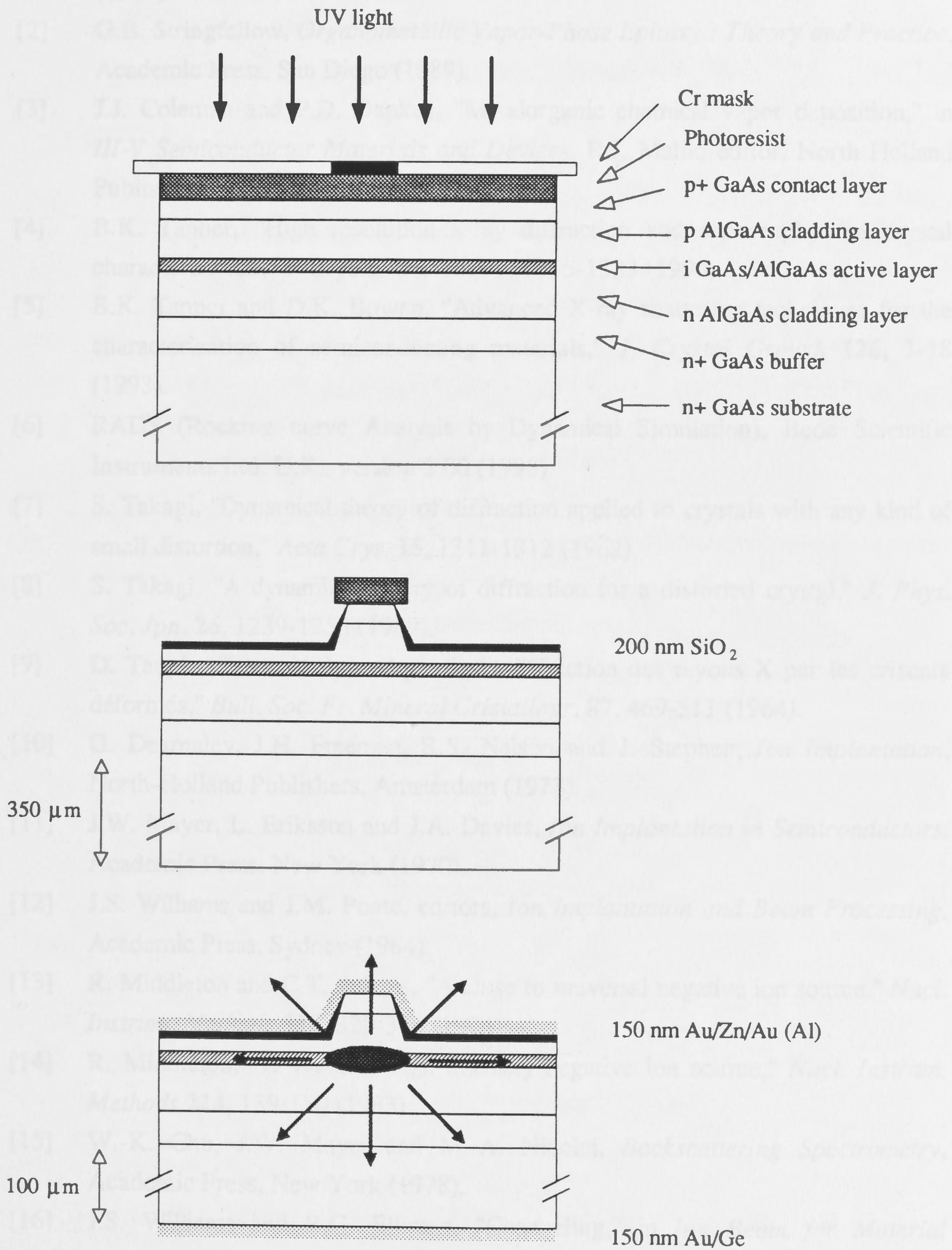

Fig. 2-16 Schematic of the three major steps in processing of a ridge-waveguide laser, from top; photolithography, etching and metallisation.

References

[1] T.F. Kuech, "Metal-organic vapor phase epitaxy," *Mat. Sci. Rept.* **2**, 1-50 (1987).

[2] G.B. Stringfellow, *Organometallic Vapor-Phase Epitaxy : Theory and Practice*, Academic Press, San Diego (1989).

[3] J.J. Coleman and P.D. Dapkus, "Metalorganic chemical vapor deposition," in *III-V Semiconductor Materials and Devices*, R.J. Malik, editor, North Holland Publishers, Amsterdam (1989).

[4] B.K. Tanner, "High resolution x-ray diffraction and topography for crystal characterization," *J. Crystal Growth* **99**, 1315-1323 (1990).

[5] B.K. Tanner and D.K. Bowen, "Advanced X-ray scattering techniques for the characterization of semiconducting materials," *J. Crystal Growth* **126**, 1-18 (1993).

[6] RADS (Rocking curve Analysis by Dynamical Simulation), Bede Scientific Instruments Ltd. U.K., version 2.00 (1993)

[7] S. Takagi, "Dynamical theory of diffraction applied to crystals with any kind of small distortion," *Acta Crys.* **15**, 1311-1312 (1962).

[8] S. Takagi, "A dynamical theory of diffraction for a distorted crystal," *J. Phys. Soc. Jpn.* **26**, 1239-1253 (1969).

[9] D. Taupin, "Theorié dynamique de la diffraction des rayons X par les cristaux déformés," *Bull. Soc. Fr. Mineral Cristallogr.* **87**, 469-511 (1964).

[10] G. Dearnaley, J.H. Freeman, R.S. Nelson and J. Stephen, *Ion Implantation*, North-Holland Publishers, Amsterdam (1973).

[11] J.W. Mayer, L. Eriksson and J.A. Davies, *Ion Implantation in Semiconductors*, Academic Press, New York (1970).

[12] J.S. Williams and J.M. Poate, editors, *Ion Implantation and Beam Processing*, Academic Press, Sydney (1984).

[13] R. Middleton and C.T. Adams, "A close to universal negative ion source," *Nucl. Instrum. Methods* **118**, 329-336 (1974).

[14] R. Middleton, "A versatile high intensity negative ion source," *Nucl. Instrum. Methods* **214**, 139-150 (1983).

[15] W.-K. Chu, J.W. Mayer and M.-A. Nicolet, *Backscattering Spectrometry*, Academic Press, New York (1978).

[16] J.S. Williams and R.G. Elliman, "Channeling," in *Ion Beam for Material Analysis*, J.R. Bird and J.S. Williams, editors, Chp. 6, 261-333, Academic Press, Sydney (1989).

[17] P.B. Hirsch, A. Howie, R.B. Nicholson, D.W. Pashley and J.M. Whelan, *Electron Microscopy of Thin Crystals*, Butterworths, London (1967).

[18] P.J. Goodhew and F.J. Humphreys, *Electron Microscopy and Analysis*, Taylor and Francis Ltd., London (1988).

[19] J.W. Edington, *Monographs in Practical Electron Microscopy in Materials Science*, vols. 1-4, Philips Technical Library, Eindhoven (1974).

[20] H. Kakibayashi and F. Nagata, "Composition dependence of equal thickness fringes in an electron microscope image of GaAs/$Al_xGa_{1-x}As$ multilayer structures," *Jpn. J. Appl. Phys.* **24**, L905-L907 (1985).

[21] P. Blood and J.W. Orton, *The Electrical Characterization of Semiconductors : Majority Carriers and Electron States*, Academic Press, London (1992).

[22] D.C. Look, *Electrical Characterization of GaAs Materials and Devices*," John Wiley and Sons, Chichester (1992).

[23] B.G. Svensson, K.-H. Rydén and B.M.S. Lewerentz, "Overlapping electron traps in n-type silicon studied by capacitance transient spectroscopy," *J. Appl. Phys.* **66**, 1699-1704 (1989).

[24] K.-H. Rydén (unpublished).

[25] H.B. Bebb and E.W. Williams, "Photoluminescence I : Theory," Chp. 4, 182-320 and E.W. Williams and H.B. Bebb, "Photoluminescence II : Gallium Arsenide," Chp. 5, 321-392 in *Semiconductors and Semimetals, Vol. 8, Transport and Optical Phenomena*, R.K. Willardson and A.C. Beer, editors, Academic Press, New York (1972).

[26] J.I. Pankove, *Optical Processes in Semiconductors*, Dover Publications Inc., New York (1971).

Chapter 3

Ion damage buildup in $Al_xGa_{1-x}As$

3.1 Introduction

Although ion beam interaction processes with Si and III-V binary compounds such as GaAs and InP have been studied extensively, there remains a lack of understanding of ion disordering processes in ternary semiconductor alloys such as AlGaAs. Several critical questions arise when dealing with this material system. For example, what is the mechanism for damage formation in AlGaAs and is the residual damage in AlGaAs similar to that of GaAs? What is the relationship between damage formation and the fraction of Al in AlGaAs? Can the commonly used linear interpolation between GaAs and AlAs be used when dealing with ion beam damage in AlGaAs? There have been several investigations in the past few years trying to identify these issues.[1-11] However, in most of these cases, multilayer structures (GaAs/AlGaAs) were used and this makes thorough understanding of ion damaging processes in AlGaAs difficult due to defect migration, annihilation and trapping processes at the surfaces, interfaces and other defects. Nevertheless, one clear outcome from these studies is that the resistance to amorphisation in AlGaAs increases with Al content. In fact, AlAs has been shown to be extremely resistant to ion beam damage even at liquid nitrogen (LN2) temperature.[4,5,8,11] In this chapter, the results of a systematic study of ion beam induced damage processes in AlGaAs of seven different Al compositions will be presented, including the conclusions that can be drawn from these results. To properly understand the damage buildup and amorphisation processes in AlGaAs, irradiations were carried out at LN2 temperature to minimise dynamic annealing effects that are expected to occur at higher temperatures. Furthermore, due the extreme resistance of AlAs to ion beam damage, low temperature irradiations would be more practical for the study of damage buildup. A major difference between this study and the others[1-11] is that 'bulk' (thick) layers were used and the influence of interfaces is minimised.

3.2 Experimental

All structures were grown on semi-insulating GaAs substrates in the MOCVD reactor. An initial GaAs buffer of ~0.5 μm was first grown on all samples followed by AlGaAs layers of > 0.8 μm which were then terminated with thin GaAs capping layers of various thicknesses (3-15 nm) to prevent oxidation of Al-rich layers. The thickness of the capping layer was carefully chosen so that a protective layer still existed after high-dose implants (> 10^{15} cm^{-2}, where a significant amount of sputtering occurs) and yet not thick enough to significantly affect ion beam interaction with the AlGaAs layer. $Al_xGa_{1-x}As$ of seven different compositions were grown (x=0, 0.26, 0.49, 0.71, 0.83, 0.95 and 1). Implantations were at LN2 temperature with low energy, 90 keV Si^- beams to ensure that the ions were confined only to the near surface regions (to minimise interfacial effects). During implantations, the samples were tilted 7° away from the beam axis to minimise channeling effects. A large range of ion doses was used ($2x10^{13}$ - $2x10^{16}$ cm^{-2}) and the dose rates were maintained in the range of $6.24x10^{10}$-$6.24x10^{13}$ ions.cm^{-2}.s^{-1}. Analysis was carried out at room temperature by the Rutherford backscattering-ion channeling technique (RBS-C). The detector was set at a glancing angle of 100° (10° grazing exit angle to the surface) to optimise the depth resolution in the regions of interest. Selected samples were analysed by cross-sectional transmission electron microscopy.

3.3 Results

3.3.1 Damage buildup as a function of Al composition

Fig. 3-1 shows the RBS-C spectra of the damage buildup in GaAs at LN2 temperature as a function of dose. As observed by channeling, the damage buildup appears similar to that previously reported[12-14] in so much as the amount of disorder increases with increasing ion dose until a buried damage peak is formed at a depth of ~70 nm, corresponding very closely to the maximum displacement (nuclear energy deposition) density of 90 keV Si ions as calculated by TRIM90.[15] The observation of this buried damage peak is a result of direct backscattering of the incident (analysing) ions and is indicative of the formation of point defects, clusters and possibly small pockets of amorphous zones created by the individual ion tracks.[16] As the ion dose is increased further, the density of these defects increases, as indicated by the increase in the backscattered yield, until a level when the aligned signal just coincides with the random

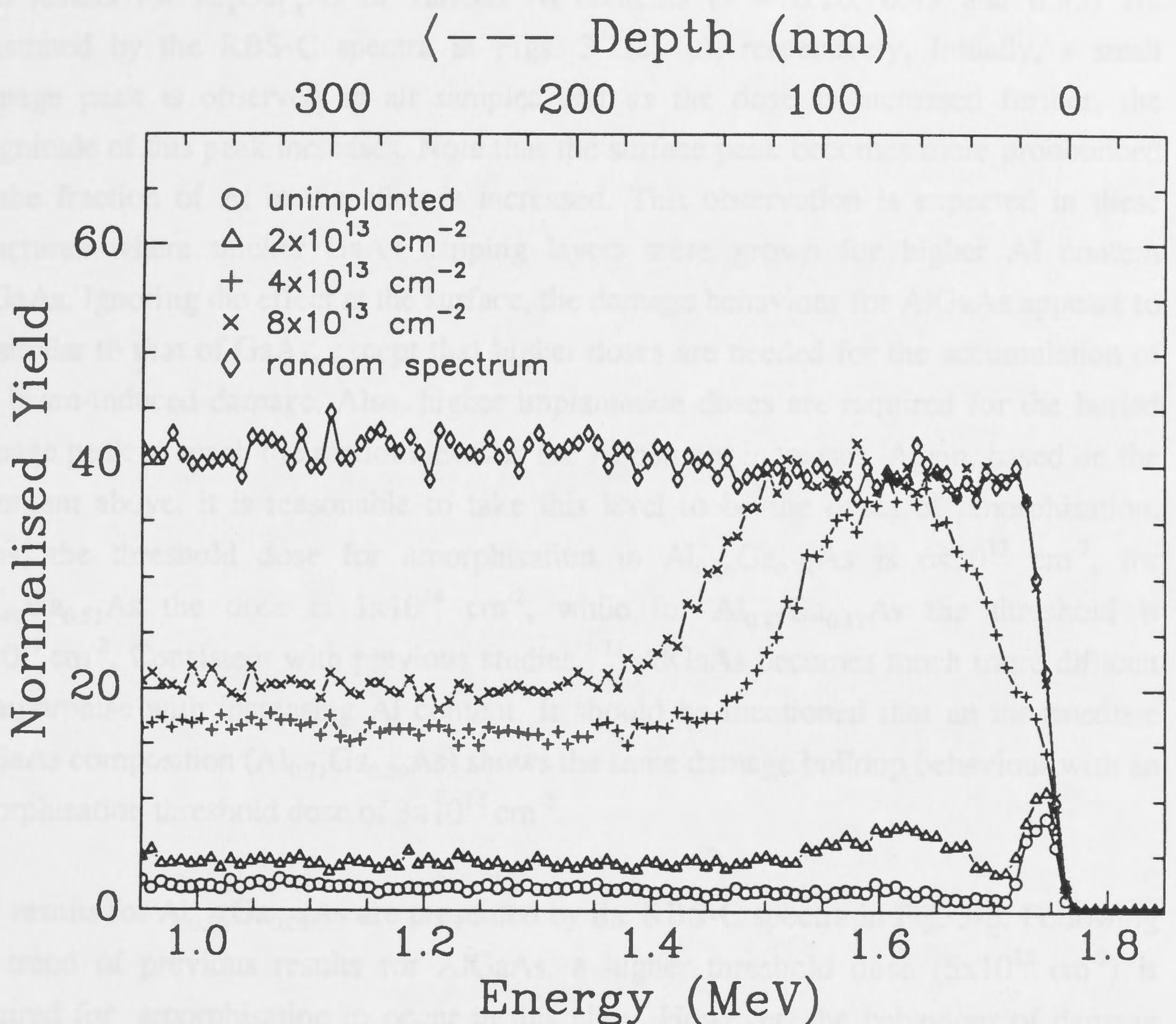

Fig. 3-1 RBS-channeling spectra showing the damage buildup for 90 keV Si implantation into GaAs.

level (at a dose of $4x10^{13}$ cm^{-2}). One interpretation of the channeling data is that, at this stage, a buried amorphous layer is just formed. Although TEM studies (results of which are discussed in more detail later) indicate that a continuous amorphous layer is not necessarily formed at such a dose, correlated TEM and RBS-C measurements show that the amount of damage is extensive and that the dose is very close to a threshold for producing amorphous material.[13,17,18] Thus, it is reasonable to take this dose as a convenient measure of the onset of amorphisation. With further bombardment, the damage peak grows both towards the surface and substrate to form a continuous layer of amorphous material.

The results for $Al_xGa_{1-x}As$ of various Al contents (x = 0.26, 0.49 and 0.83) are illustrated by the RBS-C spectra in Figs. 3-2(a)-(c), respectively. Initially, a small damage peak is observed in all samples and as the dose is increased further, the magnitude of this peak increases. Note that the surface peak becomes more pronounced as the fraction of Al in the alloy is increased. This observation is expected in these structures where thicker GaAs capping layers were grown for higher Al content AlGaAs. Ignoring the effect at the surface, the damage behaviour for AlGaAs appears to be similar to that of GaAs, except that higher doses are needed for the accumulation of ion beam-induced damage. Also, higher implantation doses are required for the buried damage peak to reach the random level as the Al content increases. Again, based on the argument above, it is reasonable to take this level to be the onset of amorphisation. Thus, the threshold dose for amorphisation in $Al_{0.26}Ga_{0.74}As$ is $6x10^{13}$ cm^{-2}, for $Al_{0.49}Ga_{0.51}As$ the dose is $1x10^{14}$ cm^{-2}, while for $Al_{0.83}Ga_{0.17}As$ the threshold is $8x10^{14}$ cm^{-2}. Consistent with previous studies,[1-11] AlGaAs becomes much more difficult to amorphise with increasing Al content. It should be mentioned that an intermediate AlGaAs composition ($Al_{0.71}Ga_{0.29}As$) shows the same damage buildup behaviour with an amorphisation threshold dose of $3x10^{14}$ cm^{-2}.

The results for $Al_{0.95}Ga_{0.05}As$ are presented by the RBS-C spectra in Fig. 3-3. Following the trend of previous results for AlGaAs, a higher threshold dose ($5x10^{15}$ cm^{-2}) is required for amorphisation to occur in this alloy. However, the behaviour of damage buildup is now quite different to the previous, lower Al content samples. In this case, no damage peak near the region of maximum nuclear energy deposition density is observed for doses up to $4x10^{15}$ cm^{-2}. (The 15 nm or so on the surface corresponds to the GaAs capping layer and for all doses shown in these spectra, this layer has been heavily damaged or essentially rendered amorphous). Instead, only an increase in the dechanneling level in the $Al_{0.95}Ga_{0.05}As$ layer is observed with increasing ion dose until a saturation level. For a further marginal increase in the ion dose (from $4x10^{15}$ to $5x10^{15}$ cm^{-2}), a buried peak which coincides with the random level suddenly appears, suggesting an abrupt crystalline to amorphous transition. Upon further bombardment the disorder peak grows towards both the surface and substrate to form a continuous layer of amorphous material.

To further investigate the different damage behaviour in AlGaAs of high Al composition, XTEM was employed on the $Al_{0.95}Ga_{0.05}As$ samples above, corresponding to three ion doses of $4x10^{15}$, $5x10^{15}$ and $8x10^{15}$ cm^{-2}, as shown in Fig. 3-4(a), (b) and (c) respectively. The arrows in this figure indicate the surface and all micrographs have the same magnification scale. At the lowest dose, a layer with extensive stacking faults (up

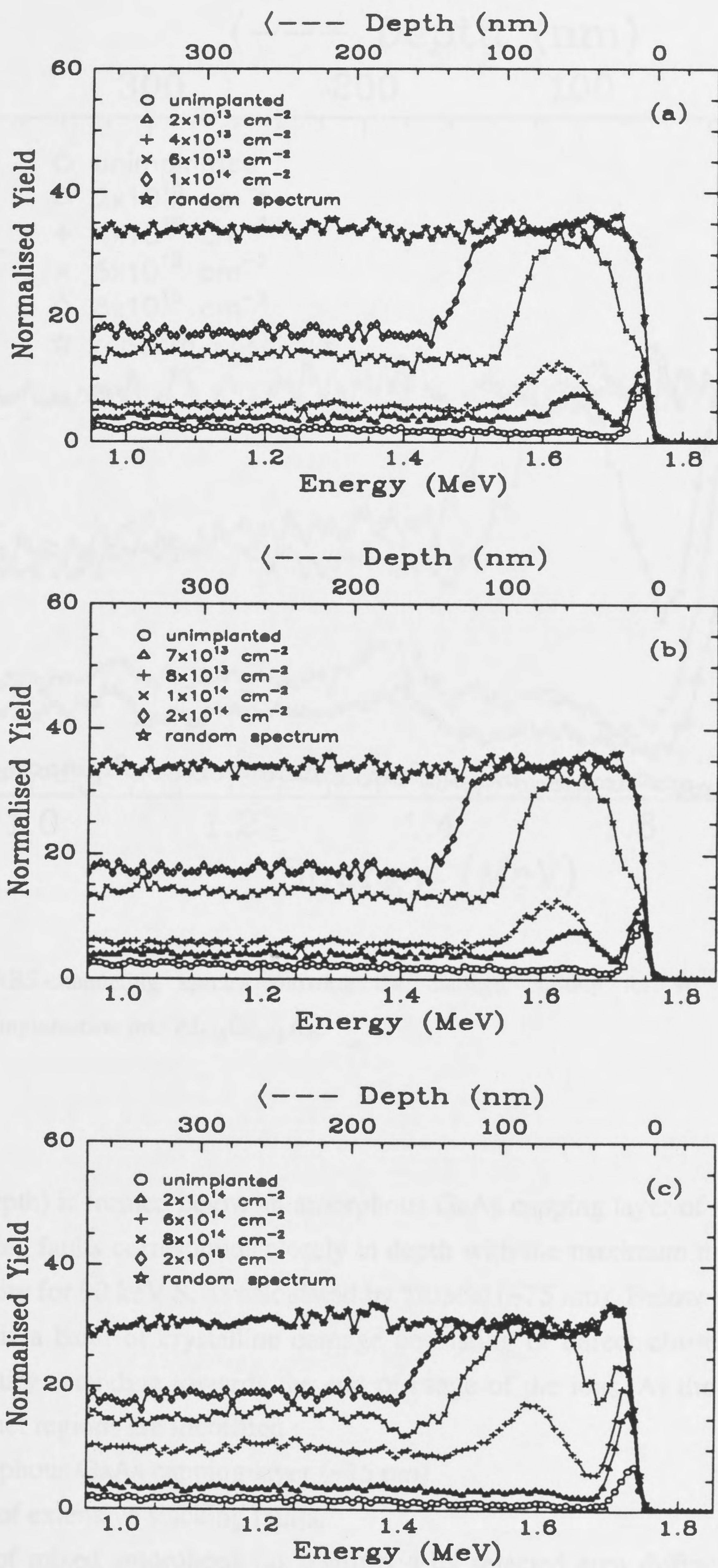

Fig. 3-2 RBS-channeling spectra showing the damage buildup for 90 keV Si implantation into (a) $Al_{0.26}Ga_{0.74}As$, (b) $Al_{0.49}Ga_{0.51}As$ and (c) $Al_{0.83}Ga_{0.17}As$.

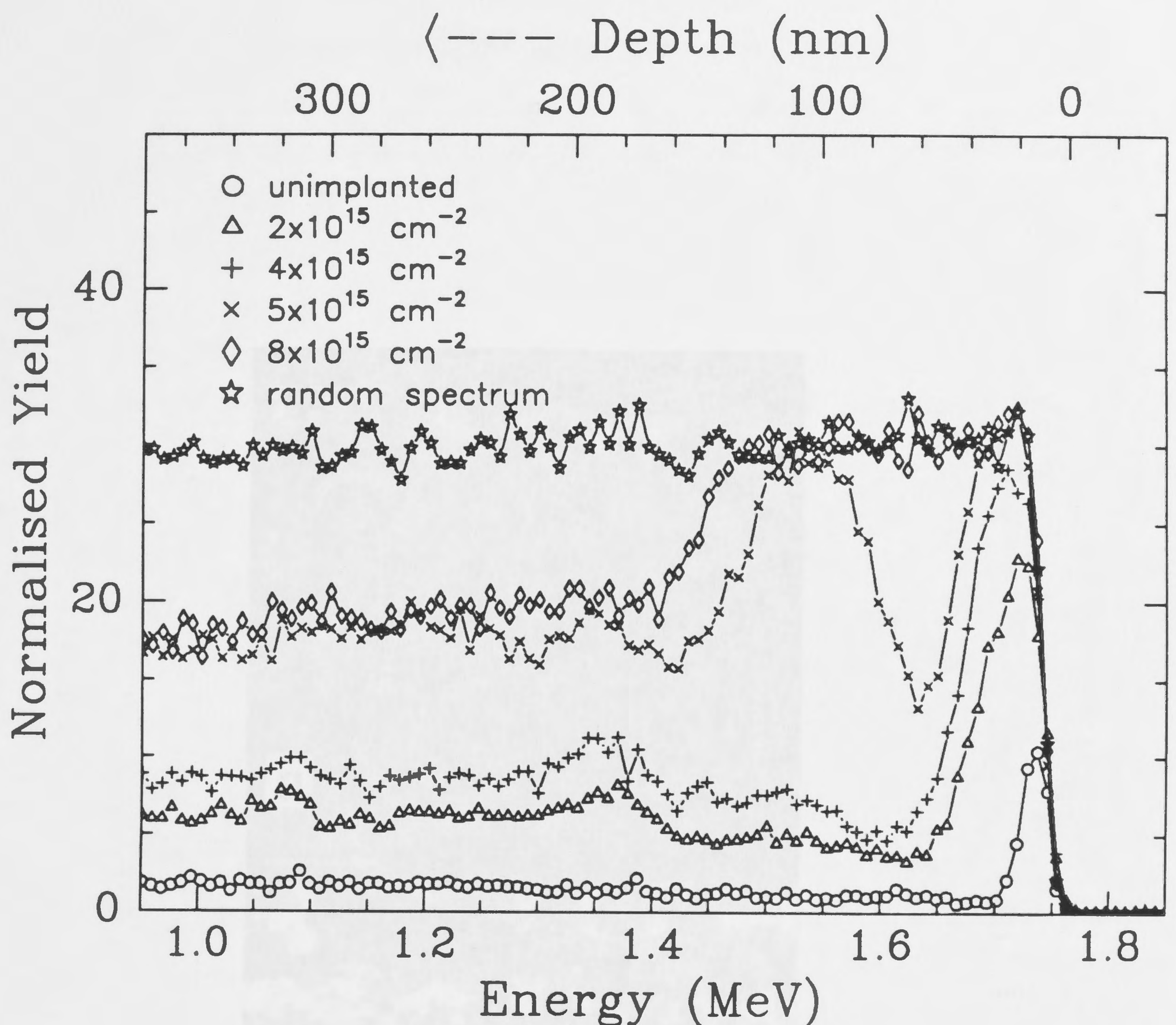

Fig. 3-3 RBS-channeling spectra showing the damage buildup for 90 keV Si implantation into $Al_{0.95}Ga_{0.05}As$.

to ~90 nm in depth) is formed below an amorphous GaAs capping layer of ~15 nm. This region of stacking faults corresponds closely in depth with the maximum nuclear energy deposition density for 90 keV Si as calculated by TRIM90 (~75 nm). Below this region of stacking faults is a band of crystalline damage consisting of defect clusters which are difficult to identify extending towards the end of range of the ions. At the next highest dose, four distinct regions are identified :

(1) an amorphous GaAs capping layer (~15 nm),

(2) regions of extensive stacking faults,

(3) a band of mixed amorphous (as confirmed by selected area diffraction pattern) and heavily damaged material,

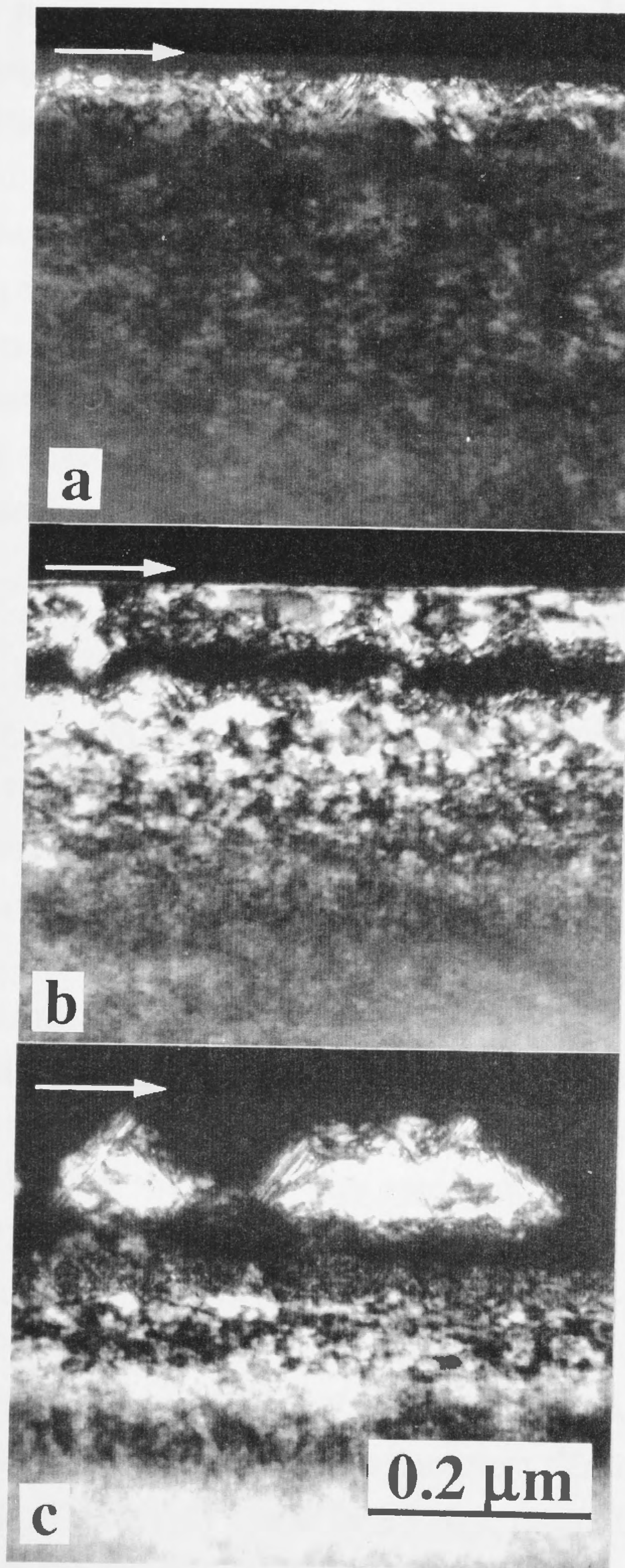

Fig. 3-4 220 dark-field XTEM images for $Al_{0.95}Ga_{0.05}As$ samples from Fig. 3-3 implanted to a dose of (a) $4x10^{15}$ cm^{-2} (b) $5x10^{15}$ cm^{-2} and (c) $8x10^{15}$ cm^{-2}.

(4) a region of crystalline damage consisting of damage clusters which are difficult to identify extending towards the end of the ions range distribution.

Region (3) is presumably formed from the collapse of the stacking faults into a dense band of defects upon further irradiation. This band, upon increasing the ion dose, subsequently nucleates a buried amorphous layer which extends towards the surface and substrate as shown in Fig. 3-4(c). At this dose of $8x10^{15}$ cm^{-2}, a continuous amorphous layer is just about to form. However, in this case, islands of crystallites, which are decorated with many stacking faults, still remain within the amorphous layer. This strongly suggests that the stacking faults act as a precursor to the formation of the amorphous material. The XTEM results are consistent with ion channeling results, where a sudden transition from a saturation defect level (in this case, stacking faults and defect clusters) to amorphous material. It is possible that the islands of crystallites are formed during warm up to room temperature (or during sample preparation) as a result of partial recrystallisation of incomplete amorphous layer formation during implantation. However, as later results will show, complete amorphous layer formed during implantation is stable during warm up to room temperature. This issue will be clarified later.

Similar ion beam damage behaviour is observed in AlAs as shown in Fig. 3-5 but at a consistently higher threshold dose of amorphisation ($8x10^{15}$ cm^{-2}). A small increment in the ion dose (from $7x10^{15}$ to $8x10^{15}$ cm^{-2}) resulted in a abrupt crystalline to amorphous phase transformation. As in the previous $Al_{0.95}Ga_{0.05}As$ case, the surface peak in the channeled spectra can be related to the damage buildup in the GaAs capping layer.

A summary of the damage buildup data is presented in Fig. 3-6 for $Al_xGa_{1-x}As$ of seven different Al compositions. These data are for energy deposition and stopping of 90 keV Si^- wholly within the AlGaAs layers at LN2 temperature. The χ_{min}=100% level corresponds to the aligned signal level just reaching the random level at a particular dose. Based on TEM observations as discussed previously, this value is used as the threshold dose for the onset of amorphisation. It is obvious from this figure that the amorphisation threshold increases with increasing Al content by more than two orders of magnitude; from $4x10^{13}$ cm^{-2} for GaAs to $8x10^{15}$ cm^{-2} for AlAs. This effect is in contrast with TRIM90 calculations where the peak displacement density (i.e. the nuclear energy deposition density) in AlAs is only about 35% lower than in GaAs. It is also in contrast with the difference in the physical properties between GaAs and AlAs which differ by not more than 40%. The relevant properties of GaAs and AlAs are listed in Table I for reference.

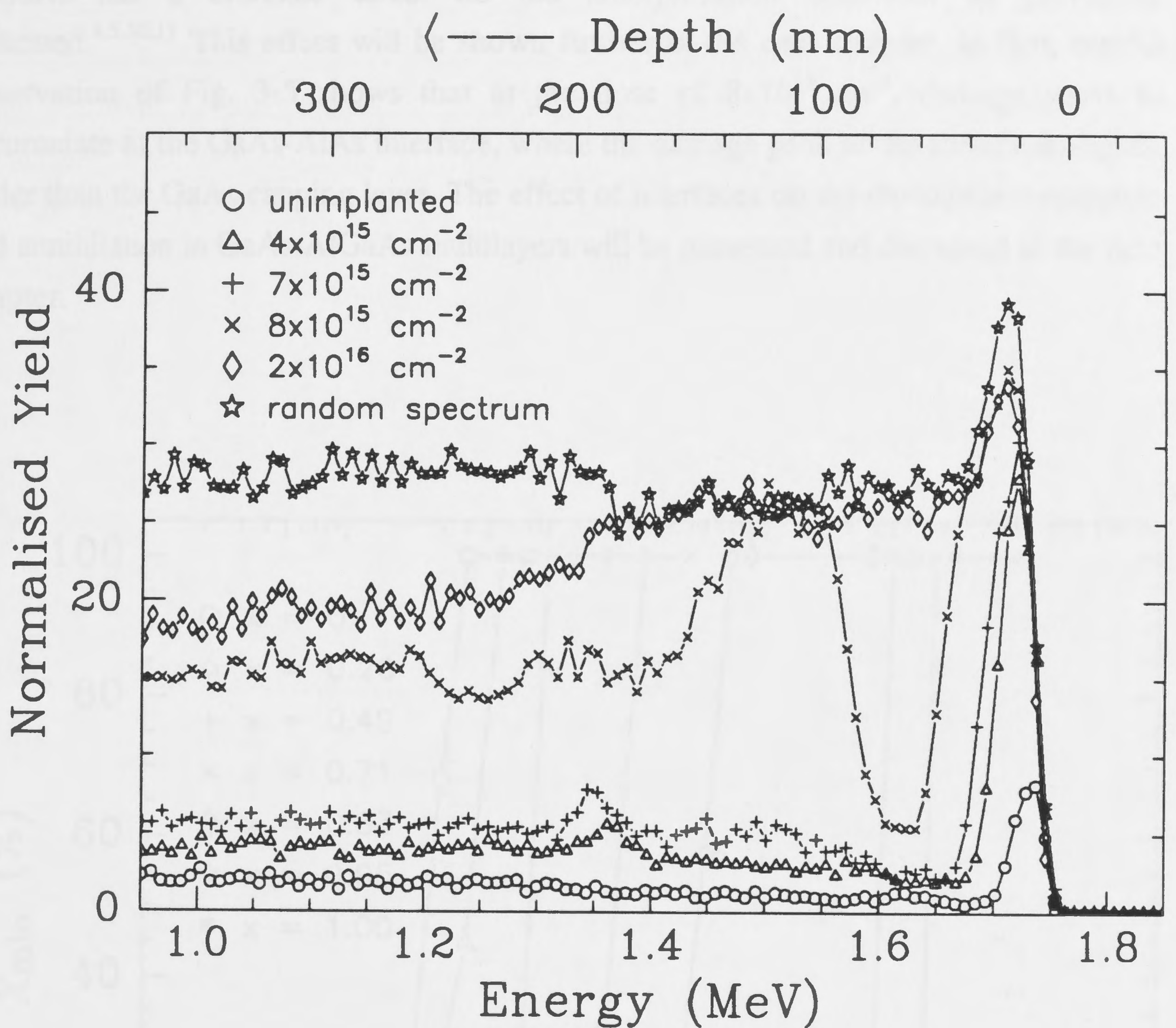

Fig. 3-5 RBS-channeling spectra showing the damage buildup for 90 keV Si implantation into AlAs.

It is interesting to note from Fig. 3-7, where the amorphisation threshold (as determined by RBS-C) is plotted against Al content, that the threshold dose does not vary linearly with Al content but according to a power law. For comparison, the data for amorphisation threshold from Cullis *et. al.*[8] are plotted onto the same figure. These points are essentially scaled by the peak nuclear energy deposition density from 150 keV Si beams (used in their experiments) to the threshold needed for 90 keV Si beams. Although the trend is in agreement with our data, the absolute threshold doses do not closely agree. One possible reason is that the dose steps used by Cullis and co-workers were large, making accurate determination of the amorphisation threshold difficult. Perhaps, more significantly, bi-layer structures were used in their experiments (compared to thick bulk layers used in this study) and the presence of adjacent GaAs or

AlGaAs has a dramatic effect on the amorphisation behaviour as previously indicated.[4,5,10,11] This effect will be shown further in the next chapter. In fact, careful observation of Fig. 3-5 shows that at the dose of $8x10^{15}$ cm^{-2}, damage starts to accumulate at the GaAs-AlAs interface, where the damage peak at the surface is slightly wider than the GaAs capping layer. The effect of interfaces on the damage accumulation and annihilation in GaAs-AlGaAs multilayers will be presented and discussed in the next chapter.

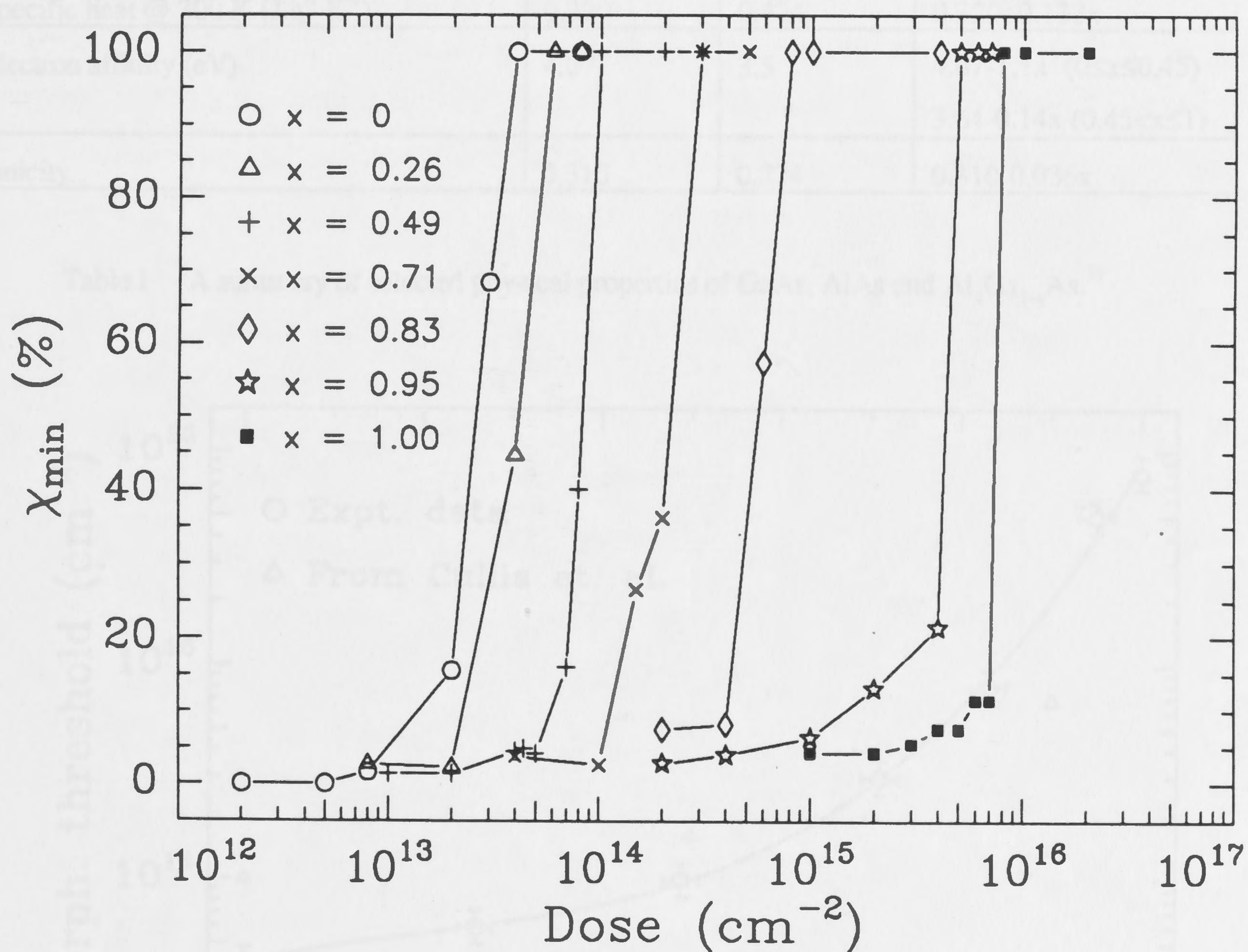

Fig. 3-6 Disorder, χ_{min}, as measured from RBS-C minimum yield for 90 keV Si implantation into $Al_xGa_{1-x}As$ at liquid nitrogen temperature for seven different Al compositions. The χ_{min} = 100% level corresponds to the yield of the aligned spectrum reaching that of the random spectrum.

Properties	*GaAs*	*AlAs*	*$Al_xGa_{1-x}As$*
Lattice constant (Å)	5.6533	5.6611	5.6533+0.0078x
Density ($g.cm^{-3}$)	5.317	3.729	5.3165-1.5875x
Elastic stiffness constants ($x10^{11}$ $dyn.cm^{-2}$)			
C_{11}	11.88	12.02	11.88+0.14x
C_{12}	5.38	5.70	5.38+0.32x
C_{44}	5.94	5.89	5.94-0.05x
Melting point (°C)	1238	1740	$1238-58x+560x^2$
Thermal expansion coefficient ($x10^{-6}$ K^{-1})	5.97	4.21	5.97-1.76x
Specific heat @ 300 K ($J.g^{-1}$ K^{-1})	0.320	0.424	0.320+0.132x
Electron affinity (eV)	4.07	3.5	4.07-1.1x (0≤x≤0.45) 3.64-0.14x (0.45<x≤1)
Ionicity	0.310	0.274	0.310-0.036x

Table I A summary of selected physical properties of GaAs, AlAs and $Al_xGa_{1-x}As$.[19]

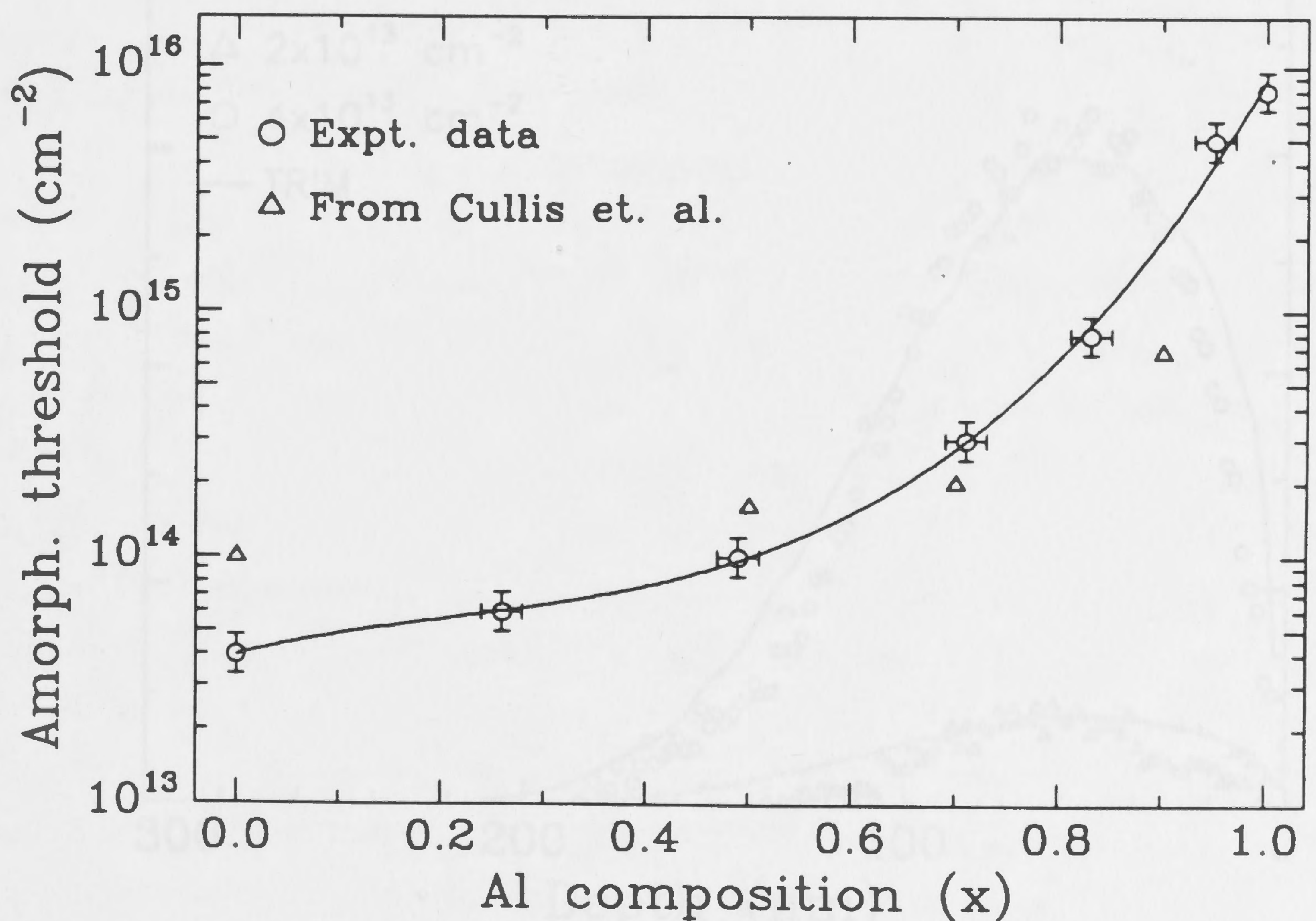

Fig. 3-7 Amorphisation threshold dose (as determined by RBS-C) in $Al_xGa_{1-x}As$ as a function of Al composition. Also included in this figure are the data from ref. [8] for comparison.

3.3.2 *Damage profiles in AlGaAs*

To gain further insights into the damage buildup in AlGaAs, damage profiles are extracted from RBS-C spectra by a simple linear subtraction of the dechanneling component. Although dechanneling analysis normally requires rigorous treatment of the energy dependence of the types of defects,[20,21] this simple procedure is sufficient to indicate the major feature of the damage profile. Fig. 3-8 shows the damage profiles (obtained by this method) for GaAs at two different ion doses. Overlaid on these profiles are the displacement density distributions created by 90 keV Si ions calculated by TRIM90. During the initial stage of implantation, where very little damage is accumulated in the crystal, some channeling effect can occur (even though the sample was tilted 7° away from the beam axis during implantation), resulting in an overall damage distribution which extends deeper into the substrate than expected from a random implant. However, when more damage is created by further increases in the ion dose,

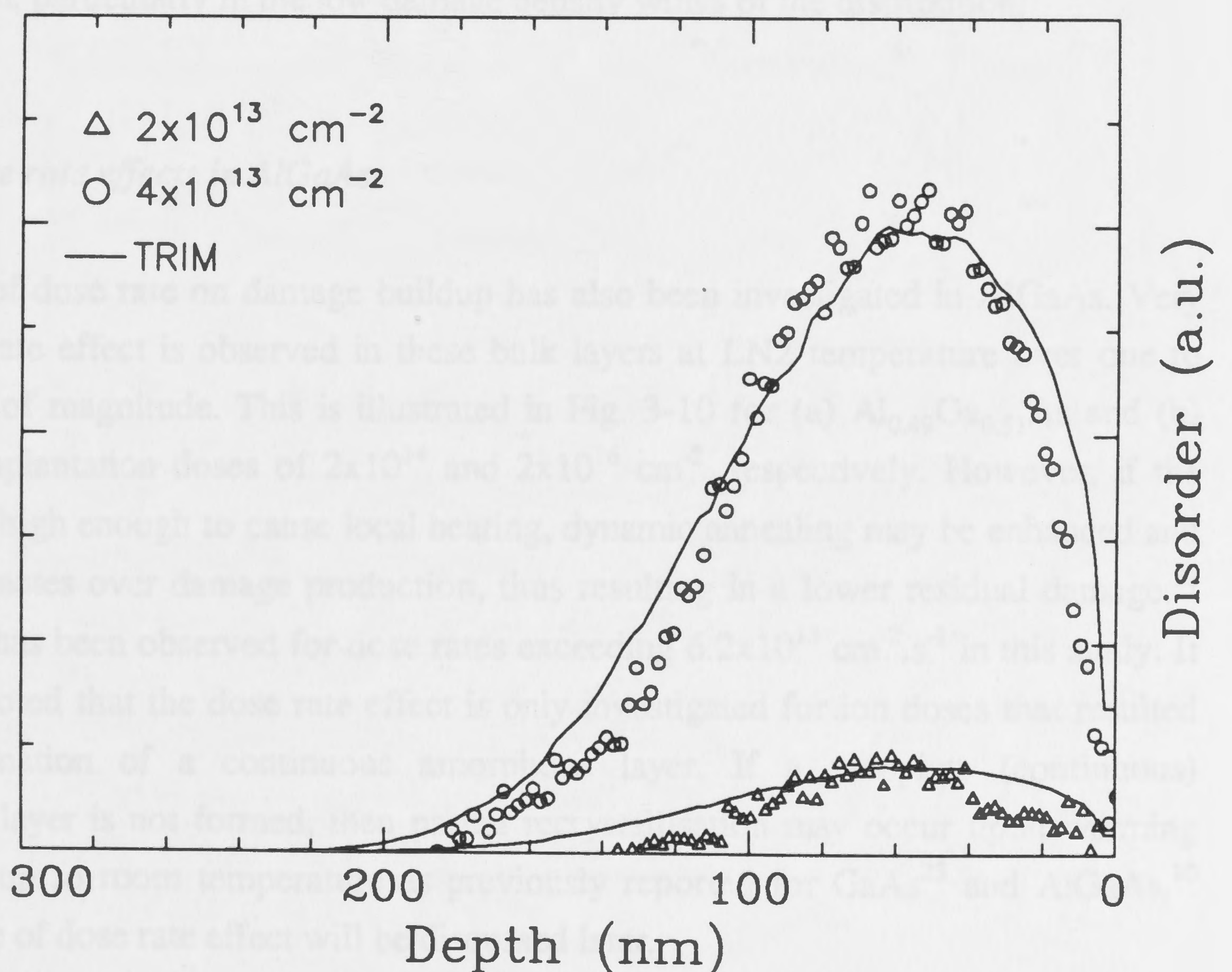

Fig. 3-8 Ion beam damage profiles in GaAs extracted from RBS-C (Fig. 3-1) results for two implantation doses. The displacement density profiles calculated by TRIM90 are overlaid for comparison.

this effect becomes less significant. Additionally, the disorder peaks may be slightly shifted towards the surface due to a channeling effect during the analysis where the stopping power for channeled ions is lower than the random case.[20,21] However, this effect is only marginal and thus not taken into account during the extraction of the damage profiles from the RBS-C spectra. It is also possible that some annealing of incomplete amorphous material occurs in GaAs or AlGaAs on warming up to room temperature. Bearing these effects in mind, the damage profiles for GaAs fit reasonably well with TRIM90 calculations. This suggests that very little dynamic annealing takes place during irradiation of GaAs, presumably most of the defects created by ion beam damage are 'frozen in' at LN2 temperature. However, in AlGaAs, as shown in Fig. 3-9, the damage profiles deviate quite significantly from TRIM90 calculations in the regions away from the peak of the distributions. This effect becomes more pronounced with increasing Al content as in the case of AlAs [Fig. 3-9(c)]. Thus, the damage profiles in AlGaAs(AlAs) are much narrower than that predicted by theory and are confined to the region of maximum nuclear energy deposition density. The much narrower profiles indicate that dynamic annealing is competing very strongly with damage creation during implantation, particularly in the low damage density wings of the distribution.

3.3.3 Dose rate effects in AlGaAs

The effect of dose rate on damage buildup has also been investigated in AlGaAs. Very little dose rate effect is observed in these bulk layers at LN2 temperature over one to two orders of magnitude. This is illustrated in Fig. 3-10 for (a) $Al_{0.49}Ga_{0.51}As$ and (b) AlAs, at implantation doses of $2x10^{14}$ and $2x10^{16}$ cm^{-2}, respectively. However, if the dose rate is high enough to cause local heating, dynamic annealing may be enhanced and hence dominates over damage production, thus resulting in a lower residual damage.[22] This effect has been observed for dose rates exceeding $6.2x10^{13}$ $cm^{-2}.s^{-1}$ in this study. It should be noted that the dose rate effect is only investigated for ion doses that resulted in the formation of a continuous amorphous layer. If a complete (continuous) amorphous layer is not formed, then partial recrystallisation may occur upon warming the sample up to room temperature as previously reported for GaAs[23] and AlGaAs.[10] The absence of dose rate effect will be discussed later.

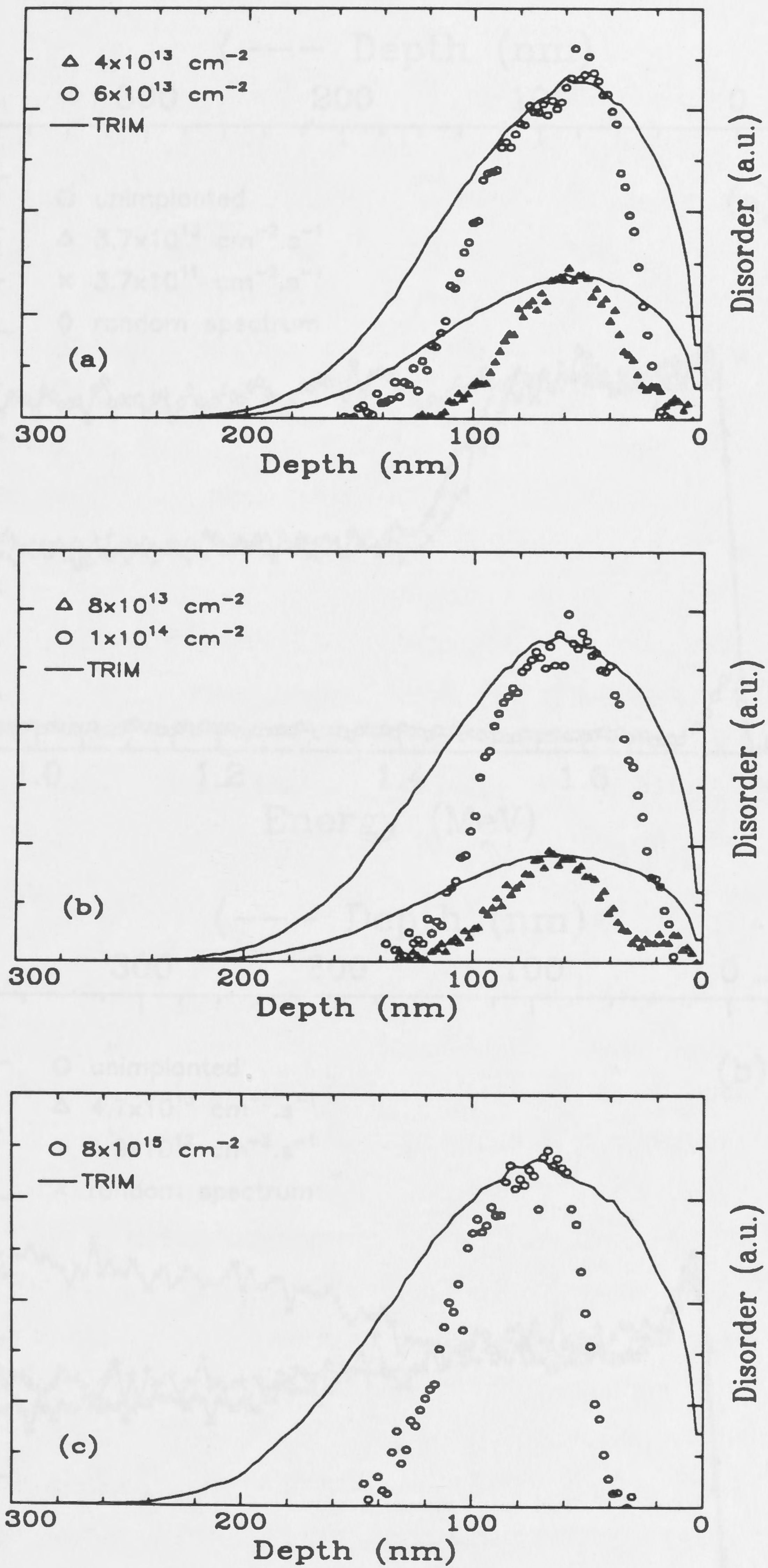

Fig. 3-9 Ion beam damage profiles extracted from RBS-C results in (a) $Al_{0.26}Ga_{0.74}As$ (b) $Al_{0.49}Ga_{0.51}As$ and (c) AlAs. The displacement density profiles calculated by TRIM90 are overlaid for comparison.

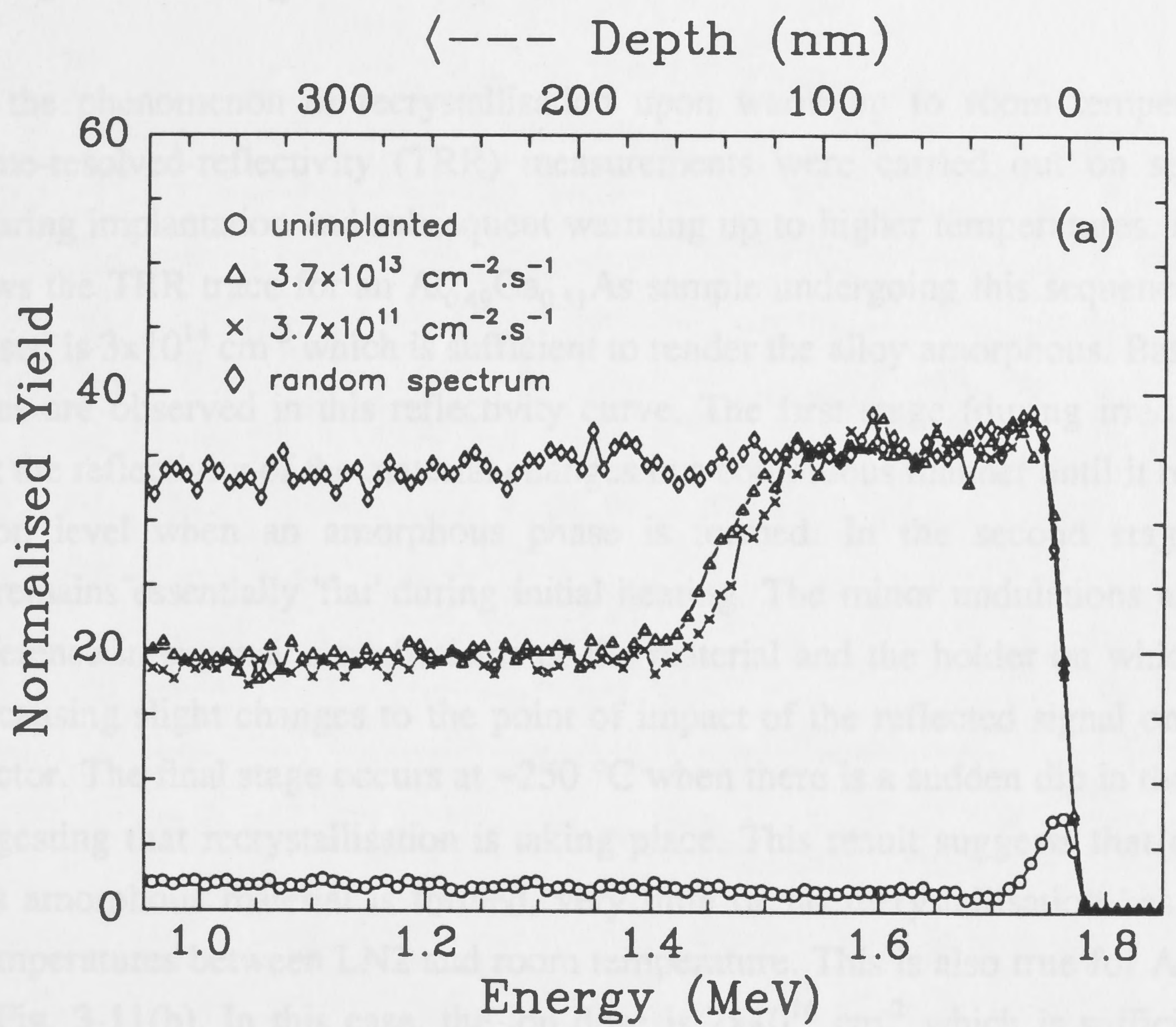

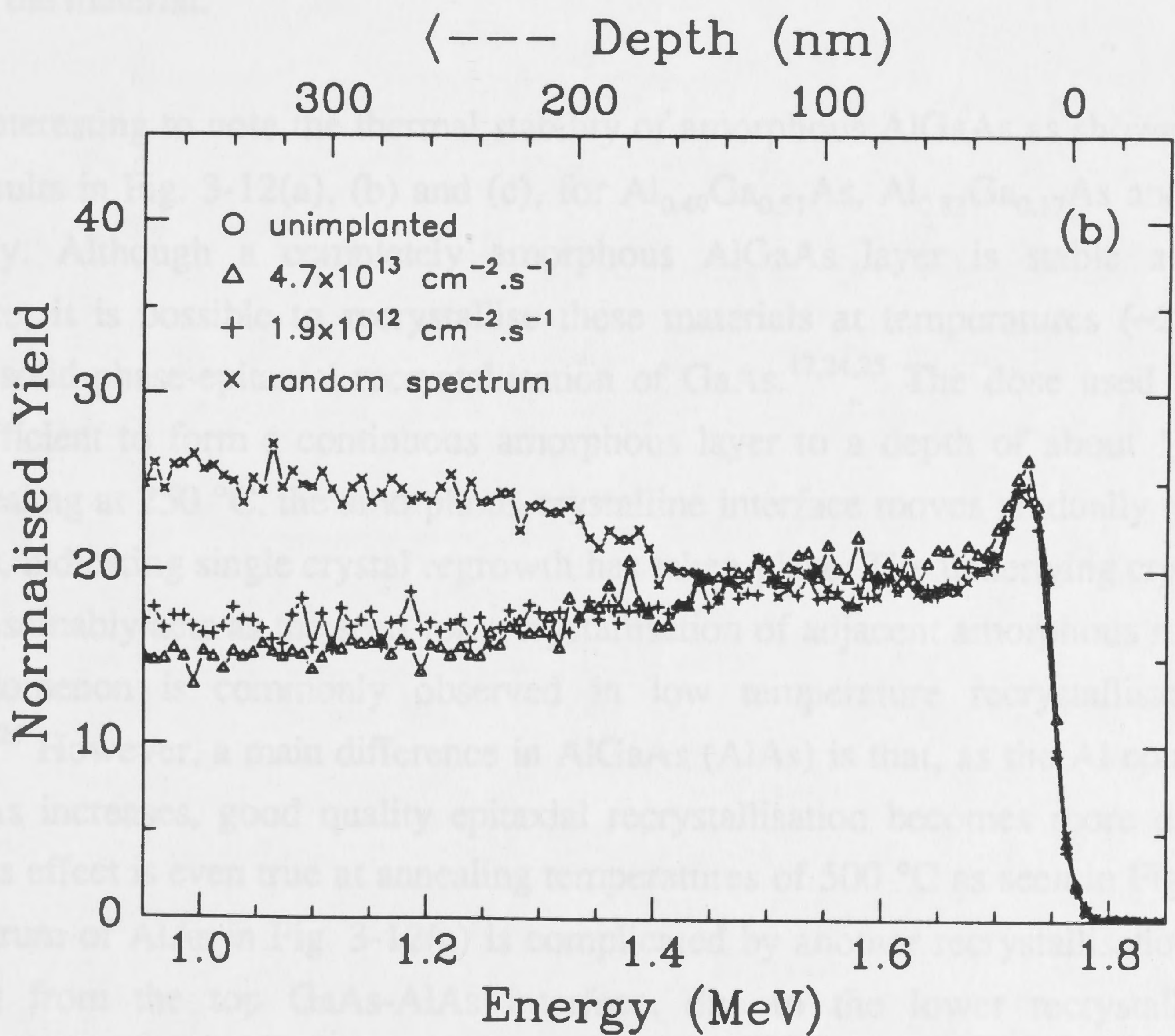

Fig. 3-10 RBS-channeling spectra for (a) $Al_{0.49}Ga_{0.51}As$ and (b) AlAs implanted with 90 keV Si ions at liquid nitrogen temperature at two different dose rates.

3.3.4 Recrystallisation effects in AlGaAs

To study the phenomenon of recrystallisation upon warm up to room temperature, *in situ* time-resolved-reflectivity (TRR) measurements were carried out on selected samples during implantation and subsequent warming up to higher temperatures. Fig. 3-11(a) shows the TRR trace for an $Al_{0.49}Ga_{0.51}As$ sample undergoing this sequence. The ion dose used is $3x10^{14}$ cm^{-2} which is sufficient to render the alloy amorphous. Basically, three stages are observed in this reflectivity curve. The first stage (during irradiation) shows that the reflectivity of the material changes in a continuous manner until it reaches a saturation level when an amorphous phase is formed. In the second stage, the spectrum remains essentially 'flat' during initial heating. The minor undulations are due to the difference in expansion coefficients of the material and the holder on which it is mounted, causing slight changes to the point of impact of the reflected signal onto the photodetector. The final stage occurs at ~250 °C when there is a sudden dip in the TRR signal suggesting that recrystallisation is taking place. This result suggests that once a continuous amorphous material is formed, very little or no recrystallisation has taken place at temperatures between LN2 and room temperature. This is also true for AlAs as shown in Fig. 3-11(b). In this case, the ion dose is $2x10^{16}$ cm^{-2} which is sufficient to amorphise the material.

It is also interesting to note the thermal stability of amorphous AlGaAs as shown by the RBS-C results in Fig. 3-12(a), (b) and (c), for $Al_{0.49}Ga_{0.51}As$, $Al_{0.83}Ga_{0.17}As$ and AlAs, respectively. Although a completely amorphous AlGaAs layer is stable at room temperature, it is possible to recrystallise these materials at temperatures (~250 °C) similar to solid-phase-epitaxial recrystallisation of GaAs.[17,24,25] The dose used in each case is sufficient to form a continuous amorphous layer to a depth of about 170 nm. Upon annealing at 250 °C, the amorphous-crystalline interface moves gradually towards the surface, indicating single crystal regrowth has taken place. The underlying crystalline region, presumably acts as the seed for recrystallisation of adjacent amorphous material. This phenomenon is commonly observed in low temperature recrystallisation of GaAs.[17,24,25] However, a main difference in AlGaAs (AlAs) is that, as the Al content of the AlGaAs increases, good quality epitaxial recrystallisation becomes more difficult. Indeed, this effect is even true at annealing temperatures of 500 °C as seen in Fig. 3-12. (The spectrum of AlAs in Fig. 3-12(c) is complicated by another recrystallisation front proceeding from the top GaAs-AlAs interface, due to the lower recrystallisation temperature of GaAs). Thus, as the fraction of Al in AlGaAs is increased, it is not only more difficult to amorphise the alloy but also harder to recrystallise once an amorphous phase is formed.

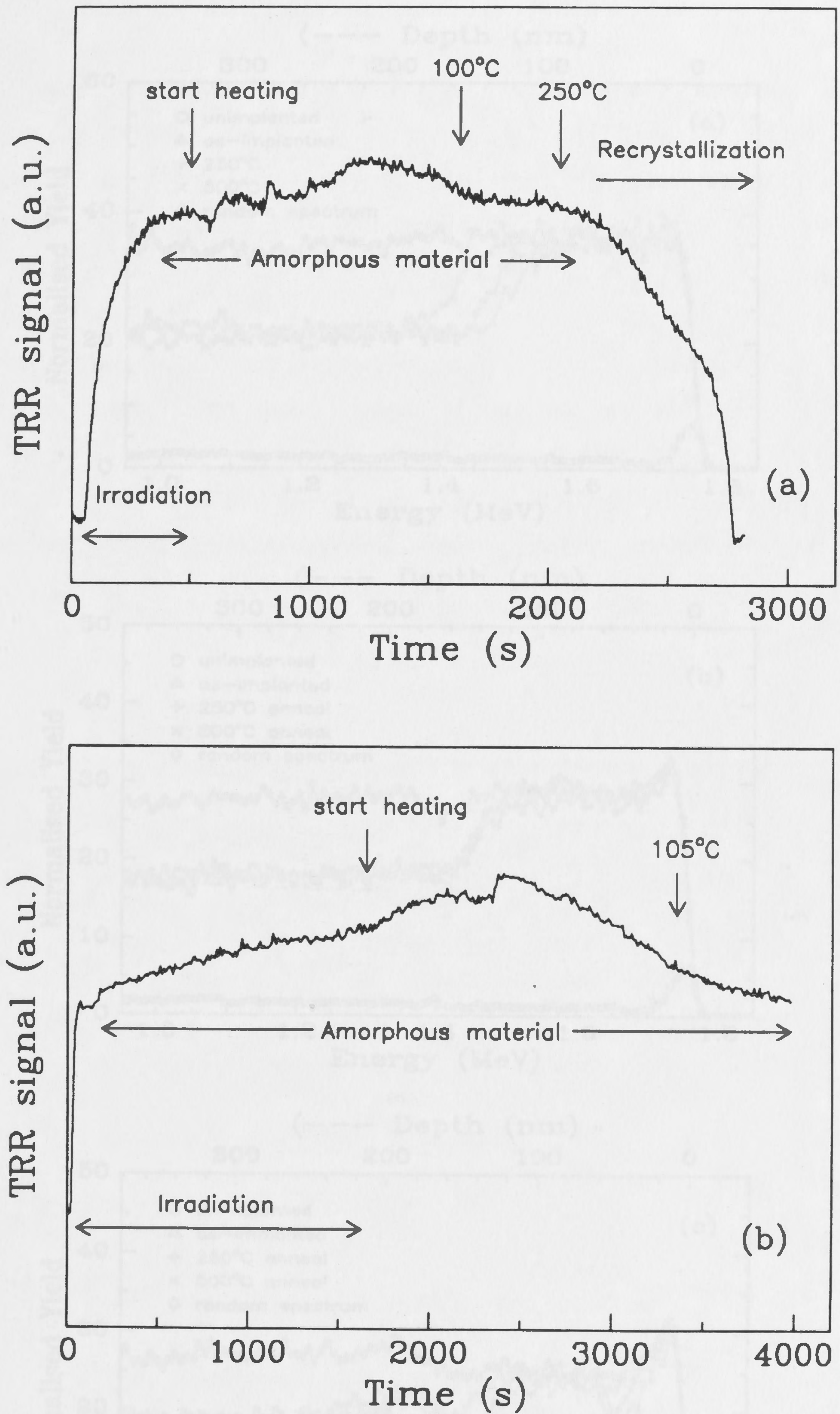

Fig. 3-11 *In situ* TRR trace during implantation at liquid nitrogen temperature and subsequent warming up in (a) $Al_{0.49}Ga_{0.51}As$ at a dose of $3x10^{14}$ cm^{-2} and (b) AlAs at $2x10^{16}$ cm^{-2}. The doses used in both cases are sufficient to render the materials amorphous.

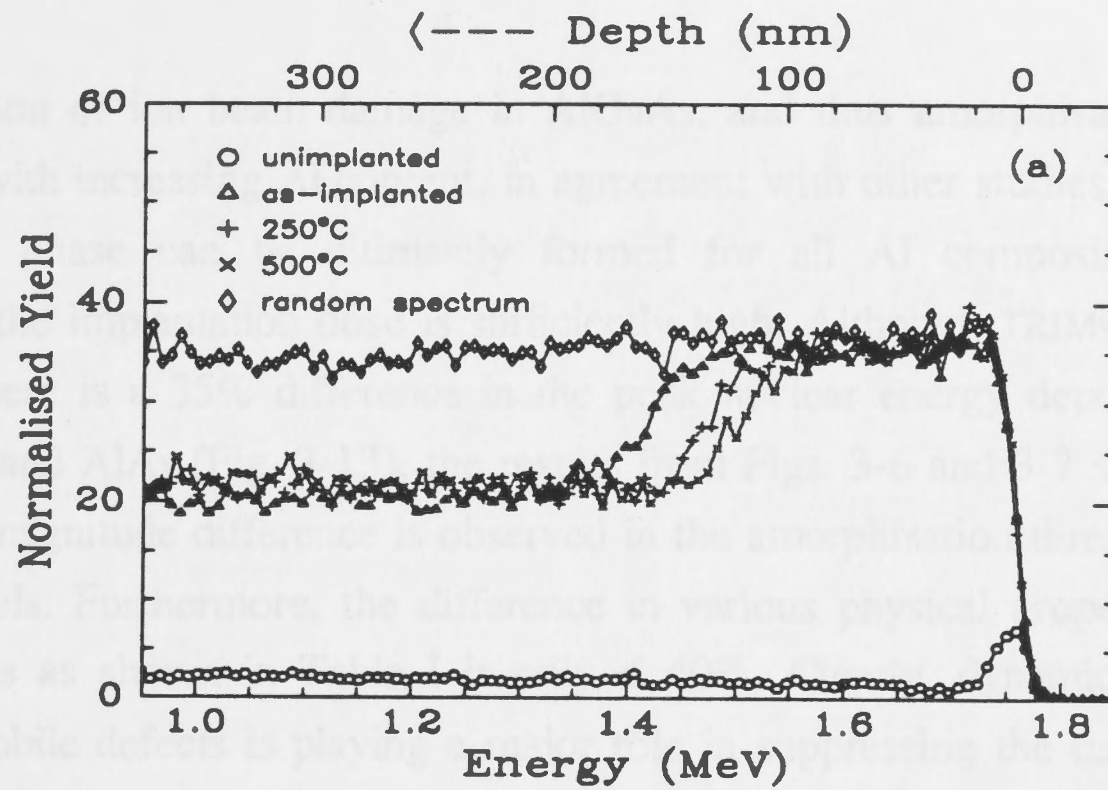

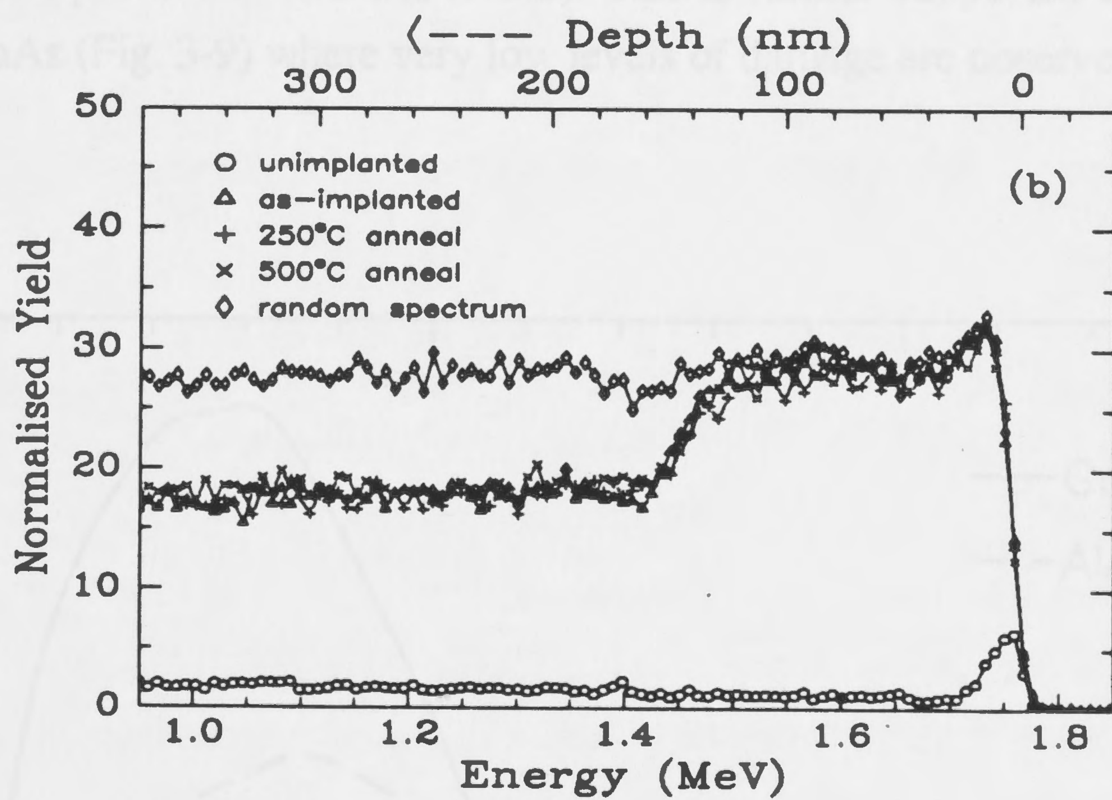

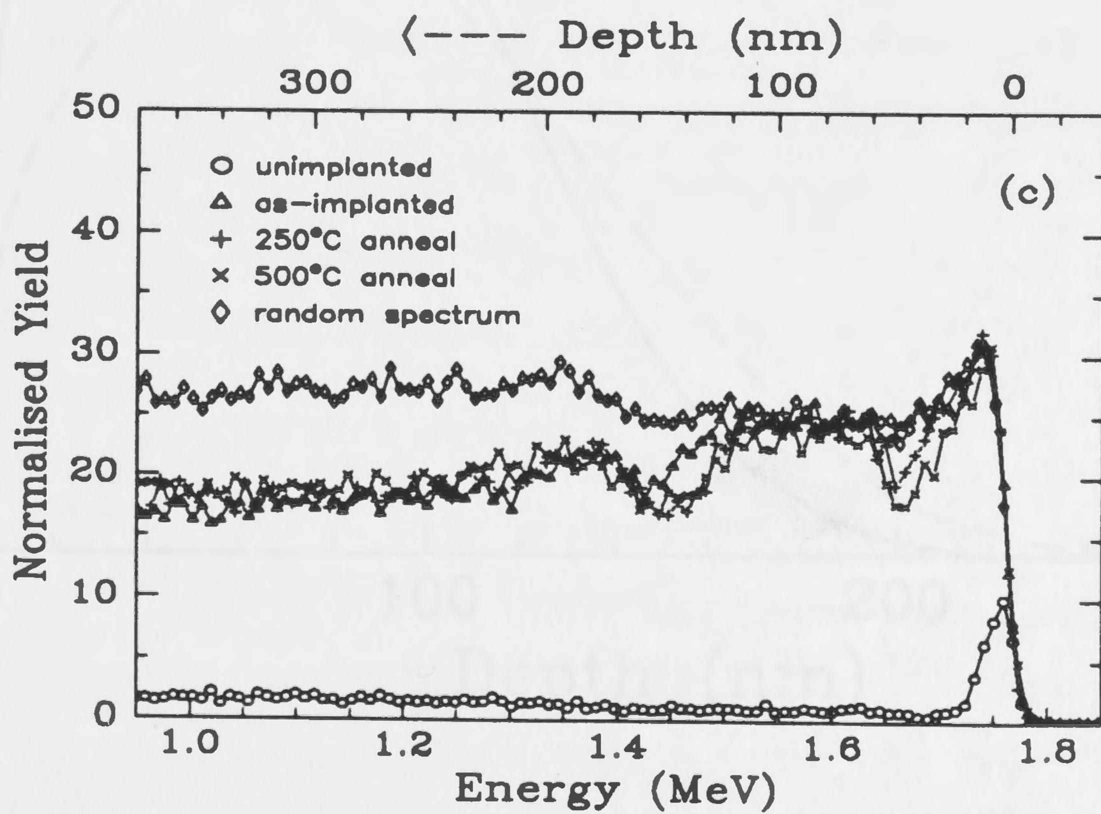

Fig. 3-12 RBS-channeling spectra showing the effect of annealing temperatures on amorphous (a) $Al_{0.49}Ga_{0.51}As$, (b) $Al_{0.83}Ga_{0.17}As$ and (c) AlAs.

3.4 Discussion

The accumulation of ion beam damage in AlGaAs, and thus amorphisation, becomes more difficult with increasing Al content, in agreement with other studies.[1-11] However, an amorphous phase can be ultimately formed for all Al compositions at LN2 temperature if the implantation dose is sufficiently high. Although TRIM90 calculations indicate that there is a 35% difference in the peak nuclear energy deposition density between GaAs and AlAs (Fig. 3-13), the results from Figs. 3-6 and 3-7 show that over two orders of magnitude difference is observed in the amorphisation threshold between the two materials. Furthermore, the difference in various physical properties between GaAs and AlAs as shown in Table I is only ≤ 40%. Clearly, dynamic annealing as mediated by mobile defects is playing a major role in suppressing the damage buildup and amorphisation process in AlGaAs (AlAs). This is further supported by the damage profiles of AlGaAs (Fig. 3-9) where very low levels of damage are observed in the wings

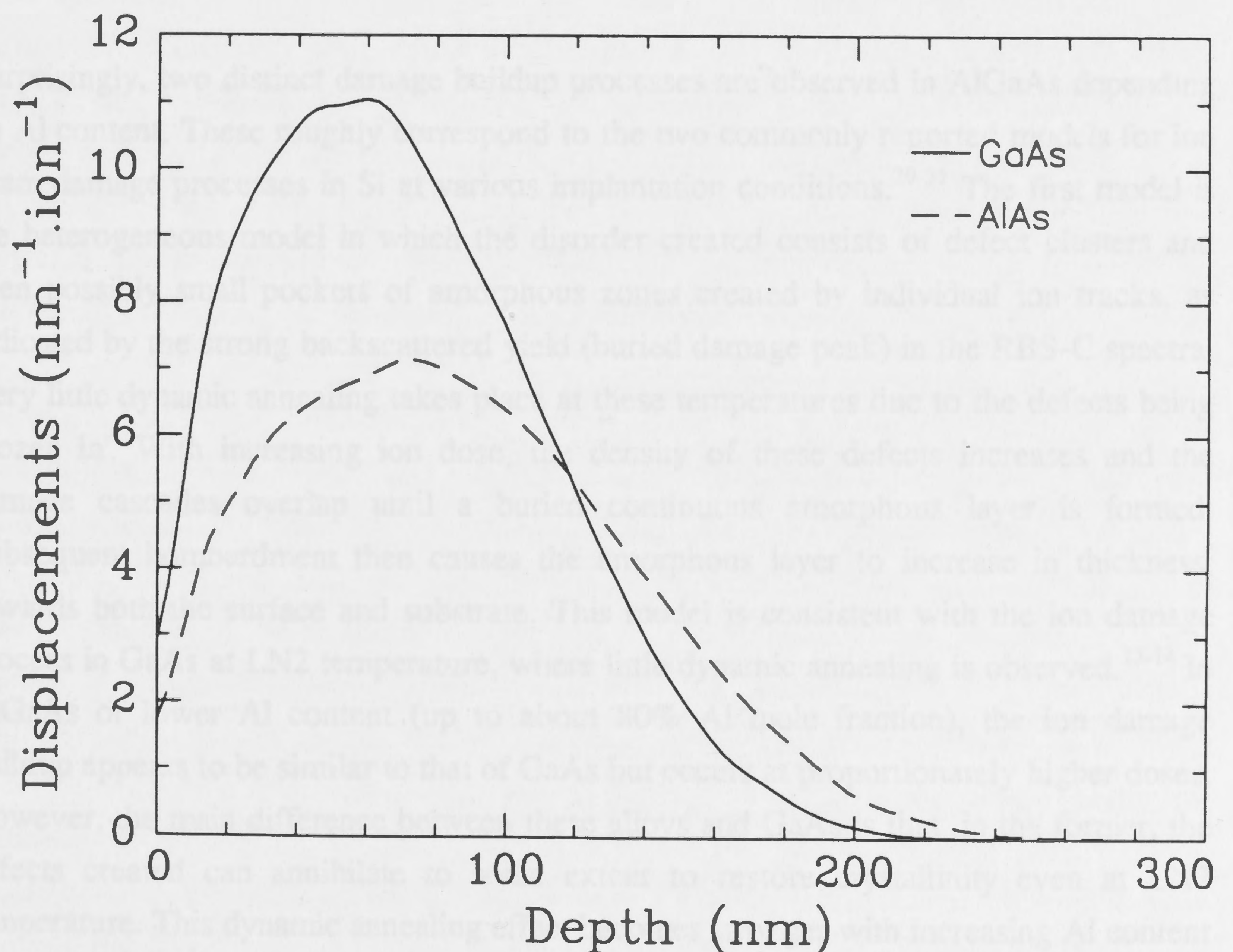

Fig. 3-13 Comparison of the displacement density profiles of GaAs and AlAs calculated by TRIM90.

of the nuclear energy deposition density profile, where the rate of damage production is lower (in comparison to the peak of the profile). Thus, dynamic annealing is competing strongly with damage production in AlGaAs. This effect is particularly accentuated for alloys with higher Al content. It has been proposed that this dynamic annealing behaviour is controlled by mobile defects in AlGaAs which mediate *in situ* annealing during implantation.[4] The data in this chapter provide further insight into the dynamic annealing processes. The observed power law of the amorphisation threshold may suggest that dynamic annealing is a 'volume-like' effect, whereby the defect density and size of the collision cascade are more important for high Al contents. Also, the insignificant dose rate effect over about two orders of magnitude at LN2 temperature suggests that dynamic annealing is very fast indeed (of the order of milliseconds or less) in AlGaAs in comparison to various reports for GaAs during room-temperature implantation.[26-28] These observations, in addition to the interesting damage buildup prior to amorphisation for high Al content AlGaAs, indicate that multiple, competing processes may be contributing to dynamic annealing and hence suppressing amorphisation.

Surprisingly, two distinct damage buildup processes are observed in AlGaAs depending on Al content. These roughly correspond to the two commonly reported models for ion beam damage processes in Si at various implantation conditions.[29-31] The first model is the heterogeneous model in which the disorder created consists of defect clusters and even possibly small pockets of amorphous zones created by individual ion tracks, as indicated by the strong backscattered yield (buried damage peak) in the RBS-C spectra. Very little dynamic annealing takes place at these temperatures due to the defects being 'frozen in'. With increasing ion dose, the density of these defects increases and the damage cascades overlap until a buried continuous amorphous layer is formed. Subsequent bombardment then causes the amorphous layer to increase in thickness, towards both the surface and substrate. This model is consistent with the ion damage process in GaAs at LN2 temperature, where little dynamic annealing is observed.[12-14] In AlGaAs of lower Al content (up to about 80% Al mole fraction), the ion damage buildup appears to be similar to that of GaAs but occurs at proportionately higher doses. However, the main difference between these alloys and GaAs is that, in the former, the defects created can annihilate to some extent to restore crystallinity even at LN2 temperature. This dynamic annealing effect becomes stronger with increasing Al content (as evident in the increase in amorphisation threshold dose with increasing Al content). Amorphisation still occurs in these alloys, most probably also by a heterogeneous process of overlap of disordered regions, but dynamic annealing results in a higher threshold dose for amorphisation.

On the other hand, amorphisation of AlGaAs of very high Al content (> 80%) proceeds *via* a homogeneous process where the route to amorphisation is *via* the accumulation of secondary defects such as point defect, clusters and extended defects. It is proposed that the high Al content greatly facilitates defect mobility and local bonding rearrangement which can act to restore local crystallinity even at low temperatures (somewhat analogous to bonding in metals). As indicated below, this process, which does not require long range defect migration, can also play a major role in retarding the damage buildup. In this case, both defect mobility and local bonding rearrangements can contribute significantly to suppressing amorphous phase formation. Nevertheless, disorder can build up in the form of stacking faults and other extended defects which are the result of imperfect dynamic annealing. Ultimately a critical defect density level is reached, upon which this heavily disordered crystal can suddenly 'collapse' into an amorphous band with the slightest increment in dose. However, it should be noted that for high Al content AlGaAs, implantation at LN2 temperature constitutes a critical temperature regime where damage creation and dynamic annealing processes are closely balanced. In this regime, a slight change in either ion dose (to change the residual disorder level) or implant temperature can favour one process over the other. This critical effect is observed in certain localised areas of the $Al_{0.95}Ga_{0.05}As$ sample where pockets of crystallinity are maintained within region (3) of Fig. 3-4(b) and is most probably due to slight inhomogeneity of the ion beam dose and/or a local variation in temperature. On average however, region (3) builds up as a band of highly defective crystal with increasing dose. This band then acts as a nucleation site for forming and extending the amorphous phase with further bombardment.

The sudden transition to an amorphous phase can be best explained by referring to Fig. 3-14 which shows schematically the free energy differences between amorphous and crystalline phases in metals and semiconductors.[18] The amorphous phase has a higher free energy than the crystalline phase. However, the amorphous phase is very unstable in pure metals due to the highly non-directional bonding nature of such elements. Hence, there is a strong tendency for displaced atoms in metals to locally rearrange during implantation to restore crystalline bond angles and preserve local crystallinity. In doing so this lowers the free energy close to that of the crystalline phase. For a highly covalent material such as Si, there is a high energy barrier (in part due to strong angular bonding rigidity) which inhibits a return to crystallinity. As in Si, there is also a kinetic barrier between the amorphous and crystalline phases for AlGaAs (GaAs and AlAs). However, in the case of AlAs and high Al content AlGaAs, it is suggested that local bonding rigidity may be lower than GaAs (more metal-like bonds), allowing the displaced atoms

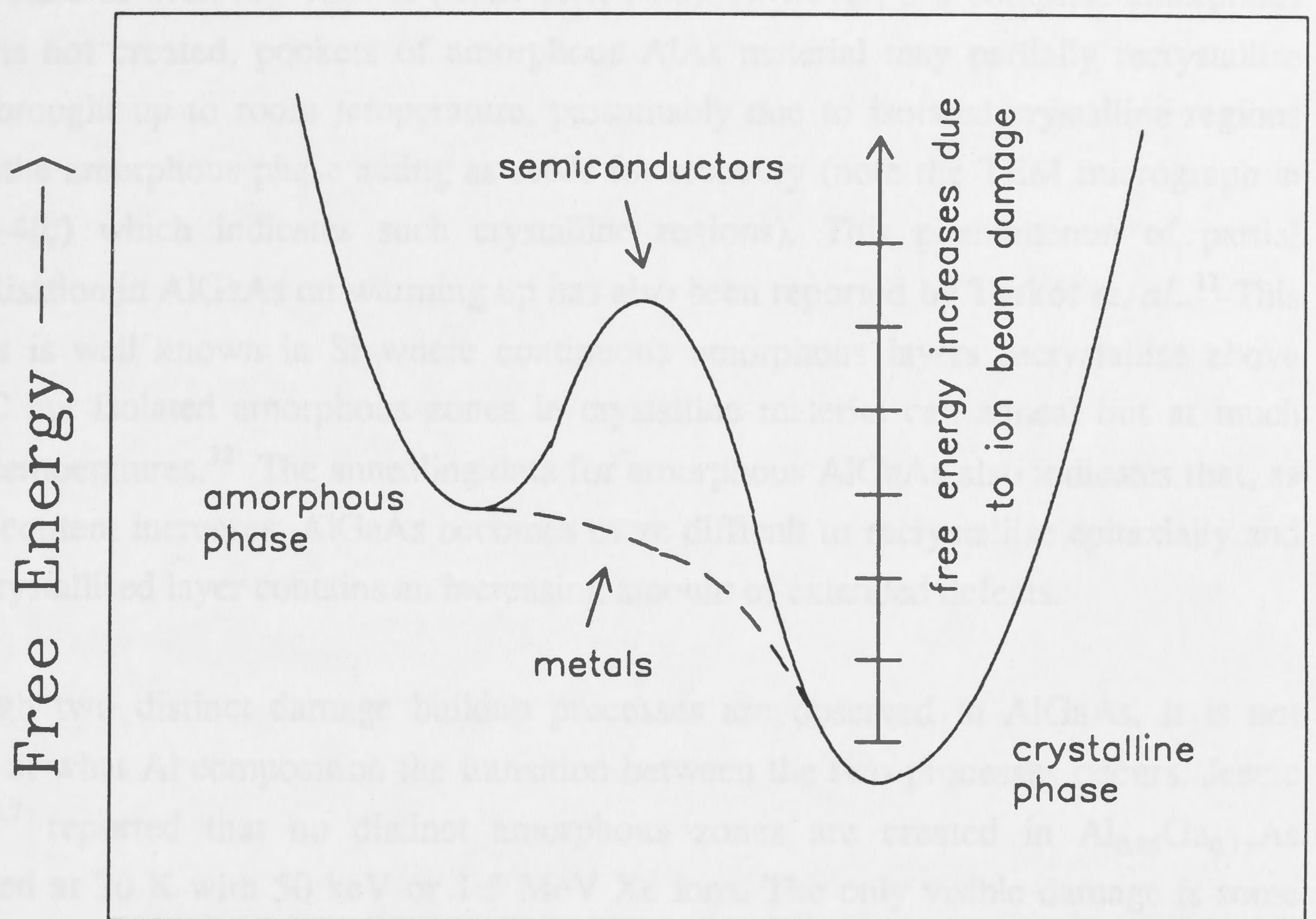

Fig. 3-14 Schematic representation of the difference in free energy between amorphous and crystalline phases in metals and semiconductors.

to rearrange more easily and preserve crystallinity during ion bombardment. This process does not require long range diffusion but may complement higher defect mobility in AlGaAs and make high Al content AlGaAs difficult to amorphise. However, the imperfect dynamic annealing leads to build up of defects and the free energy of the AlGaAs crystal will increase due in part to strain energy associated with ion damage. Amorphisation is then achieved when the free energy of the highly defective material reaches a critical limit which may even exceed that of the amorphous phase, as illustrated in Fig. 3-14. At this stage, the defective crystal may 'collapse' (relax) into an amorphous state, thereby lowering its free energy (by relieving strain).

Once a continuous amorphous layer is formed, the activation energy for crystallisation must now be overcome to partially or completely recover the crystalline structure. This can be achieved by subjecting the amorphous material to heat treatment. No recrystallisation is observed during warming up of completely amorphous AlAs to room

temperature or even to ~100 °C (from TRR data). However, if a complete amorphous phase is not created, pockets of amorphous AlAs material may partially recrystallise when brought up to room temperature, presumably due to isolated crystalline regions within the amorphous phase acting as seeds for recovery (note the TEM micrograph in Fig. 3-4(c) which indicates such crystalline regions). This phenomenon of partial crystallisation in AlGaAs on warming up has also been reported by Turkot *et. al.*.[11] This process is well known in Si where continuous amorphous layers recrystallise above 500 °C but isolated amorphous zones in crystalline material can anneal out at much lower temperatures.[32] The annealing data for amorphous AlGaAs also indicates that, as the Al content increases, AlGaAs becomes more difficult to recrystallise epitaxially and the recrystallised layer contains an increasing amount of extended defects.

Although two distinct damage buildup processes are observed in AlGaAs, it is not known at what Al composition the transition between the two processes occurs. Jencic *et. al.*[6,7] reported that no distinct amorphous zones are created in $Al_{0.85}Ga_{0.15}As$ irradiated at 30 K with 50 keV or 1.5 MeV Xe ions. The only visible damage is some weak-contrast features, presumably clusters of point defects similar to that observed in AlAs by Cullis *et. al.*.[4,5,8] The data in this work also indicate that the transition occurs at around this Al concentration.

For higher Al concentrations, the lack of amorphous regions at intermediate doses of $\sim 10^{14}$-10^{15} cm^{-2} can lead one to argue that the dynamic annealing rate is much higher than the rate of defect production. It might be expected that amorphisation would then only proceed by increasing the implant dose rate such that damage cascades overlap with existing disorder zones before defects within these zones have fully annealed. This situation may lead to a stable disordered structure and to the formation of an amorphous phase. Hence, the amorphisation process in this case would be similar to that of lower Al content AlGaAs except that the high dose rates would be necessary to induce amorphisation. However, the present data does not support this scenario; there is no dose rate effect and only extended defects and clusters are observed at pre-amorphous doses. This mode of disorder buildup and the sudden onset of amorphisation indicate a distinctly different amorphisation mechanism to that of lower Al concentrations. Indeed, the present data (particularly the sudden onset of amorphisation) suggest that amorphisation is 'nucleation-limited' for high Al content cases, whereby the free energy of the defective material prior to amorphisation actually exceeds that of the amorphous phase. When this occurs and the lattice collapses to a lower free energy, a large volume of material is amorphised for a very small increment in dose. Thereafter the buried amorphous layer extends both towards the surface and into the bulk.

In most of the previous ion damage work on AlGaAs (AlAs) by various groups,[1-11] multilayer structures were used. In such cases, the presence of GaAs adjacent to AlGaAs (AlAs) complicates the damaging and annealing processes in both GaAs and AlGaAs (AlAs) and thus the bulk behaviour of AlGaAs is obscured. For example, both Klatt and co-workers[10] and Turkot *et. al.*[11] observed asymmetric damage distributions in AlAs sandwiched between two GaAs layers and explained this behaviour in terms of different damage states existing after irradiation and warm up to room temperature. Cullis *et. al.*[4,5,8] showed that AlGaAs and AlAs are able to offer some degree of protection against ion induced damage to adjacent GaAs regions and also to act as a sink for point defects. Multiple competing processes are clearly taking place in GaAs-AlGaAs(AlAs) multilayer structures during ion implantation. Some interesting effects are further observed in multilayers : mobile defects in AlGaAs can inhibit amorphisation of surrounding GaAs regions or enhance their amorphisation depending on the particular bombardment conditions and nature of the multilayer structures. This is covered in more detail in the next chapter.

3.5 Conclusions

The systematic data from this work clearly indicate that AlGaAs becomes more difficult to amorphise with increasing Al content, consistent with other studies.[1-11] A difference of more than two orders of magnitude difference is observed in the amorphisation threshold dose between GaAs and AlAs. During implantation, dynamic annealing, as controlled by very fast mobile defects and local bonding rearrangements, and defect creation processes compete very strongly in AlGaAs even at LN2 temperatures. This effect is accentuated with increasing Al composition.

Two distinct damage build up processes are observed in $Al_xGa_{1-x}As$ depending on the Al content. For lower Al content ($x \leq 0.83$) alloys, the behaviour is similar to GaAs whereby amorphisation is *via* the overlap of damage cascades or even small amorphous zones created by individual ion tracks. For AlGaAs of high Al content ($x \geq 0.95$), disorder builds up in the form of stacking faults and other extended defects until a critical defect density (or system free energy) is reached. This strong dynamic annealing behaviour can be mediated by both the availability of very fast mobile defects and local bonding rearrangement (as a result of high Al content) to restore crystallinity. Nucleation-limited amorphisation then proceeds with increasing implantation dose and is best described by a model in which the free energy of the defective crystal exceeds that of the amorphous state. Although AlGaAs with increasing Al content becomes more difficult to amorphise, once a continuous layer is formed, it is also more difficult to recrystallise.

These results will be important as they provide a basis for understanding ion beam-induced damage accumulation in GaAs-AlGaAs multilayers where further complexities are expected due to the presence of heterointerfaces. However, this will be the subject of the following chapter. Furthermore, these results provide a new insight into the nature of ion beam-induced defects in AlGaAs which will be very important in subsequent chapters on quantum well intermixing and its applications to optoelectronic devices.

References

[1] J. Ralston, G.W. Wicks, L.F. Eastman, B.C. De Cooman and C.B. Carter, "Defect structure and intermixing of ion-implanted $Al_xGa_{1-x}As/GaAs$ superlattice," *J. Appl. Phys.* **59**, 120-123 (1986).

[2] K. Matsui, S. Takatani, T. Fukunaga, T. Narusawa, Y. Bamba and H. Nakashima, "Damage profile in GaAs, AlAs, AlGaAs, and GaAs/AlGaAs superlattices induced by Si^+-ion implantation," *Jpn. J. Appl. Phys.* **25**, L391-L393 (1986).

[3] K. Matsui, T. Takamori, T. Fukunaga, T. Narusawa and H. Nakashima, "Ion-implantation induced damage in $Al_xGa_{1-x}As$ and superlattices studied by Rutherford backscattering," *Jpn. J. Appl. Phys.* **26**, 482-486 (1987).

[4] A.G. Cullis, N.G. Chew, C.R. Whitehouse, D.C. Jacobson, J.M. Poate and S.J. Pearton, "Material-dependent amorphization and epitaxial crystallisation in ion-implanted AlAs/GaAs layer structures," *Appl. Phys. Lett.* **55**, 1211-1213 (1989).

[5] A.G. Cullis, P.W. Smith, D.C. Jacobson and J.M. Poate, "Differential ion damage and its annealing behavior in AlAs/GaAs heterostructures," *J. Appl. Phys.* **69**, 1279-1286 (1991).

[6] I. Jencic, M.W. Bench, I.M. Robertson, M.A. Kirk and J. Peternelj, "A comparison of the rates of amorphization in the $Al_xGa_{1-x}As/GaAs$ system," *Nucl. Instrum. Methods* **B59/60**, 458-461 (1991).

[7] I. Jencic, M.W. Bench, I.M. Robertson and M.A. Kirk, "A comparison of the amorphization induced in $Al_xGa_{1-x}As$ and GaAs by heavy-ion irradiation," *J. Appl. Phys.* **69**, 1287-1292 (1991).

[8] A.G. Cullis, A. Polman, P.W. Smith, D.C. Jacobson, J.M. Poate and C.R. Whitehouse, "The nature of keV and MeV ion damage in $Al_xGa_{1-x}As/GaAs$ and AlAs/GaAs heterostructures," *Nucl. Instrum. Methods* **B62**, 463-468 (1992).

[9] C. Vieu, M. Schneider, H. Launois and B. Descouts, "Damage generation and annealing in Ga^+ implanted GaAs/(Ga,Al)As quantum wells," *J. Appl. Phys.* **71**, 4833-4841 (1992).

[10] J.L. Klatt, R.S. Averback, D.V. Forbes and J.J. Coleman, "Interfacial damage in ion-irradiated GaAs/AlAs superlattices," *Phys. Rev. B* **48**, 17629-17632 (1993).

[11] B.A. Turkot, D.V. Forbes, I.M. Robertson, J.J. Coleman, L.E. Rehn, M.A. Kirk and P.M. Baldo, "Ion implantation damage in $Al_{0.6}Ga_{0.4}As/GaAs$ heterostructures," *J. Appl. Phys.* **78**, 97-103 (1995).

[12] D.K. Sadana, "Mechanisms of amorphization and recrystallization in ion implanted III-V compound semiconductors," *Nucl. Instrum Methods* **B7/8**, 375-386 (1985).

[13] S.T. Johnson, J.S. Williams, R.G. Elliman, A.P. Pogany, E. Nygren and G.L. Olson, "Characterisation of structural changes and defects in ion bombarded GaAs," *Mater. Res. Soc. Symp. Proc.* **82**, 127-132 (1987).

[14] W. Wesch, "Ion implantation in III-V compounds," *Nucl. Instrum. Methods* **B6/8**, 342-354 (1992).

[15] J.F. Ziegler, J.P. Biersack and U. Littmark, *The Stopping and Range of Ions in Solids*, vol. 1, Pergamon, New York (1989).

[16] L.C. Feldman, J.W. Mayer and S.T. Picraux, *Materials Analysis by Ion Channeling*, Academic Press, New York (1982).

[17] J.S. Williams and M.W. Austin, "Low-temperature epitaxial regrowth of ion-implanted amorphous GaAs," *Appl. Phys. Lett.* **36**, 994-996 (1980).

[18] J.S. Williams, "Ion induced damage and dynamic annealing processes," *Trans. Mater. Res. Soc. Jpn.* **17**, 417-423 (1994).

[19] S. Adachi, "GaAs, AlAs, and $Al_xGa_{1-x}As$: Material parameters for use in research and device applications," *J. Appl. Phys.* **58**, R1-R29 (1985).

[20] W.-K. Chu, J.W. Mayer and M.-A. Nicolet, *Backscattering Spectrometry*, Academic Press, New York (1978).

[21] J.S. Williams and R.G. Elliman, "Channeling," in *Ion Beam for Material Analysis*, J.R. Bird and J.S. Williams, editors, Chp. 6, 261-333, Academic Press, Sydney (1989).

[22] J.S. Williams and J.M. Poate, editors, *Ion Implantation and Beam Processing*, Academic Press, Sydney (1984).

[23] J.S. Vetrano, M.W. Bench, I.M. Robertson, and M.A. Kirk, "In situ studies of ion irradiation effects in an electron microscope," *Met. Trans.* **20A**, 2673-2680 (1989).

[24] C. Licoppe, Y.I. Nissim and C. Meriadec, "Direct measurement of solid-phase epitaxial growth kinetics in GaAs by time-resolved reflectivity," *J. Appl. Phys.* **58**, 3094-3096 (1985).

[25] S. Yokohama, D. Yui, H. Tanigawa, H. Takasugi and M. Kawabe, "Solid-phase crystal growth of molecular-beam-deposited amorphous GaAs," *J. Appl. Phys.* **62**, 1808-1814 (1987).

[26] J.S. Williams, R.G. Elliman, S.T. Johnson, D.K. Sengupta and J.M. Zemanski, "Ion beam processing of GaAs at elevated temperatures," *Mater. Res. Soc. Symp. Proc.* **144**, 355-360 (1989).

[27] E. Wendler, W. Wesch and G. Götz, "Influence of the dose rate on the damage production in ion implanted GaAs," *Nucl. Instrum. Methods* **B52**, 57-62 (1990).

[28] T.E. Haynes and O.W. Holland, "Dose rate effects on damage accumulation in Si^+-implanted gallium arsenide," *Appl. Phys. Lett.* **58**, 62-64 (1991).

[29] F. Morehead and B.L. Crowder, "A model for the formation of amorphous Si by ion bombardment," *Rad. Eff.* **6**, 27-32 (1970).

[30] F.L. Vook, "Radiation damage during ion implantation," in *Defects in semiconductors*, 60-71, Institute of Physics, London (1971).

[31] M.L. Swanson, J.R. Parsons and C.W. Hoelke, "Damaged regions in neutron-irradiated and ion-bombarded Ge and Si," *Rad. Eff.* **9**, 249-256 (1971).

[32] G.L. Olson and R.A. Roth, "Kinetics of solid phase crystallization in amorphous Si," *Mater. Sci. Rept.* **3**, 1-76 (1988) and references therein.

Chapter 4

Ion damage buildup in GaAs-$Al_xGa_{1-x}As$ multilayers

4.1 Introduction

Lattice-matched GaAs-AlGaAs based heterostructures are arguably the most important material systems in optoelectronic devices. The discovery of layer-disordering by impurity diffusion,[1,2] ion implantation[2,3] and cap annealing[4,5] has sparked considerable interest in the study of disordering behaviour, impurity-damage interactions and the fabrication of novel optoelectronic devices.[6-10] Ion implantation-induced disordering is, arguably, more advantageous than the other two techniques due to its ability to incorporate precise and controllable amounts of damage into the material to induce disordering. The application of this technique to fine tune the band gap energy of GaAs quantum wells and lasers will be discussed in Chapters 6 and 7, respectively.

It is important to first study the ion beam-induced damage buildup in these multilayer structures so that this process can be optimised for application purposes. The disordering process becomes significantly more complex in these structures due to multiple, competing disordering and reordering processes across two different materials and at their interfaces. Several, somewhat conflicting processes such as defect migration, ballistic intermixing and differences in the electronic stopping effects of the ions have been proposed to play dominant roles in damage accumulation in multilayers. Indeed, a thorough understanding of damage formation and annealing processes in GaAs-AlGaAs multilayer structures is lacking although there have been a number of reports in this area.[11-22] In order to resolve some of the complexities in multilayers, the results and insights from ion beam-induced damage buildup in bulk $Al_xGa_{1-x}As$ layers discussed in the previous chapter will provide a platform for the understanding of similar processes in multilayers.

In this chapter, ion beam-induced damage and amorphisation processes in GaAs-AlGaAs multilayers are studied by Rutherford backscattering spectrometry - ion channeling (RBS-C) and cross-sectional transmission electron microscopy (XTEM) techniques. The order of the multilayers (AlGaAs layer sandwiched between two GaAs layers and *vice versa*) is investigated. The effects of variation in the energy deposition density, i.e. keV and MeV beams, are also examined, creating either a damage profile that varies steeply across the interfaces or a fairly uniform damage profile across the interfaces, respectively.

4.2 Experimental

The multilayer structures used in this work were specifically designed to meet the above-mentioned experimental conditions. Essentially, two sets of structures, each with two $Al_xGa_{1-x}As$ (x=0.5 and 0.9) compositions were grown on semi-insulating Vertical-Gradient-Freeze GaAs (100) substrates by MOCVD. One set had an AlGaAs layer sandwiched between two GaAs layers while the other had a GaAs layer in between two AlGaAs layers. In all cases, an initial GaAs buffer of 0.5-1 μm was first grown. Implantation was carried out using either 90 keV, 1 MeV or 4 MeV Si beams with the samples held at liquid nitrogen (LN2) temperature. For keV irradiation, the energy was chosen such that the nuclear energy deposition density varied significantly across the layers with the peak around the top GaAs-AlGaAs interface. However, with MeV beams, the nuclear energy deposition density was fairly constant across the region of interest (< 600 nm) and the peak was located deep within the GaAs buffer. Analysis was carried out at room temperature by RBS-C and selected samples were then examined by XTEM. Two methods were used to prepare the samples for XTEM analysis; the cleavage (for unimplanted specimens) and the standard ion beam thinning (for implanted specimens) methods, as discussed in Chapter 2.

4.3 Results

4.3.1 AlGaAs layer between two GaAs layers (keV beams)

Fig. 4-1(a) shows FASTRIM[23] calculations of 90 keV Si bombardment into an $Al_{0.5}Ga_{0.5}As$ layer sandwiched between two GaAs layers. FASTRIM is a Monte-Carlo simulation program based on TRIM85-90[24] which corrects for the interfacial problems inherent with TRIM. The displacement density (or the nuclear energy deposition density) rises steeply in the top GaAs layer, reaching a maximum at the interface and decreases across the $Al_{0.5}Ga_{0.5}As$ layer. At the lower GaAs-AlGaAs interface however, the magnitude of the displacement density has dropped by an order of magnitude compared with the top interface. As one would expect, damage/amorphisation should start accumulating in GaAs regions near the interface, extending towards the surface and then into the underlying $Al_{0.5}Ga_{0.5}As$ layer (due to the higher threshold for amorphisation in $Al_{0.5}Ga_{0.5}As$ in comparison to GaAs). The results for this type of structure are shown in Fig. 4-1(b), with damage building up preferentially in the top GaAs layer. At a dose of $6x10^{13}$ cm^{-2}, the top GaAs appears to be heavily damaged. However, complete amorphisation has not yet occurred as indicated by the yield of the damage peak which has not quite reached the random level. In contrast to FASTRIM calculations which predict maximum disorder at the GaAs-AlGaAs interface, the damage peak in the top GaAs layer is located away from the interface. Thus, it appears that narrow regions of GaAs in proximity to an AlGaAs layer are more resistant to ion beam damage than in bulk GaAs. Very little damage is observed in the underlaying $Al_{0.5}Ga_{0.5}As$ layer. This strong differential damage effect is quite interesting considering the difference in displacement densities between the two materials is only about 25% [see profile in Fig. 4.1(a)] but is consistent with the well known observation that AlGaAs is more resistant to ion beam damage than GaAs. At the next dose shown of $1x10^{14}$ cm^{-2}, complete amorphisation of the top GaAs occurs and damage starts accumulating across the interface into the $Al_{0.5}Ga_{0.5}As$ layer. Amorphisation of the $Al_{0.5}Ga_{0.5}As$ occurs rapidly with a small increase in dose (from $1x10^{14}$ to $2x10^{14}$ cm^{-2}). Further increases in dose result in the amorphous layer growing deeper into the $Al_{0.5}Ga_{0.5}As$ layer. These observations suggest that once a complete amorphous phase is formed at the GaAs-AlGaAs interface, this region acts as a site for nucleation-limited amorphisation in AlGaAs. No damage is observable in the underlaying GaAs layer due to the low density of displacements.

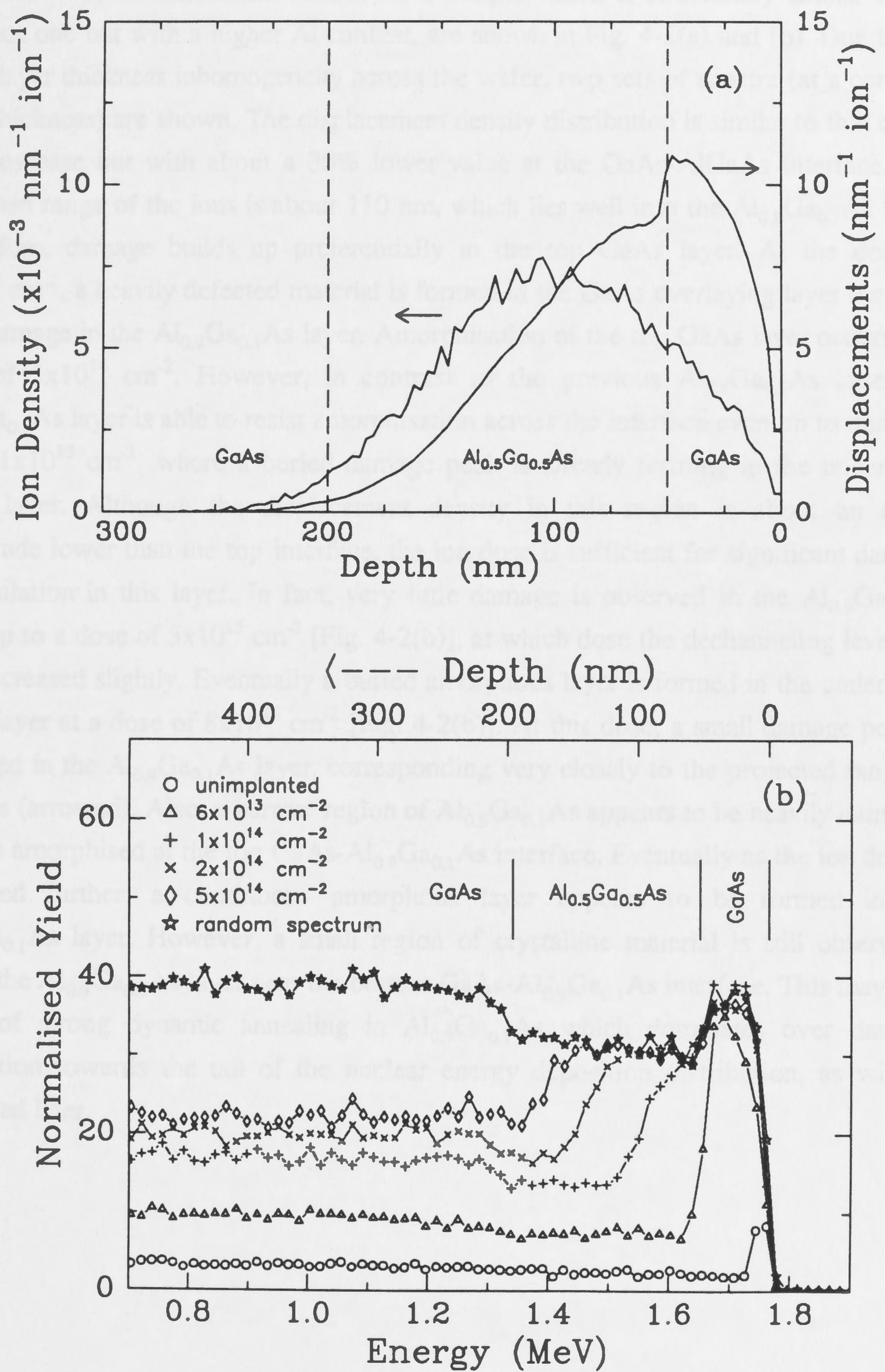

Fig. 4-1 (a) FASTRIM calculations of the ion density and displacement density profiles for 90 keV Si implantation into a GaAs-$Al_{0.5}Ga_{0.5}$As-GaAs structure. (b) RBS-C spectra showing the ion beam damage buildup in this structure.

The 90 keV Si^- bombardment results for a sample which is structurally similar to the previous one but with a higher Al content, are shown in Fig. 4-2(a) and (b). Due to the slight layer thickness inhomogeneity across the wafer, two sets of spectra (at a constant layer thickness) are shown. The displacement density distribution is similar to that of the previous case but with about a 30% lower value at the GaAs-AlGaAs interface. The projected range of the ions is about 110 nm, which lies well into the $Al_{0.9}Ga_{0.1}As$ layer. As before, damage builds up preferentially in the top GaAs layer. At the dose of $6x10^{13}$ cm^{-2}, a heavily defected material is formed in the GaAs overlaying layer but with little damage in the $Al_{0.9}Ga_{0.1}As$ layer. Amorphisation of the top GaAs layer occurs at a dose of $1x10^{14}$ cm^{-2}. However, in contrast to the previous $Al_{0.5}Ga_{0.5}As$ case, the $Al_{0.9}Ga_{0.1}As$ layer is able to resist amorphisation across the interface even up to doses of about $1x10^{15}$ cm^{-2}, where a buried damage peak is already forming in the underlying GaAs layer. Although the displacement density in this region is about an order magnitude lower than the top interface, the ion dose is sufficient for significant damage accumulation in this layer. In fact, very little damage is observed in the $Al_{0.9}Ga_{0.1}As$ layer up to a dose of $5x10^{15}$ cm^{-2} [Fig. 4-2(b)], at which dose the dechanneling level has only increased slightly. Eventually a buried amorphous layer is formed in the underlying GaAs layer at a dose of $8x10^{15}$ cm^{-2} [Fig. 4-2(b)]. At this dose, a small damage peak is observed in the $Al_{0.9}Ga_{0.1}As$ layer, corresponding very closely to the projected range of the ions (arrowed). Also, a narrow region of $Al_{0.9}Ga_{0.1}As$ appears to be heavily damaged or even amorphised at the top GaAs-$Al_{0.9}Ga_{0.1}As$ interface. Eventually as the ion dose is increased further, a continuous amorphous layer appears to be formed in the $Al_{0.9}Ga_{0.1}As$ layer. However, a small region of crystalline material is still observable within the $Al_{0.9}Ga_{0.1}As$ layer near the bottom GaAs-$Al_{0.9}Ga_{0.1}As$ interface. This may be a result of strong dynamic annealing in $Al_{0.9}Ga_{0.1}As$ which dominates over damage production towards the tail of the nuclear energy deposition distribution, as will be discussed later.

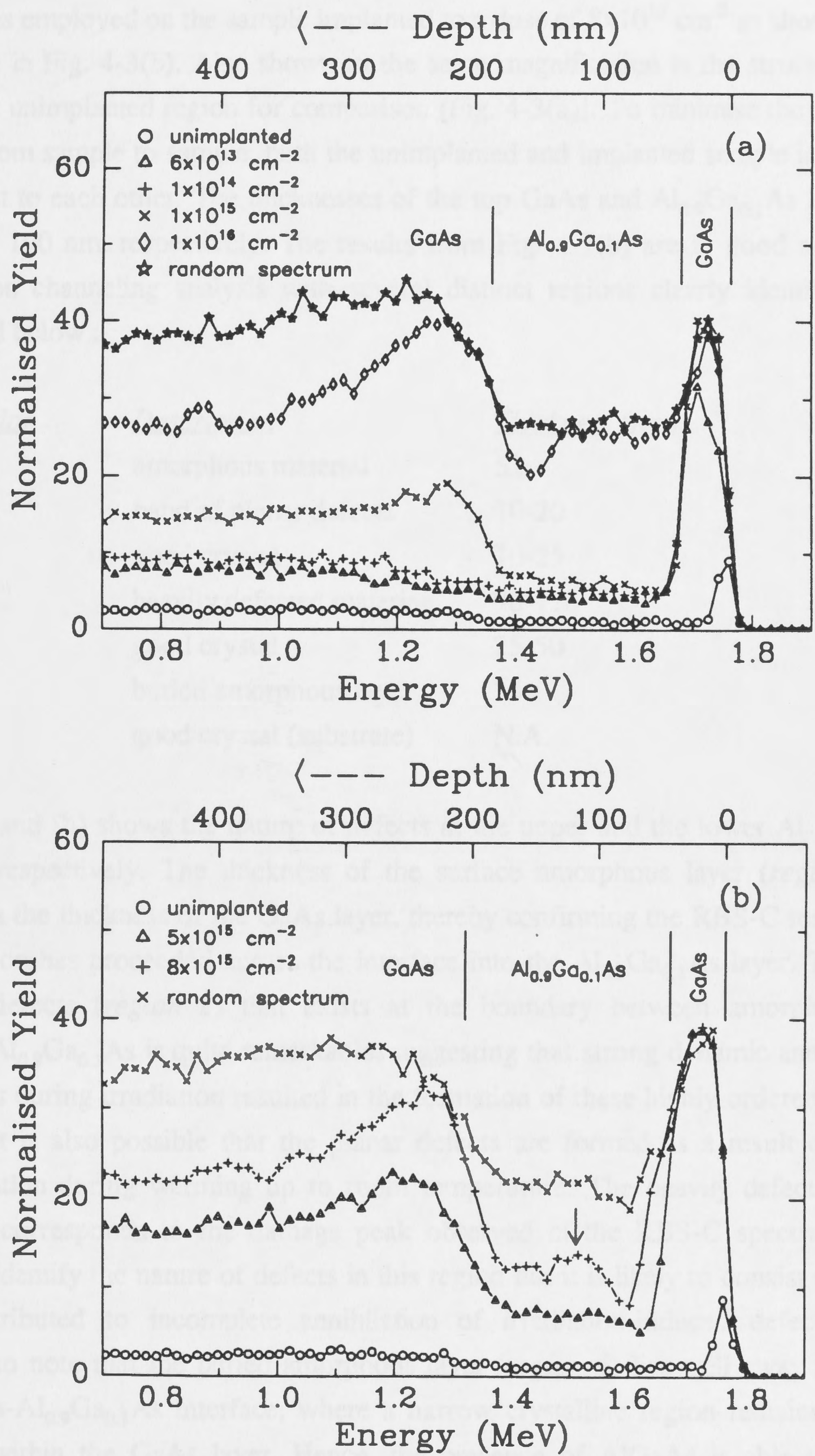

Fig. 4-2 RBS-C spectra showing the damage buildup in a GaAs-$Al_{0.9}Ga_{0.1}As$-GaAs structure implanted with 90 keV Si ions. Due to the slight layer thickness inhomogeneity across the wafer, two sets of spectra are shown (at constant layer thickness). The arrow indicates the projected range of the ions.

To gain further insight into the microstructure of the ion beam-induced damage, XTEM analysis was employed on the sample implanted to a dose of 8×10^{15} cm^{-2} as shown in the micrograph in Fig. 4-3(b). Also shown to the same magnification is the structure from an adjacent unimplanted region for comparison [Fig. 4-3(a)]. To minimise the thickness variation from sample to sample, both the unimplanted and implanted sample in Fig. 4-3 are adjacent to each other. The thicknesses of the top GaAs and $Al_{0.9}Ga_{0.1}As$ layers are 35 nm and 190 nm, respectively. The results from Fig. 4-3(b) are in good agreement with the ion channeling analysis with several distinct regions clearly identifiable, as summarised below :

Region	Description	Thickness (nm)
1	amorphous material	52
2	band of planar defects	10-20
3	good crystal	10-25
4	heavily defected material	90-120
5	good crystal	25-50
6	buried amorphous layer	34
7	good crystal (substrate)	N.A.

Fig. 4-4(a) and (b) shows the nature of defects at the upper and the lower $Al_{0.9}Ga_{0.1}As$ interfaces, respectively. The thickness of the surface amorphous layer (*region 1*) is greater than the thickness of the GaAs layer, thereby confirming the RBS-C results that amorphisation has proceeded across the interface into the $Al_{0.9}Ga_{0.1}As$ layer. The band of planar defects (*region 2*) that exists at the boundary between amorphous and crystalline $Al_{0.9}Ga_{0.1}As$ is quite remarkable, suggesting that strong dynamic annealing in $Al_{0.9}Ga_{0.1}As$ during irradiation resulted in the formation of these highly ordered defects. However, it is also possible that the planar defects are formed as a result of partial recrystallisation during warming up to room temperature. The heavily defective band (*region 4*) corresponds to the damage peak observed in the RBS-C spectrum. It is difficult to identify the nature of defects in this region but it is likely to consist of defect clusters attributed to incomplete annihilation of irradiation-induced defects. It is interesting to note that the buried amorphous layer (*region 6*) lies well away from the lower GaAs-$Al_{0.9}Ga_{0.1}As$ interface, where a narrow crystalline region remains (across *region 5*) within the GaAs layer. Hence, the presence of AlGaAs is able to inhibit amorphisation of narrow GaAs regions near the interface [Fig. 4-4(b)]. This observation is similar to previously reported results for GaAs-AlAs multilayers.[14,15,18] The relatively good crystallinity in this region suggests that dynamic annealing is dominant and, hence, amorphisation is suppressed. It may be suggested that during implantation, forward

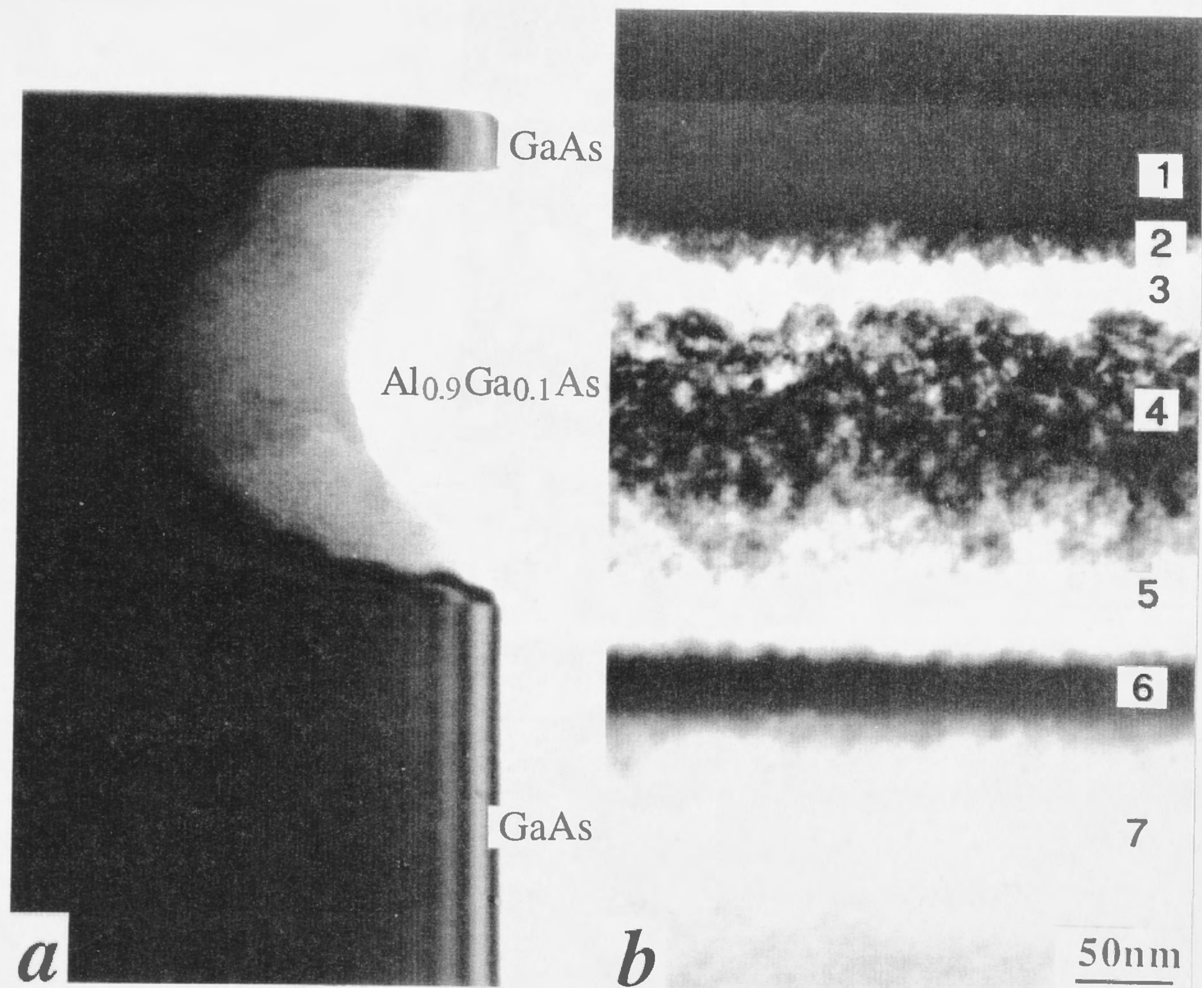

Fig. 4-3 (a) Bright-field XTEM image of a cleavage specimen from an unimplanted sample of Fig. 4-2 showing the thicknesses of the various layers. (b) Dark-field image of a similar sample implanted to a dose of $8x10^{15}$ cm^{-2}. Both images have the same magnification.

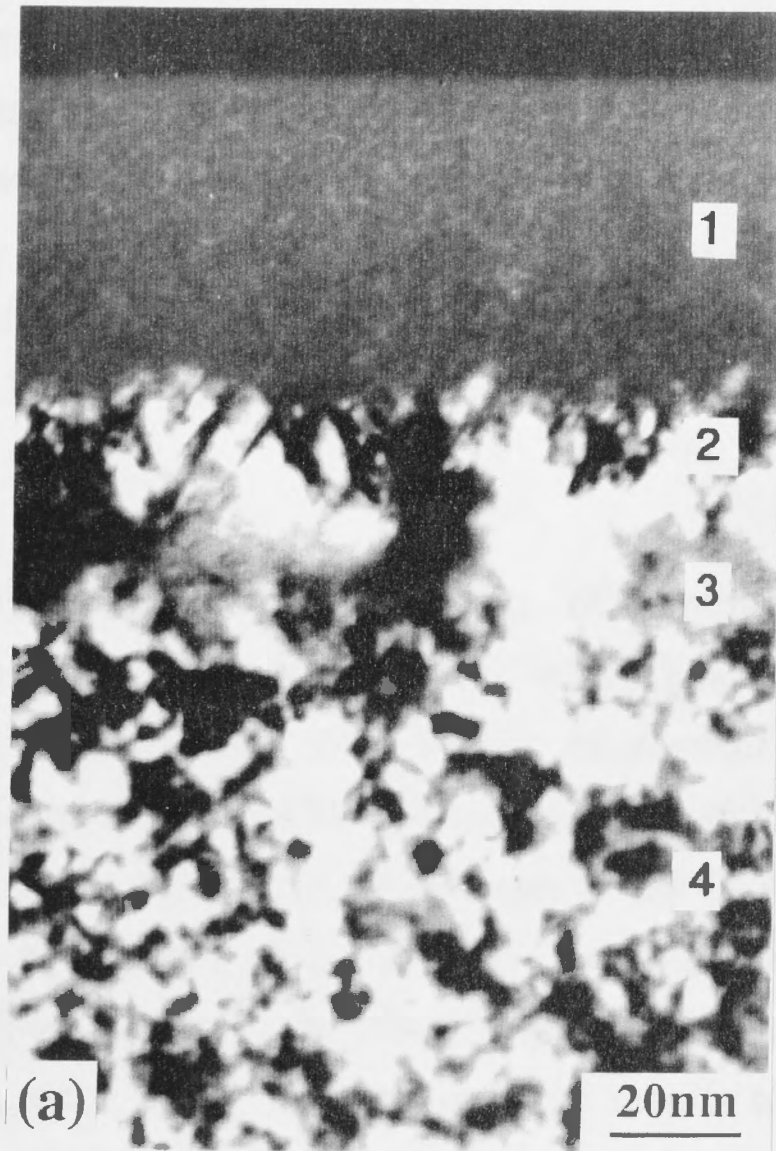

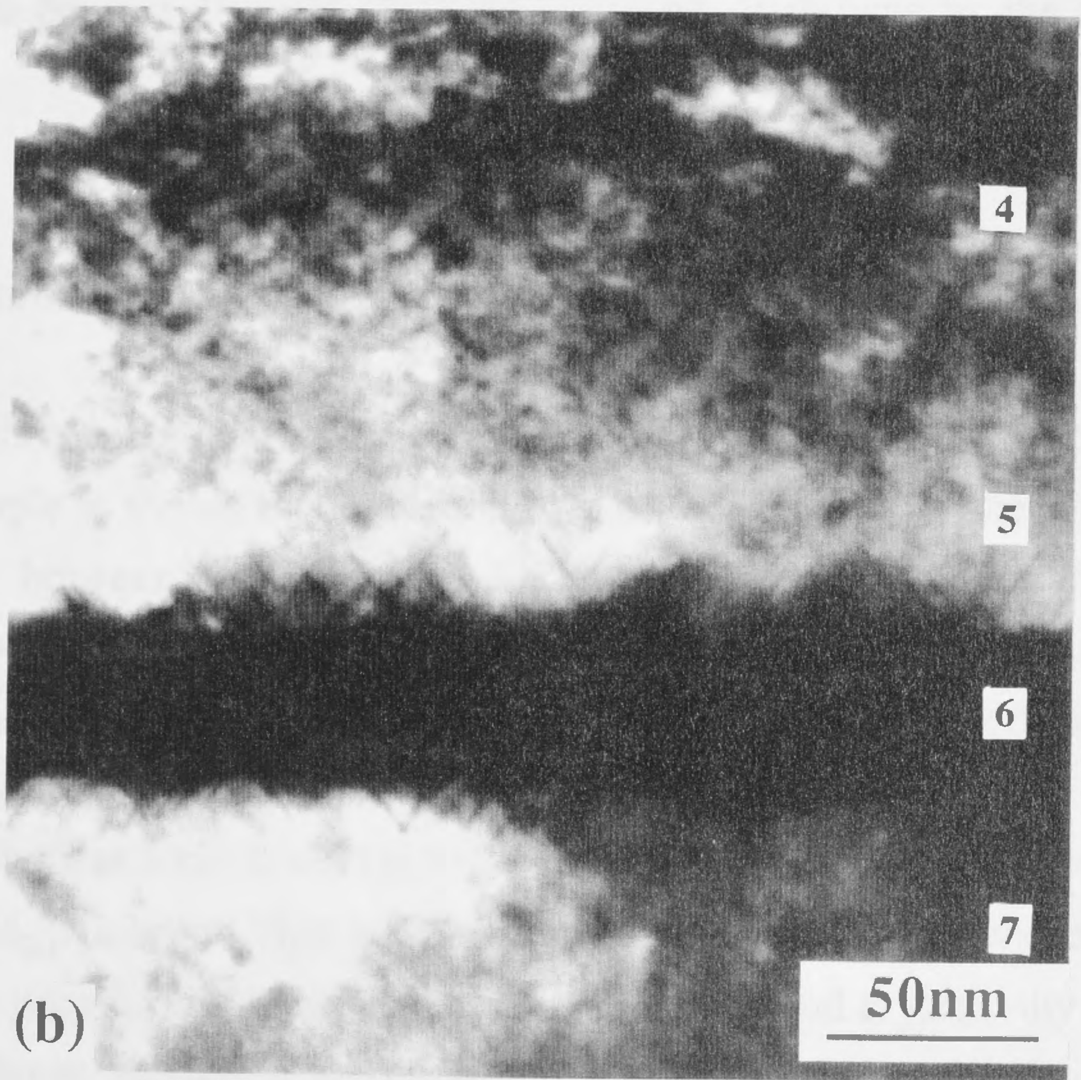

Fig. 4-4 Dark-field XTEM images of the (a) upper and (b) lower interfaces of the sample in Fig. 4-3(b) at higher magnification.

recoils may result in an increase of the Al content in this region and, therefore, increase the amorphisation threshold. However, as will be shown later, this is not the case and the processes going on at the interfaces are more complex, involving defect migration and/or trapping. The residual damage in this region is the result of a delicate balance among the various competing processes occurring at the interface during implantation and subsequent warm-up to room temperature. Planar defects are also observed at the amorphous-crystalline interfaces of this buried amorphous layer [Fig. 4-4(b)]. This effect is due to heating effects during XTEM sample preparation, an effect which will be clarified in the discussion section.

In a quick summary, the above results from both sets of samples show that amorphisation of the AlGaAs layer proceeds from the upper GaAs-AlGaAs interface *via* a nucleation-limited process. The AlGaAs layer with higher Al content is harder to amorphise, consistent with the results of bulk AlGaAs (previous chapter) and it is also able to offer more efficient protection against ion beam damage to the GaAs region that is in close proximity. In addition, in the case of the higher Al content alloy, the high concentration of implanted ions (from high dose implantation) can also act as a site to trap (stabilise) defects. However, based partly on more detailed results to follow, this latter process appears to be less efficient than the trapping of defects at the GaAs-AlGaAs interface.

4.3.2 GaAs layer between two AlGaAs layer (keV beams)

It is interesting to study the damage buildup when the order of the multilayer structure is reversed. One such example is shown by the RBS-C results in Fig. 4-5(b) where a layer of GaAs is sandwiched between two $Al_{0.9}Ga_{0.1}As$ layers. The displacement density profile, calculated by FASTRIM, is illustrated in Fig. 4-5(a). The peak of the energy deposition now lies in the GaAs layer close to the top interface. As expected, damage builds up preferentially at the GaAs layer. At the lowest dose of $6x10^{13}$ cm^{-2}, a buried amorphous layer is just about to form in the GaAs layer with very little damage observed in the overlaying $Al_{0.9}Ga_{0.1}As$ layer. This buried amorphous layer then grows towards the surface and substrate with further bombardment. Due to the good crystallinity of the overlaying $Al_{0.9}Ga_{0.1}As$ layer, the depth determination of the damage peak/amorphous layer is complicated. The depth scale plotted on the top axis is strictly valid only for a random spectrum. Below the dose of $5x10^{15}$ cm^{-2}, i.e. prior to the damage buildup in the top $Al_{0.9}Ga_{0.1}As$ layer, good channeling is preserved in this region and, due to the lower

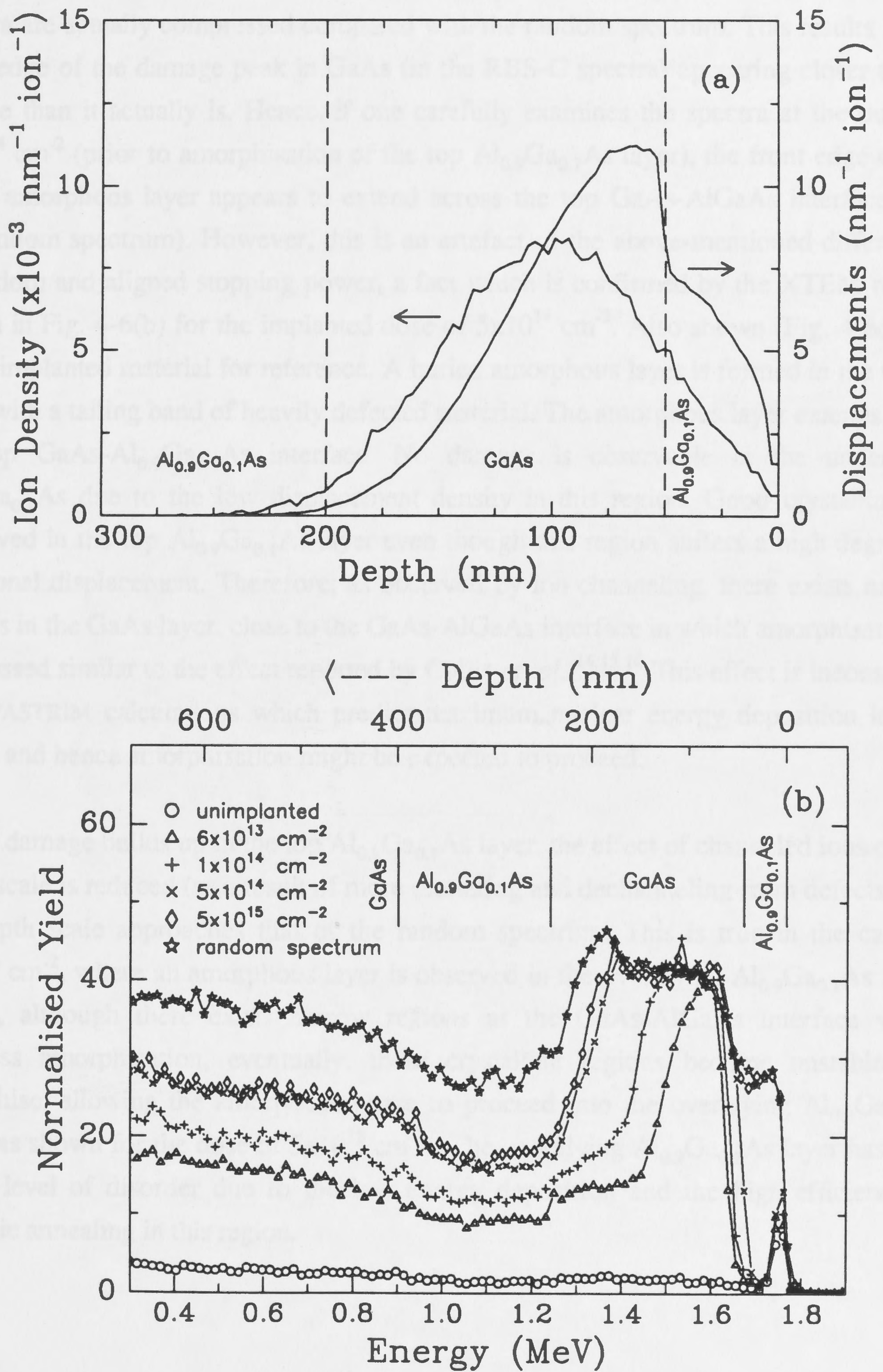

Fig. 4-5 (a) FASTRIM calculations of the ion density and displacement density profiles for 90 keV Si implantation into a $Al_{0.9}Ga_{0.1}As$-GaAs-$Al_{0.9}Ga_{0.1}As$-GaAs structure. (b) RBS-C spectra showing the ion beam damage buildup in this structure.

stopping power of channeled ions during analysis,[25,26] the depth scales of the aligned spectra are actually compressed compared with the random spectrum. This results in the front edge of the damage peak in GaAs (in the RBS-C spectra) appearing closer to the surface than it actually is. Hence, if one carefully examines the spectra at the dose of $5x10^{14}$ cm^{-2} (prior to amorphisation of the top $Al_{0.9}Ga_{0.1}As$ layer), the front edge of the GaAs amorphous layer appears to extend across the top GaAs-AlGaAs interface (c.f. the random spectrum). However, this is an artefact of the above-mentioned differences in random and aligned stopping power, a fact which is confirmed by the XTEM results shown in Fig. 4-6(b) for the implanted dose of $5x10^{14}$ cm^{-2}. Also shown [Fig. 4-6(a)] is the unimplanted material for reference. A buried amorphous layer is formed in the GaAs layer with a tailing band of heavily defected material. The amorphous layer extends up to the top GaAs-$Al_{0.9}Ga_{0.1}As$ interface. No damage is observable in the underlying $Al_{0.9}Ga_{0.1}As$ due to the low displacement density in this region. Good crystallinity is preserved in the top $Al_{0.9}Ga_{0.1}As$ layer even though this region suffers a high degree of collisional displacement. Therefore, as observed by ion channeling, there exists narrow regions in the GaAs layer, close to the GaAs-AlGaAs interface in which amorphisation is suppressed similar to the effect reported by Cullis *et. al.*.[14,15,18] This effect is inconsistent with FASTRIM calculations which predict maximum nuclear energy deposition in this region and hence amorphisation might be expected to proceed.

As the damage builds up in the top $Al_{0.9}Ga_{0.1}As$ layer, the effect of channeled ions on the depth scale is reduced (as a result of more scattering and dechanneling from defects) and the depth scale approaches that of the random spectrum. This is true in the case of $5x10^{15}$ cm^{-2}, where an amorphous layer is observed in the overlaying $Al_{0.9}Ga_{0.1}As$ layer. Hence, although there exists narrow regions at the GaAs-AlGaAs interface which suppress amorphisation, eventually, these crystalline regions become unstable and amorphise, allowing the amorphous phase to proceed into the overlaying $Al_{0.9}Ga_{0.1}As$ layer (as shown for the dose of $5x10^{15}$ cm^{-2}). The underlying $Al_{0.9}Ga_{0.1}As$ layer has only a low level of disorder due to the low energy deposition and the high efficiency of dynamic annealing in this region.

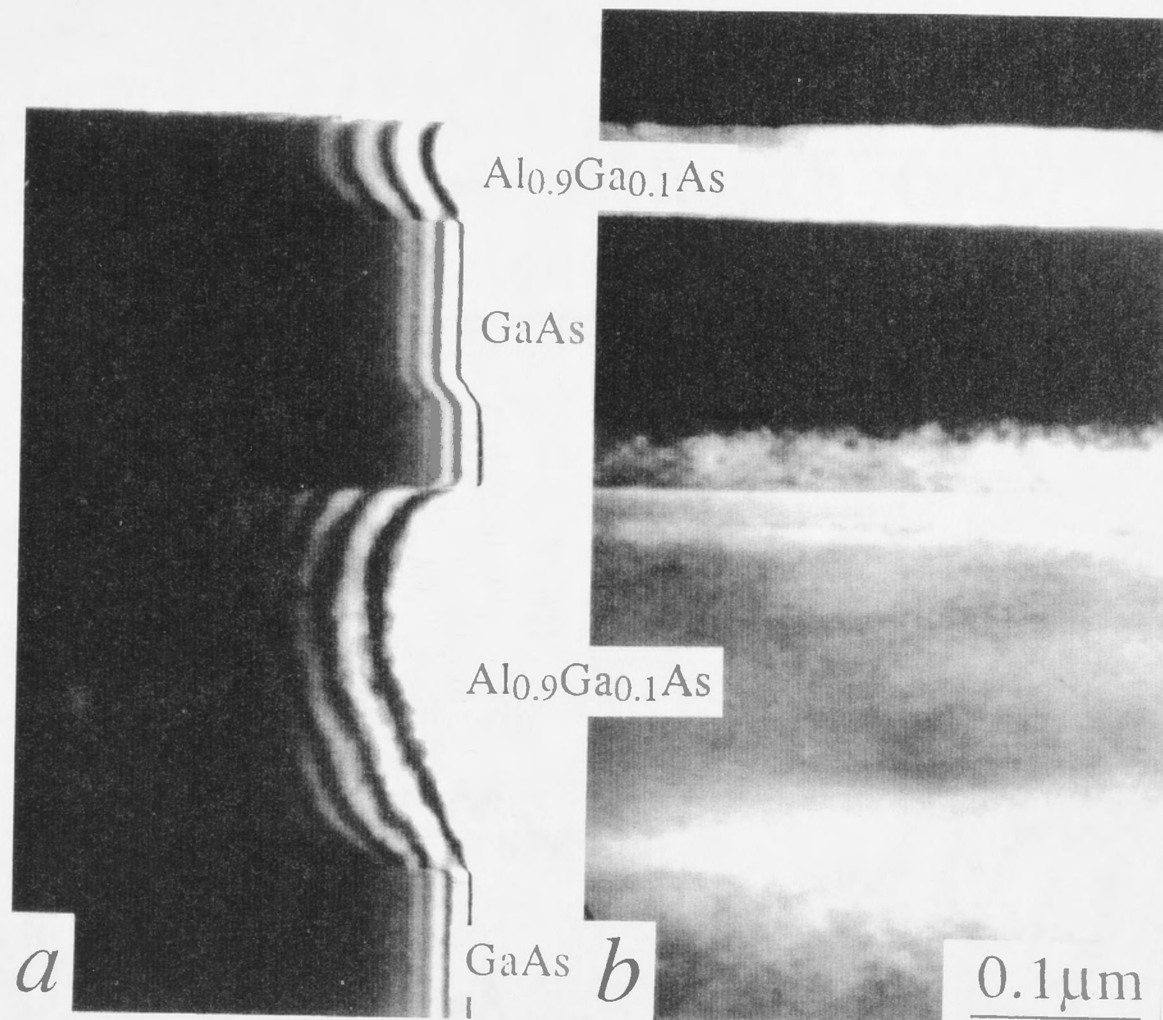

Fig. 4-6 (a) Bright-field XTEM image of a cleavage specimen from an unimplanted sample of Fig. 4-5(b) showing the thicknesses of the various layers. (b) Dark-field image of a similar sample implanted to a dose of $5x10^{14}$ cm^{-2}. Both images have the same magnification.

With AlGaAs of lower Al content, not only does amorphisation occur at a lower dose due to less efficient dynamic annealing during implantation but also the degree of protection to adjacent GaAs layers is lowered. This is illustrated in Fig. 4-7 for a structure in which the GaAs layer sits between two $Al_{0.5}Ga_{0.5}As$ layers. At a dose of $6x10^{13}$ cm^{-2}, very little damage is formed in GaAs regions close to the top GaAs-AlGaAs interface although a buried amorphous layer is just about to form deeper within the GaAs layer (taking into account the channeling/stopping power effect as described previously). With an increase in implantation dose to $1x10^{14}$ cm^{-2}, amorphisation of these narrow regions occurs, together with a rapid extension of damage accumulation

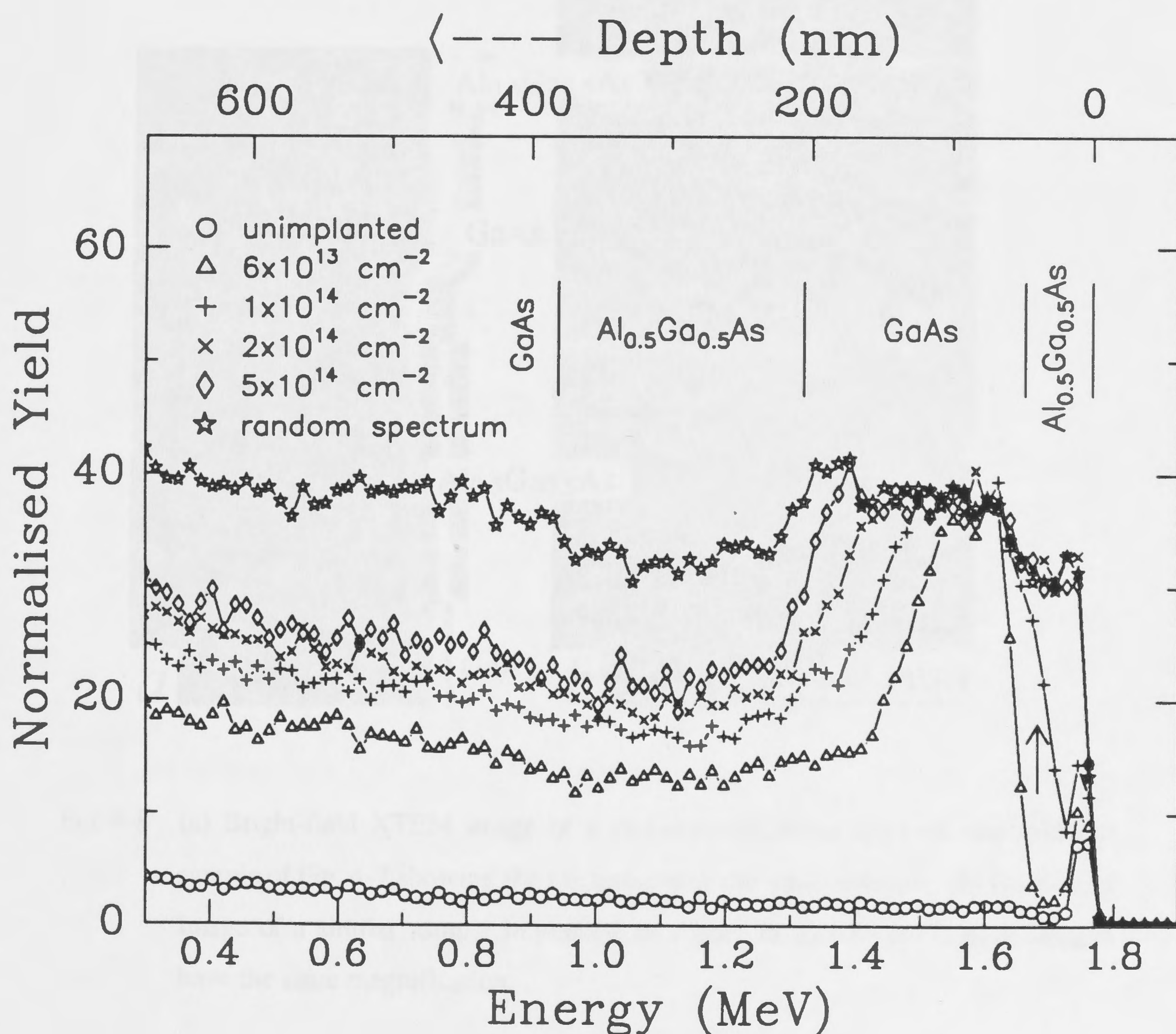

Fig. 4-7 RBS-C spectra showing the damage buildup in a $Al_{0.5}Ga_{0.5}As$-GaAs-$Al_{0.5}Ga_{0.5}As$-GaAs structure implanted with 90 keV Si ions. The arrow indicates the damage peak in the overlaying $Al_{0.5}Ga_{0.5}As$ layer.

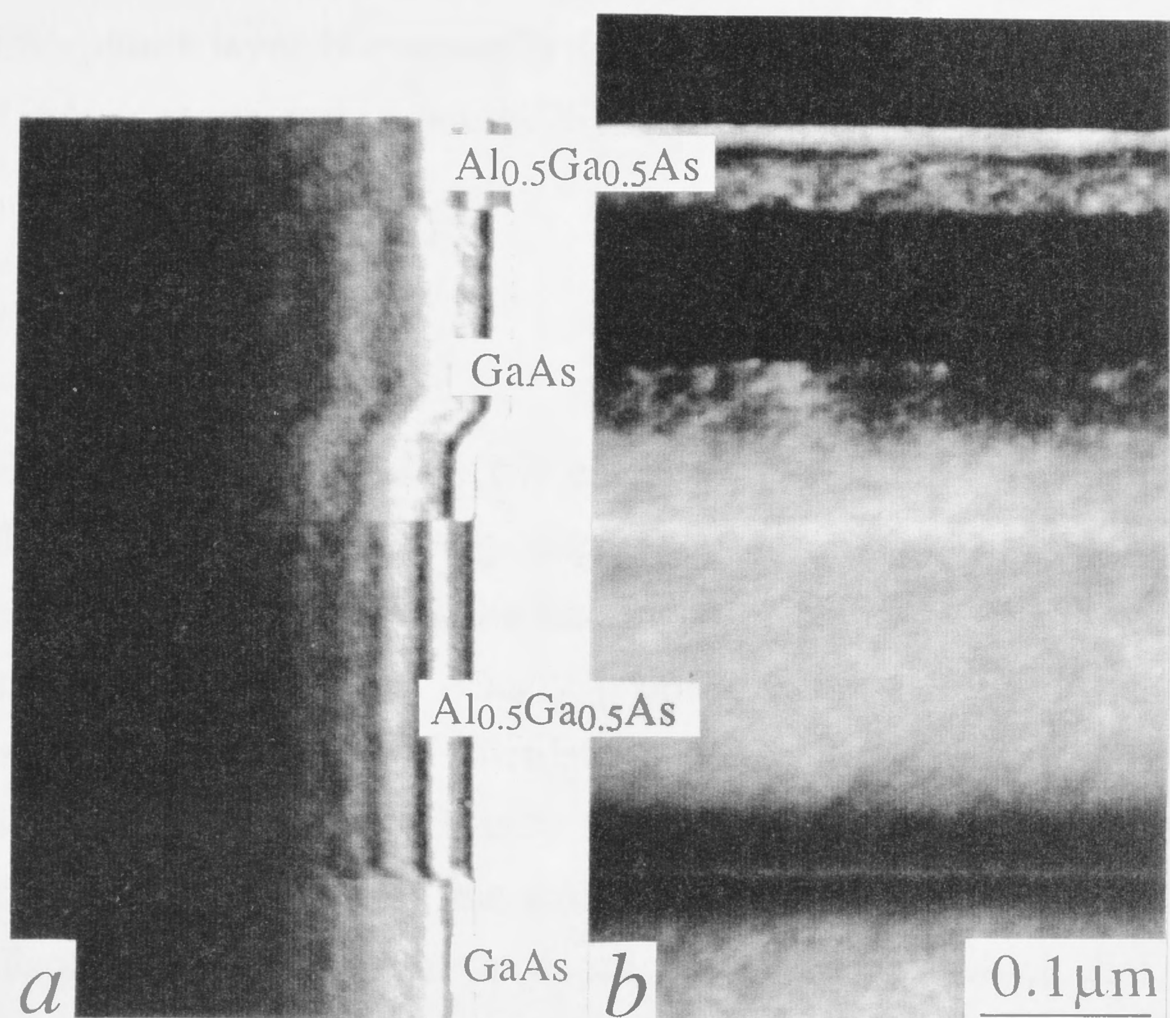

Fig. 4-8 (a) Bright-field XTEM image of a cleavage specimen from an unimplanted sample of Fig. 4-7 showing the thicknesses of the various layers. (b) Dark-field image of a similar sample implanted to a dose of $1x10^{14}$ cm^{-2}. Both images have the same magnification.

across the GaAs-AlGaAs interface into the overlaying $Al_{0.5}Ga_{0.5}As$ layer (indicated by the arrow). This is in contrast with previous $Al_{0.9}Ga_{0.1}As$ results in which the interfacial annealing effect is still observed up to a dose of about $5x10^{14}$ cm^{-2}. Hence, the overlaying $Al_{0.9}Ga_{0.1}As$ layer remains relatively damage free. Indeed, XTEM results depicted in Fig. 4-8 for $1x10^{14}$ cm^{-2} show that an amorphous layer of ~86 nm thick is formed in the GaAs layer. The top boundary of this amorphous layer extends up to the GaAs-AlGaAs interface while the lower boundary tails off into a band of defective material (within the GaAs layer). The top $Al_{0.5}Ga_{0.5}As$ layer shows some damage contrast due most likely to defect clusters corresponding in depth to the damage peak in the RBS-C spectrum. No observable damage appears in the underlying $Al_{0.5}Ga_{0.5}As$ layer, again due to the low displacement density in this region. As the dose is increased further an amorphous layer is eventually formed in the top $Al_{0.5}Ga_{0.5}As$ layer and the amorphous GaAs layer extends towards the substrate (Fig. 4-7).

4.3.3 MeV beams

The results shown thus far are for low energy (keV) beams where the displacement density or the rate of nuclear energy deposition varies significantly across a narrow depth. To gain further insights into the interfacial effect, 1 MeV Si^+ beams were used. At this energy, the displacement density profile varies slowly across the regions of interest. This is shown by FASTRIM calculations in Fig. 4-9(a), where about a factor of 2 variation in the displacement density is observed across the interfaces. The corresponding damage buildup for this structure is shown in Fig. 4-9(b). The maximum collisional displacement occurs at a depth of ~850 nm which lies in the GaAs substrate/buffer and well beyond the region of interest. The displacement density at the top GaAs layer has dropped by a factor of 3-4 from the 90 keV case. At the lowest implantation dose shown in this figure ($1x10^{14}$ cm^{-2}), damage starts building up in the GaAs substrate with only a small damage accumulation at the top GaAs layer. Very little damage is observed in both the $Al_{0.5}Ga_{0.5}As$ layers. Again, it should be stressed that due to the low level of crystalline damage in the overlaying $Al_{0.5}Ga_{0.5}As$ layer, the depth scales in the aligned spectra are compressed. The upper and lower GaAs-AlGaAs interfaces are indicated by the arrows. It is thus observed that a higher amount of damage is accumulated at the lower interface than at the upper interface. The effect of the surface Al peak (double-headed arrow) which appears close to the interface, is almost negligible. Even in the random spectrum, the contribution from this peak is only about 5% of the total yield for $Al_{0.5}Ga_{0.5}As$. The slight asymmetrical disordering effect at the top and bottom interfaces has previously been reported by Turkot *et. al.*.[21,22]

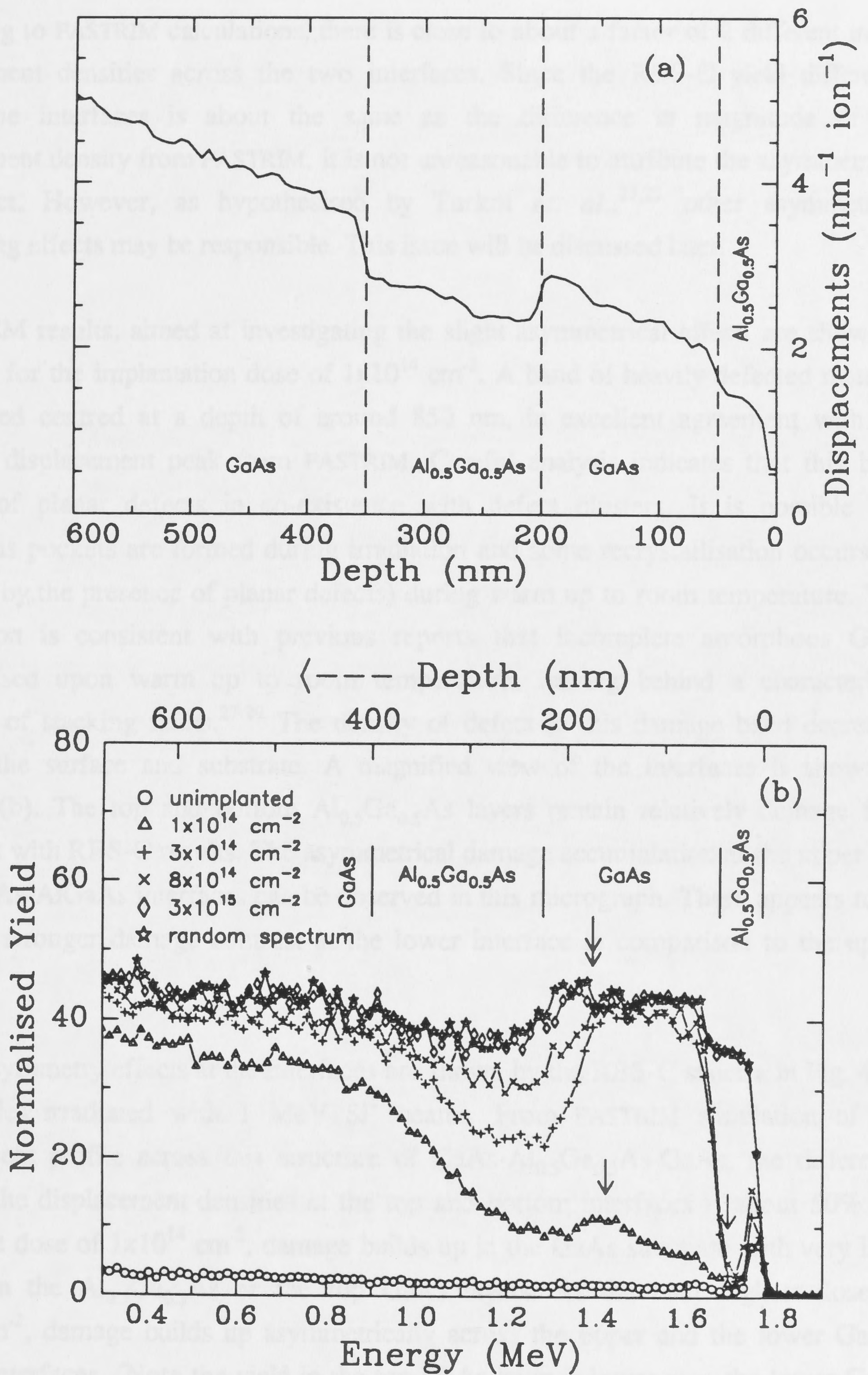

Fig. 4-9 (a) FASTRIM calculations of the displacement density profile for 1 MeV Si implantation into a $Al_{0.5}Ga_{0.5}As$-GaAs-$Al_{0.5}Ga_{0.5}As$-GaAs structure. (b) RBS-C spectra showing the ion beam damage buildup in this structure. Arrows indicate positions of the interfaces while the double-headed arrow indicates the surface Al peak.

According to FASTRIM calculations, there is close to about a factor of 2 different in the displacement densities across the two interfaces. Since the RBS-C yield difference across the interfaces is about the same as the difference in magnitude of the displacement density from FASTRIM, it is not unreasonable to attribute the asymmetry to this effect. However, as hypothesised by Turkot *et. al.*,[21,22] other asymmetrical disordering effects may be responsible. This issue will be discussed later.

The XTEM results, aimed at investigating the slight asymmetrical effect, are shown in Fig. 4-10 for the implantation dose of $1x10^{14}$ cm^{-2}. A band of heavily defected material is observed centred at a depth of around 850 nm, in excellent agreement with the expected displacement peak from FASTRIM. Careful analysis indicates that this band consists of planar defects in co-existence with defect clusters. It is possible that amorphous pockets are formed during irradiation and some recrystallisation occurs (as indicated by the presence of planar defects) during warm up to room temperature. This observation is consistent with previous reports that incomplete amorphous GaAs recrystallised upon warm up to room temperature, leaving behind a characteristic signature of stacking faults.[27-29] The density of defect in this damage band decreases towards the surface and substrate. A magnified view of the interfaces is shown in Fig. 4-10(b). The top and bottom $Al_{0.5}Ga_{0.5}As$ layers remain relatively damage free, consistent with RBS-C results. The asymmetrical damage accumulation at the upper and lower GaAs-AlGaAs interfaces can be observed in this micrograph. There appears to be a slightly stronger damage contrast at the lower interface in comparison to the upper interface.

Further asymmetry effects at the interfaces are shown by the RBS-C spectra in Fig. 4-11 for samples irradiated with 1 MeV Si^+ beams. From FASTRIM simulation of the displacement profile across this structure of GaAs-$Al_{0.5}Ga_{0.5}$As-GaAs, the difference between the displacement densities at the top and bottom interfaces is about 50%. At the lowest dose of $1x10^{14}$ cm^{-2}, damage builds up in the GaAs substrate with very little damage in the $Al_{0.5}Ga_{0.5}As$ or the top GaAs layers. At the next highest dose of $3x10^{14}$ cm^{-2}, damage builds up asymmetrically across the upper and the lower GaAs-AlGaAs interfaces. (Note the yield in the top GaAs layer is lower than the lower GaAs layer). Eventually amorphous material is formed in both the layers at $6x10^{14}$ cm^{-2}. The $Al_{0.5}Ga_{0.5}As$ layer remains fairly defect free at this stage until further irradiation ($1x10^{15}$ cm^{-2}) causes the defects to start nucleating at the lower GaAs-AlGaAs interface, consistent with the somewhat higher displacement density at this interface. Note that the slight increase in the dechanneling yield in the $Al_{0.5}Ga_{0.5}As$ layer for doses $\leq 6x10^{14}$ cm^{-2}

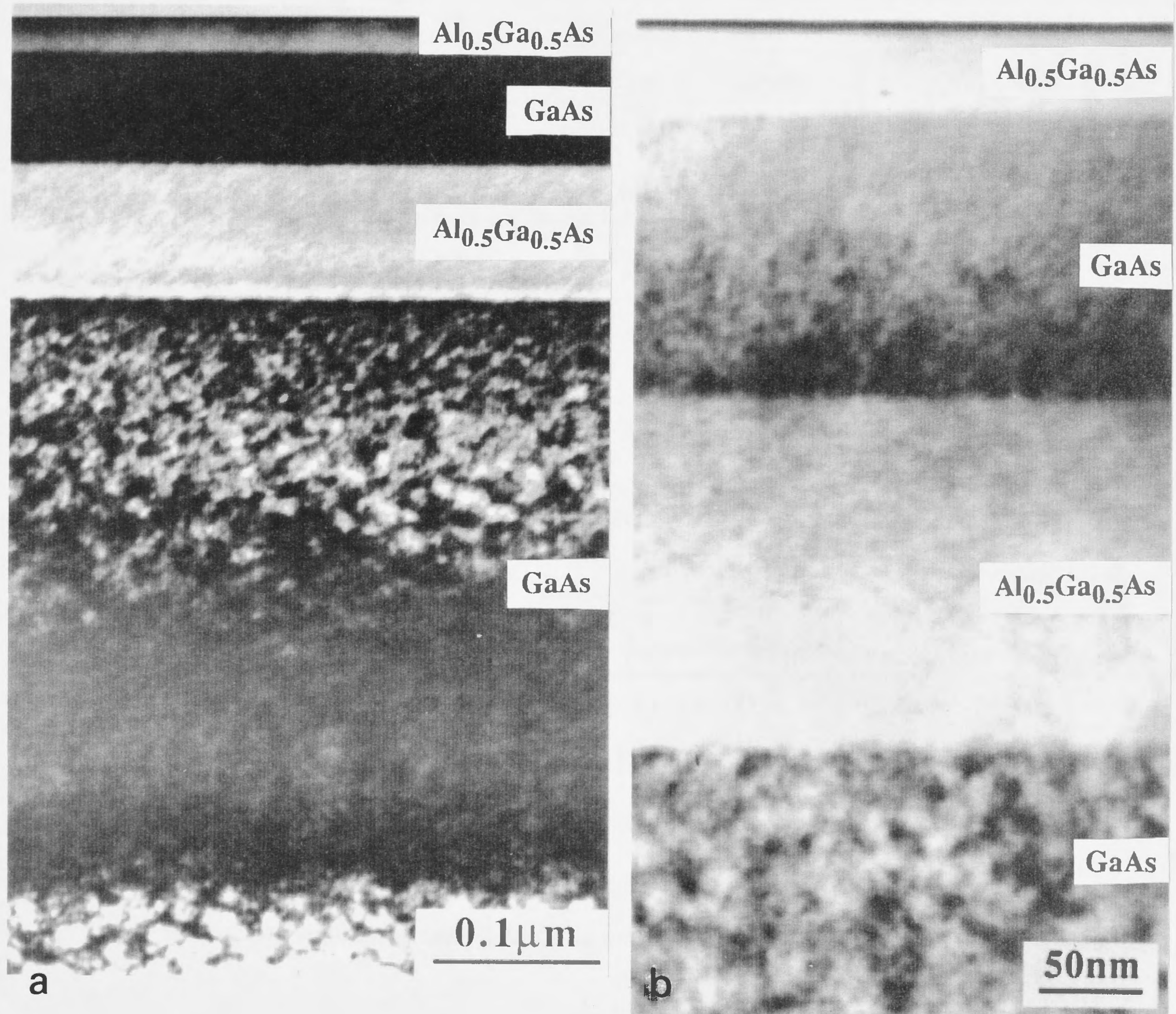

Fig. 4-10 (a) Bright-field XTEM image of the sample from Fig. 4-9 implanted with 1 MeV Si ions at $1x10^{14}$ cm^{-2}. (b) Bright-field XTEM image of the same sample at higher magnification, showing more details at the interfaces.

is consistent with little damage in this layer, the increased dechanneling component of the analysing ions resulting from traversing the top amorphous GaAs layer.

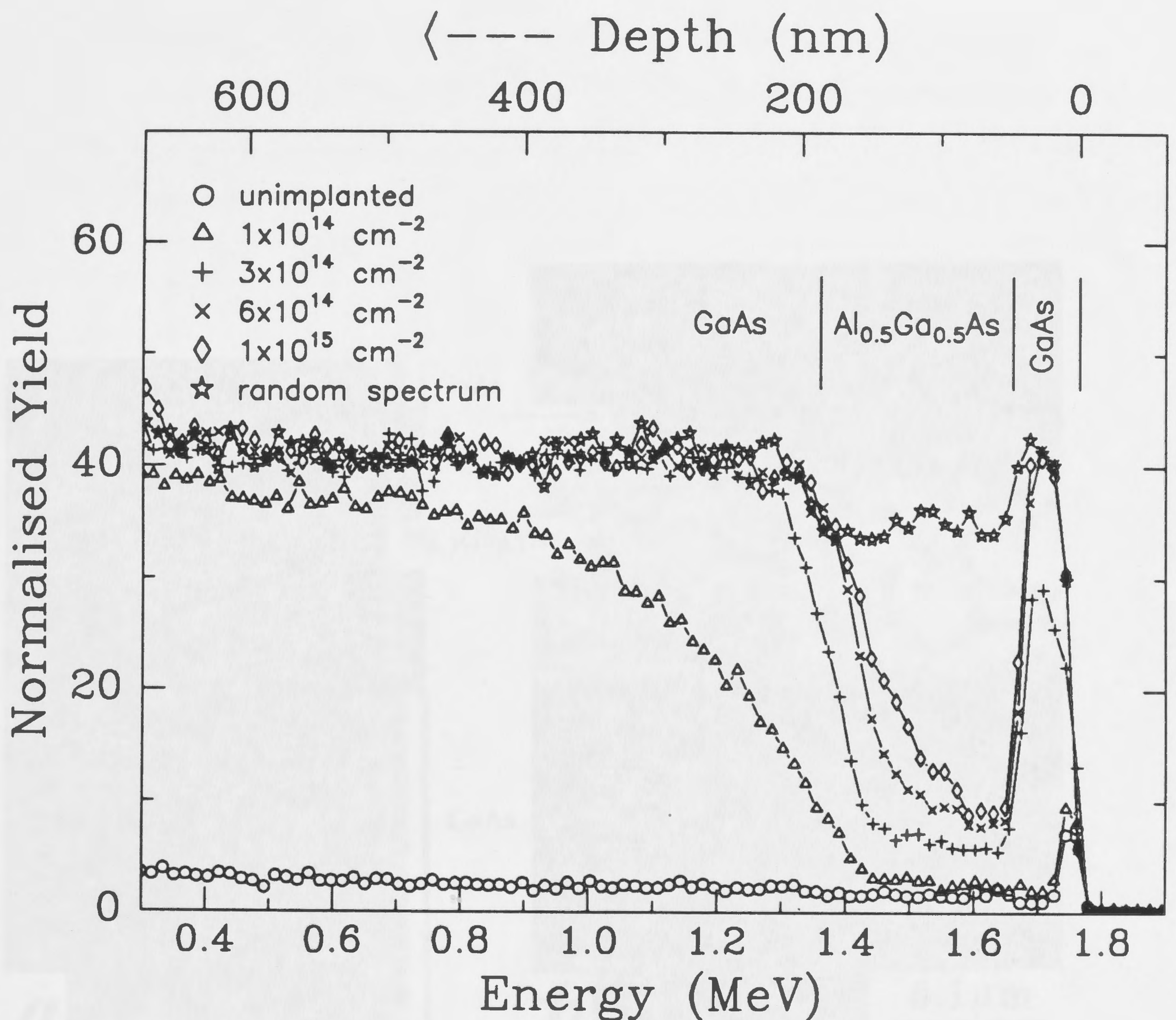

Fig. 4-11 RBS-C spectra showing the damage buildup in a GaAs-$Al_{0.5}Ga_{0.5}As$-GaAs structure implanted with 1 MeV Si ions.

The effect of suppression of amorphisation may also be observed in this figure at implantation doses of $6x10^{14}$ and $1x10^{15}$ cm^{-2}, where the widths of the top GaAs damage (amorphous) peaks are narrower than the width of the random level. Indeed, this observation is confirmed by the XTEM results in Fig. 4-12. Micrograph (a) shows the unimplanted structure taken from an area adjacent to the implanted sample (to minimise thickness variation) while the implanted specimen (dose of $1x10^{15}$ cm^{-2}) is shown in (b). Both micrographs are at the same magnification. Careful analyses indicate

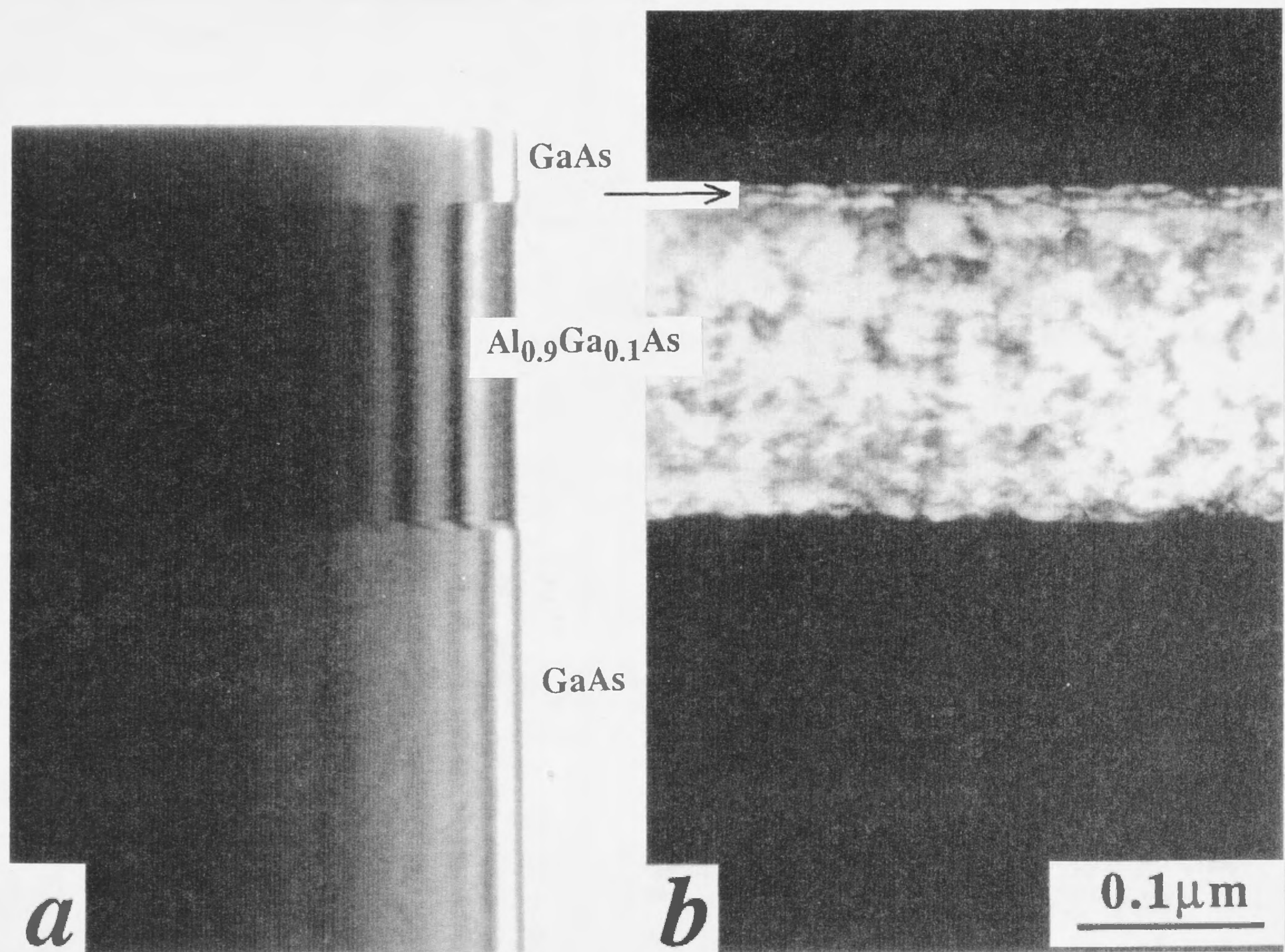

Fig. 4-12 (a) Bright-field XTEM image of a cleavage specimen from an unimplanted sample of Fig. 4-11 showing the thicknesses of the various layers. (b) Dark-field image of a similar sample implanted to a dose of $1x10^{15}$ cm^{-2}. The arrow indicates crystalline GaAs regions at the GaAs-AlGaAs interface. Both images have the same magnification.

that the thickness of the top amorphous layer is about 8-10 nm smaller than the thickness of the unimplanted top GaAs layer. It can also be seen from Fig. 4-12(b) that the upper GaAs-AlGaAs interface is identifiable by the 'rugged' edge which is still crystalline (arrowed).

Suppression of an amorphous phase in narrow regions of GaAs at the interface is further illustrated in Fig. 4-13 for a GaAs-$Al_{0.9}Ga_{0.1}As$-GaAs structure irradiated with 1 MeV Si^+ beams. Note that at the higher dose of 3×10^{14} cm^{-2}, the damage in the top GaAs layer has reached the random level, suggesting that an amorphous phase has been formed. However, the amorphous layer has not yet extended into the GaAs-AlGaAs

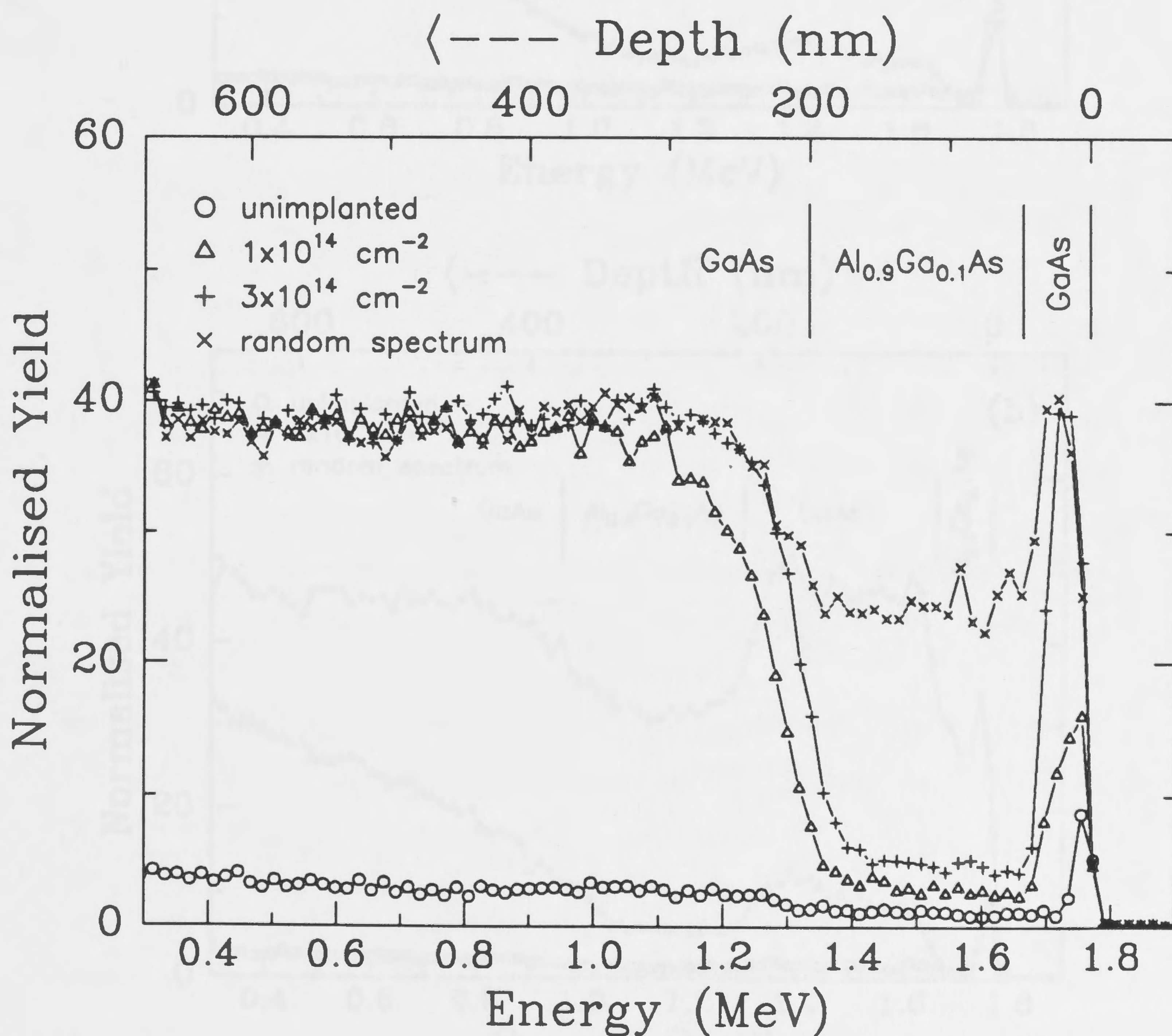

Fig. 4-13 RBS-C spectra showing the effect suppression of amorphisation at the interface in a GaAs-$Al_{0.9}Ga_{0.1}As$-GaAs structure implanted with 1 MeV Si ions. Note that at a dose of 1×10^{14} cm^{-2}, the width of the top amorphous GaAs layer is narrower than that of the GaAs layer in the random spectrum.

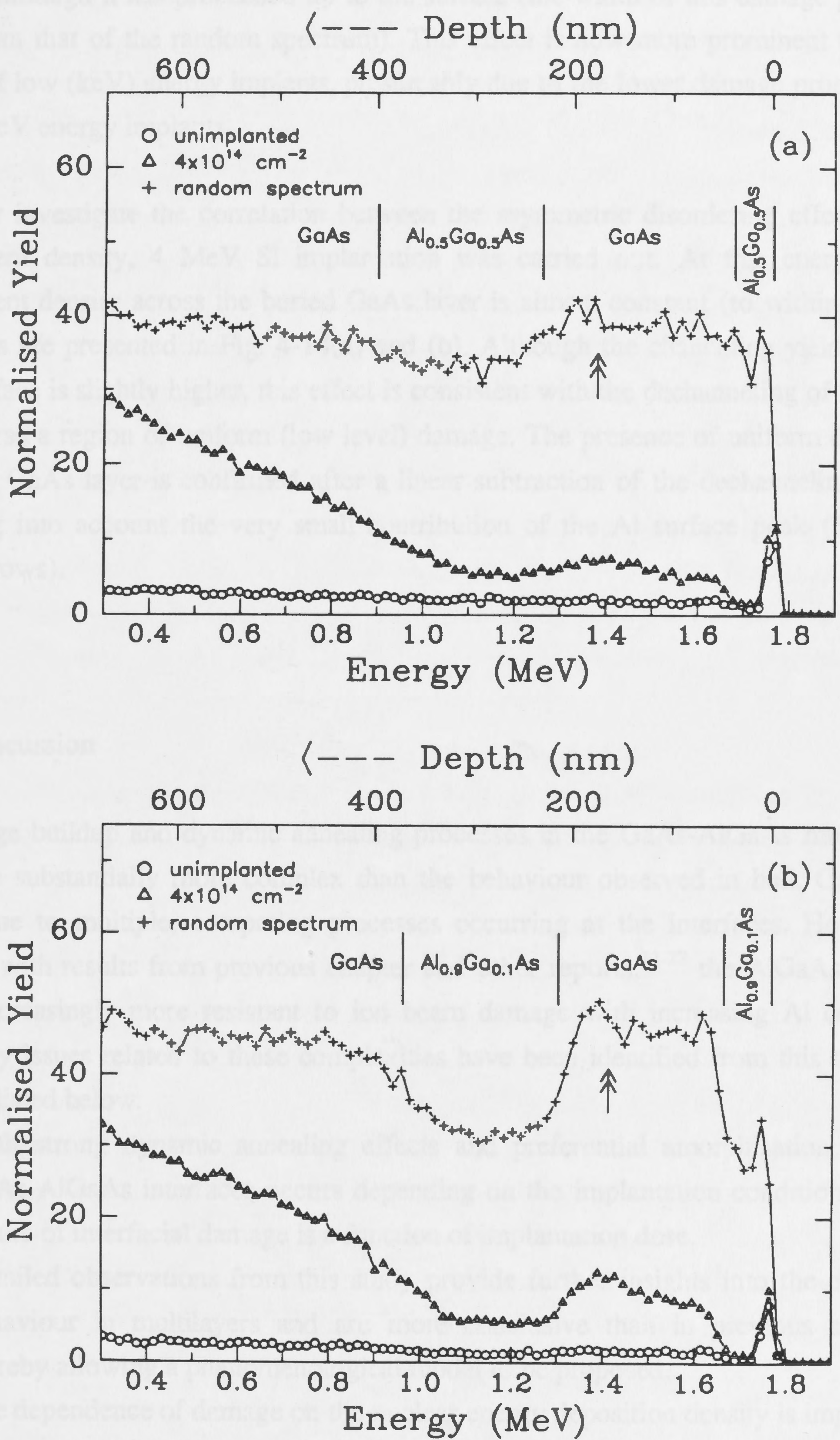

Fig. 4-14 RBS-C spectra of (a) $Al_{0.5}Ga_{0.5}As$-GaAs-$Al_{0.5}Ga_{0.5}As$-GaAs and (b) $Al_{0.9}Ga_{0.1}As$-GaAs-$Al_{0.9}Ga_{0.1}As$-GaAs structures implanted with 4 MeV Si ions. The double-headed arrows indicate the surface Al peaks.

interface although it has proceeded up to the surface (the width of this damage peak is smaller than that of the random spectrum). This effect is now more prominent than in the case of low (keV) energy implants, presumably due to the lower damage production rate for MeV energy implants.

To further investigate the correlation between the asymmetric disordering effects and displacement density, 4 MeV Si implantation was carried out. At this energy, the displacement density across the buried GaAs layer is almost constant (to within 10%). The results are presented in Fig. 4-14(a) and (b). Although the channeling yield at the back interface is slightly higher, this effect is consistent with the dechanneling of ions as they traverse a region of uniform (low level) damage. The presence of uniform damage across the GaAs layer is confirmed after a linear subtraction of the dechanneling yield and taking into account the very small contribution of the Al surface peak (double-headed arrows).

4.4 Discussion

The damage buildup and dynamic annealing processes in the GaAs-AlGaAs multilayer system are substantially more complex than the behaviour observed in bulk GaAs or AlGaAs due to multiple, competing processes occurring at the interfaces. However, consistent with results from previous chapter and other reports,[11-22] the AlGaAs layers become increasingly more resistant to ion beam damage with increasing Al content. Several key issues related to these complexities have been identified from this chapter which are listed below.

(i) Both strong dynamic annealing effects and preferential amorphisation at the GaAs-AlGaAs interfaces occurs depending on the implantation conditions. The nature of interfacial damage is a function of implantation dose.

(ii) Detailed observations from this study provide further insights into the damage behaviour in multilayers and are more conclusive than in previous studies, thereby allowing a phenomenological model to be proposed.

(iii) The dependence of damage on the nuclear energy deposition density is important and provides a comparison between keV and MeV implants in multilayers.

(iv) Thermal stability of defects at the interfaces after LN2 temperature irradiation is another critical issue in light of the observed enhanced recrystallisation during warm up to room temperature.

Each of these issues will be discussed in turn.

4.4.1 Damage buildup and dynamic annealing at heterointerfaces

The observations and implications for damage accumulation in both GaAs and AlGaAs layers at LN2 temperature as a result of the impinging Si ions are first summarised. At low doses, ion-induced defects are stable in the GaAs layers, but, due to the strong dynamic annealing in AlGaAs (as a result of defect mobility and/or local bonding rearrangements discussed in previous chapter), very little residual damage remains in these layers in the form of point defects or defect clusters. Also, at low doses the small incorporation of Si ions within the lattice (< 0.1 at.%) should not present any observable increased nucleation effect for defect clustering or amorphisation in AlGaAs. In these multilayer structures, multiple effects taking place at the GaAs-AlGaAs interface may result in a different nature of damage accumulation in both the GaAs and the AlGaAs layers than in bulk (thick) material. For example, the heterogeneous model[30,31] of damage buildup which applies to GaAs, appears to be only applicable for GaAs regions away from GaAs-AlGaAs interfaces. As the dose is increases further, an amorphous phase is created in the GaAs layers except for narrow regions near the interfaces which remains crystalline. However, these defective crystalline regions at the interfaces collapse into an amorphous phase above a critical defect density at higher irradiation doses. Once an amorphous phase is formed in these regions, further amorphisation proceeds rapidly layer-by-layer into the adjacent AlGaAs layers. Also, at high doses the high concentration of Si ions (often exceeding 1 at.%) at R_p is also a potential environment for eventual stabilisation of defects and nucleation of amorphous zones in AlGaAs, despite the strong dynamic annealing in this alloy. However, interfaces appear to be preferred sites for nucleating amorphous material.

Thus, the presence of AlGaAs is able to offer some degree of protection against damage accumulation (at the lower doses) to adjacent GaAs regions due to strong dynamic annealing even at LN2 temperatures. This effect is quite surprising as maximum nuclear energy deposition is expected, from FASTRIM calculations, to occur at the interface under the keV bombardment conditions used. It has been proposed[19] that intermixing effects increase the Al content in GaAs layers adjacent to AlGaAs to increase their resistance to ion beam damage and hence suppress amorphisation. The results shown here do not support an intermixing model since at lower doses (< $1x10^{15}$ cm^{-2}), where ballistic intermixing is expected to be negligible, the interfacial effect is still quite pronounced. Furthermore, in samples where the GaAs layer sits above the AlGaAs layer, the interfacial effect is still observed (Fig. 4-11, 4-12 and 4-13), even though ballistic intermixing effects redistribute Al in the forward collision direction and, thus, do not increase the Al content of GaAs regions on the surface side of the heterointerface. In

addition, at higher doses where this intermixing effect is expected to increase, interfacial amorphisation is observed rather than dynamic annealing. Intermixing as a result of thermal diffusion is also expected to be small since the diffusion coefficients of Ga and Al in GaAs-AlGaAs multilayers at LN2 temperature are very small[32,33] and no thermal treatment occurred other than warming up to room temperature.

Another suggestion by Cullis *et. al.*[14,15] to explain the interfacial dynamic annealing effect is that AlGaAs (AlAs) layers act as a local sink for point defects induced during irradiation in these narrow GaAs regions, resulting in the suppression of defect accumulation in GaAs and hence inhibition of amorphisation. Restructuring of the GaAs may also be enhanced by point-defect interaction and annihilation, involving, for example, Al-related defect species. However, this proposal does not satisfactorily explain some of the above observations, in particular, the final amorphisation of these regions with further bombardment.

4.4.2 Model to explain observations

Based on both the above detailed observations and arguments, the following phenomenological model is suggested to explain the damage buildup and amorphisation processes in GaAs-AlGaAs multilayers. Suppression of amorphisation in GaAs regions close to AlGaAs layers arises from mobile point defects generated in AlGaAs. Indeed, the dynamic annealing of AlGaAs arises from local bonding rearrangement and/or point defect mobility in this material even at LN2 temperatures during irradiation, as discussed in Chapter 3. However, the dynamic annealing process is not perfect and does not result in complete annihilation of defects and the residual damage in AlGaAs consists of point defects and dilute point defect clusters. Some of the point defects generated in AlGaAs during irradiation are then injected across the interface into adjacent GaAs regions. The mechanism of defect injection across the interface cannot be conclusively proven from this experiment but it is likely as a result of point defect diffusion. This is consistent with the presence of more mobile point defects in AlGaAs, as a result of stronger dynamic annealing, than in GaAs. At low doses, the diffusion of these mobile defects into GaAs mediate *in situ* annealing of the GaAs lattice close to the interface, thereby inhibiting complete amorphisation. Since only narrow regions of GaAs are affected, only short range diffusion of these defects are involved. However, the *in situ* annealing in these regions is also not perfect, resulting in residual crystalline defects (such as point defect clusters and extended defects) at the interface which increases the system's free energy. The increase in the density of crystalline defects reduces the effectiveness of dynamic

annealing in this region by stabilising/trapping more point defects that diffuse across the interface. Eventually, amorphisation is achieved at higher doses when the free energy exceeds a critical limit. At this stage, the crystalline regions relax into an amorphous phase, thereby lowering the local free energy by relieving strain energy. This is not unlike damage accumulation and amorphisation in high Al content AlGaAs reported in the previous chapter which is best described by a homogeneous amorphisation process.[34,35] Once amorphisation of these interfacial regions has occurred, point defects injected from the AlGaAs layers are then trapped and agglomerate at the amorphous-crystalline boundary. The amorphous-crystalline interface then becomes a nucleating site and amorphisation extends (layer-by-layer) across the interface into the AlGaAs layer. This effect has also been observed in Si under certain irradiation conditions.[31,34,35] Hence, GaAs-AlGaAs interface regions behave not only as a supply of point defects to facilitate dynamic annealing (below a critical dose) but also as a sink for point defects and a nucleating site for amorphisation of AlGaAs once an amorphous layer has formed up to the GaAs interface (above a critical dose). In alloys with higher Al content, defect mobility and *in situ* annealing across the interface become more efficient and higher doses are required to nucleate amorphous layers.

4.4.3 Variation of damage with nuclear energy deposition

Damage buildup in GaAs is dependent on the nuclear energy deposition density (i.e. atomic displacements) where the maximum damage usually corresponds to the maximum in the energy deposition distribution. However, the damage buildup in AlGaAs is a result of the competition between dynamic annealing and damage production (atomic displacements). For keV irradiations, the nuclear energy deposition density varies across the damage cascades. Towards the tail of each cascade, where the damage production rate (or energy deposition) is low, dynamic annealing may dominate. Efficient dynamic annealing at the GaAs-AlGaAs interfaces also dominates over damage production. The resulting residual damage in these regions could be very different from the sample near the peak of the distribution where the number of displaced atoms is much higher. Indeed, differences in residual disorder are observed throughout the AlGaAs layers, and the changes are consistent with differences in the energy deposition distribution of keV ions. For amorphisation of AlGaAs layers, the buildup of damage is not only dependent on local energy deposition density but is also strongly influenced by dynamic annealing and/or defect trapping processes occurring at GaAs-AlGaAs interfaces, due to preferential amorphisation in GaAs.

With MeV beams, the nuclear energy deposition density is much reduced in the near surface region and amorphisation would be expected to occur at proportionately higher doses, as is observed for both GaAs and AlGaAs layers. Thus, the degree of protection offered by AlGaAs to adjacent GaAs regions is enhanced in comparison to keV beams. However, since MeV beams penetrate entirely through the layers with slowly varying energy deposition density with depth, it is interesting to compare the damage and dynamic annealing processes at the top and bottom GaAs-AlGaAs interfaces. With 1 MeV beams, a slight asymmetry in the residual damage is observed between the interfaces; with damage first building up at the deeper interface. This effect has been reported previously[20-22] and Klatt *et. al.*[20] related it to the ratio of the electronic (ionisation) to nuclear (damage) energy loss of the incoming ions. However, the above results from MeV implants do not support this explanation. For 4 MeV irradiation, despite a 30-40% difference in the ratio of electronic to nuclear energy losses across the interfaces, damage accumulation is relatively constant throughout the layer, consistent with the displacement density. Furthermore, for 1 MeV irradiation, where the displacement density varies by up to a factor of 2 across the interfaces, a higher degree of asymmetry in the residual damage density is observed. However, it is difficult to ascertain whether the increase in residual disorder at the deeper interface is consistent with increased energy deposition or whether some other cause is appropriate. For example, Turkot and co-workers[21,22] observed increased damage at a deeper AlGaAs-GaAs interface but suggested that the amount of damage could not be accounted for by increased nuclear energy deposition (displacement density) alone and proposed that energetic recoil events in a particular energy range cause a larger number of cascades and intermixing at the deeper interface, thus explaining the increased disorder. However, this suggestion cannot be validated nor contradicted from the data in this work. Nevertheless, it should be stressed that there is strong dynamic annealing at such interfaces and correlations of 'amounts' of residual disorder directly with nuclear energy deposition processes are difficult.

4.4.4 Stability of (liquid nitrogen temperature) implantation damage

In some cases, the exact nature of the residual damage following implantation at LN2 temperatures is not clearly known, particularly at the heterointerfaces. The observed residual disorder appears to be dependent on the (thermal) stability of defects in these regions generated during LN2 irradiation and following subsequent heating such as warming up to room temperature and during XTEM specimen preparation. In some samples, planar defects (stacking faults) are observed, particularly at the amorphous-

crystalline interface. Vieu *et. al.*[19] reported similar defects at the interface in room temperature implanted GaAs-$Al_{0.35}Ga_{0.65}As$ structures and attributed this effect to ion beam induced epitaxial crystallisation (IBIEC). Although, this effect could well be happening under their experimental conditions, IBIEC does not occur in this work at LN2 temperature implants. Evidence of this is illustrated in the micrograph in Fig. 4-15 which is from the same specimen as that in Fig. 4-6 but has been subjected to 130 °C epoxy curing during XTEM sample preparation. The instability in interface disorder is confirmed by the observed planar defects in the GaAs layer at the amorphous-crystalline interfaces, indicating partial recrystallisation of the amorphous GaAs layer has taken place. This effect is quite surprising in this multilayer system because recrystallisation of the amorphous GaAs layer occurs at a much lower temperature than normally observed in bulk GaAs.[27-29,36,37] This type of recrystallisation, which does not occur in bulk GaAs, is efficient in GaAs regions close to adjacent AlGaAs layers which may provide a ready source of point defects with increased mobility during low temperature heating. In AlGaAs, however, the interfacial instability is more pronounced (see Figs. 4-3 and 4-4) as indicated by the presence of planar defects (*region 2*) at the amorphous-crystalline interface. A repeat of the XTEM analysis on the same sample shown in Fig. 4-4 but without the 130 °C epoxy curing showed no stacking faults surrounding the buried amorphous GaAs layer [Fig. 4-4(b)] but they remain in the AlGaAs layer at the top amorphous-crystalline interface (*region 2*) [Fig. 4-4(a)]. It is possible that, once an amorphous phase is formed in AlGaAs, the amorphous regions act as trapping sites for point defects and, due to strong local bonding rearrangements, planar defects are formed (so as to lower the system's free energy) during irradiation. However, it is equally likely that the residual damage following implantation consists of overlapping defect clusters or amorphous pockets in such cases. Upon warming the sample up to room temperature, these partly amorphous regions recrystallise imperfectly in the presence of surrounding crystalline material (which acts as the seed for recrystallisation) into planar defects. The instability of partially incomplete amorphous material in AlGaAs during warm up to room temperature has previously been observed in bulk AlGaAs layers (Chapter 3) and also in multilayers.[21-22] However, no comprehensive explanation of such low temperature annealing effects has been put forward. Despite the possibility of some annealing (on warm up to room temperature) of incomplete amorphous regions in AlGaAs, there is little evidence from the previous chapter or in this chapter to suggest recovery of completely amorphous regions in high Al-content AlGaAs until temperatures of the order of 250 °C are reached.

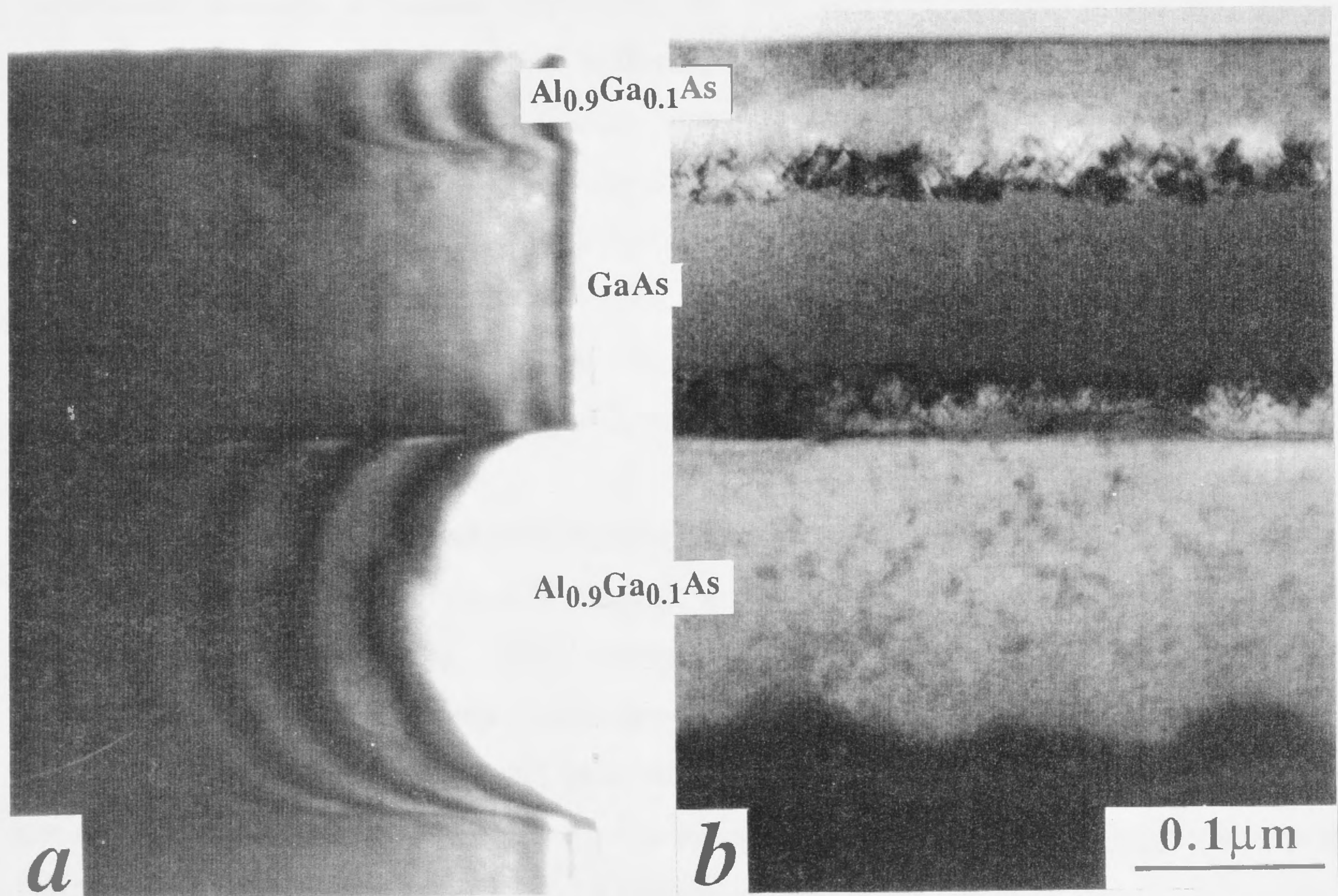

Fig. 4-15 XTEM images of the same specimen as that of Fig. 4-6 but the implanted specimen has been subjected to an epoxy curing step (at 130 °C) during sample preparation. Stacking faults are clearly observed extending from the interface into surrounding GaAs regions. Both images have the same magnification.

4.5 Conclusions

The damage buildup and amorphisation processes of GaAs-AlGaAs multilayers at LN2 temperatures have been systematically examined by ion channeling and XTEM techniques. The ion-induced damaging processes are more complex than those in bulk GaAs or AlGaAs due the preferential amorphisation of GaAs and interfacial effects. Damage builds up preferentially in the GaAs layer but the presence of adjacent AlGaAs layers inhibit disorder formation in narrow regions of GaAs close to the interface. This effect is accentuated with increasing Al content and with decreasing nuclear energy deposition density. Dynamic annealing, as mediated by defect trapping and defect migration, competes very strongly with damage production at the interface and residual damage is the result of a fine balance between these two processes. Once amorphous layers eventually form at GaAs-AlGaAs interfaces with increasing implantation doses, they act as nucleation sites for the progression of the amorphous phase into the AlGaAs layers. The presence of adjacent AlGaAs also appears to enhance the recrystallisation of amorphous GaAs at low temperature, presumably by lowering the recrystallisation temperature through the supply/injection of mobile defects across the heterointerface.

This extensive study has lead to several observations not previously reported, providing new insights into understanding of damage accumulation and amorphisation processes of GaAs-AlGaAs multilayers. The overall process has been established and a phenomenological model has been developed to explain these processes and their effects. The understanding of the behaviour of ion irradiation-induced damage in these multilayer structures is important as it allows the key issues of the applications of ion beams to optoelectronic devices to be identified and addressed.

References

[1] W.D. Laidig, N. Holonyak, Jr., M.D. Camras, K. Hess, J.J. Coleman, P.D. Dapkus and J. Bardeen, "Disorder of an AlAs-GaAs superlattice by impurity diffusion," *Appl. Phys. Lett.* **38**, 776-778 (1981).

[2] See for example review article by D.G. Deppe and N. Holonyak, Jr., "Atom diffusion and impurity-induced disordering in quantum well III-V semiconductor heterostructures," *J. Appl. Phys.* **64**, R93-R113 (1988) and references therein.

[3] J.J. Coleman, P.D. Dapkus, C.G. Kirkpatrick, M.D. Camras and N. Holonyak, Jr., "Disorder of an AlAs-GaAs superlattice by silicon implantation," *Appl. Phys. Lett.* **40**, 904-906 (1982).

[4] T.E. Schlesinger and T. Keuch, "Determination of the interdiffusion of Al and Ga in undoped (Al,Ga)As/GaAs quantum wells," *Appl. Phys. Lett.* **49**, 519-521 (1986).

[5] L.J. Guido, N. Holonyak, Jr., K.C. Hsieh, R.W. Kaliski, W.E. Plano, R.D. Burnham, R.L. Thornton, J.E. Elper and T.L. Paoli, "Effects of dielectric encapsulation and As overpressure in Al-Ga interdiffusion in $Al_xGa_{1-x}As$-GaAs quantum-well heterostructures," *J. Appl. Phys.* **61**, 1372-1379 (1987).

[6] Y. Hirayama, Y. Suzuki, S. Tarucha and H. Okamoto, "Compositional disordering of GaAs-$Al_xGa_{1-x}As$ superlattice by Ga focused ion beam implantation and its application to submicron fabrication," *Jpn. J. Appl: Phys.* **24**, L516-L518 (1985).

[7] R.P. Bryan, J.J. Coleman, L.M. Miller, M.E. Givens, R.S. Averback and J.L. Klatt, "Impurity induced disordered quantum well heterostructure stripe geometry lasers by MeV oxygen implantation," *Appl. Phys. Lett.* **55**, 94-96 (1989).

[8] P.L.K. Wa, "Intermixing of multiple quantum wells for all-optical integrated circuits," *Opt. Quantum Electron.* **23**, S925-S939 (1991).

[9] J.H. Marsh, S.I. Hansen, A.C. Bryce and R.M. de la Rue, "Applications of neutral impurity disordering in fabricating low-loss optical waveguides and integrated devices," *Opt. Quantum Electron.* **23**, S941-S957 (1991).

[10] F.E. Prins, G. Lehr, H. Schweizer and G.W. Smith, "GaAs/AlGaAs quantum dots by implantation induced intermixing," *Appl. Phys. Lett.* **63**, 1402-1404 (1993).

[11] J. Ralston, G.W. Wicks, L.F. Eastman, B.C. De Cooman and C.B. Carter, "Defect structure and intermixing of ion-implanted $Al_xGa_{1-x}As$/GaAs superlattice," *J. Appl. Phys.* **59**, 120-123 (1986).

[12] K. Matsui, S. Takatani, T. Fukunaga, T. Narusawa, Y. Bamba and H. Nakashima, "Damage profile in GaAs, AlAs, AlGaAs, and GaAs/AlGaAs superlattices induced by Si^+-ion implantation," *Jpn. J. Appl. Phys.* **25**, L391-L393 (1986).

[13] K. Matsui, T. Takamori, T. Fukunaga, T. Narusawa and H. Nakashima, "Ion-implantation induced damage in $Al_xGa_{1-x}As$ and superlattices studied by Rutherford backscattering," *Jpn. J. Appl. Phys.* **26**, 482-486 (1987).

[14] A.G. Cullis, N.G. Chew, C.R. Whitehouse, D.C. Jacobson, J.M. Poate and S.J. Pearton, "Material-dependent amorphization and epitaxial crystallisation in ion-implanted AlAs/GaAs layer structures," *Appl. Phys. Lett.* **55**, 1211-1213 (1989).

[15] A.G. Cullis, P.W. Smith, D.C. Jacobson and J.M. Poate, "Differential ion damage and its annealing behavior in AlAs/GaAs heterostructures," *J. Appl. Phys.* **69**, 1279-1286 (1991).

[16] I. Jencic, M.W. Bench, I.M. Robertson, M.A. Kirk and J. Peternelj, "A comparison of the rates of amorphization in the $Al_xGa_{1-x}As$/GaAs system," *Nucl. Instrum. Methods* **B59/60**, 458-461 (1991).

[17] I. Jencic, M.W. Bench, I.M. Robertson and M.A. Kirk, "A comparison of the amorphization induced in $Al_xGa_{1-x}As$ and GaAs by heavy-ion irradiation," *J. Appl. Phys.* **69**, 1287-1292 (1991).

[18] A.G. Cullis, A. Polman, P.W. Smith, D.C. Jacobson, J.M. Poate and C.R. Whitehouse, "The nature of keV and MeV ion damage in $Al_xGa_{1-x}As$/GaAs and AlAs/GaAs heterostructures," *Nucl. Instrum. Methods* **B62**, 463-468 (1992).

[19] C. Vieu, M. Schneider, H. Launois and B. Descouts, "Damage generation and annealing in Ga^+ implanted GaAs/(Ga,Al)As quantum wells," *J. Appl. Phys.* **71**, 4833-4841 (1992).

[20] J.L. Klatt, R.S. Averback, D.V. Forbes and J.J. Coleman, "Interfacial damage in ion-irradiated GaAs/AlAs superlattices," *Phys. Rev. B* **48**, 17629-17632 (1993).

[21] B.A. Turkot, D.V. Forbes, I.M. Robertson, J.J. Coleman, L.E. Rehn, M.A. Kirk and P.M. Baldo, "Ion implantation damage in $Al_{0.6}Ga_{0.4}As$/GaAs heterostructures," *J. Appl. Phys.* **78**, 97-103 (1995).

[22] B.A. Turkot, B.W. Lagow, I.M. Robertson, L.E. Rehn, P.M. Baldo, D.V. Forbes and J.J. Coleman, "Depth dependence of ion implantation damage in $Al_xGa_{1-x}As$ / GaAs heterostructures," *J. Appl. Phys.* **80**, 4366-4371 (1996).

[23] H.J. Hay, FASTRIM is a modified version of TRIM85-90 which takes into account the multilayer target (interfaces) problems inherent with TRIM85-90 (unpublished).

[24] J.F. Ziegler, J.P. Biersack and U. Littmark, *The Stopping and Range of Ions in Solids*, vol. 1, Pergamon, New York (1989).

[25] W.-K. Chu, J.W. Mayer and M.-A. Nicolet, *Backscattering Spectrometry*, Academic Press, New York (1978).

[26] J.S. Williams and R.G. Elliman, "Channeling," in *Ion Beam for Material Analysis*, J.R. Bird and J.S. Williams, editors, Chp. 6, 261-333, Academic Press, Sydney (1989).

[27] S.S. Kular, B.J. Sealy, K.G. Stephens, D. Sadana and G.R. Booker, "Electrical, Rutherford backscattering and transmission electron microscopy studies of furnace annealed zinc implanted GaAs," *Solid State Electron.* **23**, 831-838 (1980).

[28] C. Licoppe, Y.I. Nissim and C. Meriadec, "Direct measurement of solid-phase epitaxial growth kinetics in GaAs by time-resolved reflectivity," *J. Appl. Phys.* **58**, 3094-3096 (1985).

[29] S. Yokohama, D. Yui, H. Tanigawa, H. Takasugi and M. Kawabe, "Solid-phase crystal growth of molecular-beam-deposited amorphous GaAs," *J. Appl. Phys.* **62**, 1808-1814 (1987).

[30] D.K. Sadana, "Mechanisms of amorphization and recrystallization in ion implanted III-V compound semiconductors," *Nucl. Instrum. Methods* **B7/8**, 375-386 (1985).

[31] F. Morehead and B.L. Crowder, "A model for the formation of amorphous Si by ion bombardment," *Rad. Eff.* **6**, 27-32 (1970).

[32] P.M. Petroff, "Transmission electron microscopy of interfaces in III-V compound semiconductors," *J. Vac. Sci. Technol.* **14**, 973-978 (1977).

[33] R.M. Fleming, D.B. McWhan, A.C. Gossard, W. Wiegmann and R.A. Logan, "X-ray diffraction study of interdiffusion and growth in $(GaAs)_n(AlAs)_n$ multilayers," *J. Appl. Phys.* **51**, 357-363 (1980).

[34] F.L. Vook, "Radiation damage during ion implantation," in *Defects in Semiconductors*, 60-71, Institute of Physics, London (1971).

[35] M.L. Swanson, J.R. Parsons and C.W. Hoelke, "Damaged regions in neutron-irradiated and ion-bombarded Ge and Si," *Rad. Eff.* **9**, 249-256 (1971).

[36] S.T. Johnson, J.S. Williams, R.G. Elliman, A.P. Pogany, E. Nygren and G.L. Olson, "Characterisation of structural changes and defects in ion bombarded GaAs," *Mater. Res. Soc. Symp. Proc.* **82**, 127-132 (1987).

[37] J.S. Williams and M.W. Austin, "Low-temperature epitaxial regrowth of ion-implanted amorphous GaAs," *Appl. Phys. Lett.* **36**, 994-996 (1980).

Chapter 5

Deep levels in ion implanted GaAs at low doses

5.1 Introduction

GaAs has proven to be one of the most important materials in many optoelectronic devices. However, many of its electrical and optical properties are governed by the presence of deep levels, either intentionally or unintentionally incorporated during growth and/or subsequent processing. These deep levels are formed when discrete crystalline defects manifest themselves as carriers (both holes and electrons) trapping sites by small perturbations in the local band structure. With the introduction of deep level transient spectroscopy (DLTS) by Lang,[1] a great amount of work has been done to study, identify and characterise deep levels in GaAs. Since then, scores of defect levels have been identified in GaAs, including irradiation-induced deep levels (see references [2-7] for a summary and review of the deep levels). The most commonly used sources for irradiation are electrons and protons since they create simple defects (discrete levels) which are easily analysed. On the other hand, there are less studies in neutron and ion irradiated GaAs due to the resulting defects which are more complex and the DLTS spectra are often difficult to analyse.

However, proton irradiation has been successfully used to create current confinement and waveguiding regions in GaAs-based optoelectronic devices.[8-10] The advantage of using protons is the deep penetration required in many optoelectronic devices is not easily achievable by heavier ions. However, in many instances, the use of protons is not necessarily the ideal choice. Furthermore, with the advent of high energy (MeV energies) ion implanters, one is no longer restricted to protons. In general, defects created by light ions, such as protons, are less thermally stable than defects created by heavier ions. Thus, the understanding of defect creation and thermal stability will be useful in achieving better device performance. This chapter is dedicated to the study of ion implantation-induced deep levels in *n*-type GaAs and their thermal stability by

capacitance-voltage (C-V) profiling and DLTS techniques. Due to the sensitivity of this technique to defects, implantations were carried out at very low doses. In this dose regime, the defects created are very dilute in concentration in which point defects and defect pairs dominate. Nevertheless, the defect concentration is sufficient to modify the optical and electrical properties of the material. The effects of protons, oxygen and silicon implantation-induced deep levels are analysed and compared. This chapter concentrates only on GaAs as this material will be used as the active layer in subsequent device application chapters.

5.2 Experimental

The structures used for this experiment were grown on Vertical-Gradient-Freeze (VGF) n^+ substrates by MOCVD. The sample for proton implantation was a 10 μm thick undoped GaAs with a background carrier concentration of $1\text{-}2 \times 10^{14}$ cm^{-3} (*n*-type). Samples for oxygen and silicon implantations were in excess of 2.5 μm thick and doped with Si to carrier concentrations of about 7×10^{15} cm^{-3}. Ion implantation was carried out at room temperature with either 600 keV H, 1 MeV O or 1 MeV Si ions with doses in the range of 1×10^8 to 1×10^{10} cm^{-2}. After implantation, selected samples were annealed at various temperatures for 20 min. Low temperature annealing (400 °C and below) was carried out in an inert atmosphere while for temperature > 400 °C, annealing was carried out under arsine ambient to prevent excessive loss of As from the surface and to retain good surface morphology. All samples were chemically cleaned, including a final dip in diluted HCl acid to remove any surface oxide before being loaded into a vacuum chamber for metal deposition. Schottky barrier contacts of ~100 nm were formed by thermal evaporation of Au. Ohmic contacts to the back of the samples were made by applying In-Ga eutectic. C-V profiling and DLTS measurements were carried out on the instrument illustrated previously in Fig. 2-12 of Chapter 2.

5.3 Effects of proton irradiation and annealing in undoped (intrinsic) GaAs

5.3.1 DLTS observations

The quality of the unimplanted GaAs epilayers grown by MOCVD is excellent with only the presence of the arsenic antisite (As_{Ga})-related, EL2, traps evident in the DLTS

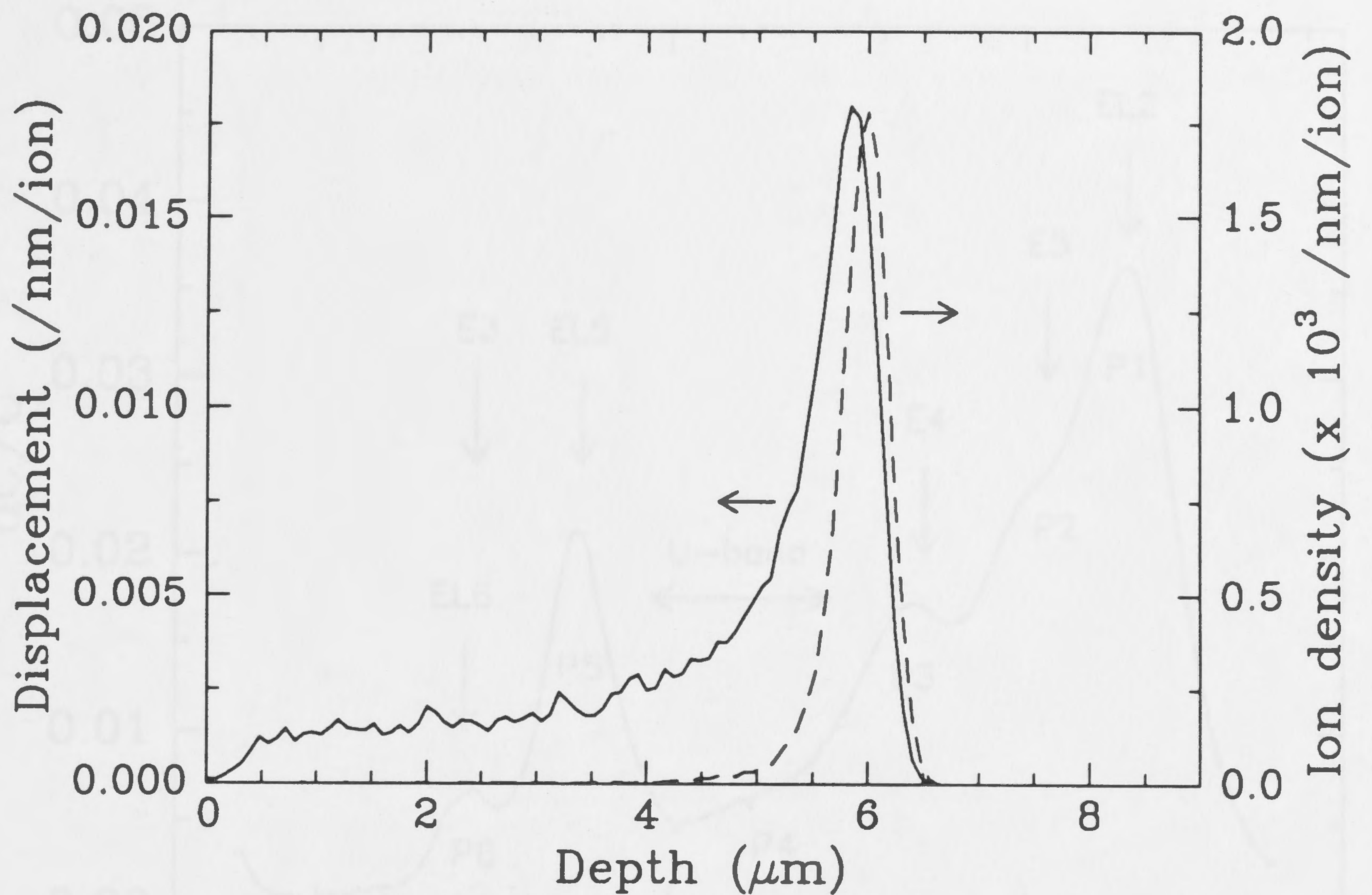

Fig. 5-1 TRIM90 simulation of the displacement density and ion range profiles for 600 keV protons into GaAs.

spectra. Although these samples were nominally undoped, the background doping level was 1-2x10^{14} cm^{-3}, *n*-type, presumably due to trace impurities from the arsine gas source.[11] The projected range and the atomic displacement density of the implanted 600 keV protons as calculated by TRIM90[12] are shown in Fig. 5-1.

After proton implantation, at least five additional deep levels are created, as shown by the DLTS spectrum in Fig. 5-2 for a rate window of 0.98 s^{-1}. These traps are labelled P1 through to P6. The arrows indicate some of the well known deep levels from the literature.[2,7] The trap signatures of the deep levels are extracted from several rate windows and plotted on the Arrhenius diagram in Fig. 5-3. The signature of the EL2 level in the starting material is also shown for comparison. Overlaying these data points are the signatures of the well known traps (solid lines). The signature of P1 is remarkably similar to that of EL2, which is an As_{Ga}-related defect. However, further results (detailed later) suggest that the microscopic nature of P1 is not identical to that of EL2 but is somehow related to it. From the trap signatures of P2 and P3, which are

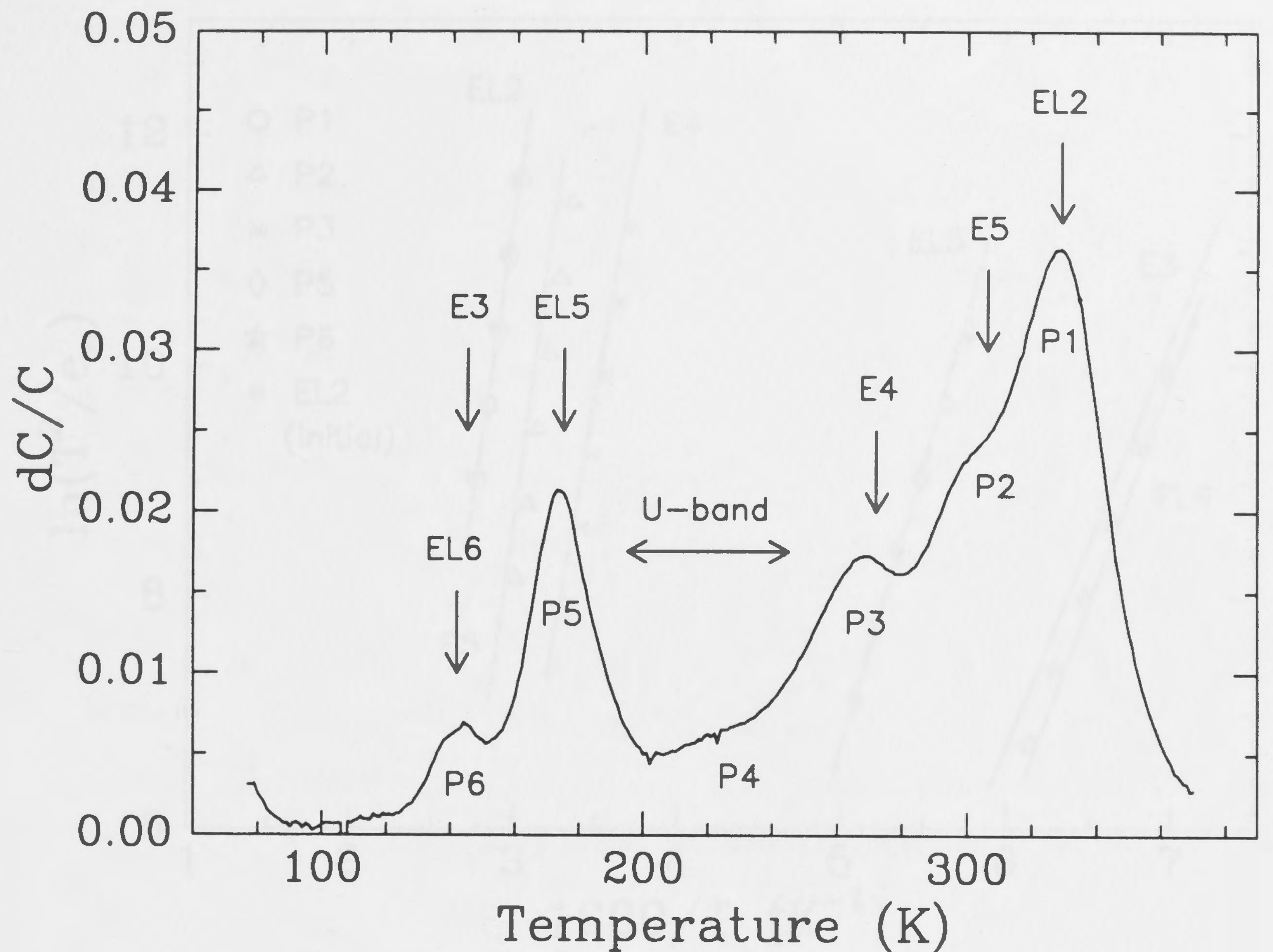

Fig. 5-2 DLTS spectrum after proton irradiation to a dose of $1x10^{10}$ cm^{-2}. The observed levels are labelled P1-P6. Arrows indicate the positions of some of the well known traps. The rate window for this spectrum is 0.98 s^{-1}.

not completely resolved from each other and from P1, it is likely that they correspond to the E5 and E4 levels, respectively, which are commonly observed in electron or proton irradiated samples.[6,7,13-21] A very broad P4 signal is observed in the temperature range of 200-240 K. This corresponds to the so-called U-band commonly observed in fast neutron and ion irradiated GaAs.[21-25] Analysis of this defect level is impossible due to the highly non-exponential nature of the capacitance transient. This effect is illustrated in Fig. 5-4 at a measurement temperature of 220 K. From this figure, it seems that there are at least three exponential decays (labelled 1, 2 and 3) in the trace. Therefore, one interpretation of this result is the overlapping of several adjacent peaks. However, as will be shown later, this is not the case but rather due to the interaction between two other defect levels. A very strong defect peak is observed at ~175 K with a signature identical to that of EL5 which is sometimes observed as a native defect of GaAs grown by a variety of techniques,[26-29] although it has not previously been reported in proton

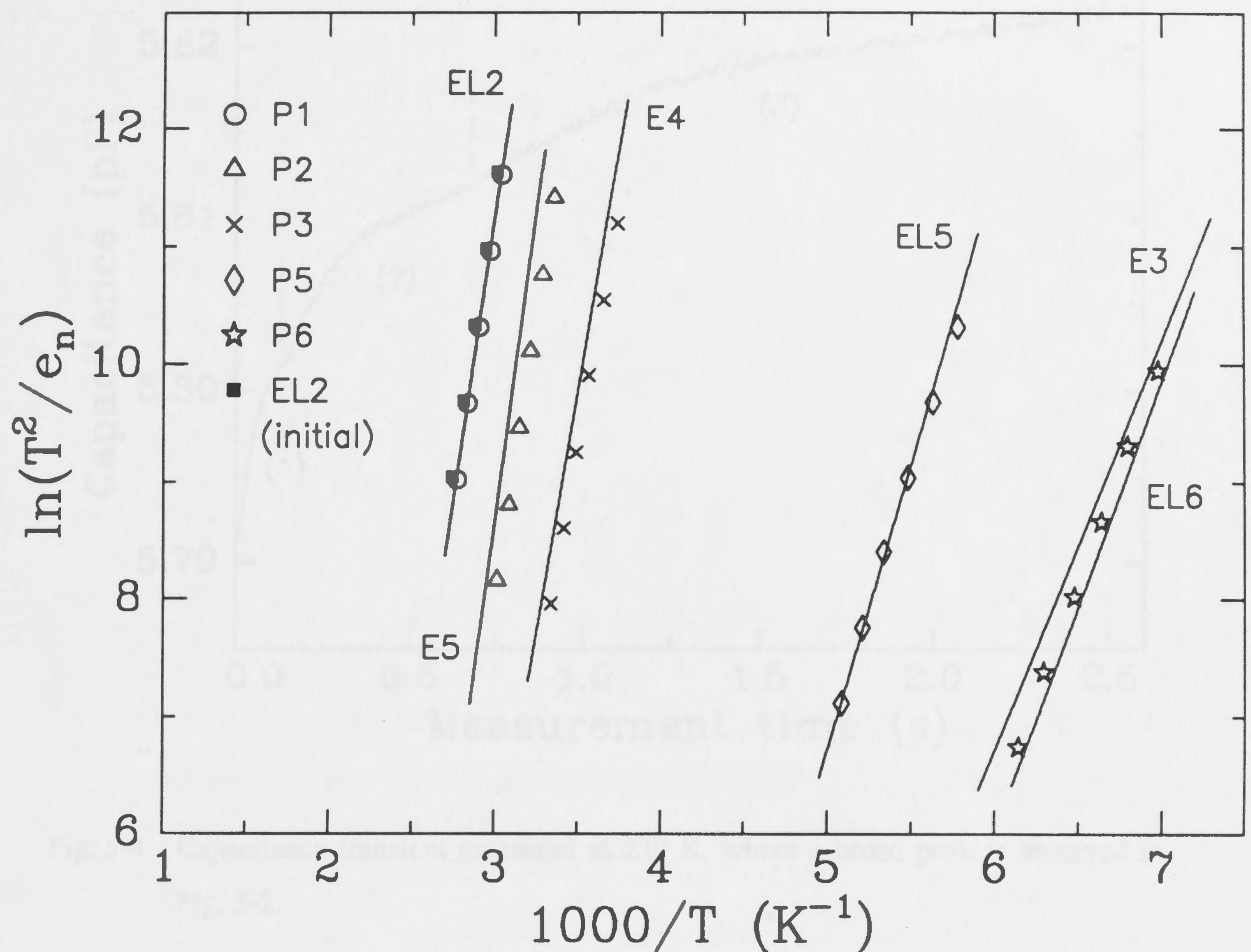

Fig. 5-3 Arrhenius plots of the EL2 level in as-grown material (initial) and the various traps after proton irradiation (data points). Also plotted are various the trap signatures from the data of refs. [2,7] (solid lines).

irradiated GaAs. Next to P5 is P6 which has a signature resembling both the EL6 and the E3 levels. Although, EL6 and E3 have almost identical signatures, it has been shown that the emission rate of E3 is a strong function of applied electric field and hence its peak position would shift with applied bias.[30] EL6 on the other hand, has a large relaxation energy and is thus not sensitive to applied electric field.[31,32] Measurements with either 5 or 10 V reverse bias do not indicate a shift of the observed P6 peak, suggesting that P6 is the EL6 level. A summary of the observed deep levels created is listed in Table I.

Toward the low temperature end of the DLTS spectrum in Fig. 5-2, a tail of a peak (P7) is just about observable. Further measurements done another instrument at liquid helium temperatures revealed two additional levels, P7 and P8, as depicted in Fig. 5-5 for a rate

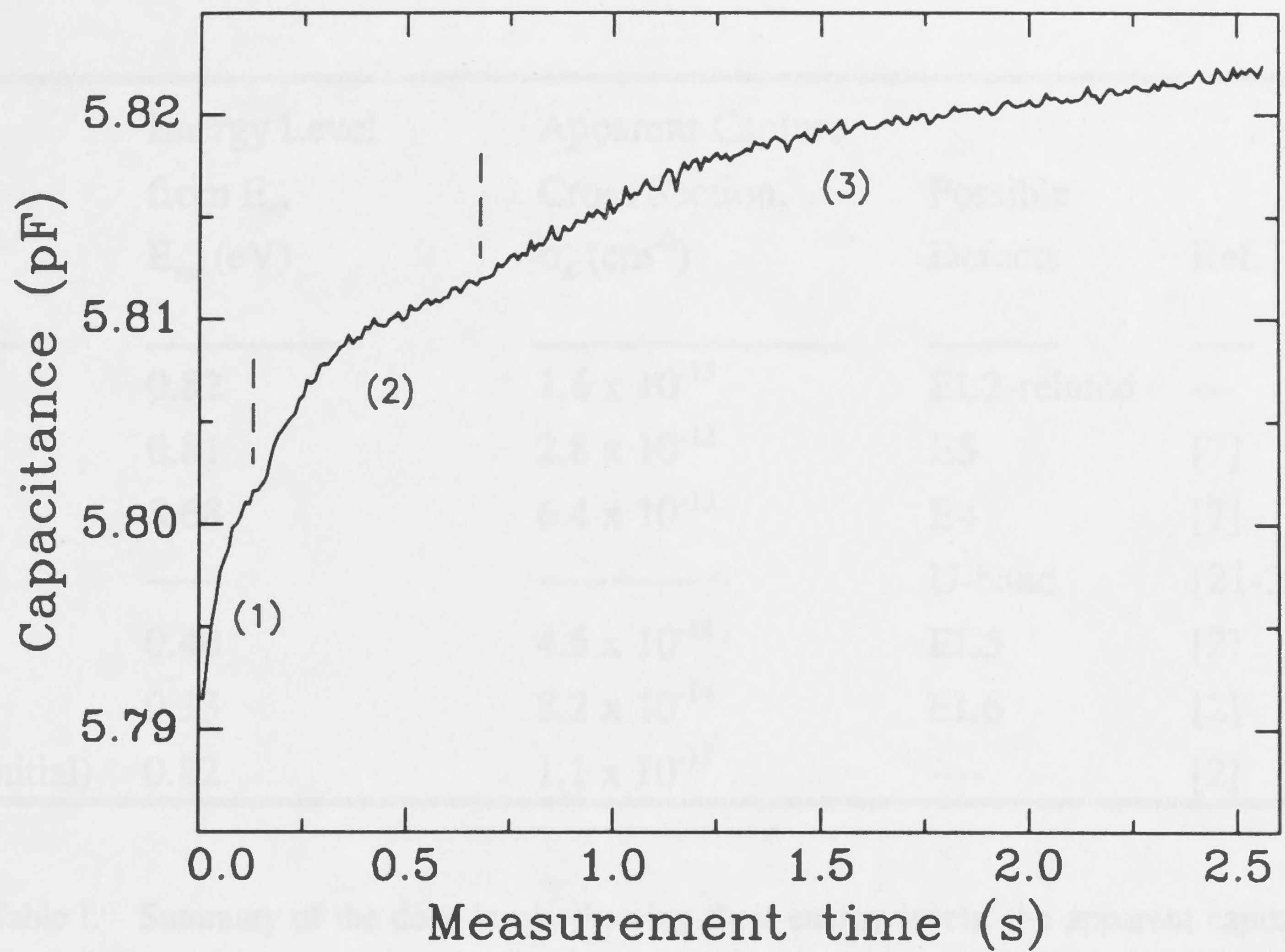

Fig. 5-4 Capacitance transient measured at 220 K, where a broad peak is observed in Fig. 5-2.

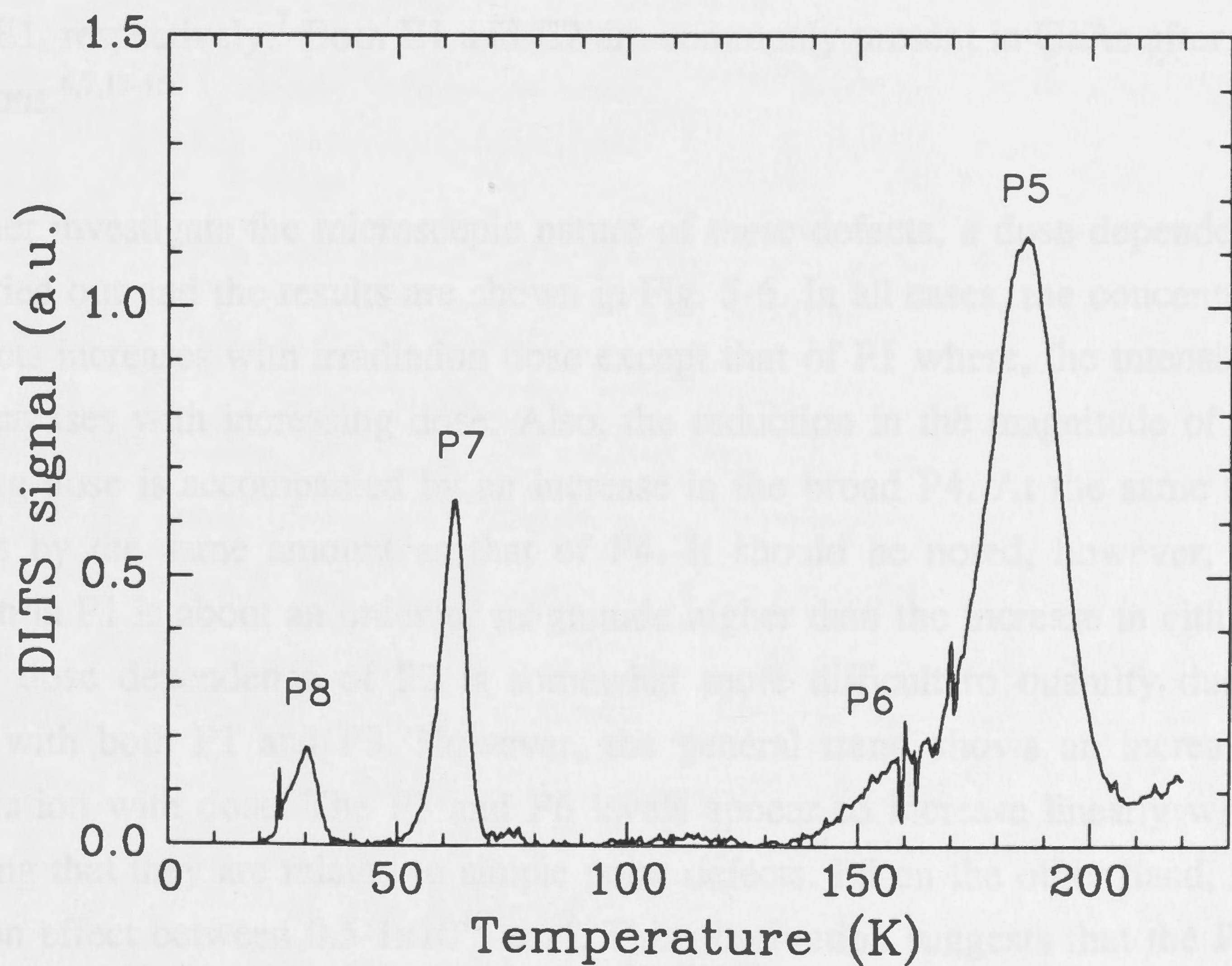

Fig. 5-5 DLTS spectrum of the same sample as in Fig. 5-2 taken with another instrument at liquid helium temperatures with a rate window of 116 s^{-1}.

Trap ID	Energy Level from E_c, E_{na} (eV)	Apparent Capture Cross Section, σ_a (cm^{-2})	Possible Defects	Ref.
P1	0.82	1.6×10^{-13}	EL2-related	---
P2	0.81	2.8×10^{-12}	E5	[7]
P3	0.68	6.4×10^{-13}	E4	[7]
P4	-----	-----------	U-band	[21-25]
P5	0.40	4.5×10^{-14}	EL5	[2]
P6	0.33	8.2×10^{-14}	EL6	[2]
EL2 (initial)	0.82	1.1×10^{-13}	----	[2]

Table I. Summary of the deep levels showing their energy levels, the apparent capture cross sections, and the possible associated defects.

window of 116 s^{-1}. The peaks of these levels correspond closely to the peak positions of E2 and E1, respectively.[7] Both E1 and E2 are commonly present in GaAs after electron irradiations.[6,7,13-16]

To further investigate the microscopic nature of these defects, a dose dependent study was carried out and the results are shown in Fig. 5-6. In all cases, the concentration of the defects increases with irradiation dose except that of P1 where, the intensity of the peak decreases with increasing dose. Also, the reduction in the magnitude of P1 with increasing dose is accompanied by an increase in the broad P4. At the same time, P6 increases by the same amount as that of P4. It should be noted, however, that the reduction in P1 is about an order of magnitude higher than the increase in either P4 or P6. The dose dependence of P2 is somewhat more difficult to quantify due to the overlap with both P1 and P3. However, the general trend shows an increase in its concentration with dose. The P3 and P6 levels appear to increase linearly with dose, suggesting that they are related to simple point defects. P5 on the other hand, shows a saturation effect between $0.5\text{-}1 \times 10^{10}$ cm^{-2}. This observation suggests that the P5 levels are not simple point defects, but rather, complex defects involving clusters and/or impurities.

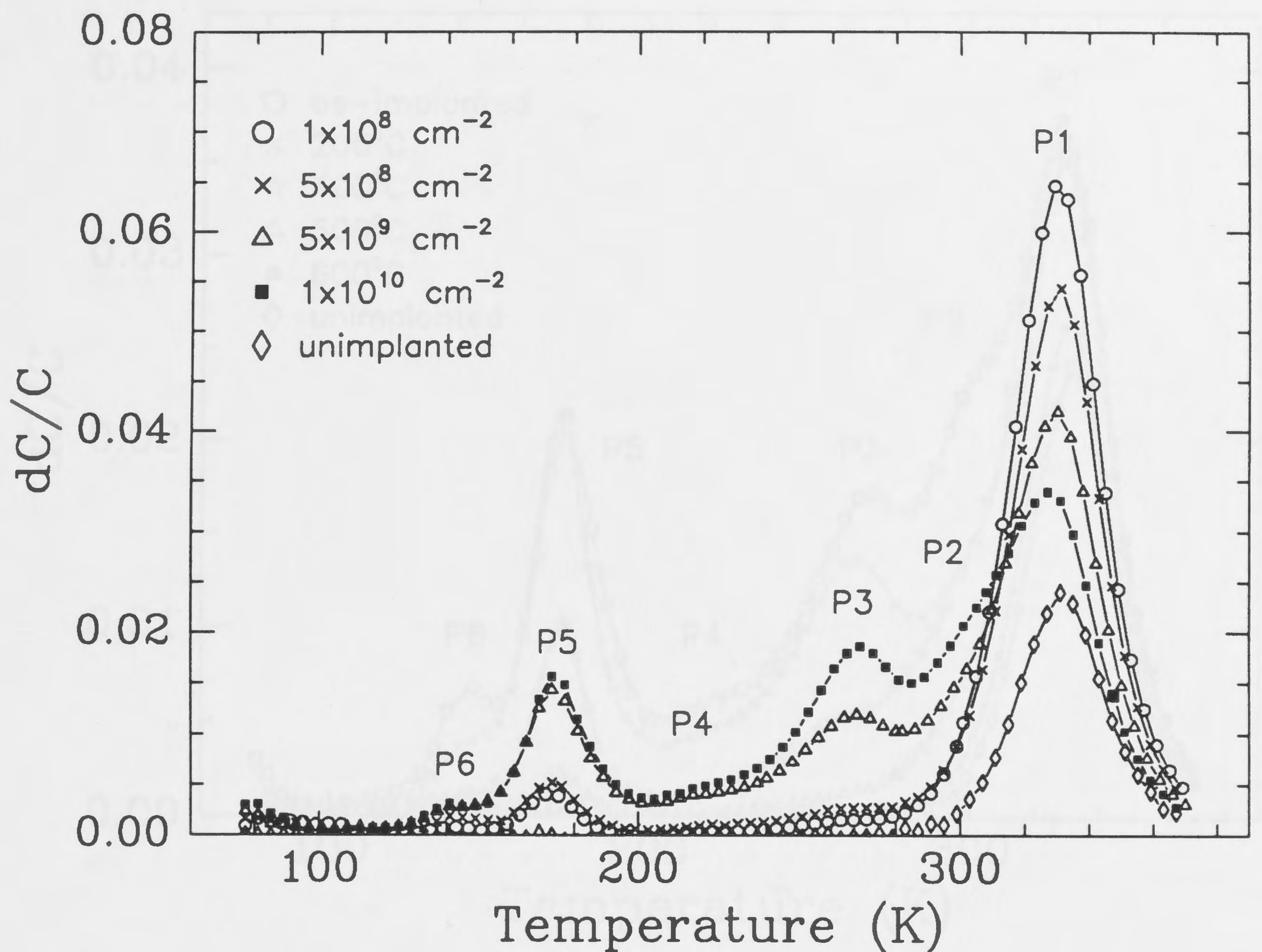

Fig. 5-6 DLTS spectra showing the dose dependence of the deep levels. The spectrum of the unimplanted sample is also shown for comparison (rate window of 0.98 s^{-1}).

The annealing behaviour of these deep levels is illustrated in Fig. 5-7 after irradiation to the dose of $1x10^{10}$ cm^{-2}. The concentration of P5 (~dC/C) is almost unchanged after 200 °C annealing and decreases slowly with annealing temperature, disappearing only at 600 °C. This recovery at high temperature is further evidence that P5 is indeed related to complex defects. On the other hand, P2 and P3 levels almost completely anneal at 500 °C. However, this temperature is slightly higher than the annealing temperature of isolated simple point defects which are expected occur at ~300 °C.[5,7,13] It is likely that these defects are defect pairs rather than isolated simple point defects. Just as the creation of P4 and P6 are almost identical, their annealing trend is also similar. At 500 °C, P4 and P6 anneal completely, while the concentration of P1 remains fairly constant even up to this temperature. However, there is a sudden decrease in the concentration of P1 at 600 °C, recovering to almost the initial value of EL2 at this temperature. So defects due to implantation are annealed out at 600 °C.

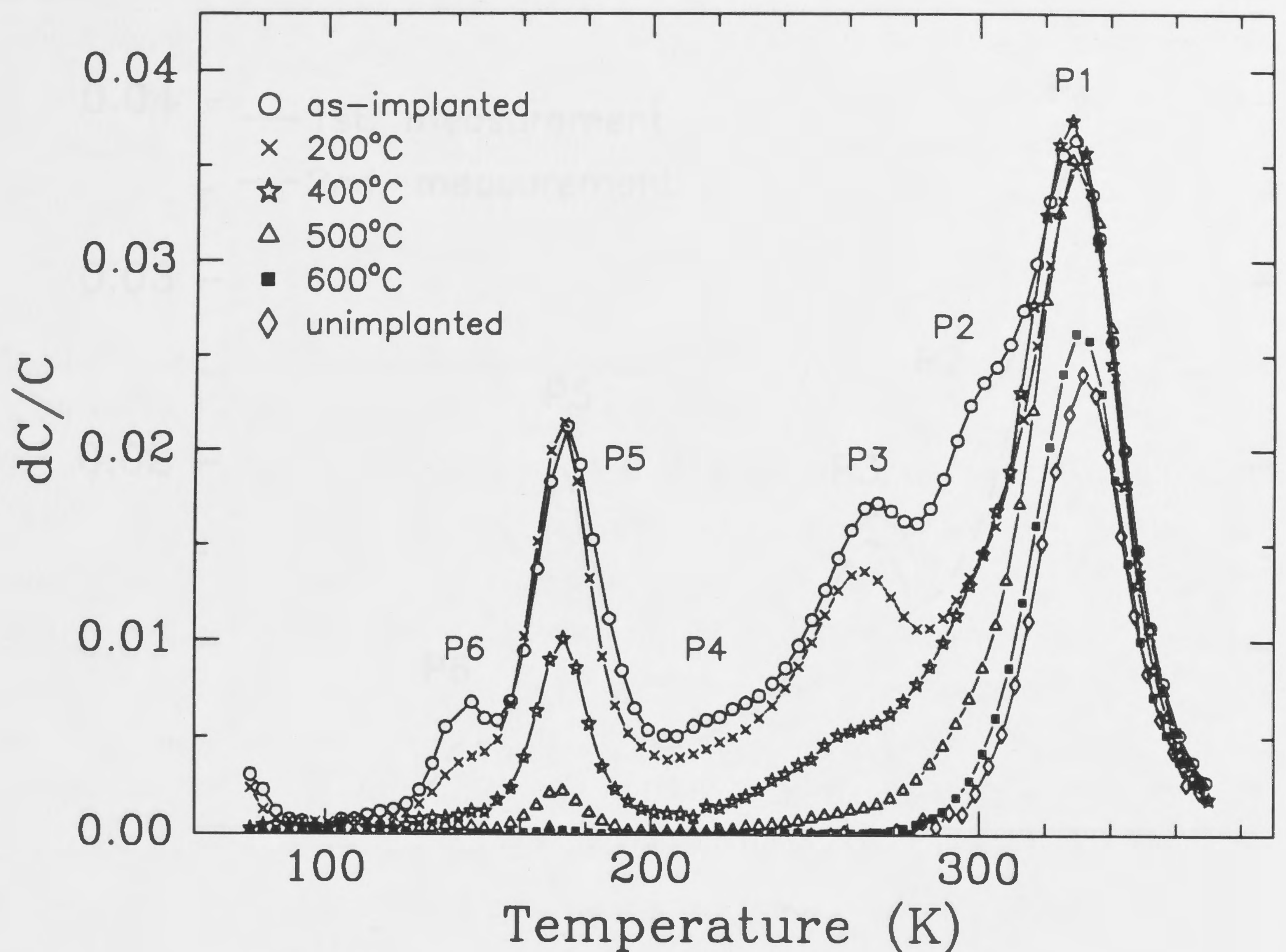

Fig. 5-7 DLTS spectra for samples implanted with $1x10^{10}$ H/cm^2 and annealed at various temperatures. The spectrum of the unimplanted specimen is also shown for comparison (rate window of 0.98 s^{-1}).

P2 also shows a very interesting annealing behaviour as depicted in Fig. 5-8. This level anneals efficiently at low temperature in the presence of carrier injection. The first measurement is made after irradiation and the second refers to a repeat of the first measurement on the same sample under the same measurement conditions. Of course, during the first measurement, the sample has been subjected to a measurement temperature of ~100 °C (during the temperature scan of the DLTS spectrum) and, at the same time, was subjected to carrier injection (from the filling pulse during measurement). A smaller but significant decrease in the magnitude of P5 is also observed after the second measurement, indicating that this level also anneals slightly at low temperature under the presence of carrier injection. This effect is surprising, considering that P5 is otherwise stable even up to 200 °C annealing (Fig. 5-7). A small change is observed in P1, P3 and P6 after the second measurement. However, it is

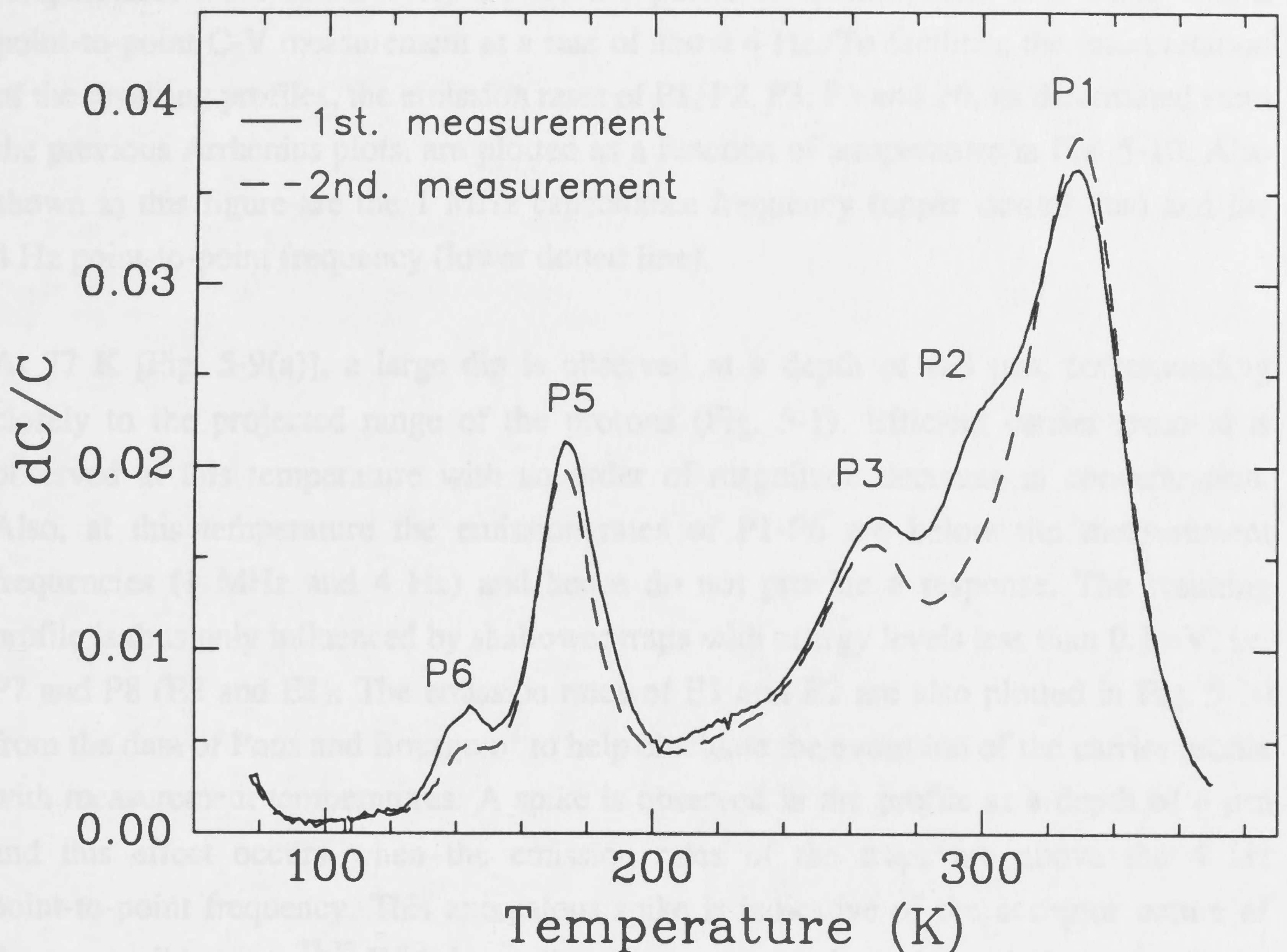

Fig. 5-8 DLTS spectra illustrating the sensitivity of P2 and P5 to low temperature annealing in the presence of carrier injection (rate window of 0.98 s^{-1}).

unlikely that these levels anneal significantly in the presence of carrier injection. The slight reductions are mainly attributable to the overlapping of these traps with either P2 or P5. Furthermore, both P3 and P6 are extremely sensitive to thermal annealing as noted previously, and 100 °C is sufficient to reduce their concentration markedly.

5.3.2 *Carrier compensation*

To study the carrier compensation behaviour, C-V profiling was carried out. In analysing the resulting profile, one has to use caution in the interpretation of the results, particularly in the presence of deep levels. Deep levels in the vicinity of the cross-over of the Fermi level within the space-charge regions are affected by the frequency response during measurements and this may cause anomalies in the carrier profiles.[33-35] The results presented in Fig. 5-9(a) (for temperatures from 77-150 K) and 5-9(b) (for

temperatures from 160-340 K) are for a capacitance measurement at 1 MHz with a point-to-point C-V measurement at a rate of about 4 Hz. To facilitate the interpretation of the resulting profiles, the emission rates of P1, P2, P3, P5 and P6, as determined from the previous Arrhenius plots, are plotted as a function of temperature in Fig. 5-10. Also shown in this figure are the 1 MHz capacitance frequency (upper dotted line) and the 4 Hz point-to-point frequency (lower dotted line).

At 77 K [Fig. 5-9(a)], a large dip is observed at a depth of 6-8 μm, corresponding closely to the projected range of the protons (Fig. 5-1). Efficient carrier removal is observed at this temperature with an order of magnitude decrease in concentration. Also, at this temperature the emission rates of P1-P6 are below the measurement frequencies (1 MHz and 4 Hz) and hence do not provide a response. The resulting profile is thus only influenced by shallower traps with energy levels less than 0.3 eV, i.e. P7 and P8 (E2 and E1). The emission rates of E1 and E2 are also plotted in Fig. 5-10 from the data of Pons and Bourgoin[7] to help elucidate the evolution of the carrier profile with measurement temperatures. A spike is observed in the profile at a depth of 8 μm and this effect occurs when the emission rates of the traps are above the 4 Hz point-to-point frequency. This anomalous spike is indicative of the acceptor nature of the responsible traps.[33-35] With increasing temperature, where the emission rates of the responsible traps are also increased, the spike moves towards the surface, resulting in the small peak in the 6-8 μm range [Fig. 5-9(a)]. This gradual movement is the expected result when the emission rates of the responsible traps exceed the 1 MHz capacitance measurement frequency. With further increase in temperature, the anomalous peak gradually disappears. These observations fit very well with the behaviour of E1, where the emission rate crosses the 4 Hz frequency at ~30 K and the 1 MHz frequency at ~70 K. Thus, it can be concluded that E1 is an acceptor-like defect. Similarly, if E2 is an acceptor-like defect, then one should see an additional spike at ~70 K with gradual movement when the measurement temperature exceeds 125 K. However, this effect could be masked by E1 and thus, the results do not conclusively indicate the nature of E2.

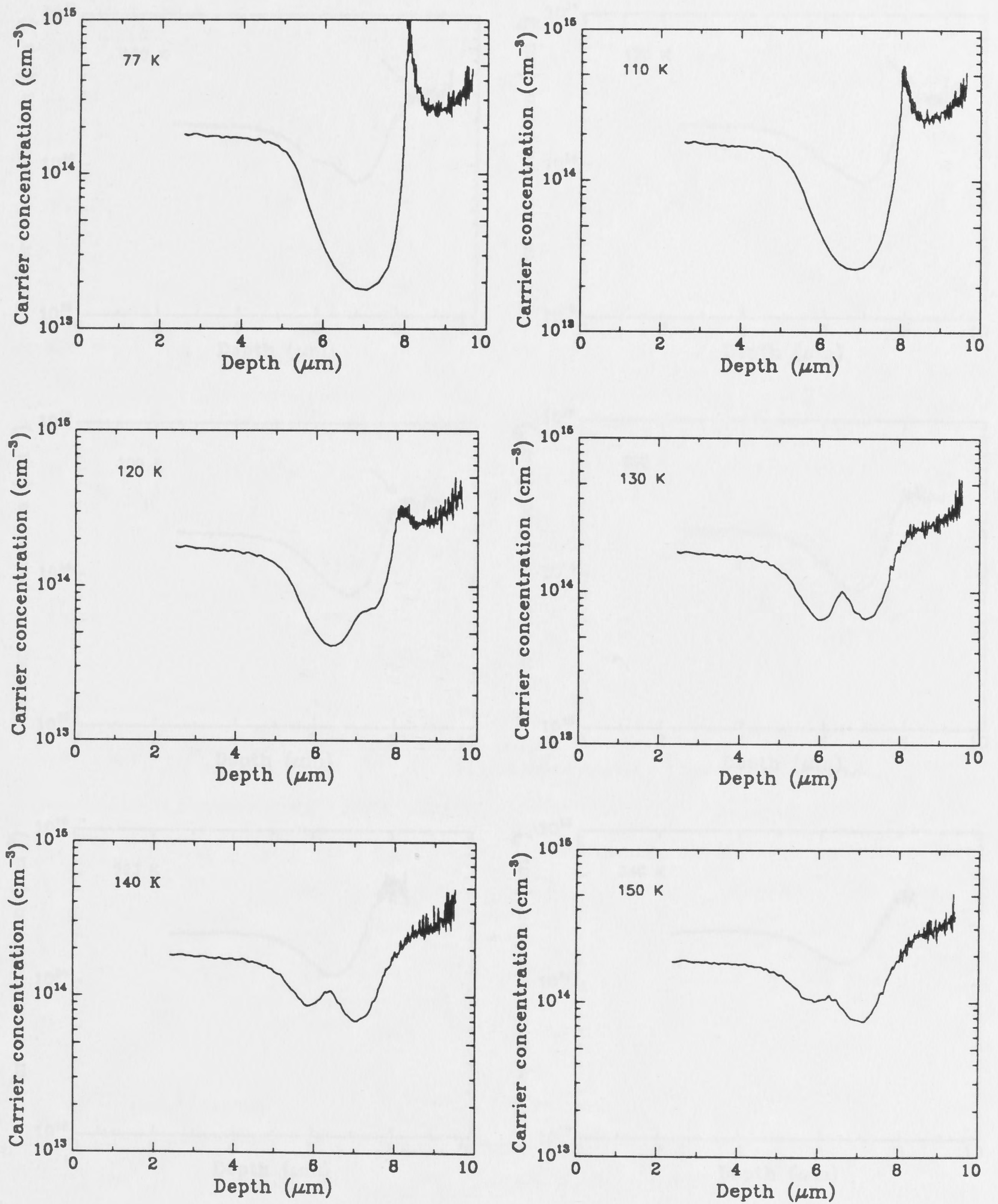

Fig. 5-9(a) Carrier profile of a sample irradiated with $1x10^{10}$ H/cm^2 as a function of measurement temperature (77-150 K) as determined from C-V profiling.

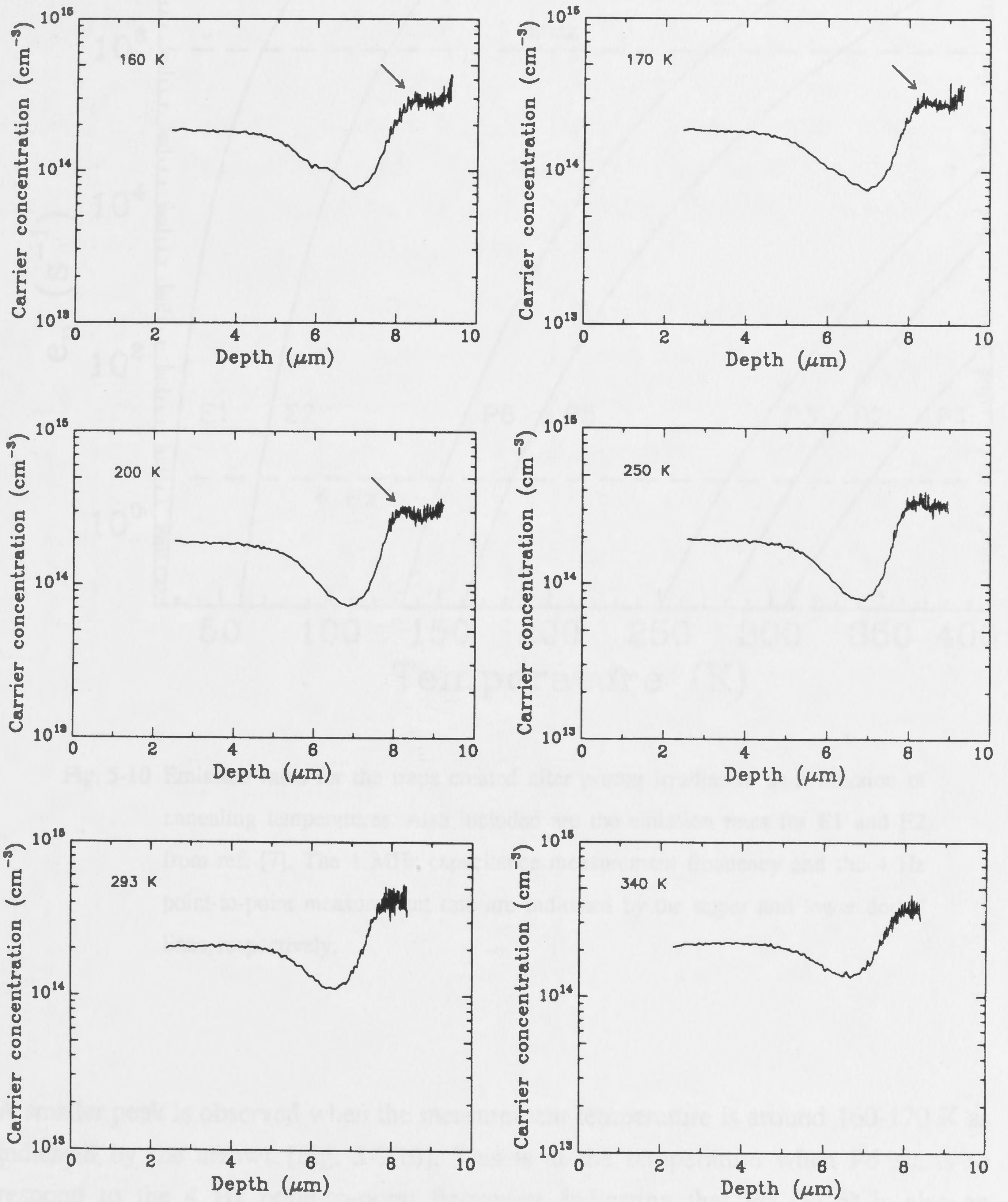

Fig. 5-9(b) Carrier profile of a sample irradiated with 1×10^{10} H/cm^2 as a function of measurement temperature (160-340 K) as determined from C-V profiling.

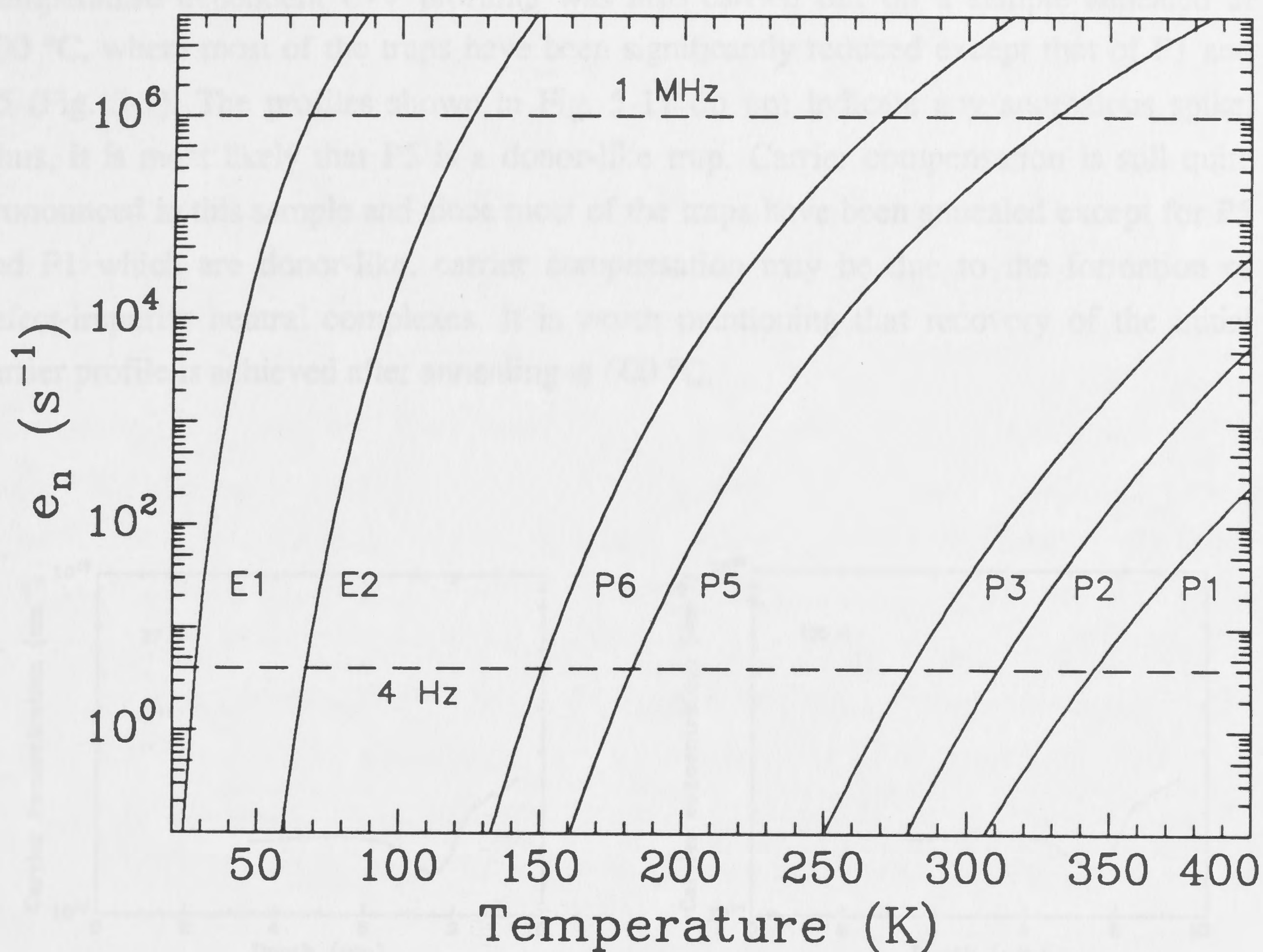

Fig. 5-10 Emission rates for the traps created after proton irradiation as a function of annealing temperatures. Also included are the emission rates for E1 and E2 from ref. [7]. The 1 MHz capacitance measurement frequency and the 4 Hz point-to-point measurement rate are indicated by the upper and lower dotted lines, respectively.

A smaller peak is observed when the measurement temperature is around 160-170 K as indicated by the arrows [Fig. 5-9(b)]. This is at the temperature when P6 starts to respond to the 4 Hz point-to-point frequency, indicating that P6 (EL6) is also an acceptor-like trap, consistent with previous reports that EL6 is an acceptor-like defect.[36,37] The P5 level, which is expected to respond above 180 K, is not observed in Fig. 5-9(b). It is possible that its effect is masked by P6 and hence the exact nature of this trap could not be determined from C-V profiling. Above 250 K, there is an increase in carrier concentration, where P3, P2 and P1 start to respond to the measurement frequency. The increase in carrier concentration and the large capture cross sections of these traps suggest that they are donor-like.

Temperature dependent C-V profiling was also carried out on a sample annealed at 400 °C, where most of the traps have been significantly reduced except that of P1 and P5 (Fig. 5-7). The profiles shown in Fig. 5-11 do not indicate any anomalous spike. Thus, it is most likely that P5 is a donor-like trap. Carrier compensation is still quite pronounced in this sample and since most of the traps have been annealed except for P5 and P1 which are donor-like, carrier compensation may be due to the formation of defect-impurity neutral complexes. It is worth mentioning that recovery of the initial carrier profile is achieved after annealing at 600 °C.

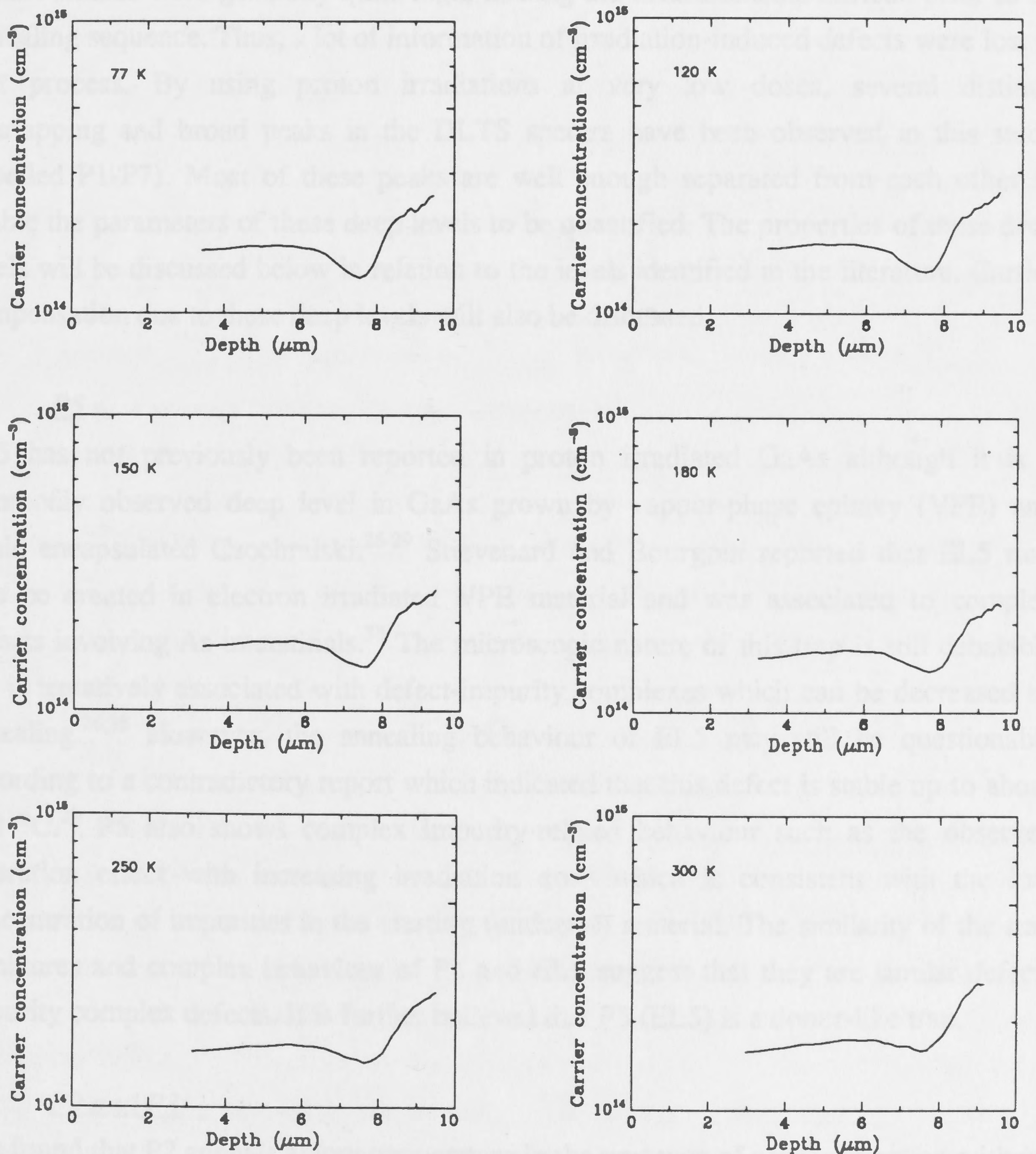

Fig. 5-11 Carrier profile at various measurement temperatures of a sample irradiated with $1x10^{10}$ H/cm^2 and annealed at 400 °C.

5.3.3 Discussion

Most of irradiation-induced defects studied by DLTS have concentrated on the use of electrons.[6,7,13-16,21,37] The main advantage with using electrons is that the defects (deep levels) created are very dilute in the form of discrete point defects of defect pairs. Thus, the resulting defect peaks of the DLTS spectra are very well separated from each other and allows them to be parameterised. However, due to the much heavier masses of ions in comparison to electrons, the damage cascades caused by the ions result in overlapping peaks in the DLTS spectra. With increasing ion mass, very often these peaks begin to merge, thus making quantitative analysis almost impossible. Furthermore, the doses used in past studies were generally quite high, making the measurements difficult prior to an annealing sequence. Thus, a lot of information of irradiation-induced defects were lost in that process. By using proton irradiations at very low doses, several distinct, overlapping and broad peaks in the DLTS spectra have been observed in this study (labelled P1-P7). Most of these peaks are well enough separated from each other to enable the parameters of these deep levels to be quantified. The properties of these deep levels will be discussed below in relation to the levels identified in the literature. Carrier compensation due to these deep levels will also be discussed.

(i) <u>*P5*</u>

EL5 has not previously been reported in proton irradiated GaAs although it is a commonly observed deep level in GaAs grown by vapour-phase epitaxy (VPE) and liquid encapsulated Czochralski.[26-29] Stievenard and Bourgoin reported that EL5 may also be created in electron irradiated VPE material and was associated to complex defects involving As interstitials.[38] The microscopic nature of this trap is still debatable but is tentatively associated with defect-impurity complexes which can be decreased by annealing.[26,38] However, the annealing behaviour of EL5 may still be questionable according to a contradictory report which indicated that this defect is stable up to about 850 °C.[29] P5 also shows complex impurity-related behaviour such as the observed saturation effect with increasing irradiation dose which is consistent with the low concentration of impurities in the starting (undoped) material. The similarity of the trap signatures and complex behaviour of P5 and EL5 suggest that they are similar defect-impurity complex defects. It is further believed that P5 (EL5) is a donor-like trap.

(ii) <u>*P2 and P3*</u>

It is found that P2 anneals at low temperature in the presence of carrier injection without any significant change in the P3 concentration, a similar observation was reported by Stievenard and Bourgoin for E4 and E5.[39] Hence, P2 and P3 may be associated with the

E5 and E4 defects, respectively. It has been suggested that both E4 and E5 are related to defect pairs of V_{As} and I_{As}.[7] The moderate annealing temperature (400-500 °C) of P2 (E5) and P3 (E4) favours this model of defect pairs since simple or isolated point defects are known to anneal at lower temperatures.[5,7,13] It is also reported that E4 and E5 are related to MG+E2 and MG+E3, respectively, where MG is the As_{Ga}-related donor level.[36] However, this could not be examined due to the absence of E3 in this work.

(iii) *P1, P4 and P6*

The drop in the P1 peak with increasing irradiation dose does not necessarily imply that the concentration of this level is reduced. Martin *et. al.*[22] proposed that the interaction with shallower traps can result in perturbation of the electrical properties of the isolated EL2 defect. Their model assumes that, after irradiation, EL2 is surrounded by shallower traps such as EL6 with distances of ~10 nm, which is of the order of the size of a damage cluster along an ion path. The proximity of these shallower traps strongly modifies the emission path of the captured electrons from EL2 to the conduction band *via* a phonon-assisted tunnelling process. This process then gives rise to the broad, non-exponential, U-band. Hence, after complete annealing of the U-band, one should recover the properties of isolated EL2. Of course, it is to be expected that the degree of perturbation to isolated EL2 (or the magnitude of the U-band) is a function of the ion mass, where a heavier ion should generate a denser damage cluster than a lighter ion. The observed behaviour of P1, P4 and P6 as a function of dose and annealing temperature is consistent with the model of Martin *et. al.*[22] Proton irradiation generates additional P1 (EL2) because its DLTS peak is more intense than the starting material. When the concentration of P6 (EL6) reaches a significant level (i.e. when the dose is high enough to form stable defect clusters), P6 and P1 may start to interact, resulting in a drop in the P1 peak and an increase in P4 (U-band). However, in the case of proton irradiation, the degree of interaction (and hence the magnitude of P4) is minimal, as compared to other heavier ions such as O or Si (see next sections), but nevertheless is significant enough to be observed. The annihilation of P6 (EL6) during annealing also leads to the disappearance of P4 (U-band), which is consistent with the model proposed by Martin *et. al.*[22] However, there are minor differences between our observations and the Martin model. The concentration of P6 (EL6) is about an order of magnitude less than the reduction in the P1 (EL2) peak. It is also possible that P1 (EL2) may be interacting with other defects of the opposite charge state (such as Ga_{As} for example) to mask its electrical properties. Also, the annihilation of P6 (EL6) and P4 (U-band) at 400-500 °C does not lead to the recovery of the P1 (EL2) peak to its initial value. In fact, annealing at ~600 °C (way above the temperature required for complete annihilation of both EL6 and the U-band) is needed to recover P1 to its initial value.

Since isolated EL2 is known to be stable to temperatures in excess of 800 °C,[40] it is possible that EL2 may start to anneal at lower temperatures in the presence of other irradiation-induced defects. However, P1 is observed to be stable up to 500 °C, where most other defects have been annealed out. Thus, the radiation-enhanced recombination process is not plausible. Furthermore, it has been reported that additional EL2 defects introduced in neutron-irradiated, plastically deformed and low temperature MBE grown GaAs, are known to anneal in the temperature range of 500-600 °C.[41] Therefore, from these results, it is proposed that, there is an equilibrium concentration of EL2 after growth which is stable to temperatures in excess of 800 °C. Additional EL2-related defects may be created by one of the means mentioned above but are thermodynamically less stable than the grown-in defects since the equilibrium concentration is exceeded. These excess antisites may then acquire sufficient energy at moderate temperatures to anneal out, regardless of any radiation-enhanced recombination process. Although the signature of P1 resembles that of EL2, the annealing behaviour suggests that the former is only related to the EL2 defect. Despite much effort studying the EL2 defect over the past two decades or so, the exact nature of this defect is still quite uncertain. However, it has generally been accepted that EL2 is a defect associated with the pairing of an As antisite and another point defect (i.e As_{Ga}-X). It is therefore quite likely that P1 is also an As antisite defect but with most likely a different point defect neighbour.

The dose and annealing temperature dependence of P6 (EL6) and P4 (U-band) are almost identical, suggesting that P6 (EL6) is very efficient in modifying the emission properties of P1 (EL2-related). The acceptor-like nature of P6 (EL6) in complementing the donor-like EL2 may be the major contributing factor. Both P6 (EL6) and P4 (U-band) anneal at 400-500 °C, in good agreement with the behaviour reported by Martin *et. al.*[22]

(iv) *Carrier removal*

Carrier removal following proton bombardment is primarily due to acceptor-like traps and neutral complexes involving impurities. The acceptor-like traps include P6 (EL6) and other traps lower than 0.3 eV from the conduction band, such as the P8 (E1) and and P7 (E2) traps. Temperature dependence measurements of the carrier profiles [Figs. 5-9(a) and (b)] indicate that P8 (E1) is acceptor-like. E1 and E2 have been associated with the same type of defect but with different charge state (i.e. E1=E2+electron).[7] Thus, although the nature of the P7 (E2) level could not be determined from the C-V profiles, this suggests that P7 (E2) is also an acceptor-like trap. The behaviour of carrier compensation involves a complex balance between a variety of traps, including neutral complexes involving impurities, which are not directly

measurable by DLTS. At a particular temperature, donor-like traps may be ionised and thus negate the compensating effect of acceptor-like traps. At moderate temperatures, both acceptor- and donor-like traps may be annealed but higher annealing temperatures (~600 °C) are required to dissociate neutral complexes, thus leading to a recovery in the initial free-carrier concentration.

5.4 Deep levels created by oxygen and silicon in n-type GaAs

5.4.1 Results

In contrast to the rather distinct DLTS peaks created by proton irradiation, the use of heavier ions results in broader DLTS peaks and the resulting spectra are difficult to analyse. The results of 1.2 MeV oxygen implantation in lightly doped (~7×10^{15} cm^{-3}) *n*-type GaAs are shown in Fig. 5-12 for four different doses. The only observed electrically active defect in the starting material is again the EL2 level, with a concentration of the order of 10^{12} cm^{-3}. The main features of the spectra include a very broad and intense peak in the temperature range of 180-280 K (U-band) and a shoulder at the temperature of ~150 K. An extraction of the emission rate of the latter peak indicates that it is most likely the EL6 level. However, no significant change in the EL2 concentration is observed as the implantation dose is increased. The broad U-band is observed even in the lowest dose of 5 x 10^8 cm^{-2}. Although the creation rate of the U-band is fairly linear with dose, the creation rate of EL6 appears to level off (saturate) at higher doses as illustrated in Fig. 5-13. Furthermore, the creation rate of EL6 is 2-4 times slower than that of the U-band.

The annealing behaviour of the deep levels is depicted in Fig. 5-14 for a sample implanted with 1×10^9 cm^{-2} of oxygen. Very little change with a small increase in the EL2 peak is observed in the shape of the DLTS spectrum following an anneal at 200 °C. However, there is a significant reduction of the EL6 concentration. At 400 °C, a significant reduction in the U-band concentration is observed, accompanied by a further slight increase of the EL2 peak. Although most of the EL6 peak is annealed at this temperature, a distinct peak is observed around 170 K. Due to the overlap of this new peak with the remainder of EL6 and the U-band, accurate determination of it is difficult, but it is most likely the EL5 peak observed in the proton implanted samples. It is also most likely that EL5 is present after oxygen implantation rather than evolved during annealing and its peak is obscured by the broad and intense U-band (Fig. 5-12). Since

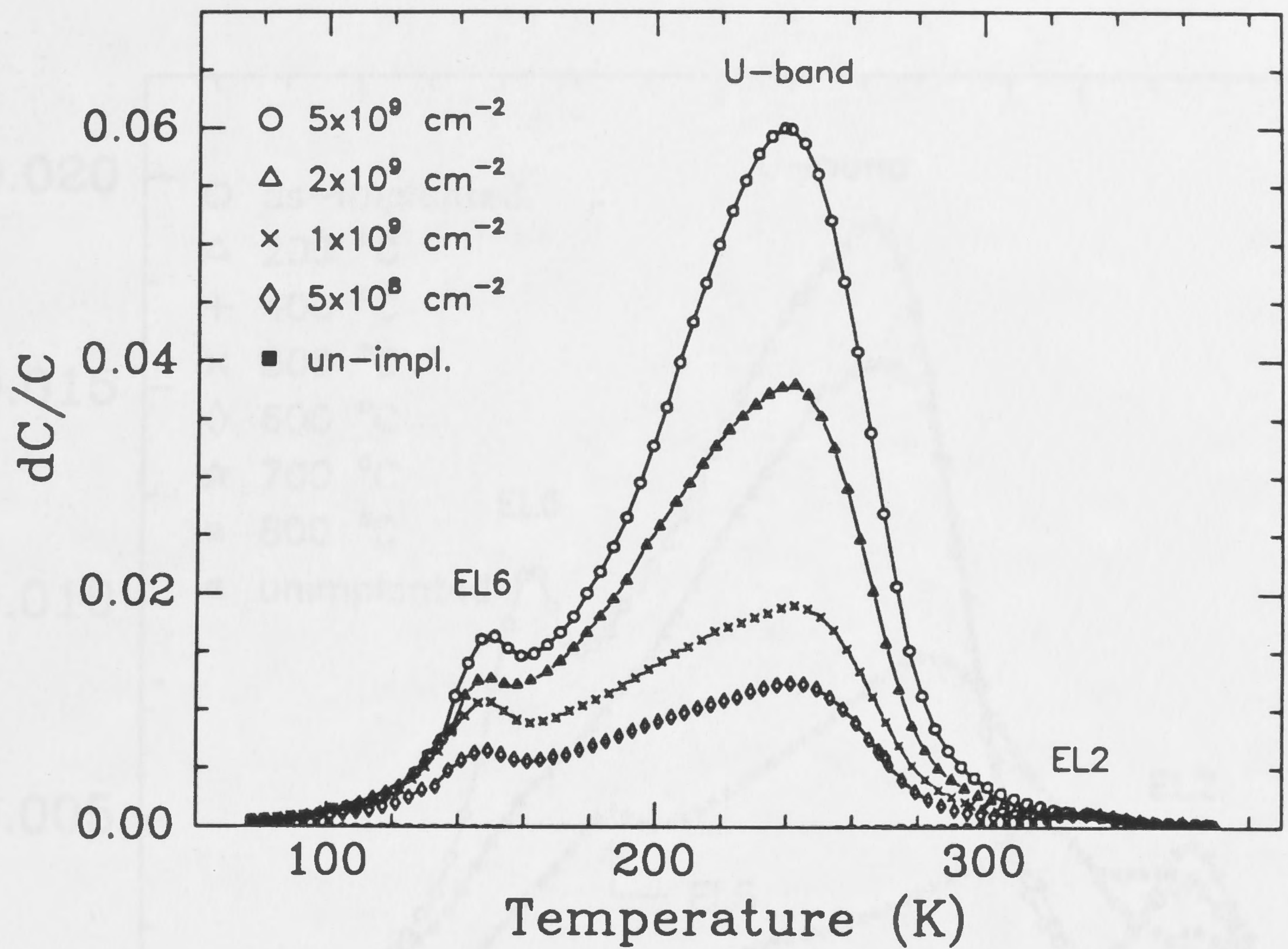

Fig. 5-12 DLTS spectra of samples implanted with oxygen ions at various doses. The spectrum of the unimplanted sample is also shown for comparison (rate window of 0.98 s^{-1}).

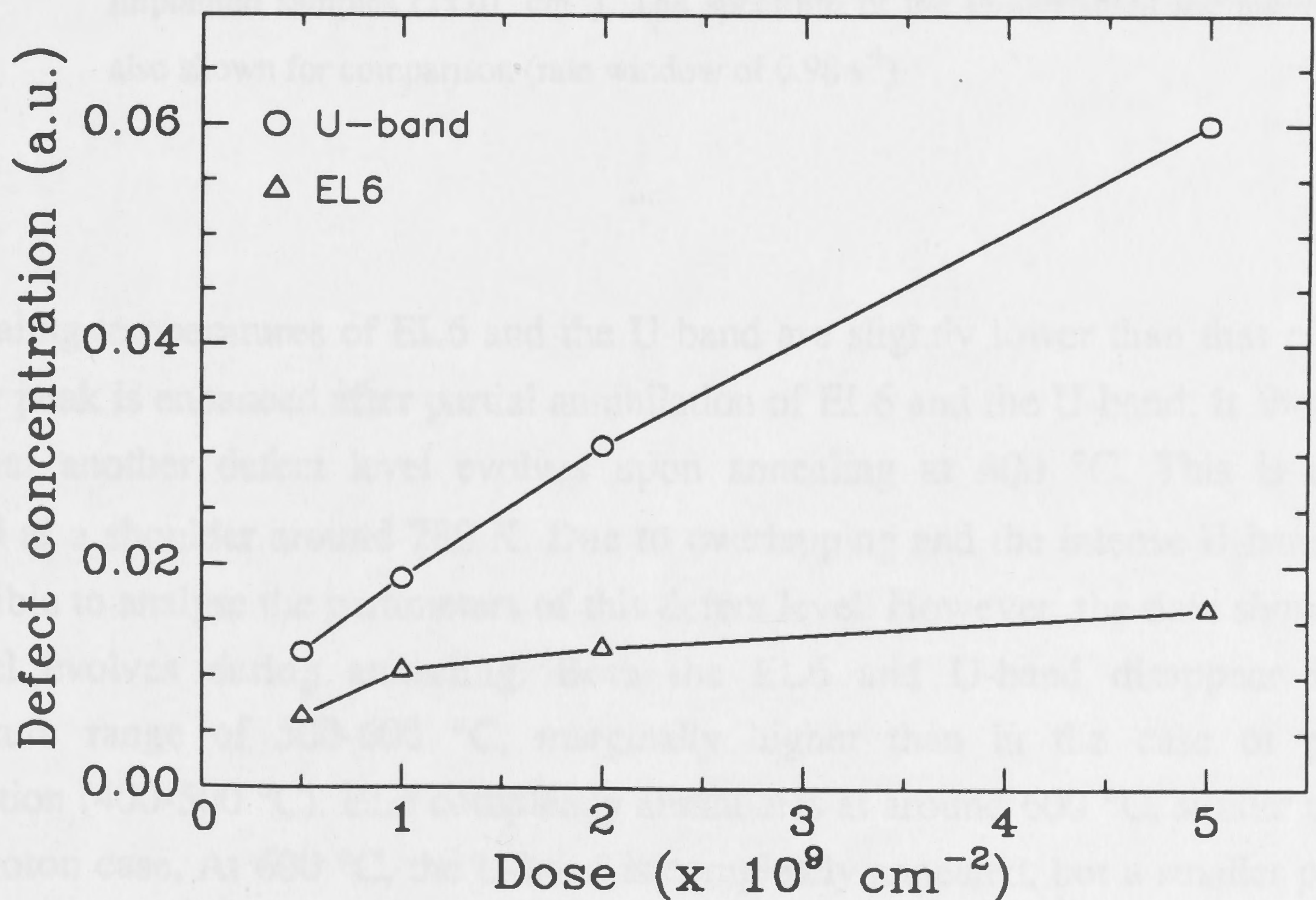

Fig. 5-13 A plot showing the dose dependence of the broad U-band and EL6 for oxygen implanted samples.

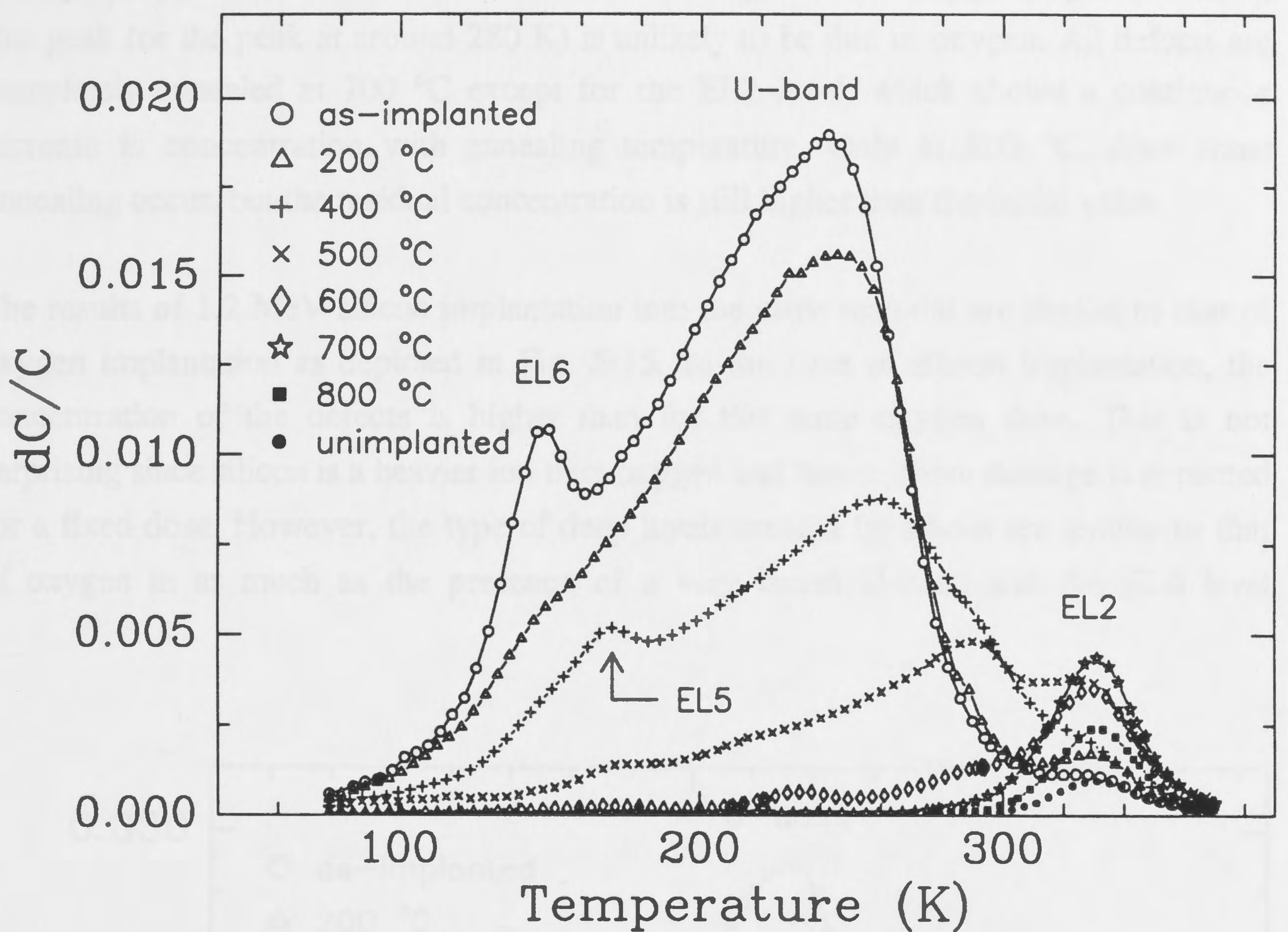

Fig. 5-14 DLTS spectra showing the annealing behaviour of the traps in oxygen implanted samples ($1x10^9$ cm^{-2}). The spectrum of the unimplanted sample is also shown for comparison (rate window of 0.98 s^{-1}).

the annealing temperatures of EL6 and the U-band are slightly lower than that of EL5, the latter peak is enhanced after partial annihilation of EL6 and the U-band. It should be noted that another defect level evolves upon annealing at 400 °C. This is clearly observed as a shoulder around 280 K. Due to overlapping and the intense U-band, it is not possible to analyse the parameters of this defect level. However, the data shows that this level evolves during annealing. Both the EL6 and U-band disappear in the temperature range of 500-600 °C, marginally higher than in the case of proton implantation (400-500 °C). EL5 completely annihilates at around 600 °C, similar to that of the proton case. At 600 °C, the U-band is completely annealed, but a smaller peak is observed at around 230 K, with an energy level, E_c, of 0.72 eV from the conduction band and an apparent capture cross-section, σ_{na}, of $2.06x10^{-10}$ cm^{-2}. However, it is impossible to determine if this level exists after implantation or whether it evolved upon annealing. Although various reports[42-45] have mentioned that an oxygen-related deep

level peak appears next to the EL2 level in both as-grown and oxygen-implanted GaAs, this peak (or the peak at around 280 K) is unlikely to be due to oxygen. All defects are completely annealed at 700 °C except for the EL2 level, which shows a continuous increase in concentration with annealing temperature. Only at 800 °C, does some annealing occur, but the residual concentration is still higher than the initial value.

The results of 1.2 MeV silicon implantation into the same material are similar to that of oxygen implantation as depicted in Fig. 5-15. In the case of silicon implantation, the concentration of the defects is higher than for the same oxygen dose. This is not surprising since silicon is a heavier ion than oxygen and hence, more damage is expected for a fixed dose. However, the type of deep levels created by silicon are similar to that of oxygen in as much as the presence of a very broad U-band and the EL6 level

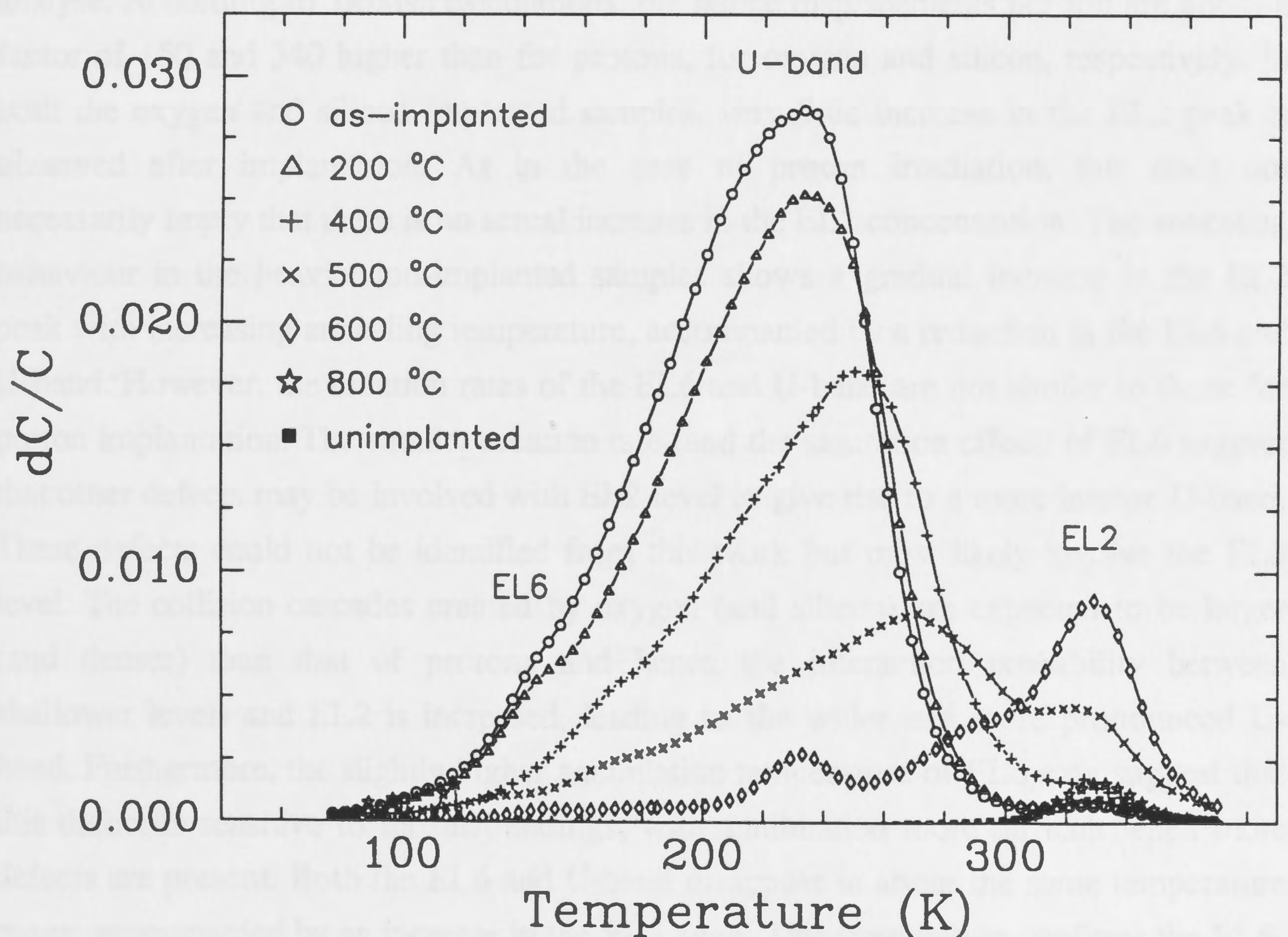

Fig. 5-15 DLTS spectra of showing the annealing behaviour of the traps in silicon implanted samples (1×10^{9} cm^{-2}). The spectrum of the unimplanted sample is also shown for comparison (rate window of 0.98 s^{-1}).

dominate. However, the EL6 peak in this case is not as pronounced as that for oxygen implantation, most likely due to the broader U-band associated with silicon implantation. Very little change in the EL2 concentration is observed after implantation. Similar annealing behaviour of these traps in comparison with the oxygen implantation is also observed in this case. A new peak (at 280 K) evolves during annealing at temperatures ≥ 400 °C with the emergence of another peak upon 600 °C annealing. This level has an identical signature ($E_c = 0.72$, $\sigma_a = 2.06 \times 10^{-10}$ cm^{-2}) to that of the peak observed in the oxygen implanted sample which is annealed at 600 °C. This observation provides strong evidence that this peak is not associated with oxygen, as pointed out earlier.

5.4.2 *Discussion*

The use of (heavier) ions generally results in broad DLTS spectra which are difficult to analyse. According to TRIM90 calculations, the lattice displacements per ion are about a factor of 150 and 340 higher than for protons, for oxygen and silicon, respectively. In both the oxygen and silicon implanted samples, very little increase in the EL2 peak is observed after implantation. As in the case of proton irradiation, this does not necessarily imply that there is no actual increase in the EL2 concentration. The annealing behaviour in the heavier ion-implanted samples shows a gradual increase in the EL2 peak with increasing annealing temperature, accompanied by a reduction in the EL6 and U-band. However, the creation rates of the EL6 and U-band are not similar to those for proton implantation. The smaller creation rate (and the saturation effect) of EL6 suggest that other defects may be involved with EL2 level to give rise to a more intense U-band. These defects could not be identified from this work but most likely involve the EL5 level. The collision cascades created by oxygen (and silicon) are expected to be larger (and denser) than that of protons and hence the interaction probability between shallower levels and EL2 is increased, leading to the wider and more pronounced U-band. Furthermore, the slightly higher annihilation temperature of EL6 may suggest that this defect is sensitive to its surroundings, with annihilation more difficult when more defects are present. Both the EL6 and U-band disappear in about the same temperature range, accompanied by an increase in the EL2 peak. This observation confirms the EL6-EL2 interaction model for the nature of the U-band. The increase of the EL2 peak with annealing temperature indicates that additional EL2 may be created after implantation. Only above 700 °C do the additional EL2 defects begin to anneal, in contrast to proton irradiation where annealing occurs at 600 °C. Again, this effect is most likely due to the formation of more stable defects (such as clusters, impurity-defect complexes) caused by the heavier ions.

Although the EL5 level is not observed after implantation, partial annealing of EL6 and the U-band reveal the presence of this trap. It is unlikely that EL5 is a defect that evolves during annealing since this defect is observed in the proton implanted samples. Moreover, this defect starts to anneal at temperatures above 200 °C, again consistent with the behaviour of EL5 in proton irradiated samples. The signal from this peak is not observed in the as-implanted sample as a result of it being masked by EL6 and the U-band. The non-saturation behaviour of EL5 (Fig. 5-6) confirms that it is an impurity-related defect. The impurity is most likely to be the Si dopant since its concentration in this case is higher than the previous undoped, proton implanted samples.

The evolution of a new defect level is observed upon annealing (at 280 K in the DLTS temperature scan). Determination of this level is impossible due to the overlapping of several traps. However, it is most likely that this level is not formed during implantation but evolved during annealing. The origin of another peak after 600 °C annealing is also unknown due to the strong U-band after implantation. Although oxygen-related peaks have previously been reported to appear in oxygen implanted GaAs,[42,43] these two defects are not related to oxygen complexes since the same defects are observed in Si implanted samples. Furthermore, in these previous reports, the oxygen doses were much higher than in the present studies. Thus, the microscopic nature of these defects must be intrinsic to the material rather than related to oxygen.

A report by Tin *et. al.*[47] argued that oxygen does not play a role in the defect chemistry of the implanted region although moderate to high doses were used. In their report, however, only the near surface regions were probed although the energy of the O ions was 2 MeV which extends beyond these regions. Thus, from the results of this chapter, it is believed that, although implanted oxygen does form complexes with the implantation-induced defects, at low implantation doses ($\leq 10^{10}$ cm^{-2}) the observed defects created are all intrinsic to the material and not related with the implanted ions. This is evident from similarities in defect creation and annealing between oxygen and silicon implantations.

5.6 Conclusions

Ion implantation at low doses has been used to study the generation of point defects and carrier compensation in n-type GaAs grown by MOCVD. Proton irradiations at these doses provide useful insight into the creation and annealing behaviour of the electron traps as compared to earlier studies where higher doses and/or heavier ion species were used. This often makes the material highly resistive and annealing is often required before any sensible measurements may be done. Six electron traps are identified from proton implantation, namely, E2, EL6, EL5, E4 , E5 and additional EL2. Furthermore, a broad U-band is observed and is associated with the interaction between EL2 and the EL6 levels. The additional EL2 levels created after implantation appear to be thermally less stable than the grown-in EL2. Carrier removal in proton implanted GaAs appears to result from both the acceptor-like E1 and E2 traps, and neutral-impurity complexes. However, complete recovery of the electrical characteristics may be achieved after annealing at 600 °C. Thus, the use of proton implantation to induce carrier compensation and isolation in GaAs should be avoided if the device processing steps include thermal treatment ≥ 600 °C.

In contrast, the defect properties of low dose oxygen or silicon implanted GaAs are more stable (up to 800 °C) than in the case of protons. Surprisingly, both oxygen and silicon implantations (in this dose regime) produced the same types of defects. The DLTS spectra are dominated by a very broad and highly non-exponential U-band. Three other deep levels, EL6 EL5 and additional EL2, are also created after implantation. During annealing the presence of two other defect levels is observed but their origins could not be determined due to the domination of the U-band after implantation. The U-band is broader than in the case of proton implantation and is also associated with the interaction between EL2 and other shallower levels. The additional EL2 level starts to anneal ≥ 700 °C. The defects created by implantation in this dose regime are all associated with intrinsic point defects and oxygen-related levels are not observed.

In concentrating on low dose proton implantation, it is possible to obtain a much clearer picture of defect creation during implantation. Although the results obtained from oxygen and silicon implantations are somewhat more complicated, they do provide some insight into the differences and similarities with that of proton implantation. Of particularly importance are the results of the annealing behaviour of these defects, as they provide a firm platform to the understanding of the electrical properties of this material for the applications of ion implantation in the following chapters.

References

[1] D.V. Lang, "Deep-level transient spectroscopy : A new method to characterize traps in semiconductors," *J. Appl. Phys.* **45**, 3023-3032 (1974).

[2] G.M. Martin, A. Mitonneau and A. Mircea, "Electron traps in bulk and epitaxial GaAs crystals," *Electron. Lett.* **13**, 191-192 (1977).

[3] A. Mitonneau, G.M. Martin and A. Mircea, "Hole traps in bulk and epitaxial GaAs crystals," *Electron. Lett.* **13**, 666-667 (1977).

[4] A.R. Peaker, J. Nicholas, M.R. Brozel, P.D. Augustus, S. Yasuami, J.M. Baranowski and R. Murray, "Defect, deep levels and their interaction," in *Properties of Gallium Arsenide, 2nd edition, EMIS Datareview Series, No. 2*, Chp. 13, 283-338, Inspec Publication (1990).

[5] J.C. Bourgoin, H.J. von Bardeleben and D. Stiévenard, "Native defects in gallium arsenide," *J. Appl. Phys.* **64**, R65-R91 (1988).

[6] D.V. Lang, "Review of radiation-induced defects in III-V compounds," *Inst. Phys. Conf. Ser.* **31**, 70-96 (1977).

[7] D. Pons and J.C. Bourgoin, "Irradiation-induced defects in GaAs," *J. Phys. C : Solid State Phys.* **16**, 3839-3871 (1985).

[8] E. Garmire, H. Stoll, A. Yariv and R.G. Hunsperger, "Optical waveguiding in proton-implanted GaAs," *Appl. Phys. Lett.* **21**, 87-88 (1972).

[9] D.E. Davies, J.K. Kennedy and A.C. Yang, "Compensation from implantation in GaAs," *Appl. Phys. Lett.* **23**, 615-616 (1973).

[10] D.C. D'Avanzo, "Proton isolation for GaAs integrated circuits," *IEEE Trans. Electron Devices* **ED-29**, 1051-1059 (1982).

[11] I.H. Goodridge, "Carrier concentration in doped and undoped, epitaxial GaAs" in *Properties of Gallium Arsenide, 2nd edition, EMIS Datareview Series, No. 2*, Chp. 3.3, 53-57, Inspec Publication (1990) and references therein.

[12] J.F. Ziegler, J.P. Biersack and U. Littmark, *The Stopping and Range of Ions in Solids*, vol. 1, Pergamon, New York (1989).

[13] D. Pons, A. Mircea, A. Mitonneau and G.M. Martin, "Electron traps in irradiated GaAs : comparison with native defects," *Inst. Phys. Conf. Ser.* **46**, 352-359 (1979).

[14] D. Pons, A. Mircea and J. Bourgoin, "An annealing study of electron irradiation-induced defects in GaAs," *J. Appl. Phys.* **51**, 4150-4157 (1980).

[15] D. Pons, P.M. Mooney and J.C. Bourgoin, "Energy dependence of deep level introduction in electron irradiated GaAs," *J. Appl. Phys.* **51**, 2038-2042 (1980).

[16] D. Stievenard, X. Boddaert, J.C. Bourgoin and H.J. von Bardeleben, "Behavior of electron-irradiation-induced defects in GaAs," *Phys. Rev. B* **41**, 5271-5279 (1990).

[17] G. Guillot, S. Loualiche, A. Nouailhat and G.M. Martin, "Study of defect states by transient capacitance methods in proton irradiated GaAs at low temperature," *Inst. Phys. Conf. Ser.* **59**, 323-328 (1981).

[18] Y. Yuba, K. Gamo, K. Murakami and S. Namba, "Proton implantation damage in GaAs studied by capacitance transient spectroscopy," *Inst. Phys. Conf. Ser.* **59**, 329-334 (1981).

[19] S.S. Li, T.T. Chiu, D.W. Schoenfeld, "Defect characterization and thermal annealing study of 200 keV proton irradiated n-GaAs LPE layers," *Inst. Phys. Conf. Ser.* **59**, 335-340 (1981).

[20] M. Roux and P. André, "Radiation-induced traps in low-energy proton-irradiated GaAs solar cells," *J. Appl. Phys.* **57**, 5192-5195 (1985).

[21] F.H. Eisen, K. Bachem, E. Klausman, K. Koehler and R. Haddad, "Ion irradiaton damage in n-type GaAs in comparison with its electron irradiation damage," *J. Appl. Phys.* **72**, 5593-5601 (1992).

[22] G.M. Martin, E. Estève, P. Langlade and S. Makram-Ebeid, "Kinetics of formation of the midgap donor EL2 in neutron irradiated GaAs materials," *J. Appl. Phys.* **56**, 2655-2657 (1984).

[23] G.M. Martin and S. Makram-Ebeid, "Manifestation of deep levels point defects in GaAs," *Physica* **116B**, 371-383 (1982).

[24] J. Samitier, J.R. Morante, L. Giraudet and S. Gourrier, "Optical behavior of the U-band in relation to EL2 and EL6 levels in boron-implanted GaAs," *Appl. Phys. Lett.* **48**, 1138-1140 (1986).

[25] J.R. Morante, A. Pérez-Rodríguez, J. Samitier and A. Romano-Rodríguez, "On the artificial creation of the EL2 center by means of boron implantation in gallium arsenide," *J. Appl. Phys.* **70**, 4202-4210 (1991).

[26] A. Mircea, A. Mittonneau, L. Hollan and A. Brière, "Outdiffusion of deep electron traps in epitaxial GaAs," *Appl. Phys.* **11**, 153-158 (1976).

[27] A. Ashby, G.G. Roberts, D.J. Ashen and J.B. Mullin, "Non-extrinsic conduction in semi-insulating GaAs," *Solid State Commun.* **20**, 61-63 (1976).

[28] M. Henini, B. Tuck and C.J. Paull, "Deep states in GaAs LEC crystals," *Solid State Electron.* **29**, 483-488 (1986).

[29] Y. Kitigawa, N. Noto, T. Takahashi and T. Takaneka, "Electron traps in dislocation-free In-alloyed liquid encapsulated Czochralski GaAs and their annealing properties," *Appl. Phys. Lett.* **48**, 1664-1666 (1986).

[30] S. Makram-Ebeid, "Effect of electric field on deep-level transients in GaAs and GaP," *Appl. Phys. Lett.* **37**, 464-466 (1980).

[31] A. Chantre, G. Vincent and D. Bois, "Deep level optical spectroscopy," *Phys. Rev. B* **23**, 5335-5359 (1981).

[32] A. Goltzené, C. Shwab, J.P. Davies and A. Roizes, "Electrical behavior of fast neutron irradiated semi-insulating GaAs during thermal recovery," *Appl. Phys. Lett.* **49**, 862-864 (1986).

[33] L.C. Kimerling, "Influence of deep traps on the measurement of free-carrier distributions in semiconductors by junction capacitance techniques," *J. Appl. Phys.* **45**, 1839-1845 (1974).

[34] P. Blood, "Carrier removal in deuterium irradiated GaAs," *Inst. Phys. Conf. Ser.* **56**, 251-258 (1980).

[35] P. Blood and J.W. Orton, *The Electrical Characterization of Semiconductors : Majority Carriers and Electron States*," Chp. 6, 266-335 Academic Press, London (1992).

[36] S. Makram-Ebeid and P. Boher, "Defect pairs and clusters related to the EL2 centre in GaAs," *Rev. Phys. Appl.* **23**, 847-862 (1988).

[37] S.T. Lai, B.D. Nener, L. Faraone, A.G. Nassibian and M.A.C. Hotchkis, "Characterization of deep-level defects in GaAs irradiated by 1 MeV electrons," *J. Appl. Phys.* **73**, 640-647 (1993).

[38] D. Stievenard and J.C. Bourgoin, "Impurity and defect interactions in GaAs," *J. Appl. Phys.* **59**, 743-747 (1986).

[39] D. Stievenard and J.C. Bourgoin, "Evaluation of a defect capture cross section for minority carriers : application to GaAs," *J. Appl. Phys.* **59**, 808-812 (1986).

[40] G.M. Martin and S. Makram-Ebeid, "The mid-gap donor level EL2 in GaAs," and G.A. Baraff "The mid-gap donor level EL2 in gallium arsenide : recent developments," in *Deep Centers in Semiconductors : A State-of-the-Art Approach*, S.T. Pantelides, editor, Chp. 6, 457-589, Gordon and Breach Science Publishers, Switzerland (1992) and references therein.

[41] M. Kaminska and E.R. Weber, "Low temperature GaAs : electrical and optical properties," *Mater. Sci. Forum* **83-87**, 1033-1044 (1992) and references therein.

[42] M. Skorowski, "Oxygen in gallium arsenide," in *Deep Centers in Semiconductors : A State-of-the-Art Approach*, S.T. Pantelides, editor, Chp. 4, 379-406, Gordon and Breach Science Publishers, Switzerland (1992) and references therein.

[43] J.W. Huang and T.F. Kuech, "Deep level structure of semi-insulating MOVPE GaAs grown by controlled oxygen incorporation," *Mat. Res. Soc. Symp. Proc.* **325**, 305-310 (1994).

[44] T. Asano, R.D. Atanassov, H. Ishiwara and S. Furukawa, "Formation of thick, thermally-stable high-resistivity-layers in GaAs by oxygen ion implantation," *Jpn. J. Appl. Phys.* **20**, 901-907 (1981).

[45 D.T. Quan, A. Le Bloa, Z. Guennouni and P.N. Favennec, "Characteristics of deep levels in oxygen-implanted and (oxygen+silicon) co-implanted n-GaAs," *Phys. Stat. Sol. (a)* **132**, 145-154 (1992).

[46] C.C. Tin, P.A. Barnes, T.T. Bardin and J.G. Pronko, "Near-surface defects associated with 2.0-MeV $^{16}O^{+}$ ion implantation in n-GaAs," *J. Appl. Phys.* **70**, 739-743 (1991).

Chapter 6

Ion beam-induced intermixing in quantum wells

6.1 Introduction

The discovery of impurity-induced layer disordering (IILD) by Laidig *et. al.*[1] has led to considerable effort in the study of defect diffusion processes and disordering mechanisms in multilayered compound semiconductors.[2] Since then, other techniques, predominantly ion implantation/irradiation[3-26] and cap layer annealing,[26-35] have also been shown to be able to create disordering and intermixing. All these techniques have gained considerable interest in recent years because of their ability to selectively change the properties of multilayered structures by modifying the optical parameters such as the band gap, absorption coefficient and refractive index.[36-42] Hence, these post-growth techniques also provide a simple way of integrating photonic devices of differing functionality onto a single chip.

Although early work in intermixing studies were carried out on superlattice-type structures,[1-11] it was soon extended to quantum well (QW) heterostructures. The clearly defined excitonic energy levels in quantum wells provide a wealth of information about the structures. In this respect, photoluminescence (PL) spectroscopy is a powerful and sensitive technique in the investigation of interdiffusion studies. Furthermore, quantum wells are incorporated into a vast array of optoelectronic devices due to their unique properties in comparison to bulk material. The most studied QW system is the lattice-matched GaAs-AlGaAs, where the absence of strain simplifies the interpretation and analysis of the results. Further insights may also be obtained in the interdiffusion mechanisms without the complexity of pseudomorphic strain.

Intermixing by all the above-mentioned techniques rely on the mechanism of defect and/or impurity enhanced/assisted interdiffusion among the various atomic species across the heterointerfaces. However, the presence of defects and/or impurities is often

undesirable in devices and the introduced defects must be removed or minimised. A high temperature treatment step is therefore usually required to anneal out these undesirable defects and initiate the intermixing process at the same time.

In this chapter, ion irradiation-induced intermixing processes in GaAs-AlGaAs quantum wells will be systematically studied because of the advantages ion irradiation has over the other intermixing methods. As mentioned earlier, the IILD technique is often not desirable in devices because it requires the introduction of additional dopant/impurities such as Si or Zn. Although SiO_x cap annealing offers an alternative impurity-free intermixing technique, this process suffers from the lack of reproducibility and controllability. Furthermore, very often in optoelectronic devices, intermixing is required in deeper regions (> 1 μm). Hence, in the SiO_x cap annealing method, which relies on the diffusion of Ga-vacancies from the surface, higher annealing temperatures and/or annealing times will be required to drive the gallium vacancy (V_{Ga}) flux into the deeper regions. This may, in turn, result in the degradation of electrical/optical properties of the device. Ion irradiation on the other hand is able to circumvent these complications. Precise and controllable incorporation of ions (and hence defects) with great reproducibility is the main advantage of this technology. Also, by carefully selecting the irradiation parameters, such as the ion species, energy, dose and irradiation temperature, the nature of ions and defects may be controlled and introduced at different depths. Furthermore, by using light ions, such as protons, or high energy MeV ions, deeper regions which require intermixing may be reached easily without the need of excessive thermal treatment. Although there have been many ion irradiation-induced GaAs-AlGaAs QW intermixing studies, most of these studies have been concentrated on the measurement of the Al-Ga interdiffusion coefficient/length.[4,6,9,10,13,15-17,20,25] Furthermore, there has only been very little work being carried out to understand the defect formation processes in multilayered structures (such as the QW structures) and the correlation with intermixing. Indeed, it is the major aim of the current study to use the damage/annealing insights from previous chapters to understand and optimise intermixing for optical wavelength shifting applications.

The first part of this chapter will be focused on the use of protons to create defects for intermixing. Protons are known to create only dilute damage cascades with a high concentration of point defects[43,44] which promote intermixing during annealing. Furthermore, as illustrated in the previous chapter and in other reports,[45-47] the defects created by protons anneal at relatively lower temperatures (about 600-650 °C) and hence, the residual defects after annealing (intermixing) may be minimised. Intermixing induced by heavier ions such as oxygen and arsenic will also be compared. Other

parameters critical to the intermixing process, such as irradiation dose, irradiation and annealing temperature and barrier composition are also investigated. Low temperature PL spectroscopy has been used to measure the degree of intermixing.

6.2 Experimental

All samples used for this study were grown on semi-insulating GaAs substrate and the epitaxial layers were nominally undoped. This was done to minimise the effect of dopant enhanced intermixing and also the built-in electric field which will complicate the issue. Four GaAs QWs of various nominal thickness, 1.4 nm (QW1), 2.3 nm (QW2), 4.0 nm (QW3) and 8.5 nm (QW4), were grown by low pressure MOCVD. Each QW was separated by a 50 nm $Al_xGa_{1-x}As$ barrier (x = 0.3, 0.54, 0.75, 1). All growths were initiated by a 0.5 µm GaAs buffer layer and terminated by a 40 nm GaAs layer to prevent the oxidation of Al-rich layers. Ion irradiation was carried out with either 40 keV protons, 280 keV oxygen or 1 MeV arsenic in the dose range of $1x10^{12}$ to $4.3x10^{16}$ cm^{-2} at various temperatures (from room temperature to 300 °C). The ions' energies were chosen such that the peak of the atomic displacement distribution coincides for all ions and lies in the GaAs buffer at a depth of ~350 nm. Therefore, the entire QW structure was subjected to irradiation with less than a factor of two variation of nuclear energy deposition across the wells, as calculated by FASTRIM,[48] (a modified version of TRIM85-90).[49] Half of the samples were masked during irradiation for direct comparison with the unirradiated material and also to minimise the thickness/composition variation across the samples. After irradiation, the samples (both the irradiated and unirradiated halves) were annealed face down on a fresh piece of semi-insulating GaAs (to prevent excessive loss of arsenic from the surface) in a rapid thermal annealer (proximity method). The annealing temperatures and times were in the range of 850-1000 °C and 15-60 s, respectively. Low temperature PL (~12 K) measurements were carried out with an Ar ion laser (514.5 nm) as the excitation source and the luminescence was detected with a silicon photodetector through a monochromator.

6.3 Proton irradiation

6.3.1 GaAs quantum wells with $Al_{0.54}Ga_{0.46}As$ barriers

The PL spectra for samples (with $Al_{0.54}Ga_{0.46}As$ barriers) irradiated with $5x10^{14}$ and $5x10^{15}$ cm^{-2} are shown in Fig. 6-1(a) and (b), respectively. The spectra for the unirradiated portions of the samples are also shown for comparison, and these are identical to those of the as-grown sample, indicating that annealing in itself is not sufficient to induce intermixing. In all cases, the samples have been annealed at 900 °C for 30 s. No PL signal was detected in the as-irradiated sample due to the high level of residual defects after irradiation which act as non-radiative recombination centres for the photoexcited carriers. The sharp peak at around 820 nm corresponds to the emission from the GaAs cap/buffer layer and/or the substrate while the smaller peak at the higher wavelength is due to an impurity-related transition. As illustrated in Fig. 6-1(a), a small blue shift in wavelength is observed in all the four QWs after irradiation and annealing. The recovery of the PL intensities is excellent and comparable to that of the unirradiated sample. (Note that although the PL intensities are in arbitrary units, the irradiated and unirradiated spectra were collected under identical conditions with the same optics setup and hence their intensities may be directly compared). As noted in Fig. 6-1(b), as the irradiation dose is increased by an order of magnitude to $5x10^{15}$ cm^{-2}, very large energy shifts are observed; in particular, QW2 and QW3 having 113 meV and 100 meV shifts, respectively. It is quite surprising that although the irradiation dose is increased by a factor of ten, the recovery of the PL intensities is quite good, only about a factor of two lower than that of the reference sample. Nevertheless, the drop in PL intensities shows that some defects are still present in the samples after annealing.

A plot of the magnitude of energy shift after a 900 °C, 30 s anneal, as a function of irradiation dose is shown in Fig. 6-2 for each of the four QWs. Both the two intermediate wells (QW2 and QW3) recorded very large energy shifts (up to ~200 meV) while the narrowest (shallowest) and the widest (deepest) wells show smaller energy shifts. In all cases, no saturation in the magnitude of the energy shifts is observed even up to a dose of $4.3x10^{16}$ cm^{-2}.

One might expect that the narrowest well (QW1) to show the largest energy shift due to the greatest relative effect that a small perturbation has on a narrow well. However, this is not observed here. In fact, both the narrowest and the widest QWs show similar energy shifts. Although, the displacement density distribution across the QWs is not constant, as calculated by FASTRIM, (Fig. 6-3), there is only about a factor of two

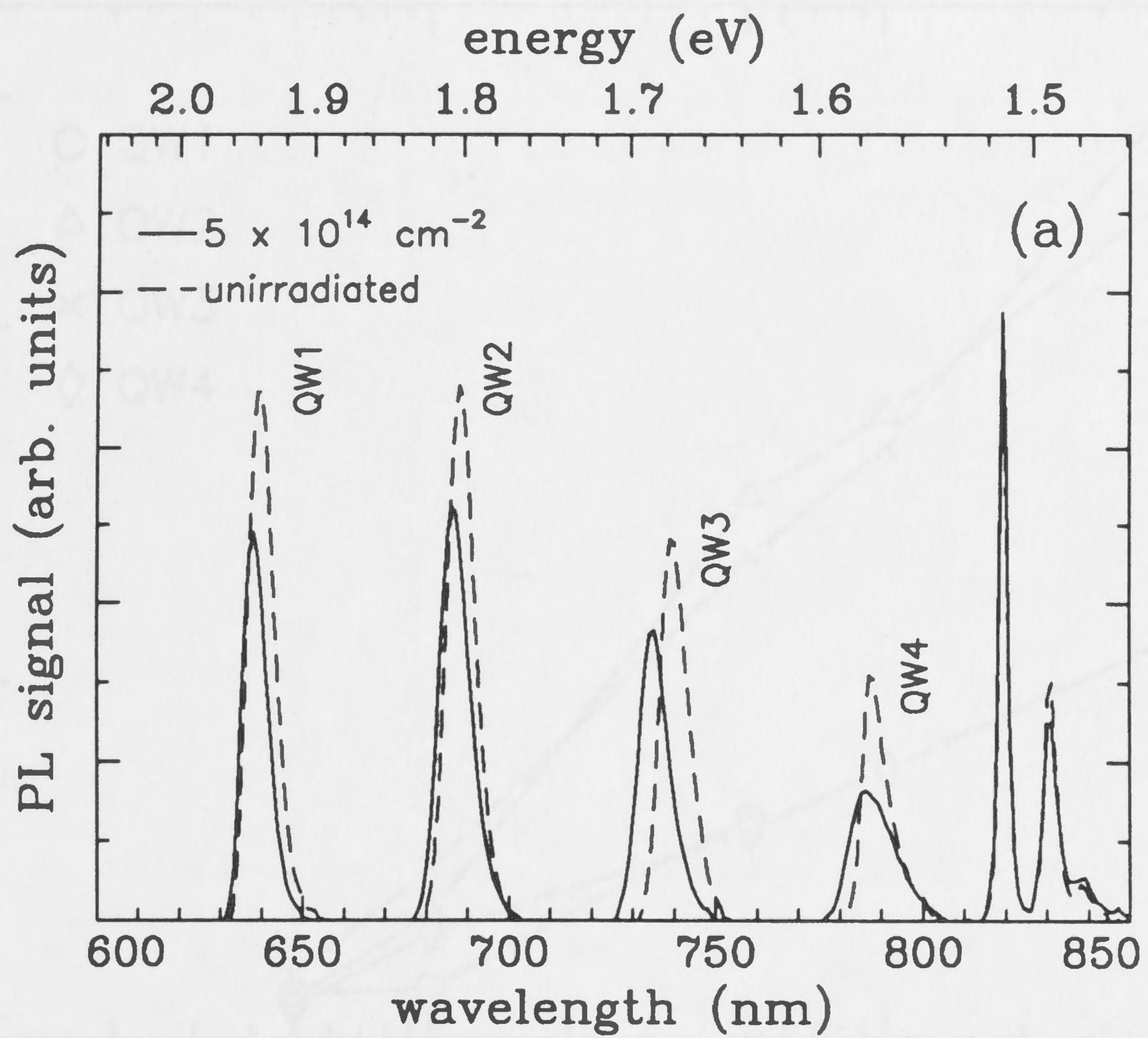

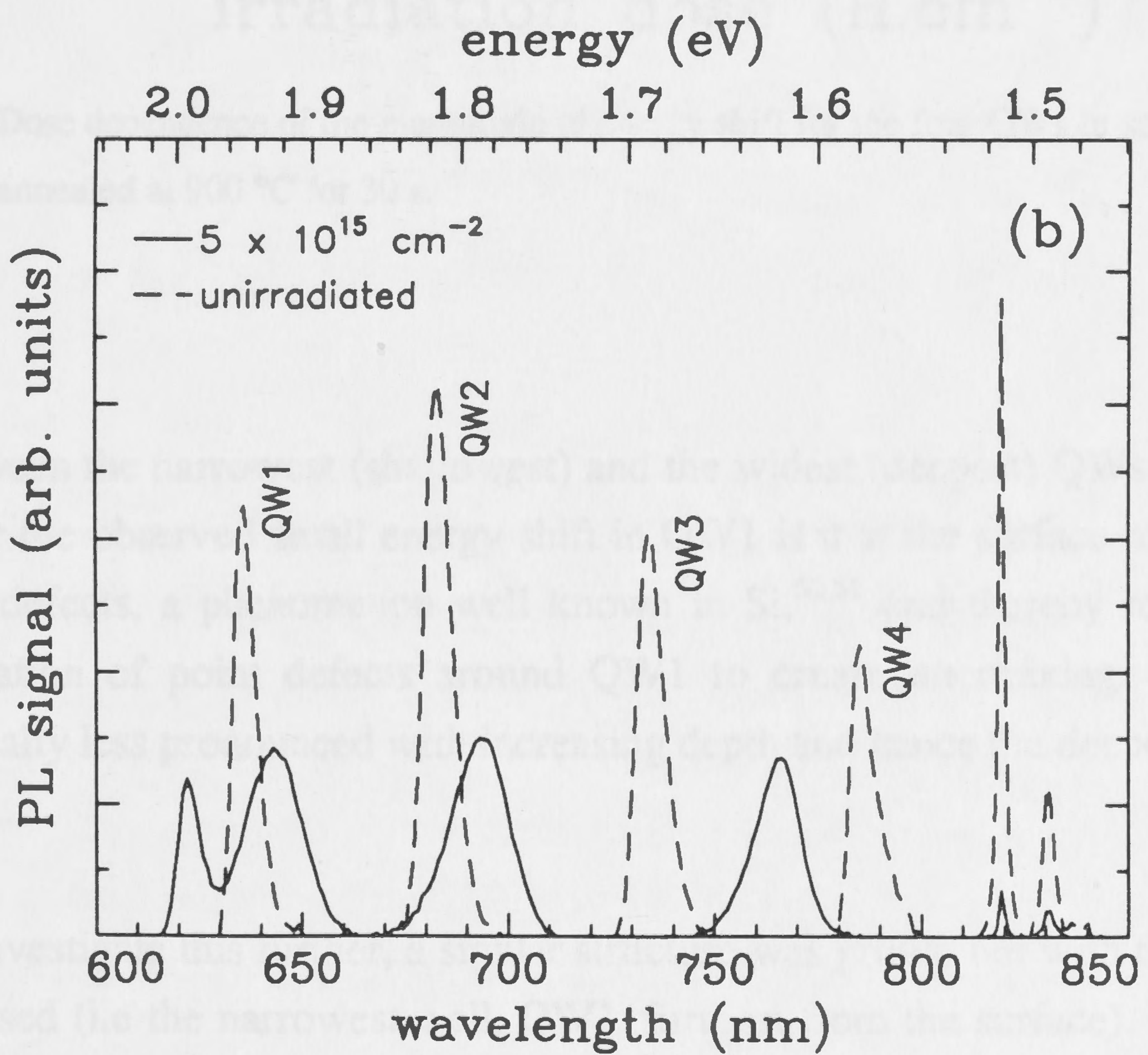

Fig. 6-1 PL spectra of proton irradiated samples to doses of (a) $5x10^{14}$ cm^{-2} and (b) $5x10^{15}$ cm^{-2}. The spectra for the unirradiated samples are also shown for reference. In all cases, the samples have been annealed at 900 °C for 30 s.

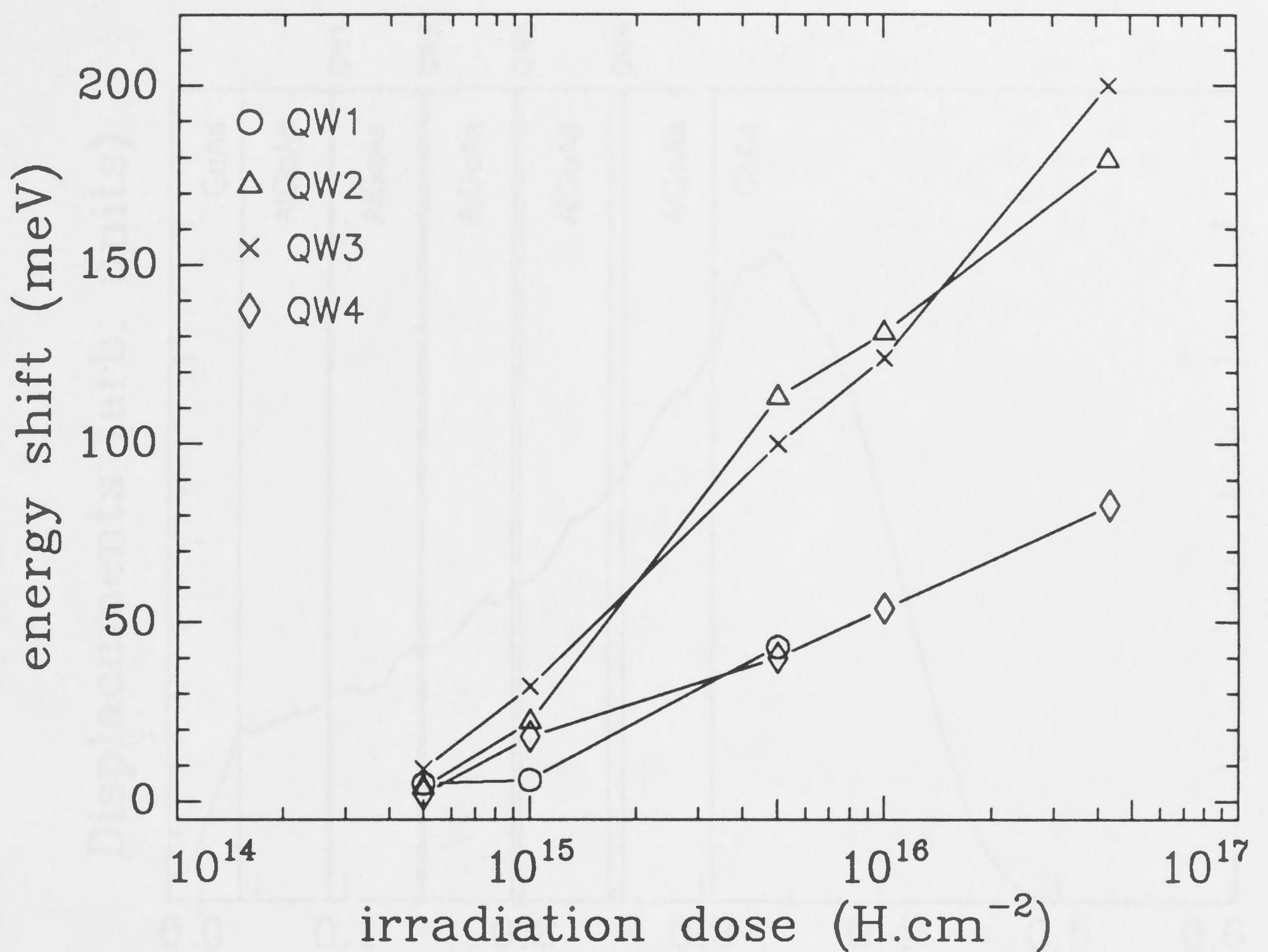

Fig. 6-2 Dose dependence of the magnitude of energy shift for the four QWs in samples annealed at 900 °C for 30 s.

difference between the narrowest (shallowest) and the widest (deepest) QWs. One likely explanation for the observed small energy shift in QW1 is that the surface may act as a sink for point defects, a phenomenon well known in Si,[50,51] and thereby reducing the local concentration of point defects around QW1 to create intermixing. This effect becomes gradually less pronounced with increasing depth and hence the deeper QWs are less affected.

However, to investigate this further, a similar structure was grown but with the order of the QWs reversed (i.e the narrowest well, QW1, furthest from the surface). The results after irradiation ($1x10^{15}$ cm^{-2}) and annealing are shown in Fig. 6-4. The presence of the PL signal from QW1 is clearly seen after irradiation and annealing although the intensity is quite weak. The intensities of QW1 are very weak even before irradiation, due to the absorption from the other three QWs. Very little shift is observed in QW1

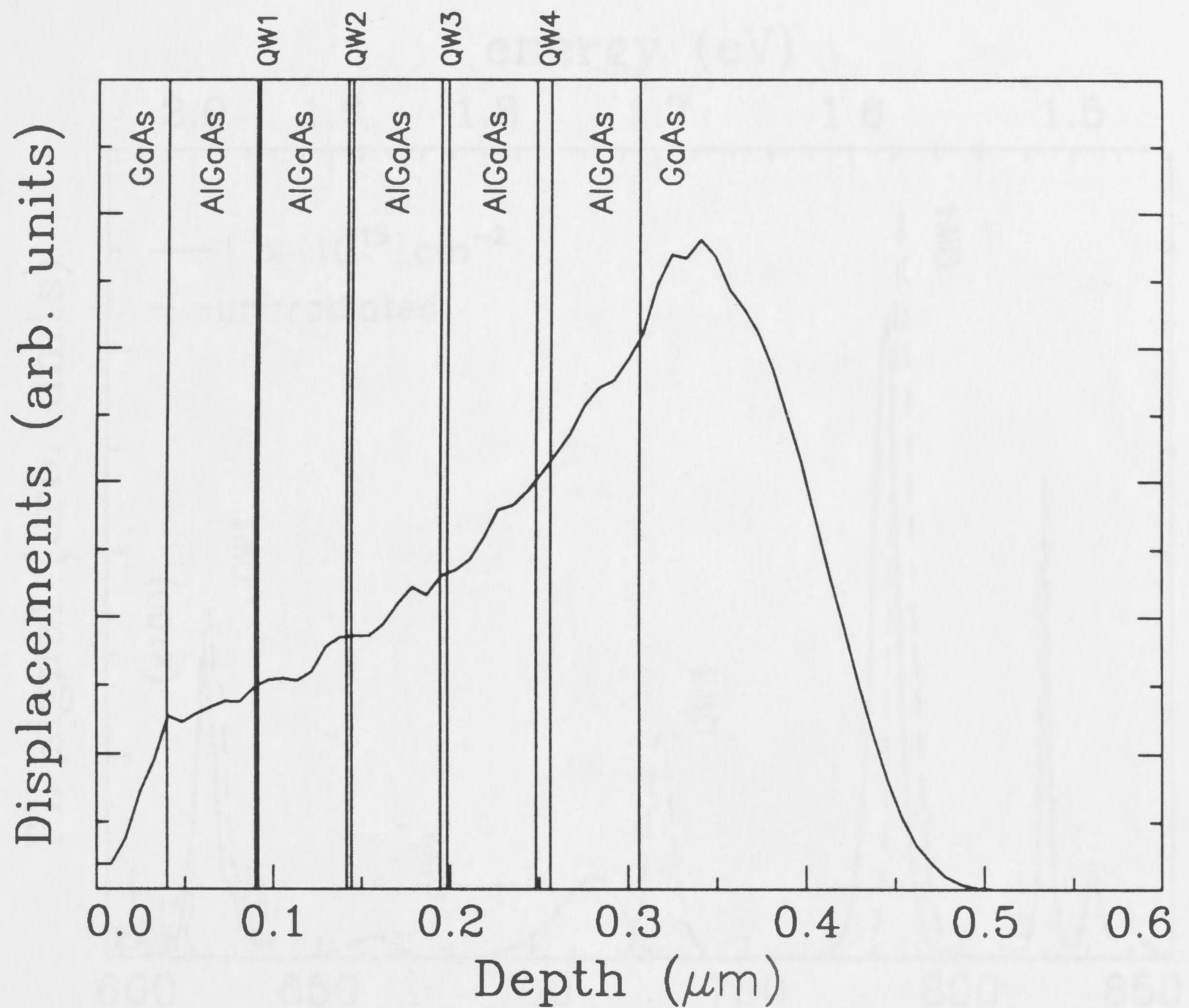

Fig. 6-3 FASTRIM calculations of the displacement density profile for 40 keV H. A schematic of the 4 QW structure is also shown.

(6 meV) although both QW2 and QW3 have quite significant energy shifts (~35 meV). QW4 also recorded a small energy shift due to the thickness of the well. Both in this case and the previous one, the magnitude of energy shift in all the four QWs are quite similar. Thus, the surface effect does not seem to be affecting the magnitude of energy shift. The small energy shift of narrow QWs is due to the higher ground state energy level and this will be discussed later.

It is also interesting to note that at higher irradiation doses (above $5x10^{15}$ cm^{-2}), the PL signal from the narrowest well (QW1) disappears completely. (See the PL spectrum in Fig. 6-8 for room temperature irradiation with a dose of $1x10^{16}$ cm^{-2}). Two immediate explanations for this effect could be that 'complete' intermixing has occurred at this stage (i.e. complete destruction of QW1) or the merging of the PL signal with that of the

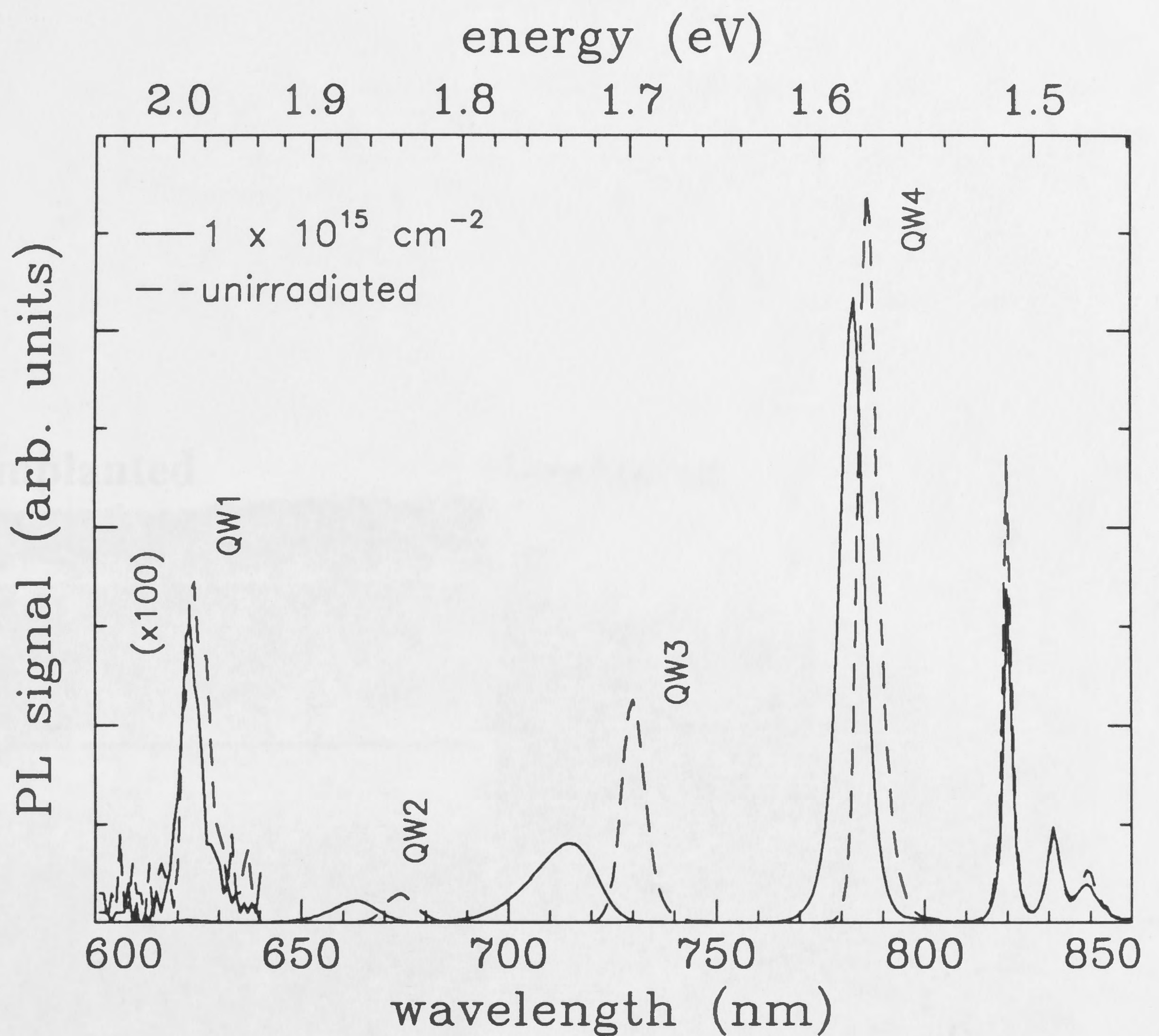

Fig. 6-4 Low temperature (12 K) PL spectra of a reverse-quantum-well structure irradiated with 1×10^{15} cm^{-2}, in which the order of the QWs are reversed (i.e. QW1 furthest from the surface).

adjacent well (QW2) to form a broader peak. The latter explanation is unlikely because the linewidth of the adjacent QW at 1×10^{16} cm^{-2} is comparable to that irradiated at lower doses. Complete intermixing of the narrowest QW has also been ruled out as indicated by the cross-sectional electron microscopy results in Fig. 6-5. Fig. 6-5(a) shows an unirradiated (but annealed) sample where the four quantum wells (arrowed) are obvious while Fig. 6-5(b) shows the sample after irradiation to a dose of 1×10^{16} cm^{-2} and annealing at 900 °C, 30 s. Although the QWs in the irradiated (and annealed) sample appear to be 'diffused', due to intermixing, all four QWs are still observable. Hence, although the PL signal from QW1 has disappeared, this well is still present and not

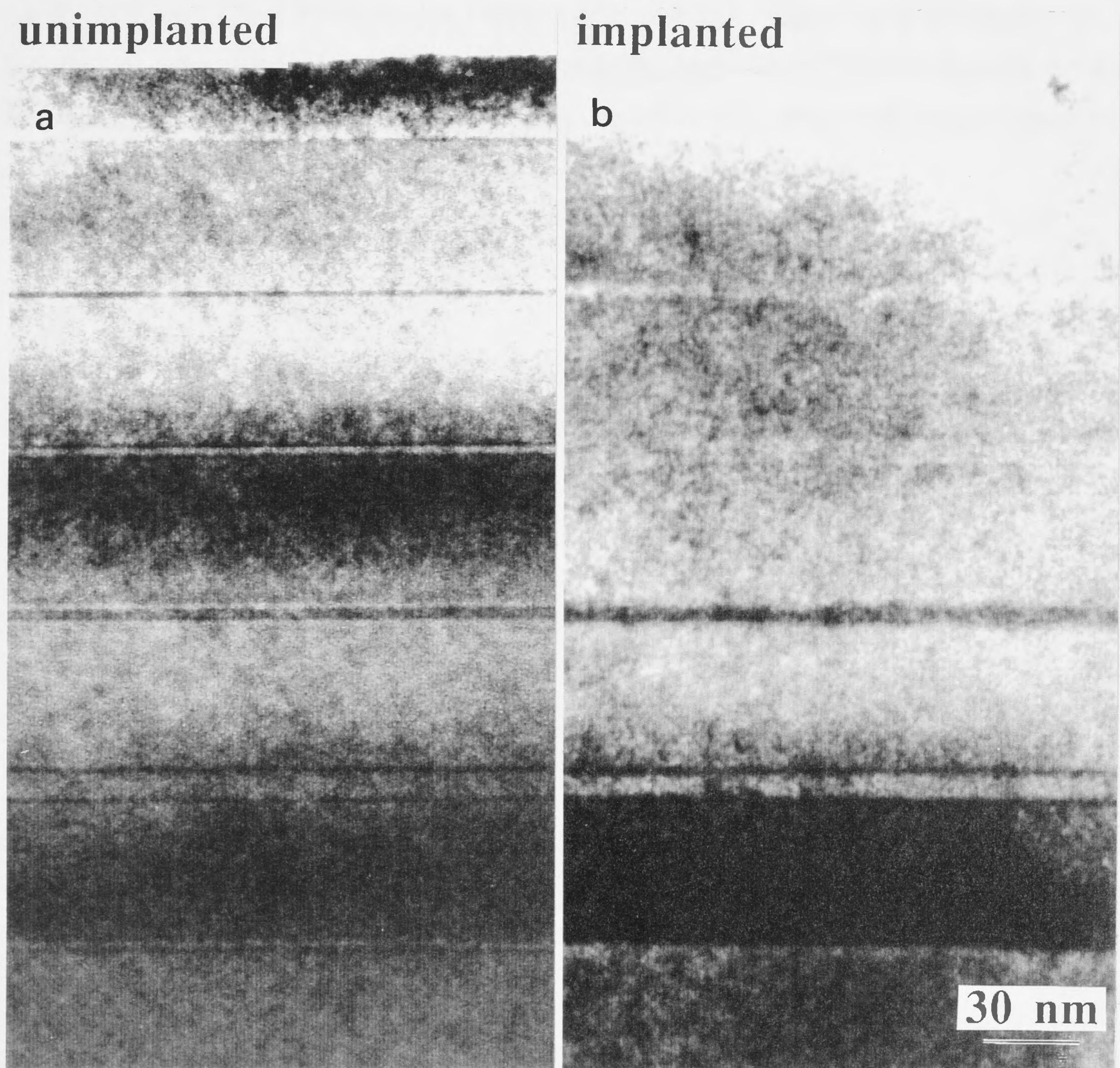

Fig. 6-5 Cross sectional transmission electron micrographs of (a) unimplanted and (b) implanted (1×10^{16} cm^{-2}) samples. Both samples have been annealed at 900 °C for 30 s.

completely intermixed with the AlGaAs barriers. Thus, the more likely explanation of the disappearance of the PL signal from the narrowest well is that, as the well becomes progressively more intermixed, the ground state energy level of the Γ-band in the QW is raised to higher energies. When this level exceeds that of the X-band in the barrier the probability of direct transition decreases, making the QW indirect, similar to the type I to type II transitions reported in some very narrow and indirect quantum wells.[52-54] This effect is further enhanced by the additional scattering of the photoexcited carriers due to the residual defect left in the sample after annealing, as depicted in Fig. 6-6. The disappearance of the PL signal at high irradiation doses has also been reported recently by Kupka and Chen.[25] Although, they attributed this effect to Γ-X scattering, their irradiation dose at which this happened was quite high ($3x10^{14}$ Ga/cm^2). It is most likely that amorphisation of the GaAs QW has occurred at this dose and the disappearance of the PL signal could be due to 'complete' intermixing in their case.

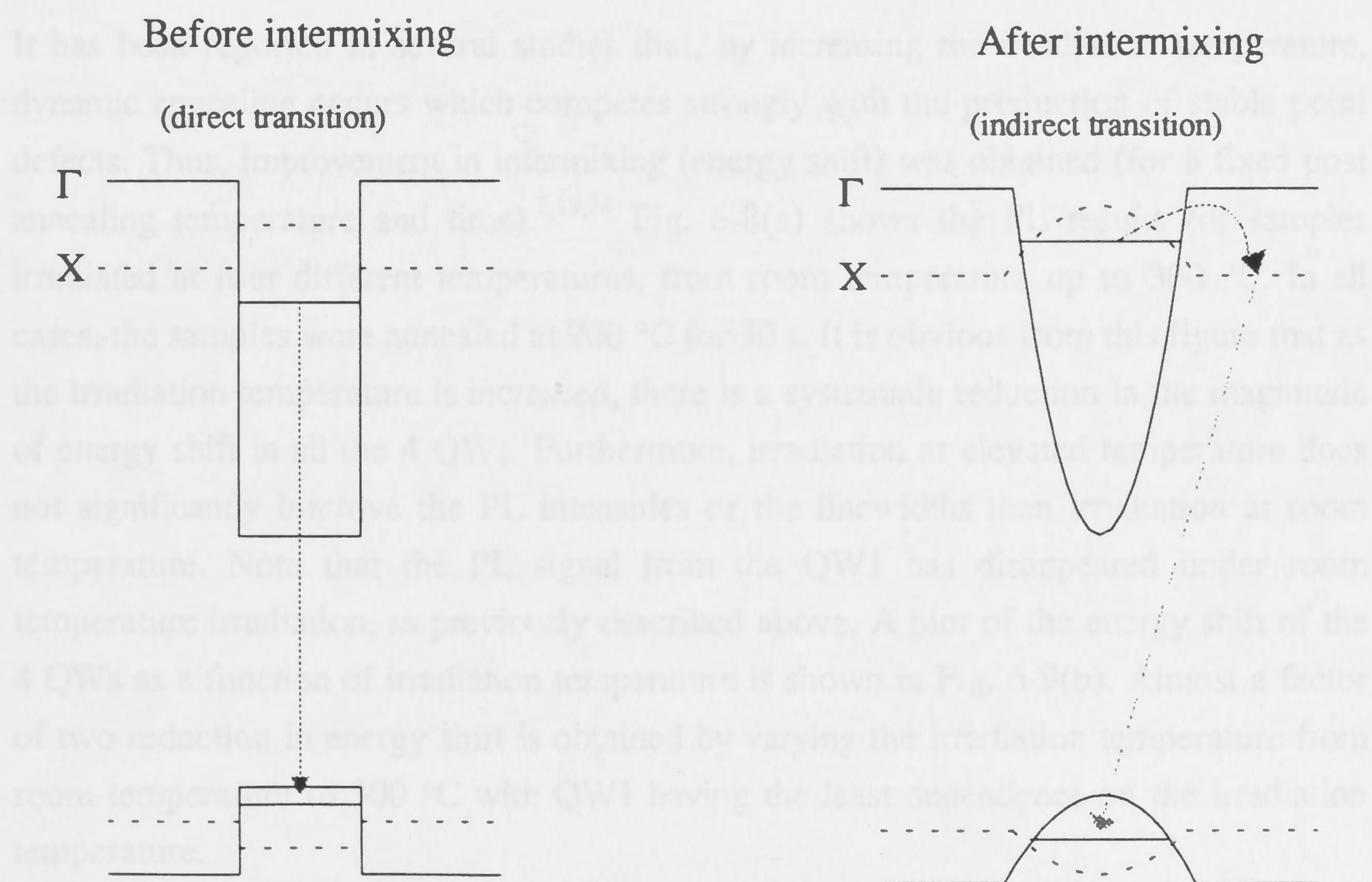

Fig. 6-6 Schematic of the direct to indirect transition of a narrow quantum well after intermixing. The solid lines represent the Γ-band while the broken lines represent the X-band.

The results of the effect of annealing temperature and time are presented in Figs. 6-7(a) and (b), respectively, for a sample irradiated to a dose of $1x10^{16}$ cm^{-2}. At a constant annealing time of 30 s, increasing the annealing temperatures from 850 °C to 950 °C has very little effect on the energy shifts of the two intermediate wells (QW2 and QW3). However, increasing the annealing temperature enhances the magnitude of energy shift of QW4 by about a factor of two from 850 °C to 900 °C. However, at 950 °C, no further improvement of the energy shift is observed in this QW. It should be noted that annealing by the proximity method at 1000 °C may at times lead to surface decomposition as observed in some of the samples. Similar annealing behaviour is also observed by increasing the annealing time at a constant annealing temperature of 900 °C [Fig.6-7(b)]. Almost no additional energy shift is observed beyond 15 s anneal for QW2 and QW3 but further improvement in the magnitude of the energy shift is seen for the deepest well (QW4). This effect can be attributed to the removal of more thermally stable defect loops and clusters which are more likely to be formed towards the end-of-range of the ions, which will be discussed later.

It has been reported in several studies that, by increasing the irradiation temperature, dynamic annealing occurs which competes strongly with the production of stable point defects. Thus, improvement in intermixing (energy shift) was obtained (for a fixed post annealing temperature and time).[7,19,24] Fig. 6-8(a) shows the PL results for samples irradiated at four different temperatures, from room temperature up to 300 °C. In all cases, the samples were annealed at 900 °C for 30 s. It is obvious from this figure that as the irradiation temperature is increased, there is a systematic reduction in the magnitude of energy shift in all the 4 QWs. Furthermore, irradiation at elevated temperature does not significantly improve the PL intensities or the linewidths than irradiation at room temperature. Note that the PL signal from the QW1 has disappeared under room temperature irradiation, as previously described above. A plot of the energy shift of the 4 QWs as a function of irradiation temperature is shown in Fig. 6-9(b). Almost a factor of two reduction in energy shift is obtained by varying the irradiation temperature from room temperature to 300 °C with QW1 having the least dependence on the irradiation temperature.

Although the above results do not support the observations reported by other groups that the degree of intermixing may be increased by increasing the irradiation temperature, it should be emphasised that their results were based on the use of heavier ions, such as As, Bi or Si. Thus, the different nature of defects caused by ions of different mass appears to be significant here. Indeed, the results in later section for oxygen and arsenic irradiations will clarify this issue.

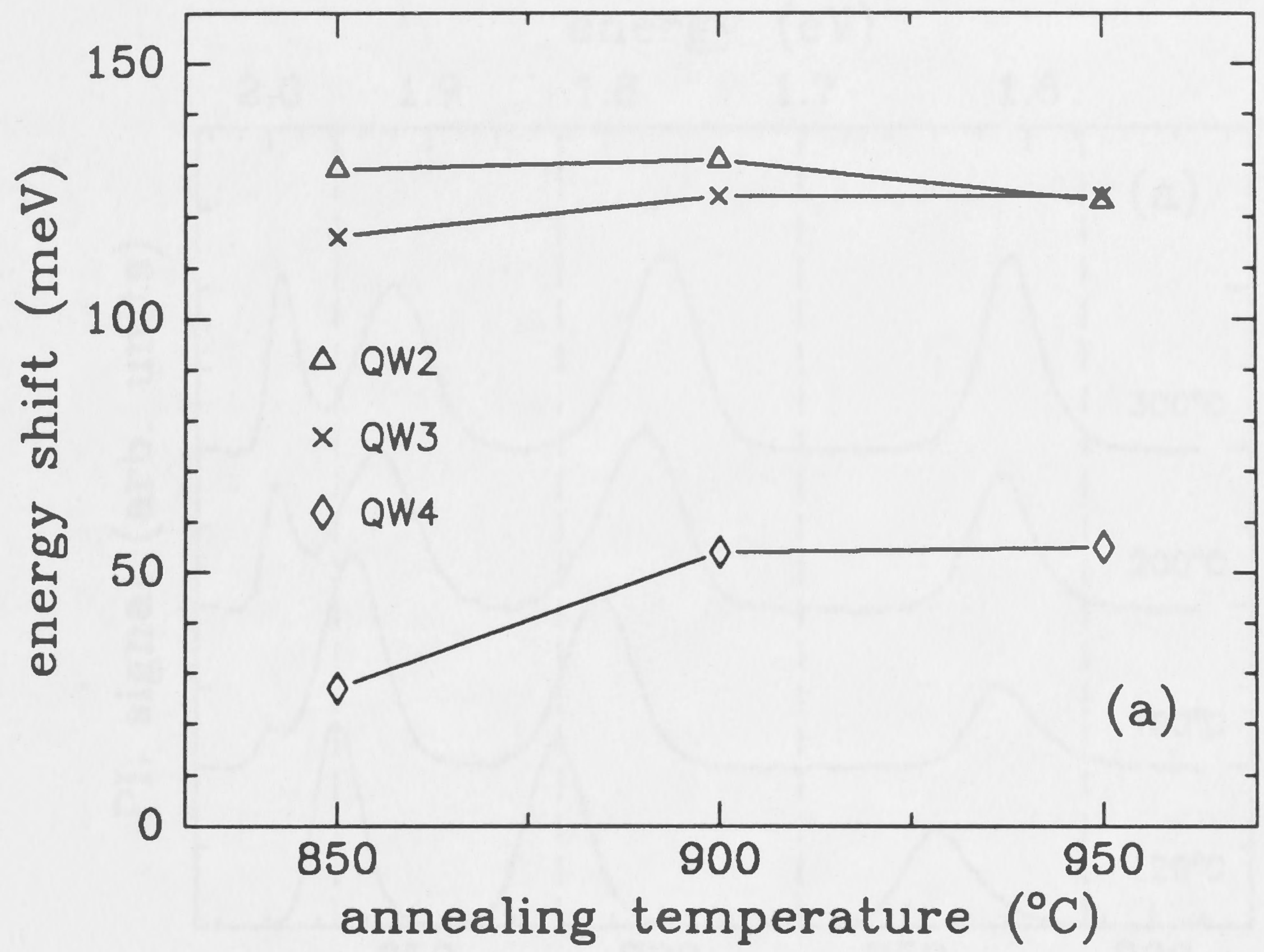

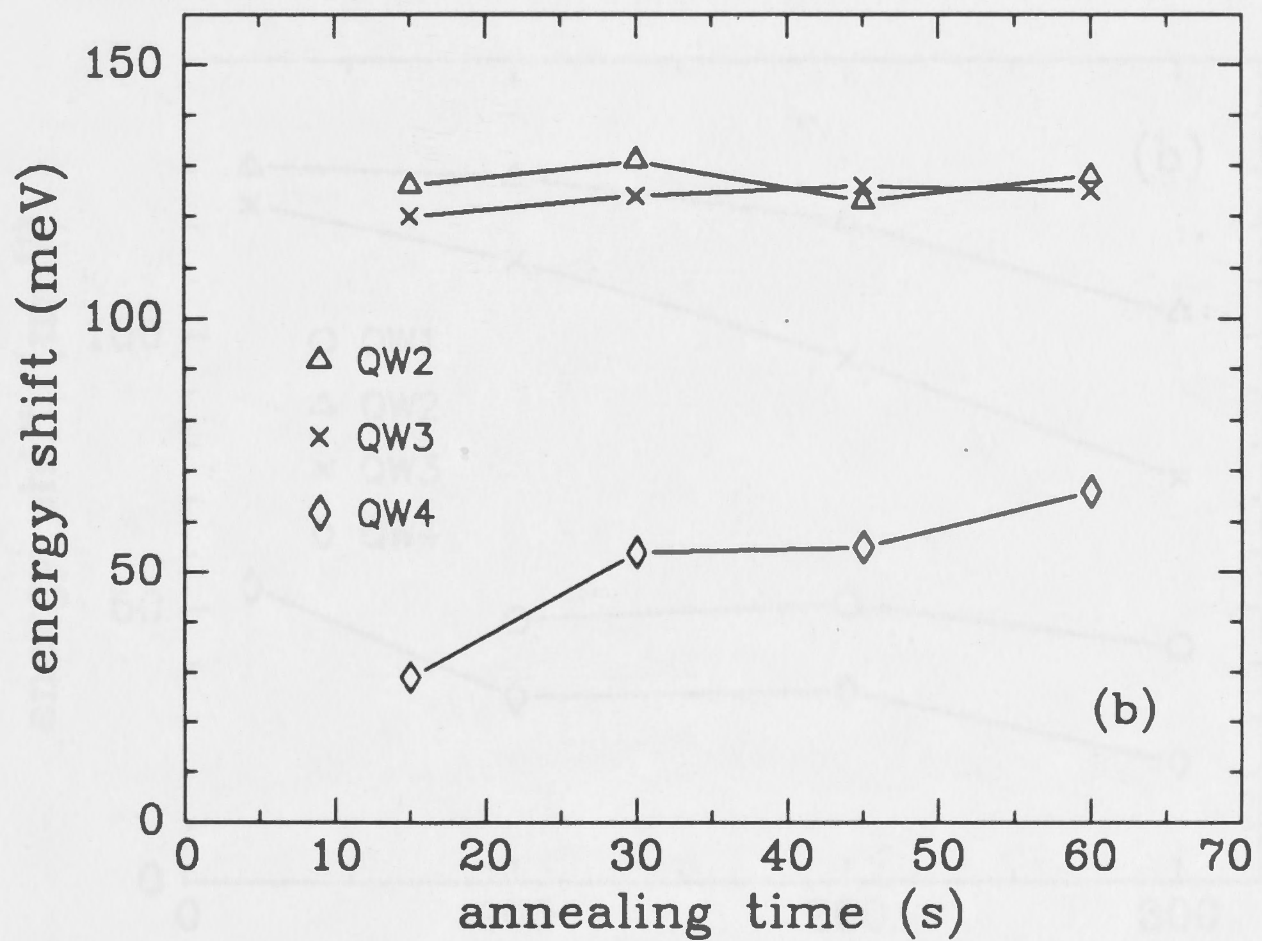

Fig. 6-7 Plots of energy shift as a function of (a) annealing temperature, at a constant time of 30 s and (b) annealing time, at a constant temperature of 900 °C. All data points are for samples irradiated with protons to a dose of $1x10^{16}$ cm^{-2}.

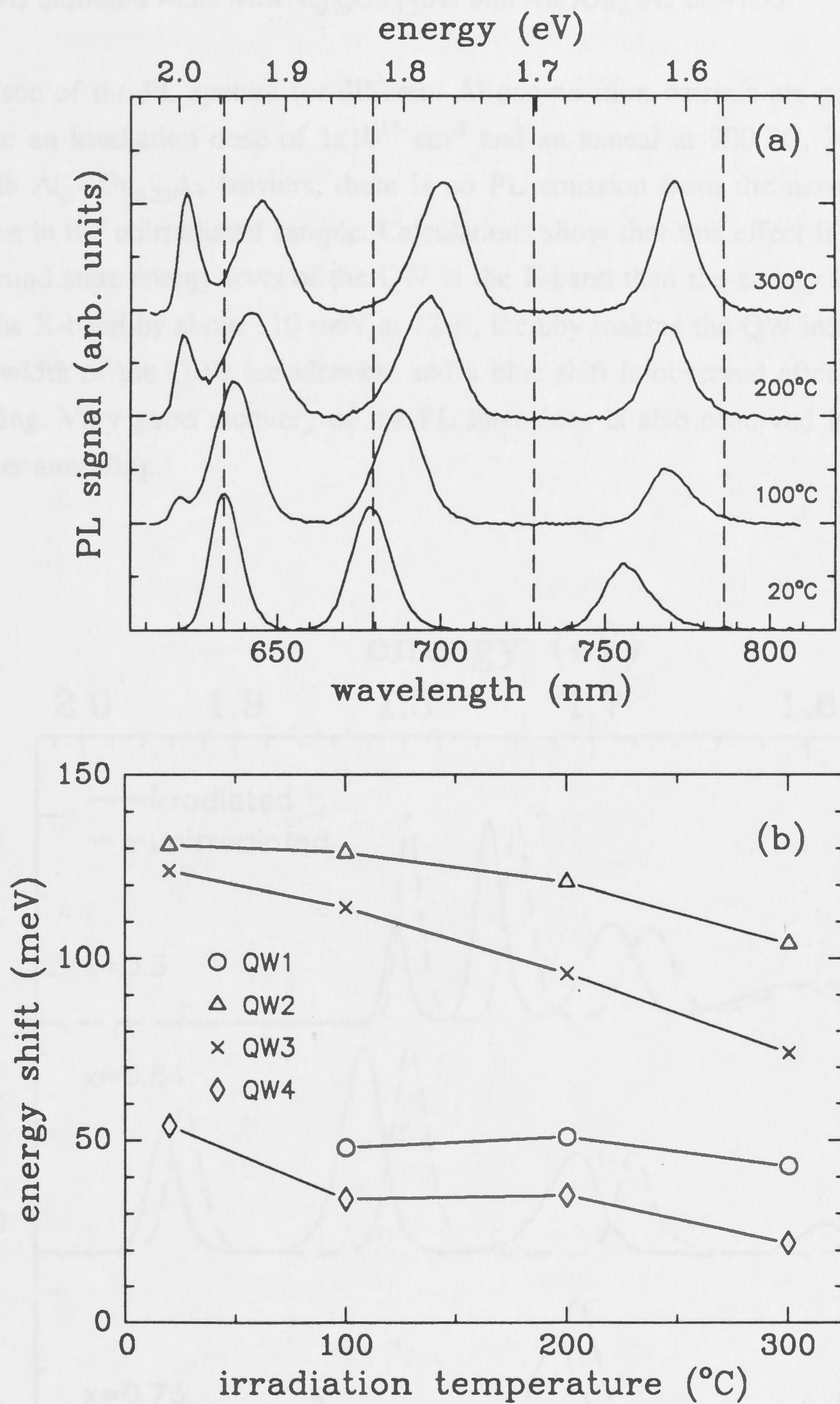

Fig. 6-8 (a) Low temperature (12 K) PL spectra from samples irradiated with protons to a dose of 1×10^{16} cm^{-2} at various temperatures. In all cases the samples have been annealed at 900 °C for 30 s. The dotted lines indicate the peak positions of the PL signals from each QW. Note the disappearance of the PL signal from QW1 at room temperature irradiation. (b) A plot of the energy shift of each QW as a function of irradiation temperature.

6.3.2 *GaAs quantum wells with $Al_{0.75}Ga_{0.25}As$ and $Al_{0.3}Ga_{0.7}As$ barriers*

A comparison of the PL spectra for different Al composition barriers are presented in Fig. 6-9 for an irradiation dose of 1×10^{15} cm^{-2} and an anneal at 900 °C, 30 s. In the sample with $Al_{0.75}Ga_{0.25}As$ barriers, there is no PL emission from the narrowest well (QW1) even in the unirradiated sample. Calculations show that this effect is due to the higher ground state energy level of the QW in the Γ-band than the energy level of the barrier in the X-band by about 110 meV at 12 K, thereby making the QW indirect. In all cases, the width of the QWs are identical and a blue shift is observed after irradiation and annealing. Very good recovery of the PL intensities is also observed in the three samples after annealing.

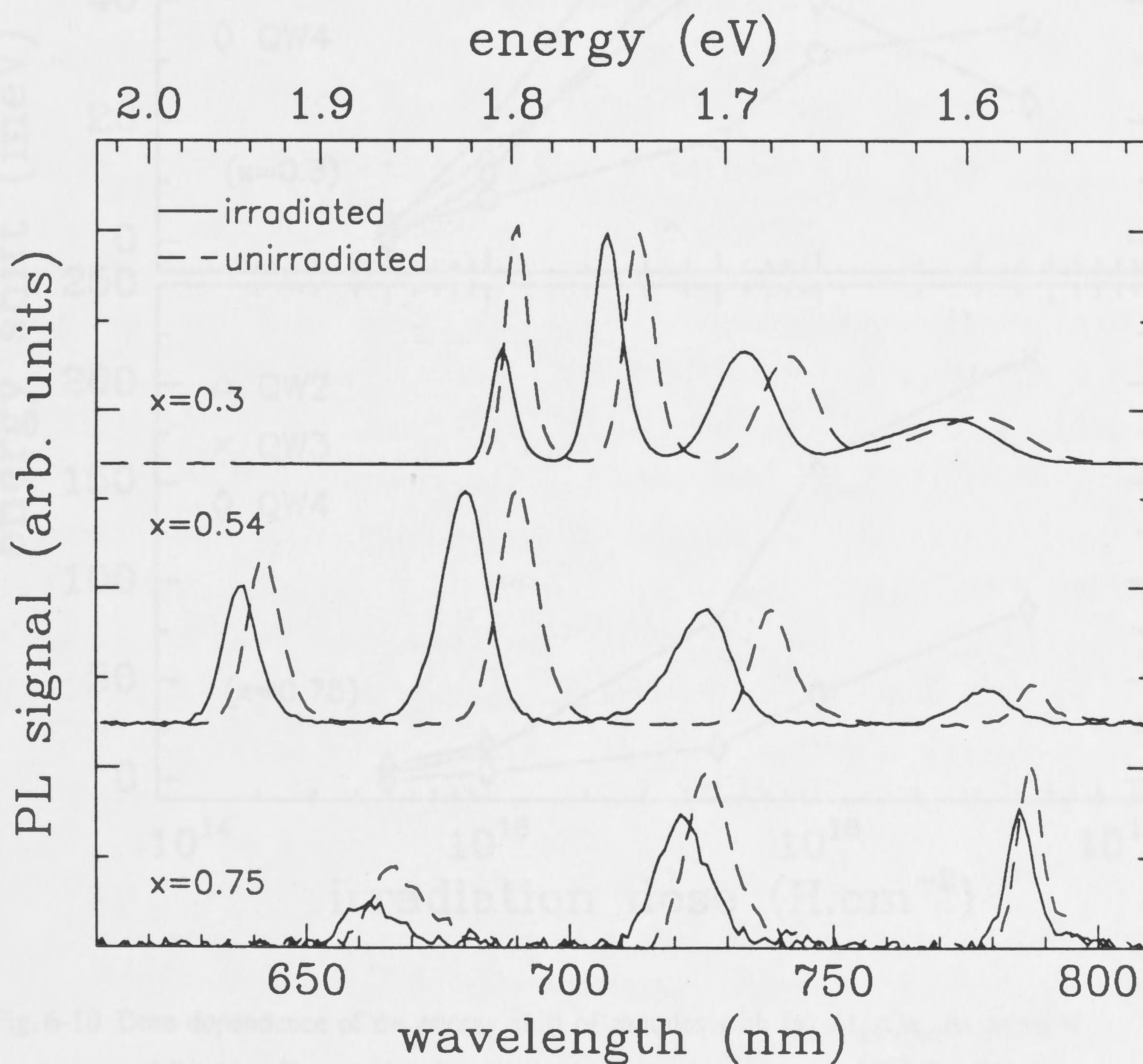

Fig. 6-9 Low temperature (12 K) PL spectra of the 4 QWs from three samples with different $Al_xGa_{1-x}As$ barriers (x=0.3, 0.54 and 0.75) irradiated with protons to a dose of 1×10^{15} cm^{-2} and annealed at 900 °C for 30 s.

A plot of the magnitude of energy shift versus irradiation dose for the two Al contents barriers ($Al_{0.3}Ga_{0.27}As$ and $Al_{0.75}Ga_{0.25}As$) are shown in Fig. 6-10. The trend for the $Al_{0.75}Ga_{0.25}As$ barriers [Fig. 6-10(b)] is very similar to that of $Al_{0.54}Ga_{0.46}As$ barriers, in as much as very large energy shifts of up to ~200 meV are obtainable with no apparent saturation. It is also interesting to note that above the dose of $5x10^{15}$ cm^{-2}, the PL signal from QW2 has disappeared (c.f. QW1 in the case of $Al_{0.54}Ga_{0.46}As$ barriers), again due to the transition from direct to indirect QW. The trend of energy shift with annealing

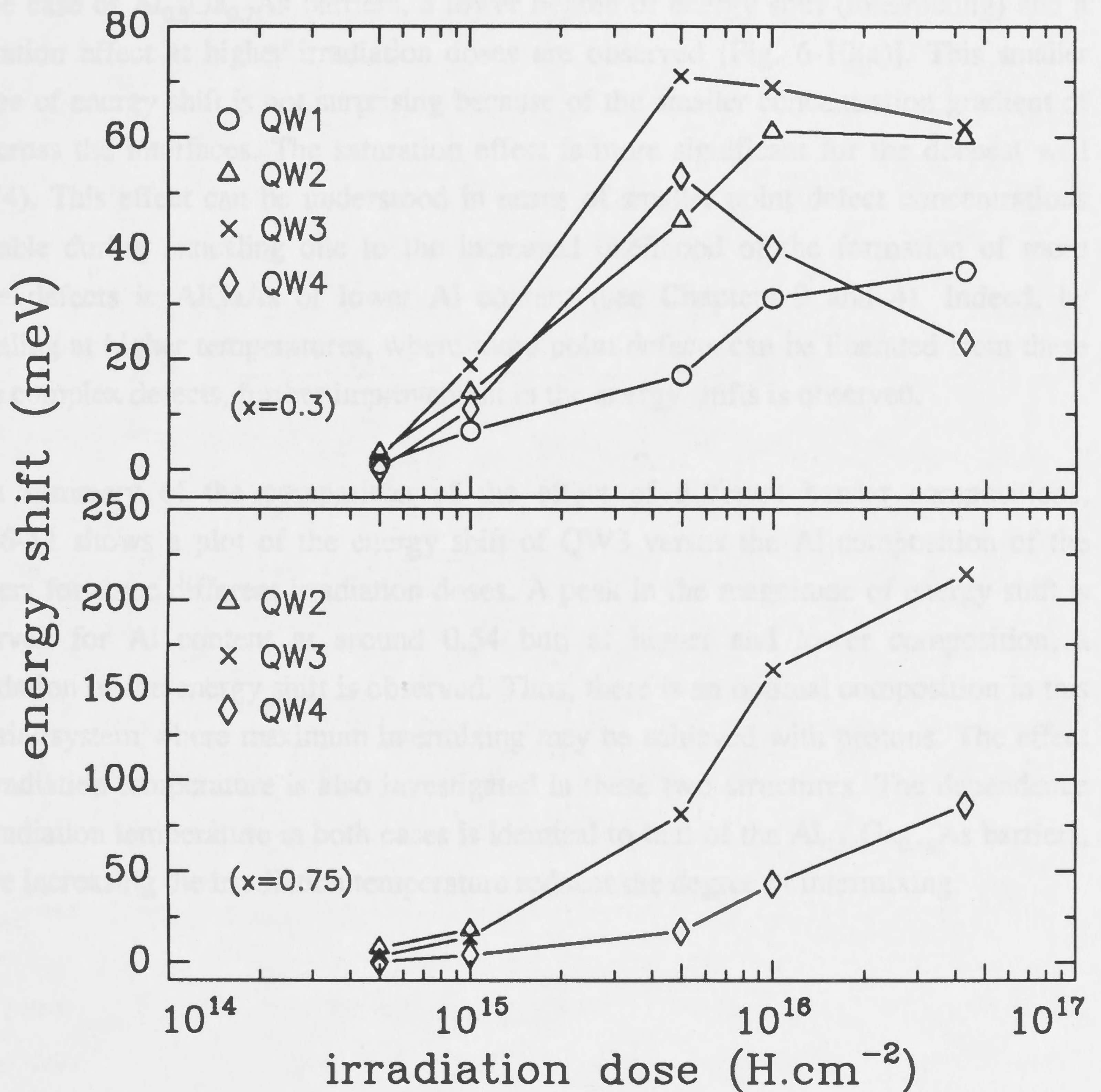

Fig. 6-10 Dose dependence of the energy shift of samples with (a) $Al_{0.3}Ga_{0.7}As$ barriers and (b) $Al_{0.75}Ga_{0.25}As$ barriers, at an annealing temperature of 900 °C (30 s).

temperature/time is similar to that of the previous case, with no further improvement observed above 900 °C or for longer than 15 s annealing time. Although much larger energy shifts are expected from this system due to the higher concentration gradient of Al across the interfaces, the magnitude of energy shift is approximately similar to that of the samples with $Al_{0.54}Ga_{0.46}As$ barriers. This effect is most likely due to the presence of a higher concentration of impurities in samples with higher Al content which will be discussed later.

In the case of $Al_{0.3}Ga_{0.7}As$ barriers, a lower degree of energy shift (intermixing) and a saturation effect at higher irradiation doses are observed [Fig. 6-10(a)]. This smaller degree of energy shift is not surprising because of the smaller concentration gradient of Al across the interfaces. The saturation effect is more significant for the deepest well (QW4). This effect can be understood in terms of smaller point defect concentrations available during annealing due to the increased likelihood of the formation of more stable defects in AlGaAs of lower Al content (see Chapters 3 and 4). Indeed, by annealing at higher temperatures, where more point defects can be liberated from these more complex defects, further improvement in the energy shifts is observed.

As a summary of the comparison of the effect of different barrier compositions, Fig. 6-11 shows a plot of the energy shift of QW3 versus the Al composition of the barriers for three different irradiation doses. A peak in the magnitude of energy shift is observed for Al content at around 0.54 but, at higher and lower composition, a retardation of the energy shift is observed. Thus, there is an optimal composition in this material system where maximum intermixing may be achieved with protons. The effect of irradiation temperature is also investigated in these two structures. The dependence of irradiation temperature in both cases is identical to that of the $Al_{0.54}Ga_{0.46}As$ barriers, where increasing the irradiation temperature reduces the degree of intermixing.

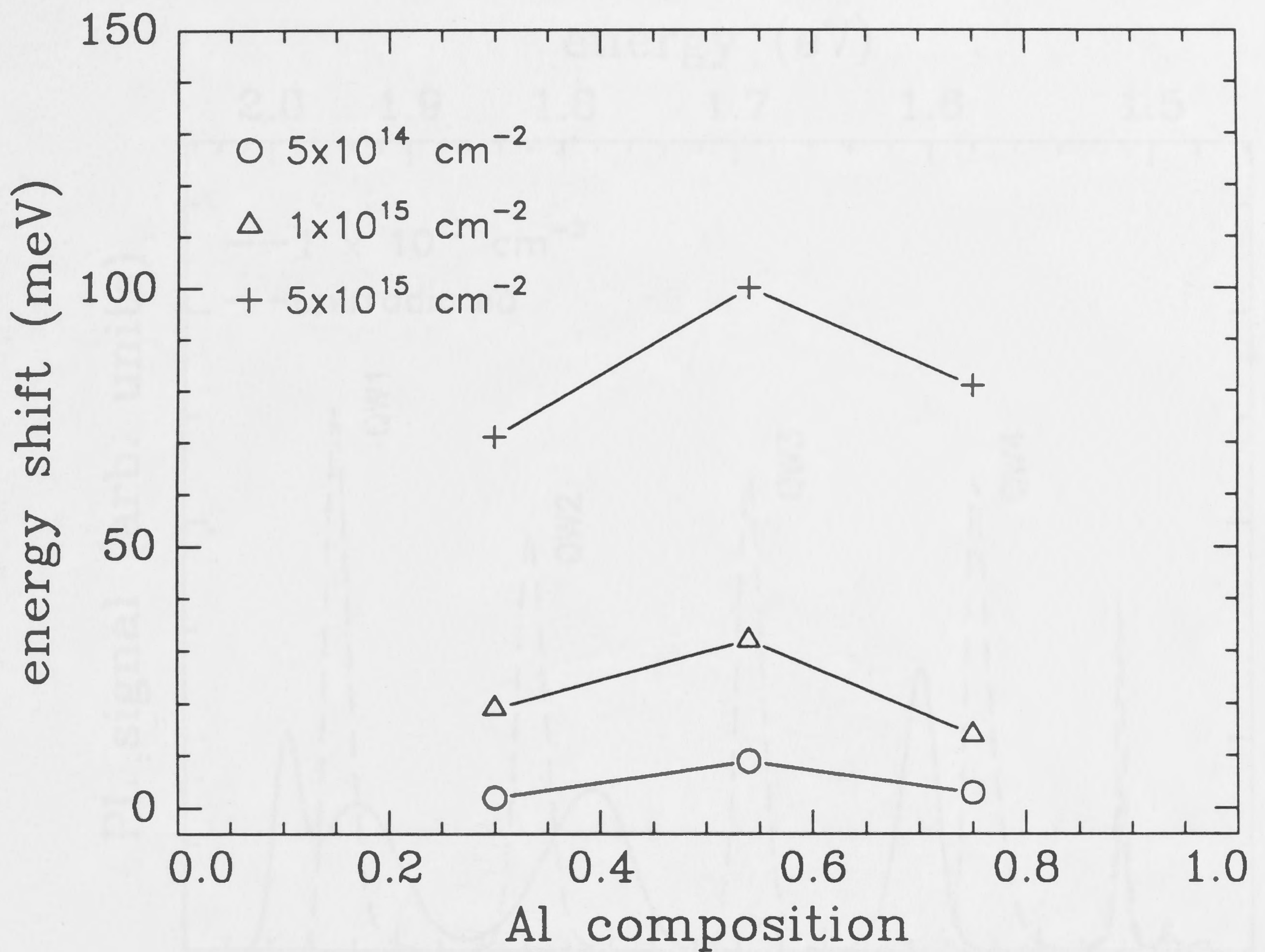

Fig. 6-11 Energy shift as a function of the Al composition in the $Al_xGa_{1-x}As$ barriers for QW3 for three different irradiation doses and annealed at 900 °C for 30 s.

6.4 Arsenic and oxygen irradiation

6.4.1 Arsenic irradiation of GaAs quantum wells with $Al_{0.54}Ga_{0.46}As$ barriers

Large energy shifts may also be obtained with heavier ion irradiation, such as arsenic, but at significantly lower irradiation doses. From FASTRIM calculations, the collisional displacement density caused by arsenic ions is expected to be a factor of ~1000 higher than that of protons. Thus, the ion doses must be reduced by about 2-3 orders of magnitude to maximise optical recovery upon annealing as shown by the PL spectrum in Fig. 6-12 for an irradiation dose of $1x10^{12}$ cm^{-2} (after 900 °C, 30 s anneal). Above a certain irradiation dose ($5x10^{12}$ cm^{-2}) the PL signal from QW1 disappears, similar to the case of proton irradiation. A plot of the dose dependence of the magnitude of energy shift is shown in Fig. 6-13. Energy shifts in excess of 200 meV are achieved at a dose of

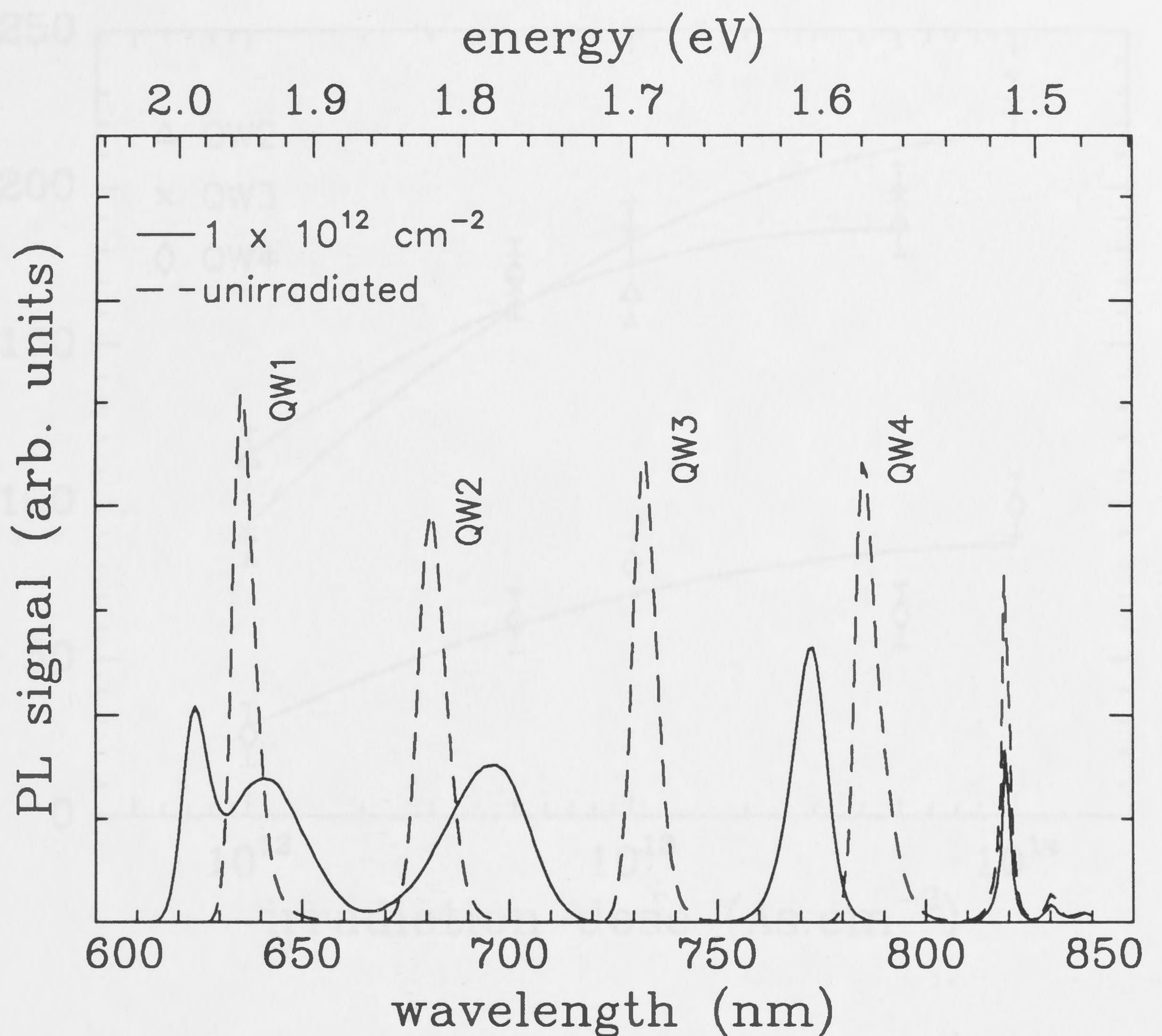

Fig. 6-12 Low temperature (12 K) PL spectrum a sample irradiated with arsenic ions to a dose of $1x10^{12}$ cm^{-2} and annealed at 900 °C for 30 s. The spectrum for the unirradiated samples is also shown for reference.

$1x10^{14}$ cm^{-2}. However, at this dose the PL intensities are quite weak and also the disappearance of the two narrower wells (QW1 and QW2) is observed. A major difference between this result and that of proton irradiation is that a saturation effect is observed in the case of arsenic ions, especially in the two deeper QWs (closer to the end-of-range of the ions). Although the irradiation doses have been lowered significantly, it is known that the nature of defects caused by heavier ions could be quite different to those from light ions.[43,44,55,56] The damage cascade caused by an individual ion track is expected to be denser and larger in size for heavier ions and, hence, increases the chance of agglomeration of the surrounding point defects into clusters and other extended defects by the overlap of these damage cascades.[43,44,55,56]

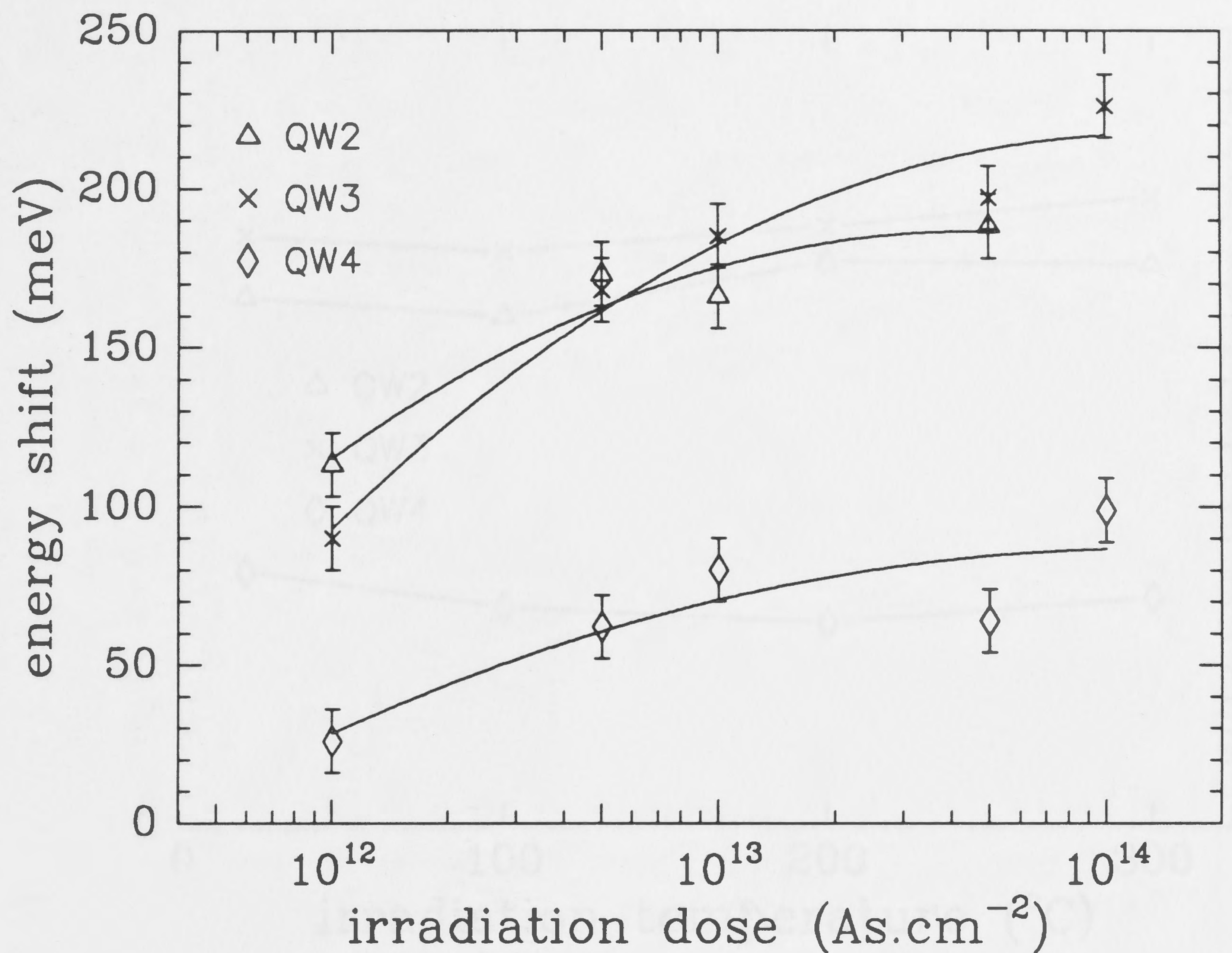

Fig. 6-13 Dose dependence of the magnitude of energy shift for the QWs in samples irradiated with arsenic ions and annealed at 900 °C for 30 s.

An irradiation-temperature study with arsenic ions was also carried out and the results are presented in Fig. 6-14 for an irradiation dose of $1x10^{13}$ cm^{-2}. This figure shows that additional improvement in the energy shift may be obtained by arsenic irradiation at elevated temperatures, although this improvement is only marginal. However, the results do not show any significant improvement in the recovery of the PL intensities at elevated irradiation temperatures. This behaviour has the opposite trend to that observed with proton irradiation where increasing the irradiation temperature retards the intermixing. Thus, as mentioned previously, the nature of defects created by heavy and light ions are fundamentally quite different and intermixing is governed by the type and stability of the defects created during and after irradiation.

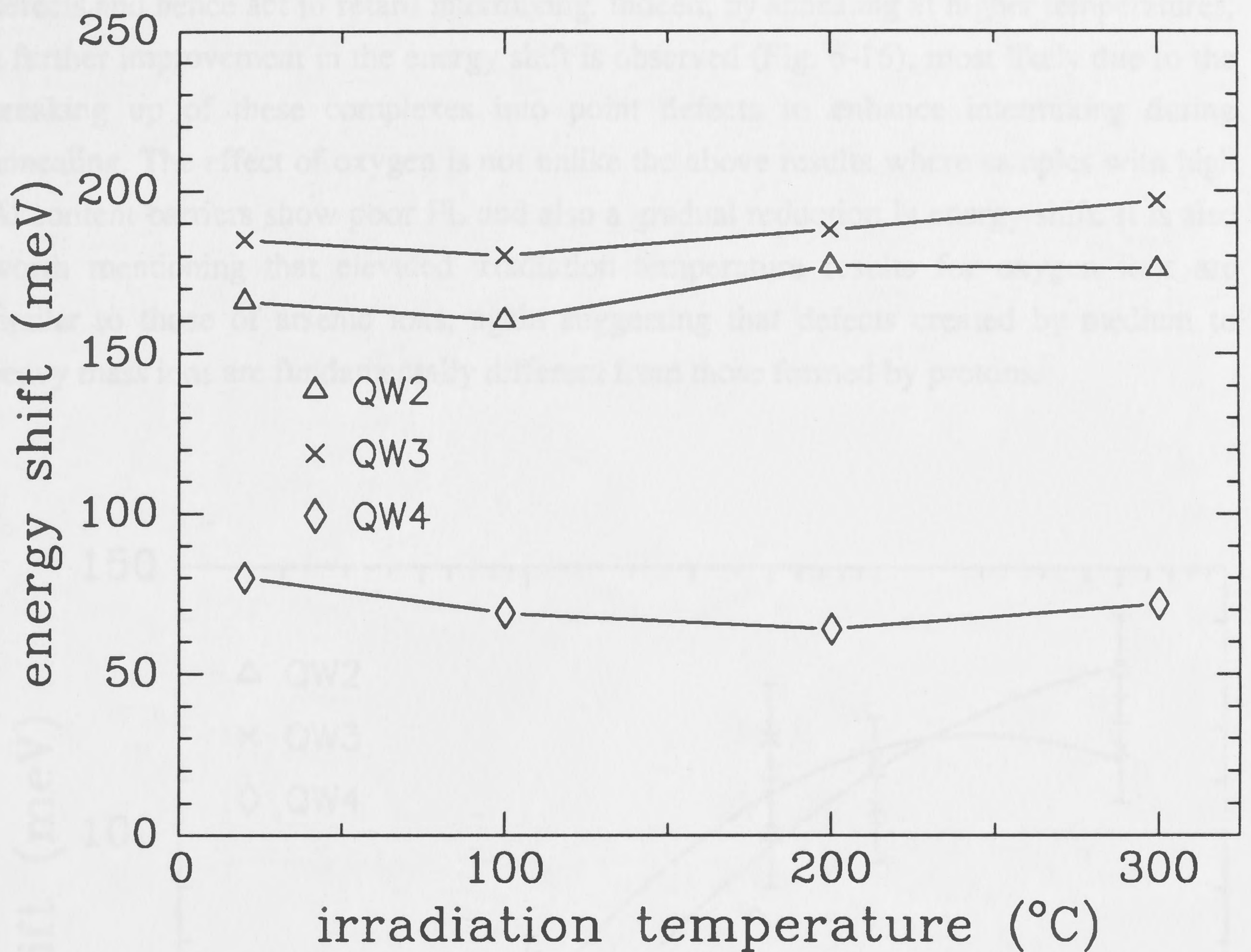

Fig. 6-14 Irradiation temperature dependence of the energy shift in arsenic irradiated samples at a dose of $1x10^{13}$ cm^{-2} after annealing at 900 °C for 30 s.

6.4.2 Oxygen irradiation of GaAs quantum wells with $Al_{0.54}Ga_{0.46}As$ barriers

Fig. 6-15 shows the dose dependence of energy shift in the oxygen irradiated sample. The irradiation doses have been scaled according to FASTRIM calculations which indicate that the displacement density due to oxygen ions is about a factor of 100 greater than that created by protons. Similar to the results of arsenic irradiations, a saturation effect is observed at higher doses but the magnitude of energy shift is somewhat reduced from either that of arsenic or proton irradiations. Nevertheless, large energy shifts of up to 130 meV may still be obtained with oxygen ions. Since the displacement density for oxygen irradiation has been scaled appropriately, the observed smaller energy shifts are due to the effect of the ions. Oxygen is known to form complexes with (point) defects in GaAs/AlGaAs,[57,58] thereby reducing the concentration of mobile point defects available for intermixing. These complexes are also more thermally stable than simple point

defects and hence act to retard intermixing. Indeed, by annealing at higher temperatures, a further improvement in the energy shift is observed (Fig. 6-16), most likely due to the breaking up of these complexes into point defects to enhance intermixing during annealing. The effect of oxygen is not unlike the above results where samples with high Al content barriers show poor PL and also a gradual reduction in energy shift. It is also worth mentioning that elevated irradiation temperature results for oxygen ions are similar to those of arsenic ions, again suggesting that defects created by medium to heavy mass ions are fundamentally different from those formed by protons.

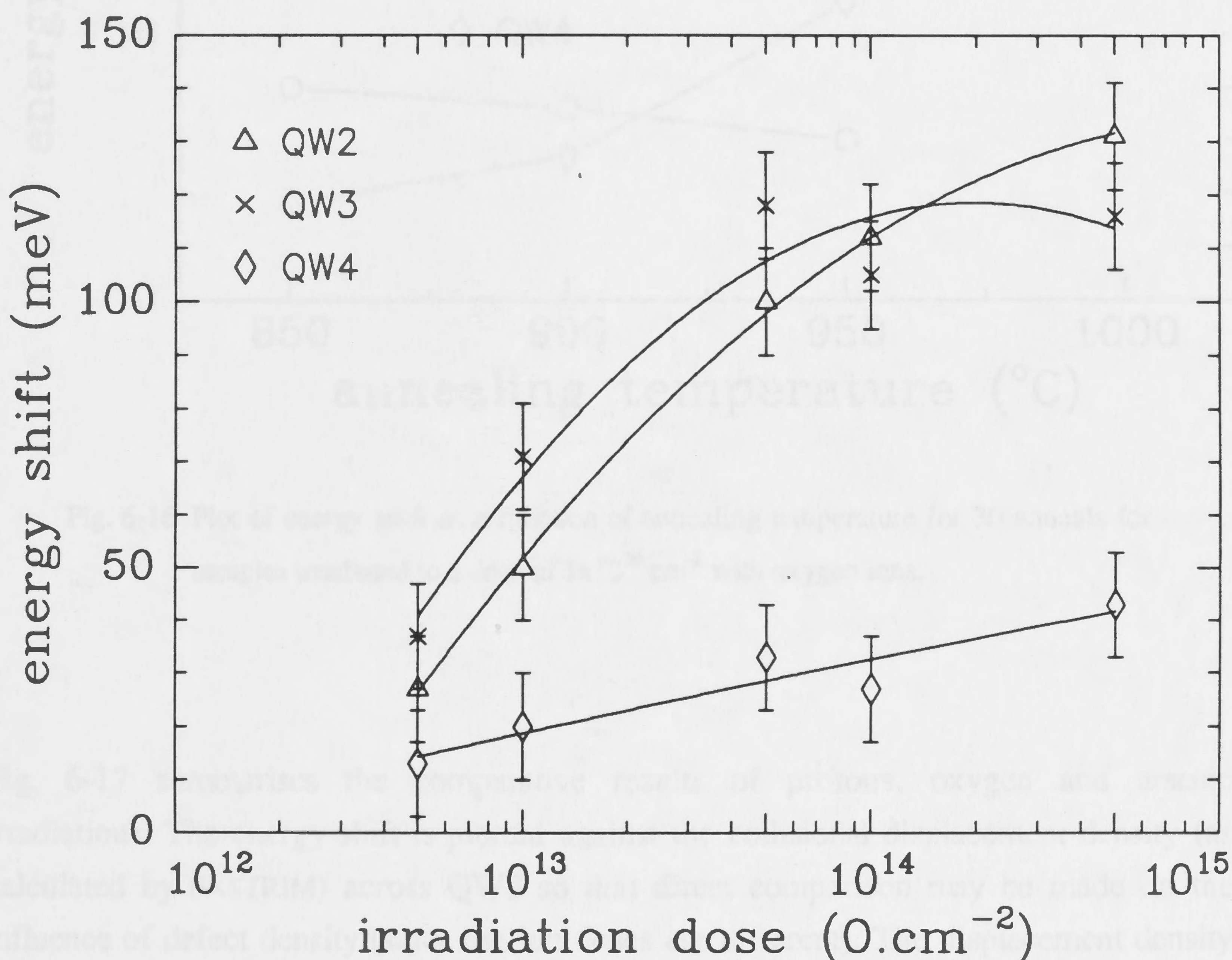

Fig. 6-15 Dose dependence of the magnitude of energy shift for the QWs in samples irradiated with oxygen ions and annealed at 900 °C for 30 s.

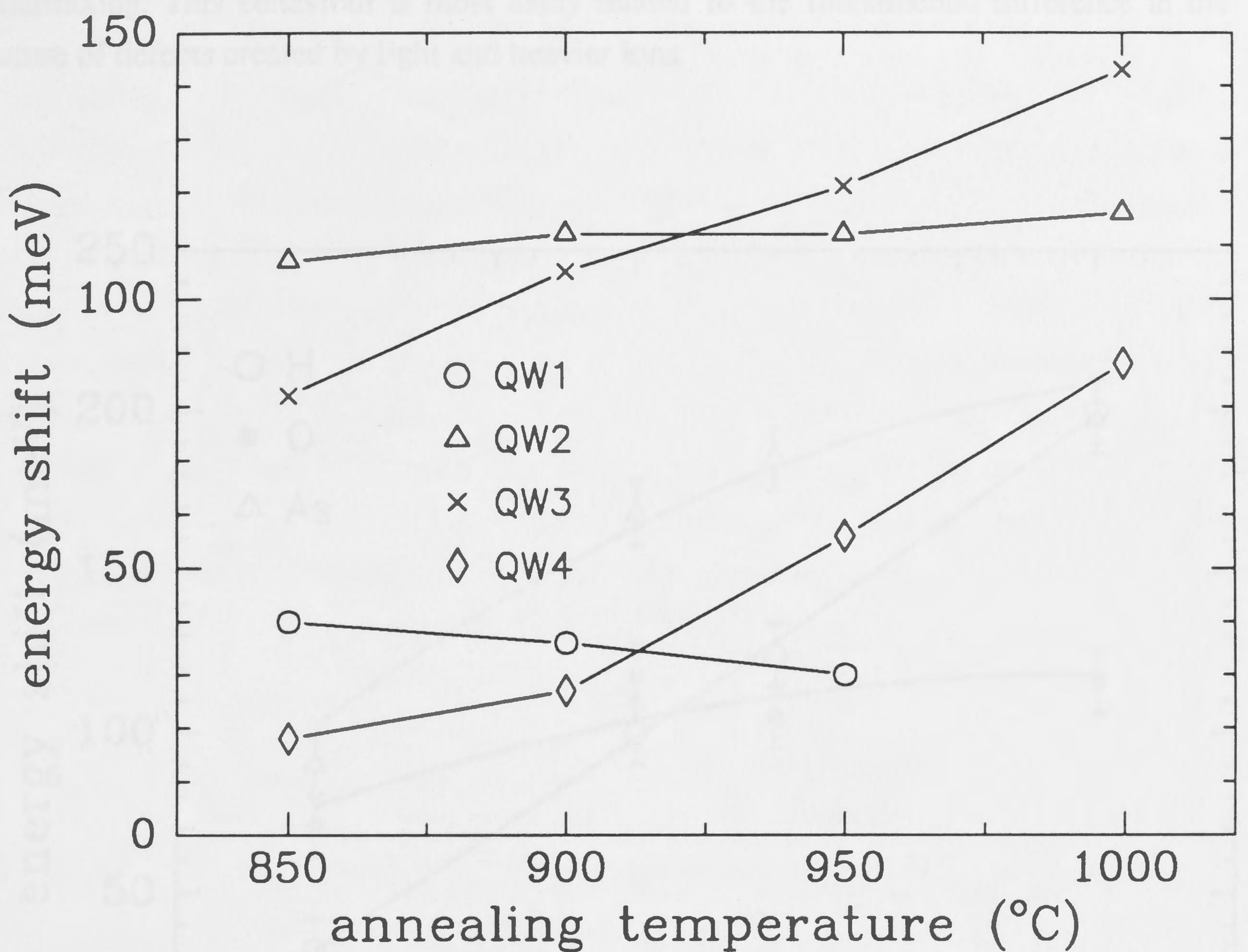

Fig. 6-16 Plot of energy shift as a function of annealing temperature for 30 anneals for samples irradiated to a dose of 1×10^{14} cm^{-2} with oxygen ions.

Fig. 6-17 summarises the comparative results of protons, oxygen and arsenic irradiations. The energy shift is plotted against the collisional displacement density (as calculated by FASTRIM) across QW3 so that direct comparison may be made on the influence of defect density (since the ion doses are different). The displacement density should only be taken as a guide and not the actual defect concentration since dynamic annealing is known to occur at room temperature in GaAs and especially in AlGaAs (see Chapters 3 and 4). Two main features can be noted from this figure. Firstly, for heavier ion (As, O) irradiations, a saturation effect in the energy shift (intermixing) is observed at higher displacement density but not for the case of protons. The saturation effect is much more pronounced with oxygen irradiation due to the chemical effect of oxygen, which is discussed below. Secondly, at lower displacement densities, heavier ions are more efficient at intermixing as indicated by the larger energy shift. However, with increasing irradiation dose (displacement density), protons becomes more efficient in

intermixing. This behaviour is most likely related to the fundamental difference in the nature of defects created by light and heavier ions.

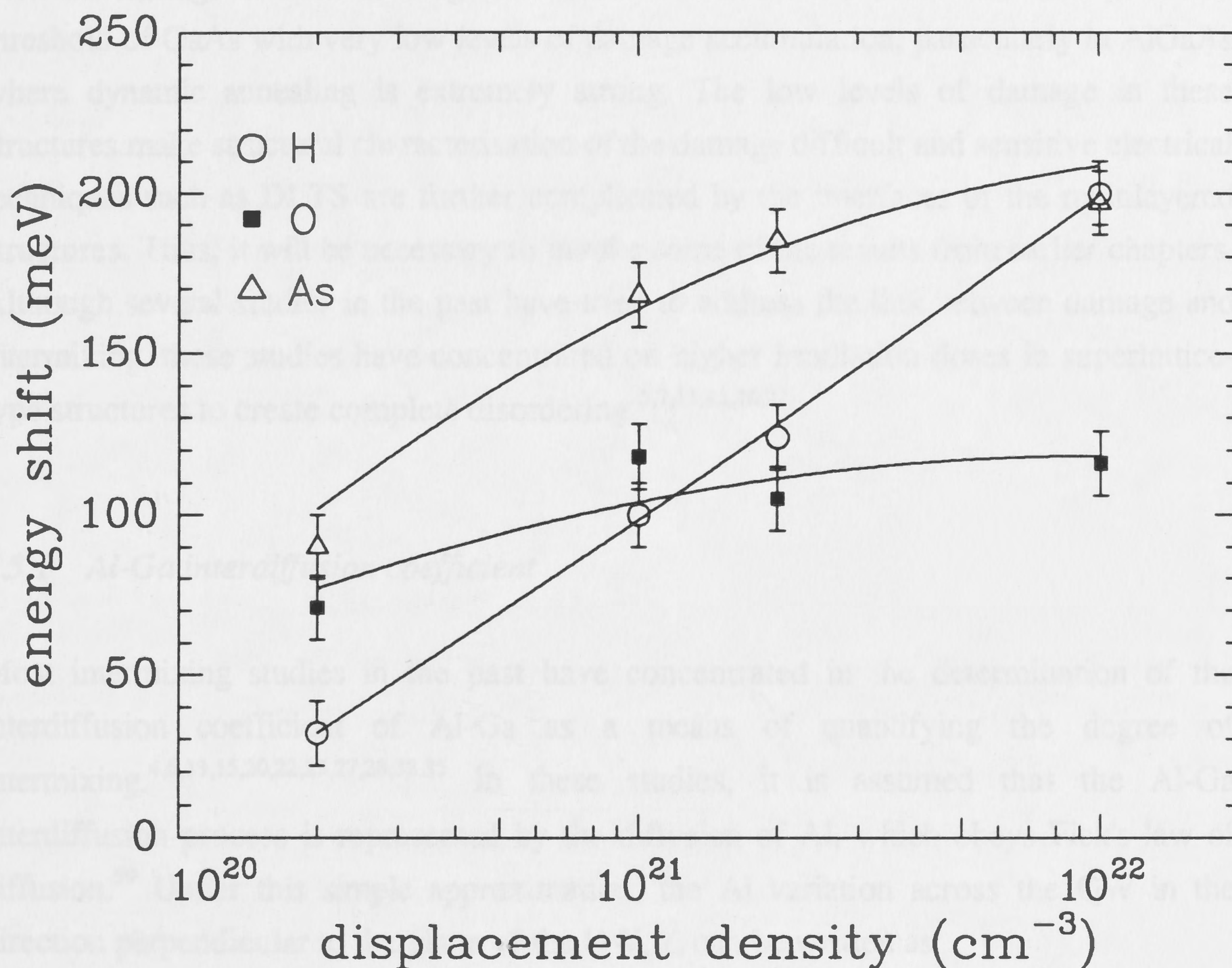

Fig. 6-17 Comparison of the energy shift of QW3 for proton, oxygen and arsenic irradiation as a function of displacement density. The irradiation doses were chosen such that they resulted in the same displacement density (as calculated by FASTRIM) in the QW for all the three ions.

6.5 Discussion

The focus of this chapter was shifted away from the more traditional literature measurements of the Al-Ga interdiffusion coefficient to understanding the relation between damage and intermixing. The irradiation doses are below the amorphisation threshold of GaAs with very low levels of damage accumulation, particularly in AlGaAs where dynamic annealing is extremely strong. The low levels of damage in these structures make structural characterisation of the damage difficult and sensitive electrical techniques such as DLTS are further complicated by the interfaces of the multilayered structures. Thus, it will be necessary to invoke some of the results from earlier chapters. Although several studies in the past have tried to address the link between damage and intermixing, these studies have concentrated on higher irradiation doses in superlattice-type structures to create complete disordering.[5,7,11,12,16,22]

6.5.1 Al-Ga interdiffusion coefficient

Most intermixing studies in the past have concentrated in the determination of the interdiffusion coefficient of Al-Ga as a means of quantifying the degree of intermixing.[4,6,13,15,20,22,25,27,28,32,35] In these studies, it is assumed that the Al-Ga interdiffusion process is represented by the diffusion of Al, which obeys Fick's law of diffusion.[59] Under this simple approximation, the Al variation across the QW in the direction perpendicular to the plane of the QW, z, can be written as

$$x(z) = x_o\left\{1+\frac{1}{2}\mathrm{erf}\left(\frac{z-\frac{L_z}{2}}{2\sqrt{Dt}}\right)-\frac{1}{2}\mathrm{erf}\left(\frac{z+\frac{L_z}{2}}{2\sqrt{Dt}}\right)\right\} \tag{6.1}$$

where x_o is the initial Al concentration in the barrier, L_z is the width of the QW, erf(z) is the error function, t is the annealing time and D is the Al-Ga interdiffusion coefficient. Equation (6.1) is represented schematically in Fig. 6-18. A numerical simulation is then made to solve Schrödinger's equation for the electron and hole energy levels using equation (6.1) as the expression of the potential well. The transition energy of the electron to heavy hole is then matched to the measured PL wavelength by fitting the value of the interdiffusion coefficient, D. This model also requires values for the conduction and valence band offsets. Although, the values of the interdiffusion coefficient determined from this model are comparable to those measured by Secondary

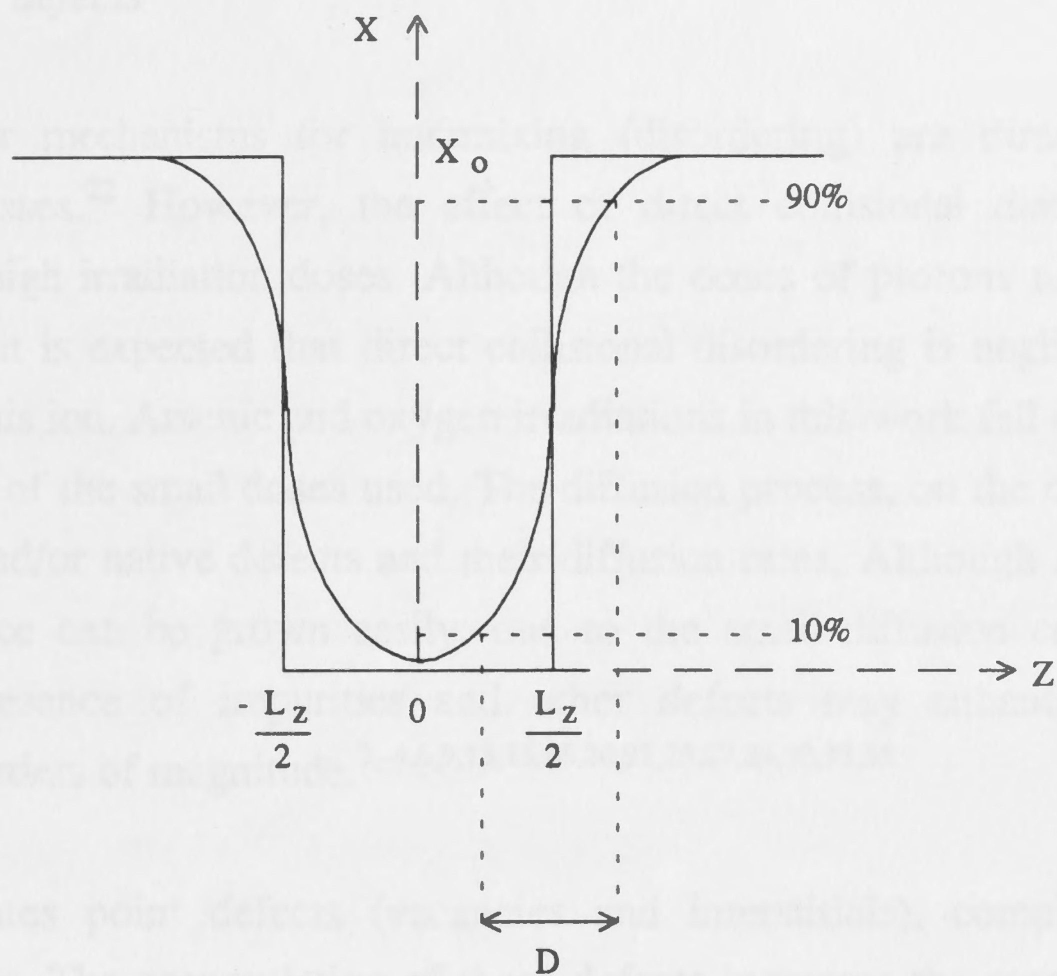

Fig. 6-18 Schematic of the double error function profile normally assumed in modelling the shape of the quantum well after intermixing. The parameters in this figure are as defined by equation (1).

Ion Mass Spectroscopy (SIMS)[9,22] and other models,[8,10,17,30] the exact shape of the QW after intermixing is not exactly known. Furthermore , the SIMS technique suffers from spatial resolution and this is critical especially in QWs. Moreover, since PL measurements only yield information of the ground state energy levels, similar values for D may also be obtained by assuming the shape of the QW to be a Gaussian- or parabolic-like after intermixing, i.e. if the Al profile in the QW does not obey Fickian diffusion. To properly model the shape of the QW, one needs to obtain the excited states by other means such as photoluminescence excitation or photoreflectance measurements or even quantitative high resolution electron microscopy analysis. Recently, there have been a few reports that the shape of the QW after intermixing does indeed follow the above model based on reflectivity measurements of the excited states[33,34] but more data and simulation are needed to confirm this. Furthermore, in these reports, the QWs were quite wide (~10 nm). Although Fick's law of diffusion may hold in wells that are wide, this is not necessarily true in narrow wells. Thus, the interpretation of Al-Ga interdiffusion results from the model above has to be exercised with caution, particularly for very narrow wells of only several monolayers width.

6.5.2 Roles of defects

The two major mechanisms for intermixing (disordering) are direct collision and diffusion processes.[22] However, the effect of direct collisional disordering is only appreciable at high irradiation doses. Although the doses of protons used in this study are quite high, it is expected that direct collisional disordering is negligible due to the small mass of this ion. Arsenic and oxygen irradiations in this work fall into the diffusion regime because of the small doses used. The diffusion process, on the other hand, relies on impurities and/or native defects and their diffusion rates. Although an abrupt GaAs-AlGaAs interface can be grown easily, due to the small diffusion coefficient of Al-Ga,[60,61] the presence of impurities and other defects may enhance this diffusion coefficient by orders of magnitude.[1,-4,6,9,13,15,16,20,22,25,27,28,30,33,35]

Irradiation creates point defects (vacancies and interstitials), complexes and other extended defects. The accumulation of these defects increases the system's free energy and during annealing, the free energy is lowered by annihilation of these excess point defects through the process of diffusion. During the diffusion process, these defects migrate across the GaAs-AlGaAs heterointerface (see Chapter 4), thereby enhancing the interdiffusion between the Al-Ga atoms. Thus, the degree of intermixing is dependent on the diffusion rates of these defects. Although a variety of mechanisms have been proposed to help understand the defect-enhanced interdiffusion process,[2,6,30,62,63] these models share a common feature where point defects (interstitials, vacancies or antisites) are assumed to be responsible for the interdiffusion. The simplest model assumes gallium vacancies, V_{Ga}, control the intermixing process.

Earlier studies of ion irradiation-induced intermixing have also concentrated on the use of dopants or other impurities, such as Si, Zn, S, Se and O.[2,4-12,15,16,18,19] More recent studies have used chemically inert ions (inert gases)[15,17] or ions that are identical to the constituent atoms of the material system (Al, Ga, As).[13-15,21-26] This so-called impurity-free intermixing method is of more interest, particularly in device fabrication because the complications and reliability problems that may be associated with dopants or impurities can be avoided. Nevertheless, the introduced defects must be removed in device applications. Again, these previous studies have been focussed on the use of medium to heavy mass ions and these ions are known to cause more damage; complexes and extended defects, which are more difficult to remove during annealing. Furthermore, with increasing ion dose, the accumulation of large damage clusters and extended defects may cause a saturation in the concentration of point defects which evolve during annealing. The stronger thermal stability of these defects also inhibit the interdiffusion

process, thus leading to a reduction (saturation) in intermixing, as indeed reported by several groups.[10,11,14,15,17,21,25,26]

6.5.3 Proton irradiation

In contrast to heavier ions, the use of protons is expected to create only point defects and dilute defect clusters.[43,44] This is supported by the large energy shifts obtained even at high doses (> $1x10^{15}$ cm^{-2}) with no apparent saturation. Since it is the point defect concentration that is responsible for the Al-Ga interdiffusion during annealing, the dose dependence results suggest that the concentration of point defects for proton bombardment does not saturate at high dose. These observations are similar to a very recent study where it was reported that large energy shifts may be obtained by protons.[20] In addition, proton bombardment is not expected to result in appreciable formation of more stable defects such as defect clusters and extended defects during annealing. This is further supported by the XTEM results in Fig. 6-5 where no extended defects are observed after annealing even for a high irradiation dose of 1 x 10^{16} cm^{-2}. This suggests that almost all of the point defects created by proton irradiation are involved in the intermixing process. The lack of defect agglomeration during annealing thus improves intermixing and optical recovery.

The annealing results of proton bombardment in GaAs-$Al_{0.54}Ga_{0.46}As$ quantum wells indicate that the annealing conditions can be adjusted to provide optimum shifts with acceptable PL signal recovery in the temperatures of 900-950 °C for 30-45 s anneal. At lower temperatures (~850 °C), not all of the dilute point defect clusters can break up to liberate point defects which contribute to the interdiffusion process. Thus, the restoration of crystalline perfection is not efficient at these temperatures. Indeed, the intensities of the PL in samples annealed at 850 °C are about a factor of 2-3 lower than in samples annealed at 900 or 950 °C. A similar proton irradiation-induced intermixing study had also used annealing at these lower temperatures where large energy shifts were obtained but the recovery of the PL intensities was rather poor,[20] consistent with these results at 850 °C. At higher temperatures (≥ 1000 °C) on the other hand, very little improvement in the magnitude is observed, most likely due to the exhaustion of the available point defects. Also at such high temperatures, degradation of the material quality such as the surface morphology, was observed in some samples. This effect becomes more prominent for material with increasing Al content, where the reactivity of the material is higher.

The results in this chapter also show that QWs of intermediate widths have the largest energy shift while very narrow or wide QWs show a smaller degree of intermixing. This effect is similar to that observed by Elman *et. al.*,[14] who attributed it to the saturation of the exciton energy at the barriers. This is best explained with reference to Fig. 6-19. As the well becomes progressively narrower, the ground state energy level, E_o, for electrons (heavy hole) moves closer to the conduction (valence) band of the barriers. Thus for very narrow wells, there is a smaller range in which this level may move for a small perturbation in the shape of the well. In contrast, however, for intermediate wells where E_o is initially at a lower level, the range in which E_o can move in response to the change in well shape is greater. On the other hand, in wide wells there is only a small range in which E_o can move for a change in the well shape due to the continuum limit for wide wells. Thus, in wells of intermediate width, E_o is most sensitive to any changes in the well shape while for very narrow or wide wells, E_o is bounded by the barrier and continuum limit, respectively.

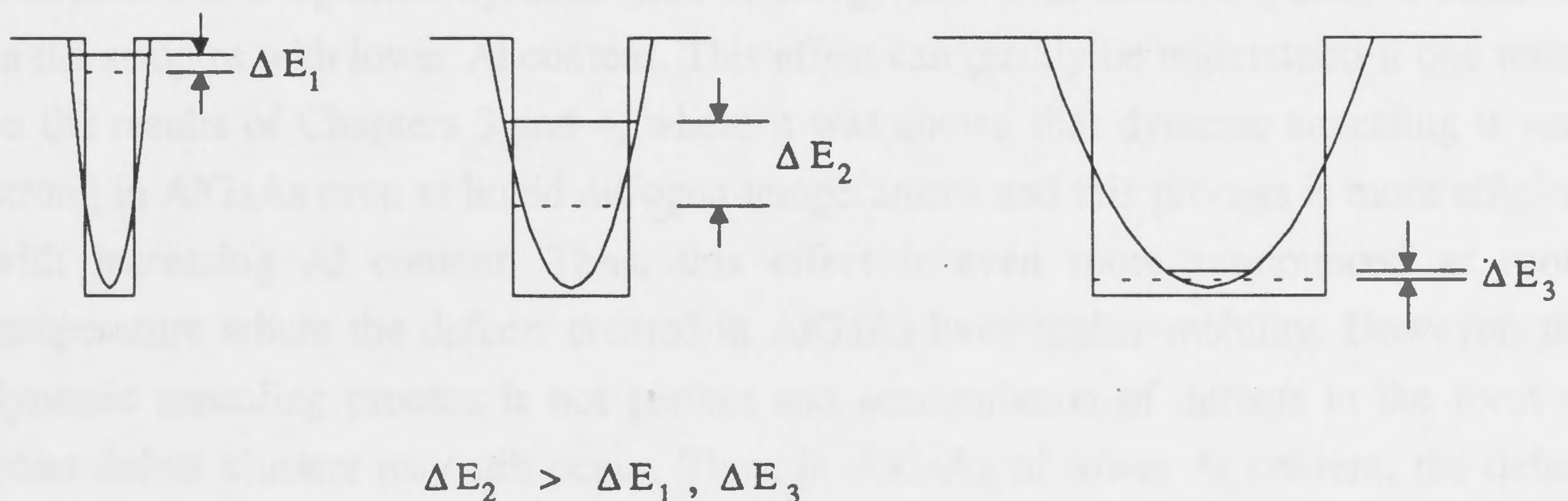

Fig. 6-19 A schematic showing the effect of well width on the energy shift. The range of energy shift in the narrowest well is limited by the barriers while in the widest well the energy shift is limited by the continuum limit.

A very similar dose dependence is observed in samples with $Al_{0.75}Ga_{0.25}As$ barriers. Although larger intermixing is expected in this system, due to the larger concentration gradient across the GaAs-AlGaAs interface, this is not observed here. This effect can be understood in terms of the increased incorporation of impurities, such as oxygen, in AlGaAs of high Al content in MOCVD grown material. It is well known that MOCVD-grown AlGaAs with standard trimethyaluminium (TMA) precursors will result in the incorporation of substantial amounts of oxygen and this effect is increased with

increasing Al content.[64,65] Furthermore, oxygen is known to be a non-radiative deep donor in AlGaAs which degrade the luminescence efficiency.[64,65] This is further supported by the weaker PL intensities in samples with $Al_{0.75}Ga_{0.25}As$ barriers in comparison to that of $Al_{0.54}Ga_{0.46}As$ barriers (Fig. 6-9). Furthermore, no PL signal was detected in the QW samples with AlAs barriers. The presence of oxygen may also affect the intermixing mechanism by forming complexes with the point defects during irradiation and/or annealing.[57,58] Since point defects are responsible for intermixing, the formation of oxygen-related complexes will deplete the point defect concentration and hence, retard the diffusion of the point defects. Thus, intermixing is somewhat suppressed for the samples with higher Al content. Moreover, the higher thermal stability of these complexes implies that less point defects may be liberated from these complexes to cause intermixing during annealing.

For samples with $Al_{0.3}Ga_{0.7}As$ barriers, the dose dependence results are somewhat different than in samples with $Al_{0.54}Ga_{0.46}As$ barriers. The lower degree of intermixing in $Al_{0.3}Ga_{0.7}As$ barriers is expected due to the smaller Al gradient across the GaAs-AlGaAs interface. More significantly, saturation in energy shift with increasing dose is observed in the samples with lower Al content. This effect can readily be understood if one refers to the results of Chapters 3 and 4, where it was shown that dynamic annealing is very strong in AlGaAs even at liquid nitrogen temperatures and this process is more efficient with increasing Al content. Thus, this effect is even more pronounced at room temperature where the defects created in AlGaAs have higher mobility. However, the dynamic annealing process is not perfect and accumulation of defects in the form of point defect clusters may still occur. Thus, in AlGaAs of lower Al content, the defect accumulation process becomes more efficient due to weaker dynamic annealing.

Hence, the following model is proposed to explain the observed behaviour. The use of light ions enables a large concentration of point defects to be accumulated in AlGaAs and this effect is enhanced with increasing Al content. During annealing these defects may then be injected (diffused) across the QW (heterointerface) to induce a larger degree of intermixing. However, the accumulation of these point defects in AlGaAs may reach a critical concentration level at a certain irradiation dose (higher for higher Al content), and ultimately agglomerate into more stable defects such as point defect clusters. Thus, for $Al_{0.3}Ga_{0.7}As$, the point defect saturation (defect agglomeration) occurs at a lower dose than, say, $Al_{0.54}Ga_{0.46}As$. Hence, during annealing, less point defects are available for the intermixing process, and consequently less energy shift occurs. If the annealing temperature/time is increased, these point defect clusters may break up to liberate more point defects to cause further intermixing, as observed in

samples with $Al_{0.3}Ga_{0.7}As$ barriers. In this study, no saturation in the point defect concentration is observed in samples with $Al_{0.54}Ga_{0.46}As$ and $Al_{0.75}Ga_{0.25}As$ up to a dose of at least 4.3×10^{16} cm^{-2}, but a saturation is observed in $Al_{0.3}Ga_{0.7}As$ at around 1×10^{16} cm^{-2}, consistent with the proposed model.

If irradiation is carried out at elevated temperatures, it is known that dynamic annealing is enhanced, whereby the defects created by the ions may annihilate *in situ* to restore crystallinity and hence the residual defect concentration may be lowered.[43,44,56,66,67] However, the type of residual defects may also be quite different at elevated irradiation temperatures.[43,44,56,66,67] Although the samples used in this chapter consist of multilayered structures, they are predominantly AlGaAs layers. The results from Chapters 3 and 4 show that dynamic annealing is very efficient in AlGaAs even at liquid nitrogen temperatures and obviously, this effect becomes more pronounced at room or elevated temperatures. The result of the strong dynamic annealing in AlGaAs is that ion beam-induced damage builds up in the form of point defects and point defect clusters. Being the lightest ion, the defects created by protons in AlGaAs are predominantly point defects. Although at elevated implant temperature additional *in situ* repair of crystalline damage may be achieved, these point defects may also acquire more energy to coalesce to form loops and larger clusters and thereby lower the system free energy. The formation of loops and clusters consumes point defects and as a result, less intermixing is achievable during annealing. Furthermore the higher thermal stability of these loops and clusters also act to retard intermixing during annealing. The results of reduction in the magnitude of energy shifts with increasing irradiation temperature suggests that point defects are predominantly created in AlGaAs by proton irradiation and the above scenario is most likely at elevated temperatures.

6.5.4 *Comparison with arsenic and oxygen irradiations*

Comparative study with heavier ions shows that arsenic may also create large energy shifts with reasonable optical recovery but at significantly lower doses (2-3 orders of magnitude lower than protons), in proportion to the higher displacement density of the heavier ions. However, with increasing irradiation dose, a saturation effect in the degree of intermixing is observed for the heavier ions. It is also observed that at lower displacement densities, heavier ions are more efficient for intermixing. This is not surprising since dilute cascades of light ions allow more efficient dynamic annealing, leaving fewer point defects for intermixing. However, as the irradiation dose (displacement density) is increased, the agglomeration of point defects into more stable

defects increases significantly for heavier ions, due to the larger and denser damage cascades caused by the heavy ions. Hence, a saturation in the energy shift is observed in heavier ions with increasing irradiation dose. Unlike proton irradiation, the results for heavier ions show that intermixing can be improved with elevated irradiation temperature, similar to some previous reports.[7,19,24] However, the issue of irradiation temperature dependence in intermixing is not very well understood and indeed, there have been several reports that the ion beam mixing rate in III-V compound semiconductors is a complicated function of irradiation temperature, whereby it increases until a critical temperature is reached after which it drops markedly.[68,69] Although the results in this chapter do not resolve this issue completely, they provide further insight into this issue.

It is proposed that the difference in the elevated irradiation temperature results between heavy and light ions is related to the fine balance between the defects created by the incoming ions and the strong dynamic annealing in AlGaAs. The size of the damage cascades created by heavier ions is reduced at elevated temperature[19,43,44,56,66,67] and hence, the overlap of these cascades created by the individual ion track to form more stable defects is proportionately reduced. This effect is further enhanced by the strong dynamic annealing in AlGaAs. Thus, a small improvement in intermixing is observed with increasing irradiation temperature. With protons, the strong dynamic annealing in AlGaAs and the small size of the damage clusters means that increasing the irradiation temperature has very little effect on the overlap of these cascades, since the defects created are predominantly point defects. However, at higher temperatures, these points defects become extremely mobile and agglomerate into more stable defects to lower the system's free energy. Hence, intermixing is retarded in this case.

The results for oxygen ions are somewhat similar to that of arsenic ions, with a saturation in the energy shifts observed with increasing dose and the implant temperature dependence on intermixing are similar. However, the lower degree of intermixing (for a fixed displacement density) may be attributed to the chemical effect of oxygen which can easily form complexes with defects and/or Al bonds in III-V materials.[57,58] The formation of these complexes consumes point defects and hence less are available for intermixing during annealing. The thermal stability of the complexes implies that higher annealing temperatures and/or longer annealing times are required to break these bonds to free the Al atoms. This effect is not unlike the effect described earlier for samples with high Al content, where grown-in impurities such as oxygen can also retard intermixing. Although Weiss *et. al.*[18] reported that large energy shifts may be

obtained for oxygen irradiated samples, the annealing temperatures were quite high (≥ 1000 °C).

6.6 Conclusions

The results from this chapter show that the highest energy shifts (intermixing), up to ~200 meV, may be achieved with proton irradiation. Although higher irradiation doses are required, good recovery in the optical properties may be achieved by standard annealing conditions. Furthermore, the results from the previous chapter show that complete recovery in the electrical properties in GaAs may be achieved by annealing above 600 °C. The use of heavier ions, such as arsenic, can also achieve similar results but at significantly lower doses. However, with increasing dose, heavier ions may inhibit the interdiffusion process due to the formation of more stable clusters and extended defects which consume point defects that are required for intermixing. Although oxygen is a good candidate for electrical isolation, it should be avoided for intermixing applications, where oxygen-related complexes may be easily formed during bombardment and/or annealing which then retards intermixing.

The results from this work give new insight into the understanding of optimising wavelength shifting by ion irradiation. These results and their understanding are important for novel optoelectronic device applications such as wavelength-shifted QW lasers. The results from proton irradiation show that protons are the best candidate for applications that require an ion beam-induced intermixing process. Thus, the results of proton irradiations in the fabrication of these lasers which will be discussed in the next chapter.

References

[1] W.D. Laidig, N. Holonyak, Jr., M.D. Camras, K. Hess, J.J. Coleman, P.D. Dapkus and J. Bardeen, "Disorder of an AlAs-GaAs superlattice by impurity diffusion," *Appl. Phys. Lett.* **38**, 776-778 (1981).

[2] See for example review article by D.G. Deppe and N. Holonyak, Jr., "Atom diffusion and impurity-induced disordering in quantum well III-V semiconductor heterostructures," *J. Appl. Phys.* **64**, R93-R113 (1988) and references therein.

[3] J.J. Coleman, P.D. Dapkus, C.G. Kirkpatrick, M.D. Camras and N. Holonyak, Jr., "Disorder of an AlAs-GaAs superlattice by silicon implantation," *Appl. Phys. Lett.* **40**, 904-906 (1982).

[4] Y. Hirayama, Y. Horikoshi and H. Okamoto, "Interdiffusion of Al and Ga in Si-implanted GaAs-AlAs superlattice," *Jpn. J. Appl. Phys.* **23**, 1568-1572 (1984).

[5] J. Ralston, G.W. Wicks, L.F. Eastman, B.C. De Cooman and C.B. Carter, "Defect structure and intermixing of ion-implanted $Al_xGa_{1-x}As$/GaAs superlattices," *J. Appl. Phys.* **59**, 120-123 (1986).

[6] J. Cibert, P.M. Petroff, D.J. Werder, S.J. Pearton, A.C. Gossard and J.H. English, "Kinetics of implantation enhanced interdiffusion of Ga and Al at GaAs-$Ga_xAl_{1-x}As$ interfaces," *Appl. Phys. Lett.* **49**, 223-225 (1986).

[7] E.A. Dobsiz, B. Tell, H.G. Craighead and M.C. Tamargo, "Disordering of AlAs-GaAs superlattices by Si and S implantation at different implant temperatures," *J. Appl. Phys.* **60**, 4150-4153 (1986).

[8] S.-T. Lee, G. Braunstein, P. Fellinger, K.B. Kahen and G. Rajeswaran, "Disordering of Si-implanted GaAs-AlGaAs superlattices by rapid thermal annealing," *Appl. Phys. Lett.* **53**, 2531-2533 (1988).

[9] E.P. Zucker, A. Hashimoto, T. Fukunaga and N. Watanabe, "Ion-implanted Zn diffusion and impurity-induced disordering of an AlGaAs superlattice," *Appl. Phys. Lett.* **54**, 564-566 (1989).

[10] K.B. Kahen and G. Rajeswaran, "Study of the interdiffusion of GaAs-AlGaAs interfaces during rapid thermal annealing of ion-implanted structures," *J. Appl. Phys.* **66**, 545-551 (1989).

[11] S. Chen, S.-T. Lee, G. Braunstein and T.Y. Tan, "Void formation and inhibition of layer intermixing in ion-implanted GaAs/AlGaAs superlattices," *Appl. Phys. Lett.* **55**, 1194-1196 (1989).

[12] L.J. Guido, K.C. Hsieh, N. Holonyak, Jr., R.W. Kaliski, V. Eu, M. Feng and R.D. Burnham, "Impurity induced layer disordering of Si implanted $Al_xGa_{1-x}As$-GaAs quantum-well heterostructures : layer disordering via diffusion from extrinsic dislocation loops," *J. Appl. Phys.* **61**, 1329-1334 (1987).

[13] K. Kash, B. Tell, P. Grabbe, E.A. Dobsiz, H.G. Craighead and M.C. Tamargo, "Aluminum ion-implanted enhanced intermixing of GaAs-AlGaAs quantum well structures," *J. Appl. Phys.* **63**, 190-194 (1988).

[14] B. Elman, E.S. Koteles, P. Melman and C.A. Armiento, "GaAs/AlGaAs quantum-well intermixing using shallow ion implantation and rapid thermal annealing," *J. Appl. Phys.* **66**, 2104-2107 (1989).

[15] H. Leier, A. Forchel, G. Hörcher, J. Hommel, S. Bayer, H. Rothfritz, G. Weimann and W. Schlapp, "Mass and dose dependence of ion-implantation-induced intermixing of GaAs/GaAlAs quantum-well structures," *J. Appl. Phys.* **67**, 1805-1813 (1990).

[16] E.G. Bithell, W.M. Stobbs, C. Phillips, R. Eccleston and R. Gwilliam, "Correlated transmission electron microscopy and photoluminescence studies of the Se^+-ion implantation of a GaAs/(Al,Ga)As multiple quantum well," *J. Appl. Phys.* **67** 1279-1287 (1990).

[17] K.B. Kahen, D.L. Peterson and G. Rajeswaran, "Effect of ion implantation dose on the interdiffusion of GaAs-AlGaAs interfaces," *J. Appl. Phys.* **68**, 2087-2090 (1990).

[18] B.L. Weiss, I.V. Bradley, N.J. Whitehead and J.S. Roberts, "Disordering of AlGaAs/GaAs quantum well structures using low dose oxygen implantation," *J. Appl. Phys.* **71**, 5715-5717 (1992).

[19] R. Kalish, L.C. Feldman, D.C. Jacobson, B.E. Weir, J.L. Merz, L.-Y. Kramer, K. Doughty, S. Stone and K.-K. Lau, "Implantation induced changes in quantum well structures," *Nucl. Instrum. Methods* **B80/81**, 729-733 (1993).

[20] G.F. Redinbo, H.G. Craighead and J.M. Hong, "Proton implantation intermixing of GaAs/AlGaAs quantum wells," *J. Appl. Phys.* **74**, 3099-3102 (1993).

[21] P.J. Poole, P.G. Piva, M. Buchanan, G.C. Aers, A.P. Roth, M. Dion, Z.R. Wasilweski, E.S. Koteles, C, Charbonneau and J. Beauvais, "The enhancement of quantum well intermixing through repeated ion implantation," *Semicond. Sci. Technol.* **9**, 2134-2137 (1994).

[22] C. Vieu, "Selective mixing of GaAs/(Ga,Al)As interfaces by Ga^+ implantation," *Defect and Diffusion Forum*, **119-120**, 127-174 (1995).

[23] P.J. Poole, S. Charbonneau, G.C. Aers, T.E. Jackman, M. Buchanan, M. Dion, R.D. Goldberg and I.V. Mitchell, "Defect diffusion in ion implanted AlGaAs and InP : consequences for quantum well intermixing," *J. Appl. Phys.* **78**, 2367-2371 (1995).

[24] S. Charbonneau, P.J. Poole, P.G. Piva, G.C. Aers, E.S. Koteles, M. Fallahi, J.-J. He, J.P. McCaffrey, M. Buchanan, M. Dion, R.D. Goldberg and I.V. Mitchell,

"Quantum well intermixing for optoelectronic integration using high energy ion implantation," *J. Appl. Phys.* **78**, 3697-3705 (1995).

[25] R.K. Kupka and Y. Chen, "Gallium-implantation-enhanced intermixing of close-surface GaAs/AlAs/AlGaAs double-barrier quantum wells," *J. Appl. Phys.* **78**, 2355-2361 (1995).

[26] E.S. Koteles, B. Elman, P. Melman, J.Y. Chi and C.A. Armiento, "Quantum well shape modification using vacancy generation and rapid thermal annealing," *Opt. Quantum Electron.* **23**, S779-S787 (1991).

[27] T.E. Schlesinger and T. Keuch, "Determination of the interdiffusion of Al and Ga in undoped (Al,Ga)As/GaAs quantum wells," *Appl. Phys. Lett.* **49**, 519-521 (1986).

[28] L.J. Guido, N. Holonyak, Jr., K.C. Hsieh, R.W. Kaliski, W.E. Plano, R.D. Burnham, R.L. Thornton, J.E. Elper and T.L. Paoli, "Effects of dielectric encapsulation and As overpressure in Al-Ga interdiffusion in $Al_xGa_{1-x}As$-GaAs quantum-well heterostructures," *J. Appl. Phys.* **61**, 1372-1379 (1987).

[29] L.J. Guido, N. Holonyak, Jr., K.C. Hsieh and J.E. Baker, "Depth-dependent native-defect-induced layer disordering in $Al_xGa_{1-x}As$-GaAs quantum well heterostructures," *Appl. Phys. Lett.* **54**, 262-264 (1989).

[30] K.B. Kahen, D.L. Peterson, G. Rajeswaran and D.J. Lawrence, "Properties of Ga vacancies in AlGaAs materials," *Appl. Phys. Lett.* **55**, 651-653 (1989).

[31] X. Wen, J.M. Chi, E.S. Koteles, B. Elman and P. Melman, "Processing parameters for selective intermixing of GaAs/AlGaAs quantum wells," *J. Electron. Mater.* **19**, 539-542 (1989).

[32] M. Ghisoni, P.J. Stevens, G. Parry and J.S. Roberts, "Post-growth tailoring of the optical properties of GaAs/AlGaAs quantum well structures," *Opt. Quantum Electron.* **23**, S915-S924 (1991).

[33] H. Peyre, J. Camassel, W.P. Gillin, K.P. Homewood, R. Grey, "Thermally induced change in the profile of GaAs/AlGaAs quantum wells," *Mater. Sci. Eng.* **B28**, 332-336 (1994).

[34] I. Gontijo, Y.S. Yang, R.M. De La Rue, C.M. Sotomayor Torres, J.S. Roberts and J.H. Marsh, "Photoreflectance and photoluminescence of partially intermixed GaAs/AlGaAs double quantum wells," *J. Appl. Phys.* **76**, 5434-5438 (1994).

[35] Y.T. Oh, T.W. Kang, C.Y. Hong, K.T. Kim and T.W. Kim, "The relation between Ga vacancy concentrations and diffusion lengths in intermixed GaAs/$Al_{0.35}Ga_{0.65}As$ multiple quantum wells," *Solid State Comm.* **96**, 241-244 (1995).

[36] Y. Hirayama, Y. Suzuki, S. Tarucha and H. Okamoto, "Compositional disordering of GaAs-$Al_xGa_{1-x}As$ superlattice by Ga focused ion beam

implantation and its application to submicron fabrication," *Jpn. J. Appl. Phys.* **24**, L516-L518 (1985).

[37] R.P. Bryan, J.J. Coleman, L.M. Miller, M.E. Givens, R.S. Averback and J.L. Klatt, "Impurity induced disordered quantum well heterostructure stripe geometry lasers by MeV oxygen implantation," *Appl. Phys. Lett.* **55**, 94-96 (1989).

[38] T. Hirata, M. Maeda, M. Suehiro and H. Hosomatsu, "GaAs/AlGaAs GRIN-SCH-SQW DBR laser diodes with passive waveguides integrated by compositional disordering of the quantum well using ion implantation," *Jpn. J. Appl. Phys.* **29**, L961-L963 (1990).

[39] P.L.K. Wa, "Intermixing of multiple quantum wells for all-optical integrated circuits," *Opt. Quantum Electron.* **23**, S925-S939 (1991).

[40] J.H. Marsh, S.I. Hansen, A.C. Bryce and R.M. de la Rue, "Applications of neutral impurity disordering in fabricating low-loss optical waveguides and integrated devices," *Opt. Quantum Electron.* **23**, S941-S957 (1991).

[41] F.E. Prins, G. Lehr, H. Schweizer and G.W. Smith, "GaAs/AlGaAs quantum dots by implantation induced intermixing," *Appl. Phys. Lett.* **63**, 1402-1404 (1993).

[42] C. Kaden, H.-P. Gauggal, V. Hofsäss, A. Hase, H. Schweizer and H. Künzel, "Gain coupled distributed feedback lasers realized by masked implantation enhanced intermixing," *Appl. Phys. Lett.* **65**, 3170-3172 (1994).

[43] J.S. Williams and J.M. Poate, editors, *Ion Implantation and Beam Pocessing*, Academic Press, Sydney (1984).

[44] J.S. Williams, "Ion induced damage and dynamic annealing processes," *Trans. Mater. Res. Soc. Jpn.* **17**, 417-423 (1994).

[45] K. Steeples, G. Dearnaley and A.M. Stineham, "Hydrogen-ion bombardment of GaAs," *Appl. Phys. Lett.* **36**, 981-983 (1980).

[46] J.M. Zavada, H.A. Jenkinson, R.G. Sarkis and R.G. Wilson, "Hydrogen depth profiles and optical characterization of annealed, proton-implanted n-type GaAs," *J. Appl. Phys.* **58**, 3731-3734 (1985).

[47] S.J. Pearton, F. Ren, S.N.G. Chu, C.R. Abernathy, W.S. Hobson and R.G. Elliman, "Defects and ion redistribution in implant-isolated GaAs-based device structures," *J. Appl. Phys.* **74**, 6580-6586 (1993).

[48] H.J. Hay, FASTRIM is a modified version of TRIM85-90 which takes into account the multilayer target (interfaces) problems inherent with TRIM (unpublished).

[49] J.F. Ziegler, J.P. Biersack and U. Littmark, *The Stopping and Range of Ions in Solids*, vol. 1, Pergamon, New York (1989).

[50] K.L. Wang, Y.H. Lee and J.W. Corbett, "Defect distribution near the surface of electron-irradiated silicon," *Appl. Phys. Lett.* **33**, 547-548 (1978).

[51] C. Jagadish, B.G. Svensson, N. Hauser and J.S. Williams, "Deep level transient spectroscopy study of defects in megaelectronvolt germanium ion implanted silicon," *Thin Solid Films* **222**, 173-175 (1992).

[52] Y. Masumoto and T. Tsuchiya, "Optical study of $Al_xGa_{1-x}As$-AlAs ternary alloy multi-quantum-well structures around two Γ-X crossovers," *J. Physical Soc. Jpn.* **57**, 4403-4408 (1988).

[53] D.B. Holt, C.E. Norman, G.Salviati, S. Franchi and A. Bosacchi, "Type II indirect and type I direct recombinations in GaAs/AlAs single quantum wells," *Mater. Sci. Eng.* **B9**, 285-288 (1991).

[54] C.N. Yeh, L.E. NcNeil, L.J. Blue and T. Daniels-Race, "Measurement of the GaAs/AlAs valence-band offset from a single quantum well near the Γ-X crossover," *J. Appl. Phys.* **77**, 4541-4543 (1995).

[55] F.L. Vook, "Radiation damage during ion implantation," in *Defects in Semiconductors*, Inst. Phys. Conf. Ser. 16, 60-71 (1972).

[56] D.K. Sadana, "Mechanism of amorphization and recrystallization in ion implanted III-V compound semiconductors," *Nucl. Instrum. Methods* **B7/8**, 375-386 (1985).

[57] M. Skorowski, "Oxygen in gallium arsenide," in *Deep Centers in Semiconductors : A State-of-the-Art Approach*, S.T. Pantelides, editor, Chp. 4, 379-406, Gordon and Breach Science Publishers, Switzerland (1992) and references therein.

[58] S.J. Pearton, M.P. Iannuzzi, C.L. Roberts, C.L. Reynolds, Jr. and L. Peticolas, "Formation of thermally high-resistivity AlGaAs by oxygen implantation," *Appl. Phys. Lett.* **52**, 395-397 (1988).

[59] J. Crank, *The Mathematics of Diffusion*, Oxford University Press, Oxford, 1975.

[60] P.M. Petroff, "Transmission electron microscopy of interfaces in III-V compound semiconductors," *J. Vac. Sci. Technol.* **14**, 973-978 (1977).

[61] R.M. Fleming, D.B. McWhan, A.C. Gossard, W. Wiegmann and R.A. Logan, "X-ray diffraction study of interdiffusion and growth in $(GaAs)_n(AlAs)_n$ multilayers," *J. Appl. Phys.* **51**, 357-363 (1980).

[62] J.A. Van Vechten, "Intermixing of an AlAs-GaAs superlattice by Zn diffusion," *J. Appl. Phys.* **53**, 7082-7084 (1982).

[63] S. Mitra and J.P. Stark, "Role of vacancies and implantation defects in GaAs/AlAs superlattice intermixing," *J. Mater. Sci.* **26**, 6650-6654 (1991).

[64] T.F. Kuech, "Metal-organic vapor phase epitaxy of compound semiconductors," *Mater. Sci. Rept.* **2**, 1-50 (1987) and references therein.

[65] G.B. Stringfellow, *Organometallic Vapor-Phase Epitaxy : Theory and Practice*, Chp. 7, 285-345, Academic Press, San Diego (1989) and references therein.

[66] J.S. Williams, R.G. Elliman, S.T. Johnson, D.K. Sengupta and J.M. Zemanski, "Ion beam processing of GaAs at elevated temperatures," *Mater. Res. Soc. Symp. Proc.* **144**, 355-360 (1089).

[67] W. Wesch, "Ion implantation in III-V compounds," *Nucl. Instrum. Methods* **B68**, 342-354 (1992).

[68] J.L. Klatt, R.S. Averback, D.V. Forbes and J.J. Coleman, "Temperature dependence of ion beam mixing in GaAs, AlAs, and GaAs/AlAs/GaAs," *Appl. Phys. Lett.* **63**, 976-978 (1993).

[69] D.V. Forbes, J.J. Coleman, J.L. Klatt and R.S. Averback, "Temperature dependence of ion-beam mixing in III-V semiconductors," *J. Appl. Phys.* **77**, 3543-3545 (1995).

Chapter 7

Optoelectronic device applications of ion beams

7.1 Introduction

Although the use of ion beams have been successfully demonstrated in optoelectronic devices and fabrication technology, most of them concerned electrical isolation[1-4] and waveguide properties.[5-9] However, these applications involve only passive devices. For ion irradiation to be a feasible technique in photonic integrated circuit (PIC) fabrication, tailoring of the electrical and optical properties in active components of the PICs may be required. In this chapter, the use of ion beams in device fabrication will be illustrated by two examples.

Firstly, ion beam induced-intermixing will be demonstrated in GaAs quantum well lasers whereby the emission wavelength of the lasers is fine-tuned (wavelength shifting). This has a very important application in optical communications, especially in wavelength-division-multiplexing (WDM) applications, where multiple lasers of different wavelengths may be integrated with ease onto a single chip as the WDM source. Similarly, this technique may be extended to the modification of other components, for example an integrated laser and waveguide/modulator circuit. Recently, there has been great interest in wavelength shifting in quantum well (QW) lasers created by intermixing and several reports have appeared on this subject. Most of the work in these reports have utilised impurity diffusion[10,11] or cap layer annealing[12,13] with only one report on the use of ion beams,[14] which involves InP-based materials. No report has appeared to date on wavelength shifting in ion implanted GaAs-based lasers. It has also been reported that the two material systems (InP and GaAs) behave quite differently in ion implantation-induced intermixing.[15] In P-based materials, interdiffusion may be enhanced by long-range defect migration, whereas, short range defect migration is the main intermixing process in the As-based systems. Hence, in the former case, defects may be incorporated far away from the active regions. This contrasting behaviour is potentially

a more critical issue in GaAs-based devices as this may cause severe reliability problems if defects have to be introduced in the vicinity of the active regions. However, the promising results from the previous chapter suggest that wavelength shifting in ion implanted GaAs lasers may be achieved.

The second application will deal with the use of ion beams for electrical isolation and intermixing in quantum wire (QWR) laser arrays grown on non-planar substrates. The area of quantum wire lasers is also of great interest because of lower threshold currents, higher efficiencies and narrower linewidths due to the additional degree of quantisation. Although there have been reports on the successful fabrication of quantum wire lasers on non-planar substrates, they were for single QWR lasers.[16-19] Since the power output of a single QWR laser is normally very small (μW), QWR lasers arrays may be used to increase the power output. However, due to various difficulties in fabrication, such as alignment, there has been very little work done in the area of arrays.[19,20] In this chapter, a self-aligned dual-implantation technique is proposed by utilising the natural geometry of V-grooves.

7.2 Experimental

7.2.1 Wavelength shifting in ion implanted GaAs lasers

The structure used in this study was a GRaded-INdex Separate-Confinement-Heterostructure (GRINSCH) grown by MOCVD. Initially a 0.5 μm GaAs buffer was grown on a (100) 2° off axis toward (110) n^+ GaAs wafer. A graded layer of 0.15 μm was then deposited, followed by a 1 μm thick $Al_{0.7}Ga_{0.3}As$ cladding layer. All layers up to this point were heavily doped *n*-type with Si to levels of ~10^{18} cm^{-3}. The dopant source was then removed and a further 0.1 μm of the cladding was grown followed by an optical confinement layer which was linearly graded from $Al_{0.7}Ga_{0.3}As$ to $Al_{0.3}Ga_{0.7}As$ over 0.15 μm. The active region consisted of three 7 nm GaAs QWs separated by 10 nm $Al_{0.3}Ga_{0.7}As$ barriers. A symmetrical optical confinement layer was then deposited. The V/III ratio was lowered before growing a 1.1μm top $Al_{0.7}Ga_{0.3}As$ cladding layer followed by another linearly graded layer of 0.15 μm. The V/III ratio was chosen such as to utilise the background C (*p*-type) doping in AlGaAs[21] to a level of 10^{17}-10^{18} cm^{-3}. Finally, a 0.3 μm GaAs layer was grown at 600 °C with Zn doping (~10^{19} cm^{-3}) to form the top contact layer. A schematic of the structure is shown in Fig. 7-1.

Protons of 220 keV were used for implantation in the dose range of 5×10^{13} to 1×10^{15} cm^{-2} at room temperature. To ensure direct comparison and minimise the effect of uniformity spread across the wafer, strips of about 2 mm wide were masked adjacent to implanted areas. The energy of the ions were chosen such that it corresponds to creating maximum displacements in the active region. The displacement profile, as calculated by FASTRIM,[22] is overlaid on the schematic of the structure in Fig. 7-1. After irradiation, the samples (both the implanted and masked regions) were annealed simultaneously at 900 °C for 30 s in a rapid thermal annealer. To minimise surface degradation at this temperature, the samples were placed face down in contact with a fresh piece of semi-insulating GaAs during annealing.

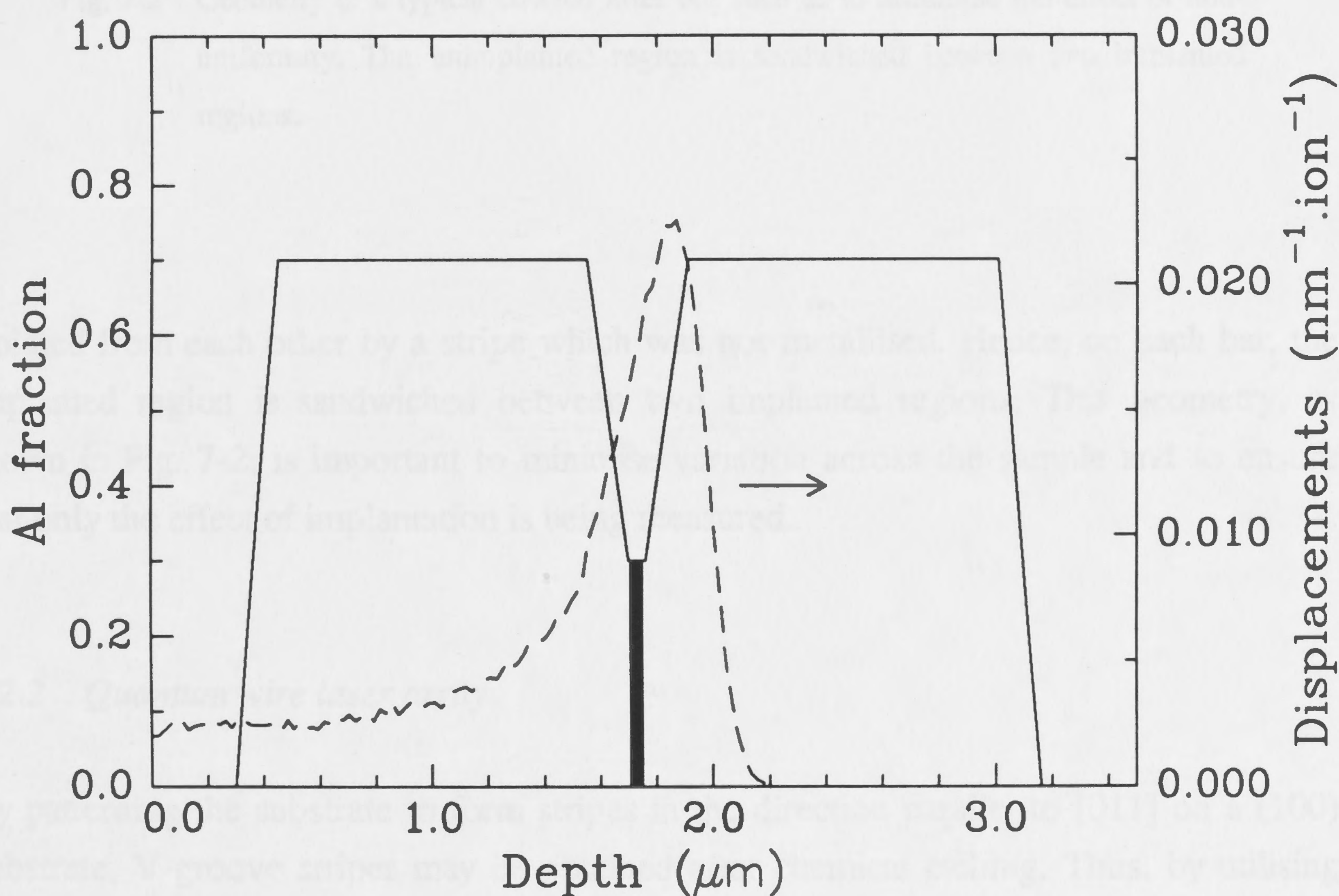

Fig. 7-1 Schematic (Al profile) of the GaAs GRINSCH QW laser structure used for wavelength shifting study. Overlaid is the calculated displacement density profile of 220 keV protons.

After annealing, the samples were fabricated into 50 μm stripe width broad-area lasers by standard photolithography techniques (see Appendix A). The lasers were then cleaved into bars with each bar containing about 20 lasers spaced 300 μm apart and

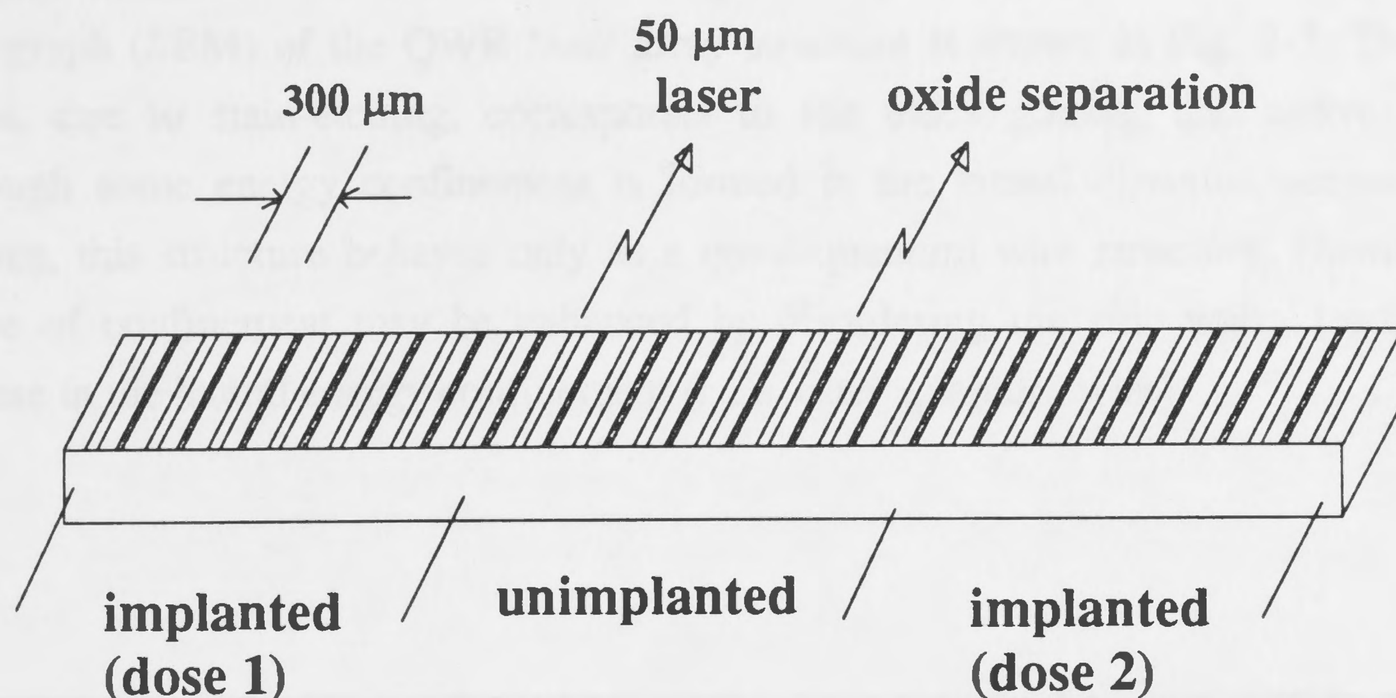

Fig. 7-2 Geometry of a typical cleaved laser bar such as to minimise the effect of non-uniformity. The unimplanted region is sandwiched between two implanted regions.

isolated from each other by a stripe which was not metallised. Hence, on each bar, the implanted region is sandwiched between two implanted regions. This geometry, as shown in Fig. 7-2, is important to minimise variation across the sample and to ensure that only the effect of implantation is being measured.

7.2.2 Quantum wire laser arrays

By patterning the substrate to form stripes in the direction parallel to [011] on a (100) substrate, V-groove stripes may be obtained after chemical etching. Thus, by utilising the properties of V-grooves, quantum wire-like structures may be grown.[16-20] Quantum confinement in the lateral direction is further enhanced by the difference in the growth rates between the (100) and the (111) surfaces, where the lower growth rate on the (111) surface leads to segregation of materials into the bottom of the V-groove. The patterning process was again done by standard photolithography techniques. Wet etching to form V-grooves was done in a controlled temperature environment to ensure consistent etch rates. Prior to loading the patterned substrate in the MOCVD reactor, various cleaning processes were carried out to ensure that the surface of the non-planar substrate was suitable for epitaxial growth. The details of the photolithography, etching and cleaning processes are listed in the Appendix A. A triple GaAs QW GRINSCH laser

structure similar to the one above was grown by MOCVD. An scanning electron micrograph (SEM) of the QWR laser array structure is shown in Fig. 7-3. The bright region, due to stain-etching, corresponds to the index guiding and active regions. Although some energy confinement is formed in the lateral direction across the V-grooves, this structure behaves only as a quasi-quantum wire structure. However, the degree of confinement may be enhanced by disordering the side walls, leading to a increase in the lateral energy confinement (i.e a 'truer' quantum wire).

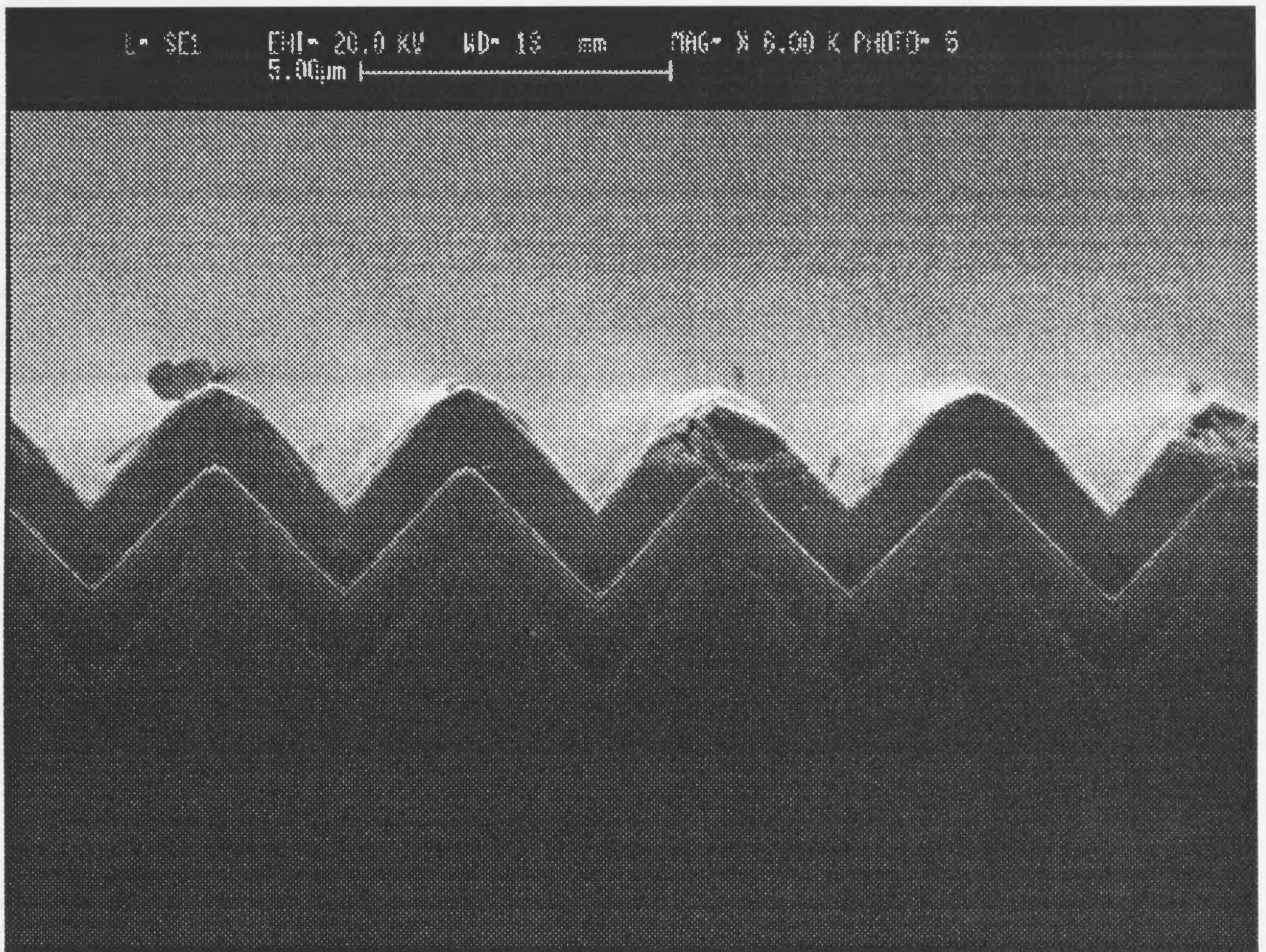

Fig. 7-3 Scanning electron micrograph of the QWR laser array. The bright band corresponds to the GRIN and active regions (stain-etched). The angle of the side walls to the (100) surface normal is about ±45°.

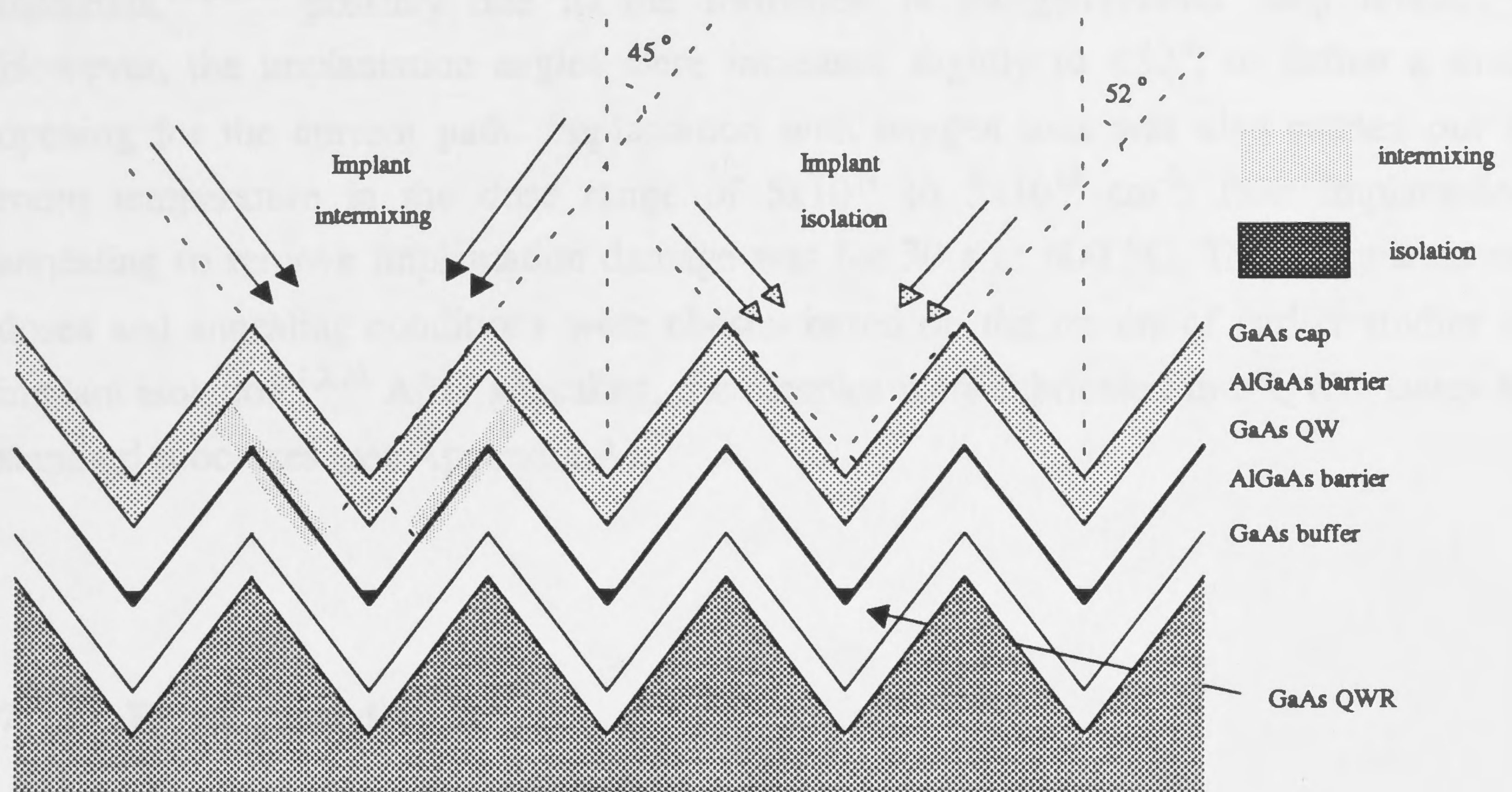

Fig. 7-4 Schematic of the dual-implantation scheme. A high energy double implantation at ±45° is side wall intermixing while a low energy implantation at ±52° is for defining current confinement regions.

By utilising the natural geometry of these structures, a simple self-aligned dual implantation scheme to create intermixing in the side walls and also current guiding/confinement regions is proposed. This scheme essentially involves a dual-ion implantation step at the angles formed by the non-planar surfaces and the surface normal, as indicated by the arrows in Fig. 7-4. From SEM results, these values are about ±45°. Hence, the quantum wire regions will essentially be free from the influence of the ions.

Implantation to create intermixing was carried out at implantation angles of ±45° with 2.5 MeV arsenic ions. This energy was chosen such that maximum damage was created on the active region of the side walls. Although protons would be a better candidate, the required energy for the protons (160 keV) to create maximum damage at similar depth was inaccessible by the ion implanter (see Chapter 2). Implantation was carried out at room temperature with doses in the range of $5x10^{12}$ to $5x10^{13}$ cm^{-2}. Annealing was at 900 °C for 30 s in a rapid thermal annealer using the proximity method as before. For current guiding regions (electrical isolation), shallow implantation with oxygen ions was used. It is well known that oxygen implantation can create highly resistive layer in III-V

materials,[1-3,23-24] possibly due to the formation of oxygen-related deep levels.[23,24] However, the implantation angles were increased slightly to ±52°, to define a small opening for the current path. Implantation with oxygen ions was also carried out at room temperature in the dose range of 5×10^{14} to 5×10^{15} cm^{-2}. Post implantation annealing to remove implantation damage was for 30 s at 600 °C. These implantation doses and annealing conditions were chosen based on the results of earlier studies of implant isolation.[1,2,23] After annealing, the samples were fabricated into QWR lasers by standard processes (see Appendix A).

7.3 Results and discussion

7.3.1 Wavelength shifting in ion implanted GaAs lasers

The light output-current (L-I) and spectral characteristics of the lasers were tested without any additional heat sinking under pulsed conditions of 1% or 30% duty cycle using a pulse width of 2 μs. The L-I curves of the implanted lasers (doses of 3×10^{14} and 1×10^{15} cm^{-2}) are compared to that of the unimplanted lasers as shown in Fig. 7-5 for a 400 μm long bar. In all cases, the curves are essentially identical and the threshold currents of the lasers are found to be about 90 mA (J_{th} ~0.45 kA/cm^2). Hence, the current threshold characteristics are not affected by the process of intermixing/implantation at these doses.

However, the emission spectra of the implanted lasers show a small but significant shift in the wavelengths as illustrated in Fig. 7-6. The spectra were collected under identical conditions at an injected current of 130 mA in all three cases. Since the L-I curves are almost identical in all three lasers and measurements were collected under identical conditions, the effect of implantation can be directly compared. This is a very important issue because if there is a large difference in the L-I curves or the spectral measurements are collected under somewhat different conditions, the thermal generation/dissipation of the lasers will be different and any comparison would be meaningless.

The lasing wavelengths of the implanted lasers are blue-shifted by 1 nm (2 meV) and 5 nm (10 meV) in comparison with the unimplanted sample, for the lower and higher doses, respectively. Although the wavelength shift is small, these values are what would be expected for a 7 nm GaAs QW with $Al_{0.3}Ga_{0.7}As$ barriers (see Chapter 6). It should

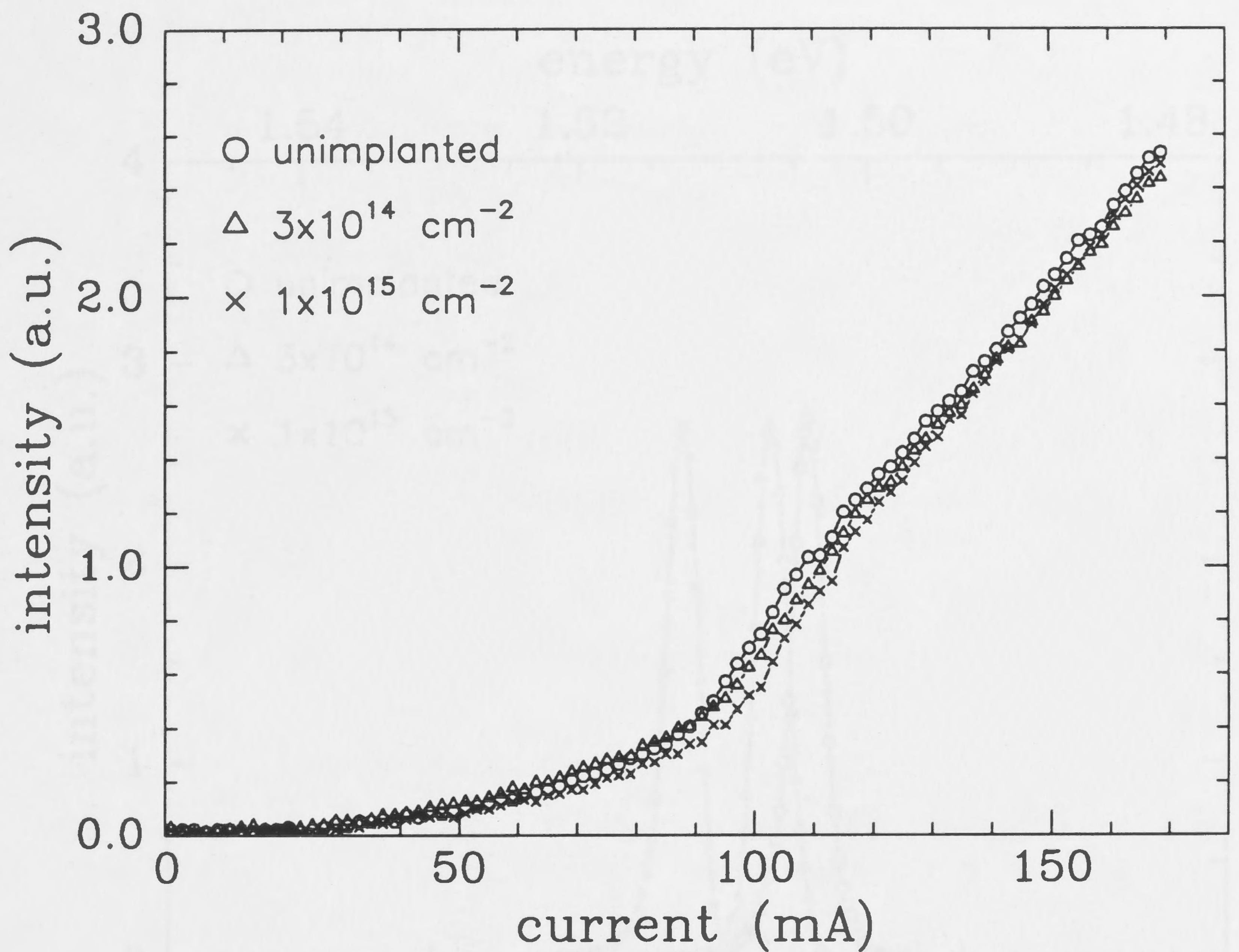

Fig. 7-5 L-I curves of the implanted and unimplanted lasers under pulsed condition with 2 μs pulses of 1% duty cycle.

be noted that at lower implantation doses (< $3x10^{14}$ cm^{-2}), no measurable wavelength shift is observed, there is a threshold dose to induce wavelength shifting in this structure. The L-I and spectral characteristics measured at 30% duty cycle are also similar to those at 1% duty cycle.

These results are the first reported successful demonstration of wavelength shifting in GaAs-AlGaAs laser structures by ion implantation. The results also show that ion implantation is a very promising and simple technique of integrating lasers of different wavelengths for optical communication applications, particularly as WDM sources. To achieve wavelength shifts of more than 5 nm, higher doses are required. However, at higher doses, reliability problems may arise as a result of the increase in defect concentration which may result in the formation of defect complexes and extended defects which are more stable during annealing. Although there is probably some

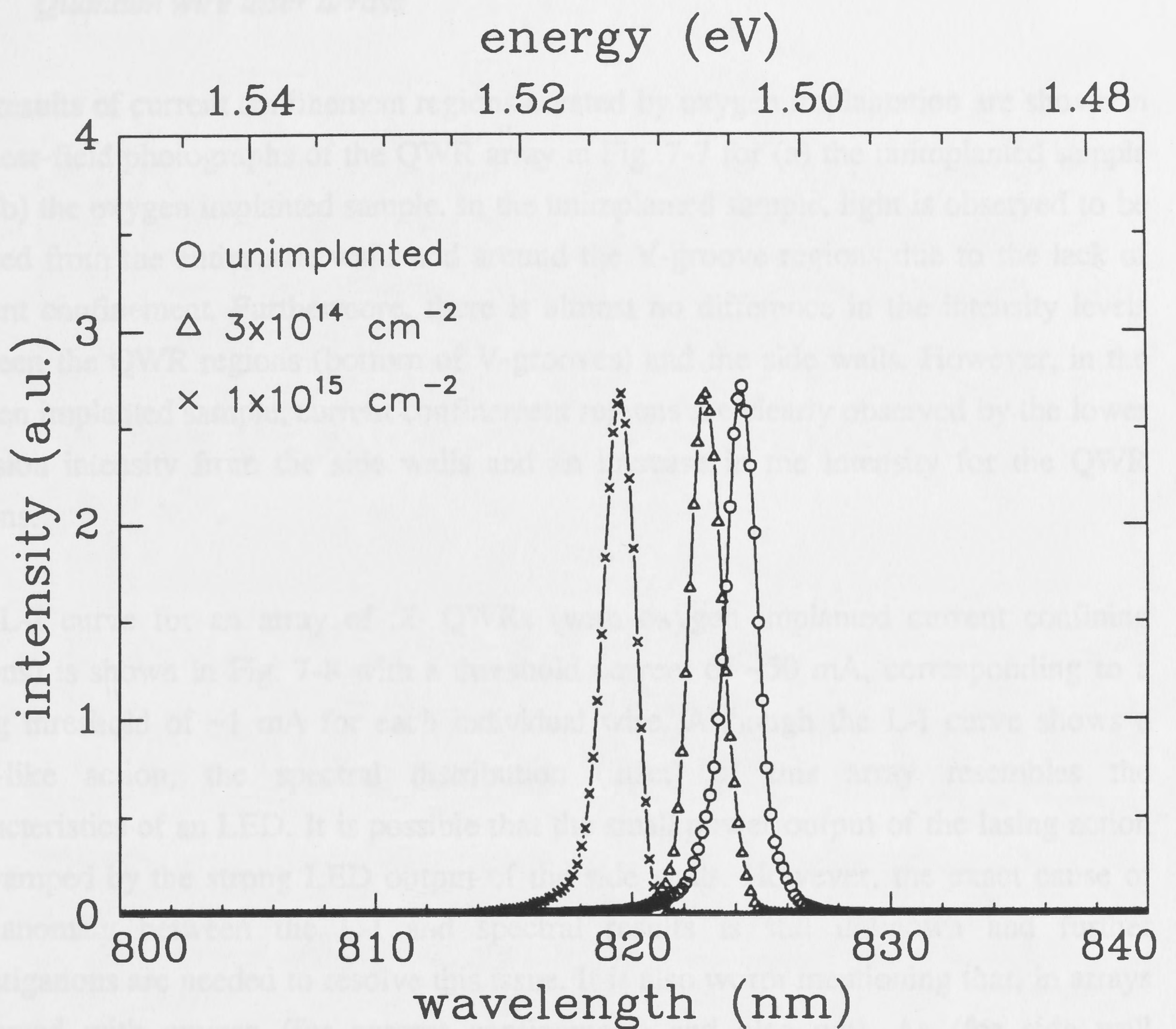

Fig. 7-6 Lasing spectra of the implanted and unimplanted lasers at an injected current of 130 mA under pulsed condition (2 μs pulses, 1% duty cycle).

intermixing effect due to the diffusion of Zn from the contact layer during annealing, it is expected that this effect is similar in the unimplanted and implanted (i.e. annealed only and implanted+annealed) samples, and hence, direct comparison of the effect of implantation alone is possible. Further studies are still required to optimise the degree of wavelength shift and examine the reliability issues of these lasers.

7.3.2 *Quantum wire laser arrays*

The results of current confinement regions created by oxygen implantation are shown in the near-field photographs of the QWR array in Fig. 7-7 for (a) the unimplanted sample and (b) the oxygen implanted sample. In the unimplanted sample, light is observed to be emitted from the entire side walls and around the V-groove regions due to the lack of current confinement. Furthermore, there is almost no difference in the intensity levels between the QWR regions (bottom of V-grooves) and the side walls. However, in the oxygen implanted sample, current confinement regions are clearly observed by the lower emission intensity from the side walls and an increase in the intensity for the QWR regions.

The L-I curve for an array of 50 QWRs (with oxygen implanted current confining regions) is shown in Fig. 7-8 with a threshold current of ~50 mA, corresponding to a lasing threshold of ~1 mA for each individual wire. Although the L-I curve shows a laser-like action, the spectral distribution (inset) of this array resembles the characteristics of an LED. It is possible that the small power output of the lasing action is swamped by the strong LED output of the side walls. However, the exact cause of this anomaly between the L-I and spectral results is still unknown and further investigations are needed to resolve this issue. It is also worth mentioning that, in arrays implanted with oxygen (for current confinement) and also with As (for side wall intermixing), similar results to that of oxygen only implanted samples have been obtained. Although several issues need to be addressed to achieve laser action, all indications (in particular, the current confinement) are that it can be achieved with further fine tuning. Thus, the feasibility of the proposed self-aligned dual-implantation technique for QWR laser array fabrication is very promising and has already generated interest in using this technique for QWR laser array fabrication.

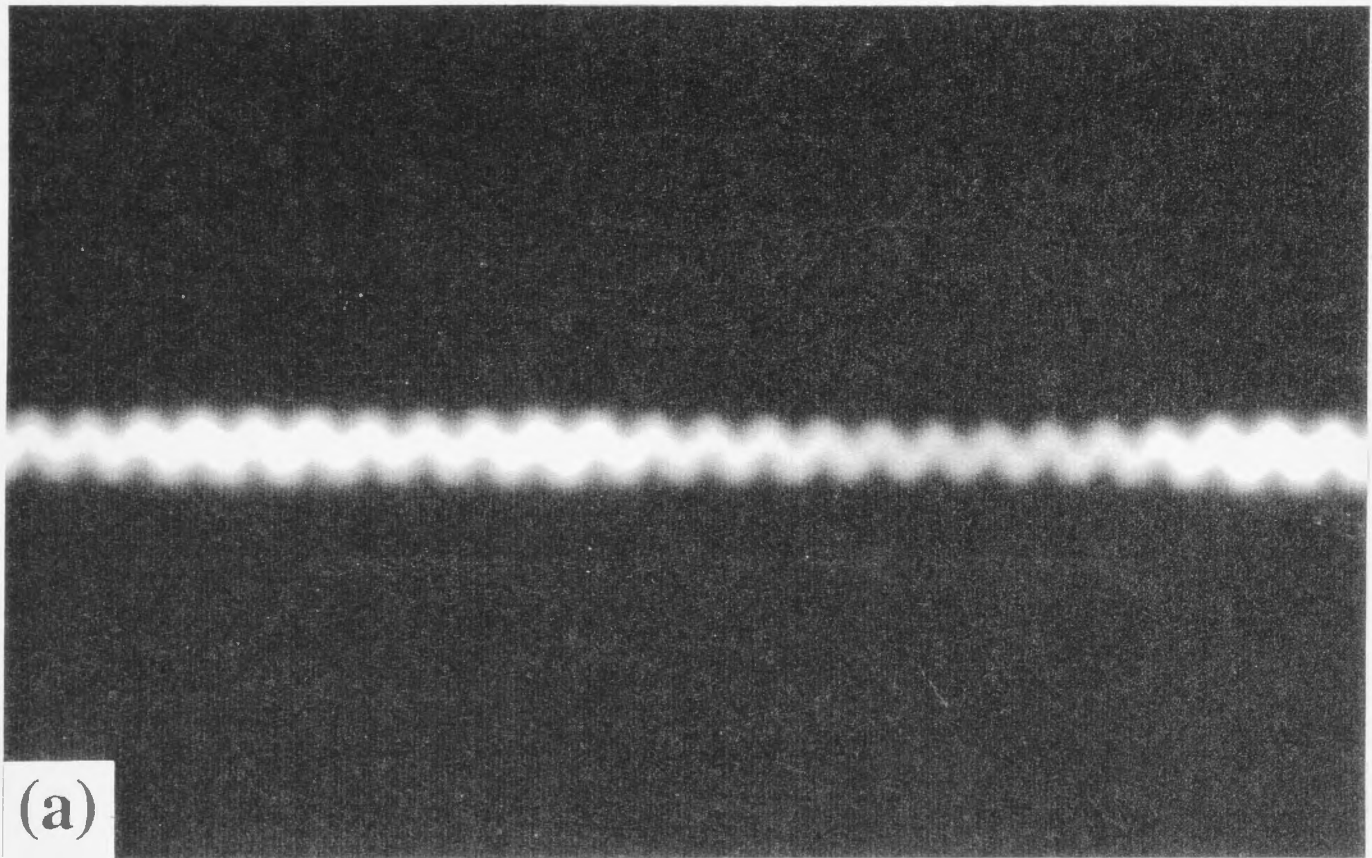

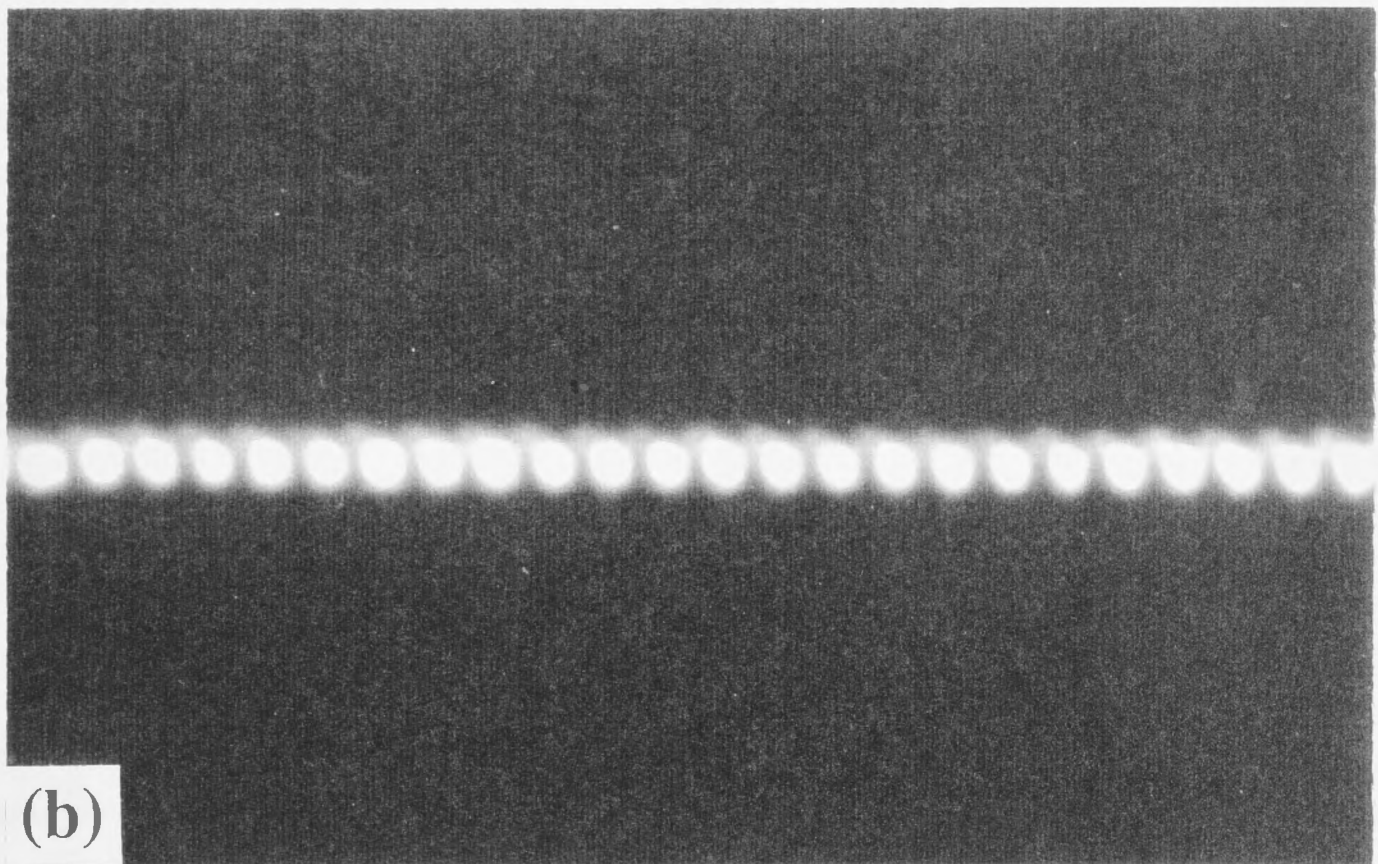

Fig. 7-7 Near-field pattern of the (a) unimplanted and (b) oxygen implanted (current confined) QWR array.

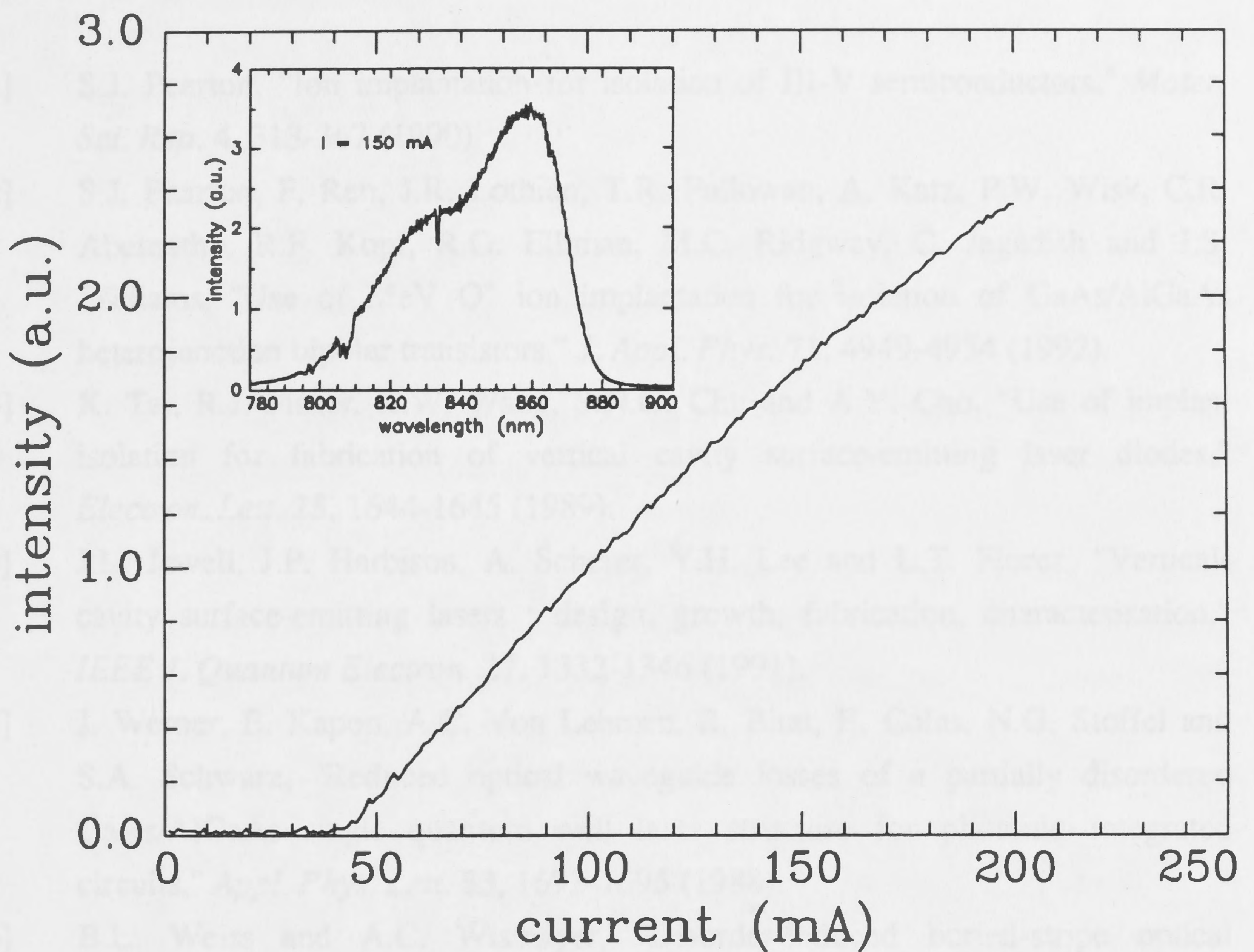

Fig. 7-8 L-I curve of a quantum wire array (50 QWRs) under CW condition. The inset show the spectrum of this array at an injected current of 150 mA (CW).

7.4 Conclusions

The use of ion beams to modify the band gap of a GaAs-AlGaAs laser has been successfully demonstrated by a shift in lasing wavelength by 5 nm with virtually no degradation in the threshold current characteristics. This technique is very promising in integrating multiple lasers of different wavelengths onto a single chip for WDM applications and can also be extended to the fabrication of other photonic integrated circuits.

A simple self-aligned dual-implantation technique is proposed and used to define current confinement regions in V-groove quantum wire lasers. This method can also be extended to create intermixing/disordering of the side walls such that the lateral energy confinement of the quantum wire regions may be enhanced.

References

[1] S.J. Pearton, "Ion implantation for isolation of III-V semiconductors," *Mater. Sci. Rep.* **4**, 313-367 (1990).

[2] S.J. Pearton, F. Ren, J.R. Lothian, T.R. Fullowan, A. Katz, P.W. Wisk, C.R. Abernathy, R.F. Kopf, R.G. Elliman, M.C. Ridgway, C. Jagadish and J.S. Williams, "Use of MeV O^+ ion implantation for isolation of GaAs/AlGaAs heterojunction bipolar transistors," *J. Appl. Phys.* **71**, 4949-4954 (1992).

[3] K. Tai, R.J. Fisher, K.W. Wang, S.N.G. Chu and A.Y. Cho, "Use of implant isolation for fabrication of vertical cavity surface-emitting laser diodes," *Electron. Lett.* **25**, 1644-1645 (1989).

[4] J.L. Jewell, J.P. Harbison, A. Scherer, Y.H. Lee and L.T. Florez, "Vertical-cavity surface-emitting lasers : design, growth, fabrication, characterisation," *IEEE J. Quantum Electron.* **27**, 1332-1346 (1991).

[5] J. Werner, E. Kapon, A.C. Von Lehmen, R. Bhat, E. Colas, N.G. Stoffel and S.A. Schwarz, "Reduced optical waveguide losses of a partially disordered GaAs/AlGaAs single quantum well laser structure for photonic integrated circuits," *Appl. Phys. Lett.* **53**, 1693-1695 (1988).

[6] B.L. Weiss and A.C. Wismayer, "Disorder-induced buried-stripe optical waveguides in GaAs/AlGaAs MQW material," *Electron. Lett.* **25**, 653-655 (1989).

[7] J.E. Zucker, K.L. Jones, B. Tell, K. Brown-Goeneler, C.H. Joyner, B.I. Miller and M.G. Young, "InGaAsP/InP quantum well buried heterostructure waveguides produced by ion implantation," *Electron. Lett.* **28**, 853-855 (1992).

[8] F. Xiong, T.A. Tombrello, H. Wang, T.R. Chen, H.Z. Chen, H. Morkoç and A. Yariv, "High efficiency single quantum well graded-index separate-confinement heterostructure lasers fabricated by MeV oxygen ion implantation," *Appl. Phys. Lett.* **54**, 730-732 (1989).

[9] R.P. Bryan, J.J. Coleman, L.M. Miller, M.E. Givens, R.S. Averback and J.L. Klatt, "Impurity induced disordered quantum well heterostructure stripe geometry lasers by MeV oxygen implantation," *Appl. Phys. Lett.* **55**, 94-96 (1989).

[10] Y. Nagai, K. Shigihara, S. Karakida, S. Kakimoto, M. Otsubo and K. Ikeda, "Characteristics of laser diodes with a partially intermixed GaAs-AlGaAs quantum well," *IEEE J. Quantum Electron.* **31**, 1364-1370 (1995).

[11] K.J. Beernink, D. Sun, R.L. Thornton and D.W. Treat, "Dual-wavelength AlGaAs/GaAs laser by selective removal of a quantum well in an asymmetric dual quantum well structure," *Appl. Phys. Lett.* **68**, 284-286 (1996).

[12] S. Bürkner, J.D. Ralston, S. Weisser, J. Rosenzweig, E.C. Larkins, R.E. Sah and J. Fleissner, "Wavelength tuning of high speed InGaAs-GaAs-AlGaAs pseudomorphic MQW lasers via impurity-free interdiffusion," *IEEE Photon. Tech. Lett.* **7**, 941-943 (1995).

[13] B.S. Ooi, S.G. Ayling, A.C. Bryce and J.H. Marsh, "Fabrication of multiple wavelength lasers in GaAs-AlGaAs structures using a one-step spatially controlled quantum-well intermixing technique," *IEEE Photon. Tech. Lett.* **7**, 944-946 (1995).

[14] P.J. Poole, S. Charbonneau, M. Dion, G.C. Aers, M. Buchanan, R.D. Goldberg and I.V. Mitchell, "Demonstration of an ion-implanted wavelength-shifted quantum-well laser," *IEEE Photon. Tech. Lett.* **8**, 16-18 (1996).

[15] P.J. Poole, S. Charbonneau, G.C. Aers, T.E. Jackman, M. Buchanan, M. Dion, R.D. Goldberg and I.V. Mitchell, "Defect diffusion rates in ion implanted AlGaAs and InP : Consequences for quantum well intermixing," *J. Appl. Phys.* **78**, 2367-2371 (1995).

[16] E. Kapon, D.M. Hwang and R. Bhat, "Stimulated emission in semiconductor quantum wire heterostructures," *Phys. Rev. Lett.* **63**, 430-433 (1989).

[17] E. Kapon, "Quantum wire lasers," *Proc. of the IEEE* **80**, 398-410 (1992).

[18] S. Tiwari, G.D. Pettit, K.R. Milkove, F. Legouse, R.J. Bavis and J.M. Woodall, "High efficiency and low threshold current strained V-groove quantum-wire lasers," *Appl. Phys. Lett.* **64**, 3536-3538 (1994).

[19] R. Bhat, E. Kapon, S. Simhony, E. Colas, D.M. Hwang, N.G. Stoffel and M.A. Koza, "Quantum wire lasers by OMCVD growth on nonplanar substrates," *J. Cryst. Growth* **107**, 716-723 (1991).

[20] E. Kapon, J.P. Harbison, C.P. Yun and L.T. Florez, "Patterned quantum well semiconductor laser arrays," *Appl. Phys. Lett.* **54**, 304-306 (1989).

[21] G.B. Stringfellow, in *Organometallic Vapor-Phase Epitaxy : Theory and Practice*, Chp. 7, 285-345, Academic Press, San Diego (1989).

[22] H.J. Hay, FASTRIM is a modified version of TRIM85-90 which takes into account the multilayer target (interfaces) problems inherent with TRIM (unpublished).

[23] S.J. Pearton, M.P. Iannuzzi, C.L. Reynolds, Jr. and L. Peticolas, "Formation of thermally stable high-resistivity AlGaAs by oxygen implantation," *Appl. Phys. Lett.* **52**, 395-397 (1988).

[24] M. Skorowski, "Oxygen in gallium arsenide," in *Deep Centers in Semiconductors : A State-of-the-Art Approach*, S.T. Pantelides, editor, Chp. 4, 379-406, Gordon and Breach Science Publishers, Switzerland (1992).

Chapter 8

Summary

Ion beam effects in GaAs-AlGaAs materials and devices have been investigated.

The ion beam-induced damage buildup and amorphisation processes at liquid nitrogen temperatures were systematically studied for 'bulk' $Al_xGa_{1-x}As$ of various Al mole fractions (x=0, 0.26, 0.49, 0.71, 0.83, 0.95 and 1). It was found that with increasing Al content, ion beam-induced damage became more difficult to accumulate in AlGaAs due to strong dynamic annealing which competed very strongly with damage production in AlGaAs even at liquid nitrogen temperatures. However, the dynamic annealing processes were not perfect and amorphisation in AlGaAs occurred at high implantation doses. A difference in the amorphisation threshold of more than two orders of magnitude dose was observed between GaAs and AlAs, despite a difference of only 30-40% in their physical parameters. Two different amorphisation processes were observed in AlGaAs depending on the Al content. At lower Al content (x < 0.85), amorphisation occurred *via* the overlap of individual damage cascades caused by the incoming ions. On the other hand, at very high Al content, this process occurred *via* an accumulation of defect clusters and extended defects until a critical density was reached when the crystal collapsed into an amorphous phase.

The damage and amorphisation processes became more complex in GaAs-AlGaAs multilayers due to the presence of heterointerfaces. Damage (amorphisation) built up preferentially in the GaAs layer, but there were narrow regions in the GaAs layer near the heterointerface in which amorphisation were suppressed by efficient dynamic annealing as a result of point defect injection across the interface from the AlGaAs layer. Nevertheless, the dynamic annealing processes were not perfect and these regions collapsed into an amorphous phase with increased implantation doses. Once, amorphisation occurred in these regions, the amorphous phase acted as nucleation sites for the progression of the amorphous phase into the AlGaAs layers. Dynamic annealing,

as mediated by defect trapping and defect migration, competed very strongly with damage production at the interface and residual damage was the result of a fine balance between these two processes. The presence of adjacent AlGaAs enhanced the recrystallisation of amorphous GaAs at low temperature, presumably by lowering the recrystallisation temperature through the supply/injection of mobile defects across the heterointerface.

The detailed studies in this work have provided new insights into the damage accumulation and amorphisation processes in AlGaAs which has led to further understanding of these processes in GaAs-AlGaAs multilayers. The understanding of these processes in multilayer structures is important for the successful use of ion implantation to incorporate controllable amounts of defects for device applications.

In a parallel study, a controllable amount of damage was introduced at low doses ($\leq 10^{10}$ cm^{-2}) into GaAs. In this dose regime, where discrete (simple) defects dominate, their creation and annealing behaviours were studied by the deep level transient spectroscopy technique. Proton irradiation provided invaluable insights into the generation of the point defects where discrete defect levels could be determined from the DLTS spectrum. Six electron traps were identified together with a broad U-band which was associated with the interaction between the defects, in particular the EL6 and the EL2 levels. The resulting carrier compensation profiles were also investigated by temperature dependent capacitance-voltage profiling. With heavier ions, such as oxygen or silicon, the resulting DLTS spectrum was dominated by the broad U-band, due to stronger defect interactions between damage cascades caused by the heavier ions. Full recovery of the electrical properties was achieved at 600 °C for samples implanted with protons but at higher temperatures ($\geq$ 800 °C) for oxygen or silicon implanted samples. In this low dose regime, no chemical effects were observed for either oxygen or silicon implantations. Both ion species resulted in similar type of defects which were predominantly intrinsic defects generated by the incoming ions. Such annealing studies of discrete defects provides a platform for using defects to modify the properties of multilayers and applications.

Indeed, ion implantation was used to induce intermixing in GaAs quantum well structures. Protons were very efficient in creating intermixing with the largest reported blue shift (> 200 meV) in the excitonic energies of the wells attained, with little loss in the photoluminescence intensities after annealing. This indicates that most of the optically-active defects were annihilated. Large energy shifts could also be obtained with heavier ions, such as arsenic, but at much lower implantation doses. Although no

saturation in the degree of intermixing was observed with protons, the use of heavier ions resulted in a saturation in the magnitude of energy shifts with increasing dose. With oxygen on the other hand, the degree of intermixing was reduced due the formation of oxygen-related complexes which were thermally more stable than simple point defects that are required to induce intermixing during annealing. The effects of Al content in the (AlGaAs) barriers have also been investigated. As the Al content in the barriers was increased, an enhancement in the degree of intermixing was observed, whereas at higher Al content, the degree of intermixing was retarded. This effect was associated with the increased incorporation of impurities (such as O) in high Al content AlGaAs grown by MOCVD.

Finally, ion implantation was used for the first time to successfully modify the band structure and hence, the emission wavelengths of quantum well lasers. Preliminary results showed that a 5 nm shift in wavelength was achievable in broad area GaAs-AlGaAs GRINSCH quantum well lasers with almost no degradation in the current threshold characteristics. This technique is very promising in integrating multiple lasers of different wavelengths onto a single chip for WDM applications and can also be extended for the fabrication of other photonic integrated circuits. Ion beam-induced electrical isolation was also used to selectively define current confinement regions in III-V semiconductors. A simple self-aligned dual-implantation technique was proposed and used to define current confinement regions in quantum wire laser arrays grown on V-groove patterned substrates. This self-aligned technique, which relies on defects and/or deep levels to create electrical isolation, was successfully demonstrated to confine the current paths through the quantum wire regions and thus, provided a very simple method of defining contact regions in quantum wire laser arrays without the need for further photolithography steps. This method can also be extended to create intermixing/disordering of the side walls of these V-groove structures such that the lateral energy confinement of the quantum wire regions may be enhanced.

This ambitious project has covered the area of epitaxial growth and ion beam processing of III-V semiconductors, characterisation of discrete and macroscopic defects, applications of controllable amounts of defects to optoelectronic structures. Device fabrication involving ion beam technique has been extremely successful. No previous study has succeeded in such a comprehensive investigation in this area which is only possible with unique cluster of facilities. This project is in a sense unique that it has addressed multilayer growth, ion beam processing, characterisation and device fabrication within a single theme. Very often than not, there is a gap in appreciation of the key issues of ion implantation science and technology by researchers in the

optoelectronic device area and *vice versa*. Therefore, this thesis has provided a platform to bridge this gap where an extensive and systematic study of the material aspects of ion beam processing in complex multilayer structures to address the critical parameters in device processing has been undertaken. This thesis also shows that the future for ion beam processing of III-V optoelectronic devices is promising and with further fine tuning, novel integrated devices are just around the corner.

Appendix A - Processing schedules

I. Photolithography

Standard process using AZ5214-E as a positive photoresist (suitable for wet etching)

1. Spin at 5000 rpm, 30 sec.
2. Soft bake at 85 °C, 15 min.
3. Exposure through mask, 12 sec.
4. Develop in AZ312 developer, 40-50 sec.
5. Hard bake at 115 °C, 2 min.

Image reversal process with AZ5214-E photoresist (suitable for metal lift-off)

1. Spin at 5000 rpm, 30 sec.
2. Soft bake at 85 °C, 15 min.
3. Exposure through mask, 3 sec.
4. Bake at 115 °C, 8 min.
5. Flood exposure, 12 sec.
6. Develop in AZ312 developer, 40-50 sec.

multiple exposures are possible with the image reversal process
(repeat step 3 above with mask over different positions)

II. Process overview for ridge waveguide lasers

1. Cleaning
   - rinsing in acetone
   - N_2 blow dry
   - 85 °C, 5 min. bake

2. Photoresist (AZ5214-E)
   - 5000 rpm, 30 sec. spin
   - 85 °C, 15 min. bake

3. Exposure
   - mask aligner, 12 sec. exposure with stripes mask parallel to (011)
   - develop (AZ312), 40-50 sec.
   - N_2 blow dry
   - 115 °C, 2 min. hard bake

4. Wet etching
   - $H_3PO_4 : H_2O_2 : H_2O = 3:1:1$
   - at 0 °C (ice bath), etch rate ~ 0.75 μm/min.
   - stop 0.1-0.2 μm before active region
   - rinse thoroughly with DI water
   - N_2 blow dry

5. Passivation
   - SiO_2 deposition (PECVD), 200-300 nm

6. Photoresist removal and oxide bake
   - remove photoresist with acetone
   - N_2 blow dry
   - bake oxide at 450 °C for 5 min. under Ar flow

7. Device isolation (optional, if laser bars required)
   - rinsing in acetone
   - N_2 blow dry
   - 85 °C, 5 min. bake
   - hexamethyldisilazane (HMDS), 5000 rpm, 30 sec.
   - AZ5214-E, 5000 rpm, 30 sec.
   - 85 °C, 15 min. bake
   - dark field mask, 3 sec. exposure with stripes aligned between ridges
   - 115 °C, 8 min. bake
   - flood exposure, 12 sec.
   - develop (AZ312), 40-50 sec.
   - rinse thoroughly with DI water
   - N_2 blow dry

8. Removal of native oxide
   - 10% HCl in H_2O, 1 min.
   - rinse thoroughly with DI water
   - N_2 blow dry

9. *p*-type contact metal evaporation
   - Au/Zn/Au (~20/50/100 nm) or Al (~150 nm)
   - rapid thermal annealing of contact at 430 °C, 1 min.

10. Polishing
    - mount with paraffin wax (surface facing down)
    - polish in steps of 20, 10 and 5 μm with gradual change to finer grade SiC paper
    - polish down to ~140 μm thick

- chemical polish with NaOCl to 100-120 μm
- remove sample in trichloroethylene (TCE)
- rinsing sample in isopropanol
- N_2 blow dry

11. *n*-type contact metal evaporation
    - Au/Ge (12% Ge by weight) ~150 nm
    - rapid thermal annealing of contact at 380 °C, 1 min.

12. Cleaving of mirror edges
    - scribe notch at edge with diamond scriber (L ≤ 1 mm)
    - cleave from the back with steel rod over a rubber mat
    - do not handle sample at the cleaved mirror edges

III. Process overview for growth of quantum wire structures on non-planar substrates

1. Cleaning
   - rinse in acetone
   - N_2 blow dry
   - 85 °C, 5 min. bake

2. Photoresist (AZ5214-E)
   - 5000 rpm, 30 sec. spin
   - 85 °C, 15 min. bake

3. Exposure
   - mask aligner, 12 sec. exposure with stripes parallel to $[01\bar{1}]$
   - develop (AZ312), 40-50 sec.
   - N_2 blow dry
   - 115 °C, 2 min. hard bake

4. Wet etching
   - $H_3PO_4 : H_2O_2 : H_2O = 3:1:1$ at 0 °C (ice bath)
   - etch until sharp and well defined V-grooves are obtained (inspect with high power optical microscope) (typically 4-5 min. for 2 μm wide stripes array)
   - rinse thoroughly with DI water
   - N_2 blow dry

5. Photoresist removal
   - rinse in acetone
   - to ensure complete removal, leave sample overnight in acetone (or use O plasma)

6. Cleaning
   - clean sample in hot trichloroethylene (TCE), hot acetone and hot methanol in this sequence for ~10 min. each
   - rinse thoroughly with DI water
   - N_2 blow dry

7. Oxide removal
   - immerse sample in concentrated HCl for 2 min.
   - rinse thoroughly with DI water
   - N_2 blow dry

8. Trim etch
   - $H_2SO_4 : H_2O_2 : H_2O = 20:1:1$ for 20 sec.
   - rinse thoroughly with DI water
   - leave sample in beaker of DI water

9. Growth on patterned V-grooves substrates
   - N_2 blow dry
   - load sample immediately in MOCVD reactor for growth

Appendix B - Publication list

Journals

1. Optical measurement of the distribution of damage in ion-implanted GaAs
P. Kraisingdecha, C. Shwe, M. Gal, H.H. Tan and C. Jagadish
Semiconductor Science and Technology **9**, 1489-1492 (1994).

2. Ion damage buildup and amorphization processes in $Al_xGa_{1-x}As$
H.H. Tan, C. Jagadish, J.S. Williams, J. Zou, D.J.H. Cockayne and A. Sikorski
Journal of Applied Physics **77**, 87-94 (1995).

3. Measurement of the distribution of damage in ion-implanted GaAs by differential reflectance spectroscopy
P. Kraisingdecha, M. Gal, H.H. Tan, C. Jagadish and J.S. Williams
Nuclear Instruments and Methods in Physics Research B **96**, 109-112 (1995).

4. Characterization of deep levels and carrier compensation created by proton irradiation in undoped GaAs
H.H. Tan, J.S. Williams and C. Jagadish
Journal of Applied Physics **78**, 1481-1487 (1995).

5. Picosecond carrier lifetime in GaAs implanted with high doses of As ions - an alternative material to low temperature GaAs for optoelectronic applications
A. Krotkus, S. Marcinkevicius, J. Jasinski, M. Kaminska, H.H. Tan and C. Jagadish
Applied Physics Letters **66**, 3304-3306 (1995).

6. High resistivity and picosecond carrier lifetime of GaAs implanted with MeV Ga ions at high fluences
C. Jagadish, H.H. Tan, J. Jasinski, M. Palczewska, M. Kaminska, A. Krotkus and S. Marcinkevicius
Applied Physics Letters **67**, 1724-1726 (1995).

7. A comparative study of deep levels created by low dose implantation of H, O and Si into MOCVD grown n-GaAs
H.H. Tan, J.S. Williams and C. Jagadish
Nuclear Instruments and Methods in Physics Research B **106**, 313-317 (1995).

8. Ion damage buildup and amorphization processes in GaAs-$Al_xGa_{1-x}As$ multilayers
H.H. Tan, C. Jagadish, J.S. Williams, J. Zou and D.J.H. Cockayne
Journal of Applied Physics **80**, 2691-2701 (1996).

9. Large energy shifts in GaAs-AlGaAs quantum wells by proton irradiation-induced intermixing
H.H. Tan, J.S. Williams, C. Jagadish, P.T. Burke and M. Gal
Applied Physics Letters **68**, 2401-2403 (1996).

10. Recrystallization of high energy As implanted GaAs studied by TEM
J. Jasinski, Y. Chen, J. Washburn, Z. Liliental-Weber, H.H. Tan, C. Jagadish and M. Kaminska
Applied Physics Letters **68**, 1501-1503 (1996).

11. Ultrafast carrier trapping in high energy ion implanted GaAs
C. Jagadish, H. H. Tan, A. Krotkus, S. Marcinkevicius, K.P. Korona and M. Kaminska
Applied Physics Letters **68**, 2225-2227 (1996).

12. Damage to epitaxial GaN layer by Si implantation
H.H. Tan, J.S. Williams, J. Zou and D.J.H. Cockayne, S.J. Pearton and R.A. Stall
Applied Physics Letters **69**, 2364-2366 (1996)

13. Photo-modulated photoluminescence in semiconductor quantum wells
T. Baars, A. Chtanov, M. Gal, H.H. Tan and C. Jagadish
Physical Review B (submitted, Aug. 1996).

14. Ion implanted GaAs for subpicosecond optoelectronic applications
H.H. Tan, C. Jagadish, K.P. Korona, J. Jasinski, M. Kaminska, R. Viselga, S. Marcinkevicius and A. Krotkus
Special issue of IEEE Journal of Quantum Electronics (submitted, Sept. 1996).

Conference papers

1. Damage in $GaAs/Al_xGa_{1-x}As$ structures by keV and MeV Si ion beams
   H.H. Tan, J.S. Williams and C. Jagadish
   Proceedings of the Australian Compound Optoelectronic Materials and Devices Conference, Canberra, Australia 201-205 (1993).

2. Dynamic annealing and amorphous phase formation in Si, GaAs and AlGaAs under ion irradiation
   J.S. Williams, H.H. Tan, R.D. Goldberg, R.A. Brown and C. Jagadish
   Material Research Society Symposium Proceedings **316**, 15-25 (1994).

3. Measurement of ion induced damage profiles in GaAs using differential reflectance
   M. Gal, P. Kraisingdecha, C. Shwe, M. Gross, H.H. Tan and C. Jagadish
   Proceedings of the 22nd. International Conference on The Physics of Semiconductors, Vancouver, Canada, 141-144 (1994).

4. Characterization of deep levels created by proton irradiation in GaAs using deep level transient spectroscopy
   H.H. Tan, J.S. Williams and C. Jagadish
   Proceedings of the Australian Compound Optoelectronic Materials and Devices Conference, Sydney, Australia 166-170 (1994).

5. Electrical, optical and structural properties of MeV As implanted and annealed GaAs
   M. Kaminska, J. Jasinski, A. Kurprewski, K.P. Korona, M. Palczewska, A. Krotkus, S. Marcinkevicius, H.H. Tan and C. Jagadish
   Proceedings of the Australian Compound Optoelectronic Materials and Devices Conference, Sydney, Australia 117-120 (1994).

6. Measurement of damage in keV ion implanted GaAs by differential reflectance spectroscopy
   P. Kraisingdecha, M. Gal, H.H. Tan and C. Jagadish
   Proceedings of the Ninth Conference on Ion Beam Modification of Materials, Canberra, Australia, J.S. Williams, R.G. Elliman and M.C. Ridgway, editors, 1118-1122 (1996).

7. Picosecond lifetime and high resistivity in As or Ga implanted GaAs : an alternative material for fast optoelectronic applications
H.H. Tan, C. Jagadish, M. Kaminska, J. Jasinski, A. Krotkus and S. Marcinkevicius
Proceedings of the IEEE LEOS'95 8th. annual meeting, San Francisco, U.S.A. vol. 1, 345-346 (1995).

8. Quantum well intermixing by proton irradiation
H.H. Tan, C. Jagadish and M. Gal
Proceedings of the IEEE LEOS'95 8th. annual meeting, San Francisco, U.S.A. vol. 2, 94-95 (1995).

9. Irradiation-induced damage and intermixing of GaAs-AlGaAs quantum wells
H.H. Tan, J.S. Williams, C. Jagadish and M. Gal
Material Research Society Symposium Proceedings **396**, 823-827 (1996).

10. Ion damage and annealing of epitaxial GaN layers and comparison with GaAs/AlGaAs materials
H.H. Tan, J.S. Williams, C. Yuan, and S.J. Pearton
Material Research Society Symposium Proceedings (in press, 1996)

11. Ion implantation processing of GaN epitaxial layers
H.H. Tan, J.S. Williams, J. Zou, D.J.H. Cockayne, S.J. Pearton and C. Yuan
Proceeding of the 189th. Electro-chemical Society Meeting, Los Angeles, U.S.A. (in press, 1996).

12. High dose Si- and Mg-implantation in GaN : electrical and structural analysis
J.C. Zolper, M.H. Crawford, J.S. Williams, H.H. Tan and R.A. Stall
Proceedings of the Tenth Conference on Ion Beam Modification of Materials, Albuquerque, U.S.A. (in press, 1996).

13. InGaAs GRINSCH-SQW lasers with novel carbon delta doped contact layer
S. Yuan, G. Li, H.H. Tan, C. Jagadish and F. Karouta
IEEE LEOS'96 9th. annual meeting, Boston, U.S.A. (Nov. 1996).

14. Solid-phase epitaxial growth of $Al_xGa_{1-x}As$: compositional dependence on regrowth
S.M. Hogg, H.H. Tan and M.C. Ridgway
Conference on Optoelectronic and Microelectronic Materials and Devices, Canberra, Australia (Dec. 1996).

15. Ion implantation for wavelength-shifting and quantum wire lasers
H.H. Tan, Y. Kim and C. Jagadish
Conference on Optoelectronic and Microelectronic Materials and Devices, Canberra, Australia (Dec. 1996).

16. Ion implantation intermixing of quantum wells and its applications to optoelectronic devices
H.H. Tan, F. Karouta, Y. Kim, C. Jagadish, P.T. Burke and M. Gal
Progress In Electromagnetics Research Symposium '97, Kowloon, Hong Kong (Jan. 1997).